Summer 2023

Expanding on the Solid State Chemistry of *f*-Element Chalcogenides

Logan Skyler Breton

Recommended Citation

Breton, L. S.(2023). *Expanding on the Solid State Chemistry of f-Element Chalcogenides.* (Doctoral dissertation). Retrieved from https://scholarcommons.sc.edu/etd/7475

Expanding on the Solid State Chemistry of *f*-element Chalcogenides

by

Logan Skyler Breton

Bachelor of Science
Florida State University, 2018

Submitted in Partial Fulfillment of the Requirements

For the Degree of Doctor of Philosophy in

Chemistry

College of Arts and Sciences

University of South Carolina

2023

Accepted by:

Hans-Conrad zur Loye, Major Professor

Aaron K. Vannucci, Committee Member

Linda S. Shimizu, Committee Member

Theodore M. Besmann, Committee Member

Ann Vail, Dean of the Graduate School

DEDICATION

For the numerous friends, family, teachers, and mentors that helped me along the way, and to myself, who has endured this journey and emerged a better scientist and person.

ACKNOWLEDGMENTS

There are many people who have helped me along this journey to obtain my PhD. I would firstly like to thank my advisor, Prof. zur Loye, for his support and guidance. He not only helped me build a foundation of chemistry knowledge, but also allowed me the freedom to explore my research interests fueling my passion for materials synthesis. I would also like to thank my committee members, for their time and expertise that helped bolster my presentation and question answering skills.

I especially want to thank my family as it was with their endless love and support that helped me push on even in the hardest times of this PhD journey. Additionally, I thank my friends who were there to listen and give advice whenever I needed it.

I would also like to thank God who has always been by my side and gave me the strength to press on.

ABSTRACT

An overarching goal in solid state chemistry is to achieve predictability regarding the synthesis of compounds with desired properties. While this goal is far from being reached, solid state chemists are hard at work synthesizing and characterizing new materials to further our understanding of structure-property relationships, and to expand our fundamental knowledge to rationalize the outcomes of solid-state syntheses. With the advent of new solid state synthetic methods, novel compounds exhibiting exciting properties are still being discovered today. The infancy of these synthetic methods promises a myriad of undiscovered compounds with potentially interesting properties which has resulted in a recent renaissance of research into solid state materials.

Metal chalcogenides are currently among the most important classes of materials based on their structural and compositional diversity. These materials have exhibited many attractive magnetic, electronic, and optical properties placing them in the spotlight for both fundamental studies and industrial applications. Unfortunately, obtaining metal chalcogenides is difficult, especially relative to metal oxides, which has warranted further research into the synthetic pathways utilize to obtain them. This dissertation will expand on research in the solid-state syntheses of metal chalcogenides, pointing out synthetic trends to help rationalize syntheses, tackling persistent synthetic issues barring the synthesis and property measurements of these materials, and carving new synthetic paths to novel and existing metal chalcogenide materials.

TABLE OF CONTENTS

LIST OF TABLES

LIST OF FIGURES

LIST OF SYMBOLS

K	Kelvin
ºC	Degrees Celsius
º	Degrees
λ	Wavelength, normally expressed in nanometers
ν	Frequency, normally expressed in cm^{-1}
Å	Angstrom
$K\alpha$	X-ray emission due to electron transition from a 2p → 1s orbital
2θ	Diffraction angle
g	Gram
Z	Number of formula units
F	Structure factor
F^2	The structure factor squared
R	Residual factor
R_1	Residual factor for refinement against F
wR_2	Residual factor for refinement against F^2
R_{int}	Merging error; a measure of the precision/reproducibility
μ_B	Bohr magneton, a constant quantifying the magnitude of a magnetic moment
μ_{eff}	Effective magnetic moment
T	Tesla, a unit representing magnetic flux density
θ	Weiss Temperature

eV	Electronvolt
T_N	Neel temperature, the temperature at the onset of an antiferromagnetic interaction
$\Delta_f G^\circ$	Gibbs free energy of formation at 0 Kelvin
$\Delta_f H^\circ$	Enthalpy of formation at 0 Kelvin
χ	Temperature dependent magnetic susceptibility
χ^{-1}	Temperature dependent inverse magnetic susceptibility
χ^0	Temperature independent magnetic susceptibility

LIST OF ABBREVIATIONS

BCM	Boron-Chalcogen Mixture
BVS	Bond Valence Sums
CIF	Crystallographic Information File
EDS	Energy Dispersive Spectroscopy
FC	Field Cooled
FU	Formula Units
ICSD	Inorganic Crystal Structure Database
NLO	Nonlinear Optical Spectroscopy
OQMD	Open Quantum Material Database
PL	Photoluminescence
PXRD	Powder X-ray Diffraction
SEM	Scanning Electron Microscopy
SHG	Second Harmonic Generation
SQUID	Superconducting Quantum Interference Device
SXRD	Single Crystal X-ray Diffraction
UV-Vis	Ultraviolet-Visible Spectroscopy
WPPF	Whole Powder Pattern Fit
XRD	X-ray Diffraction
ZFC	Zero-Field Cooled

LIST OF COMPOUNDS BY CHAPTER

INTRODUCTION

The synthesis of new materials and compounds relies on the controlled ability to both break and form bonds. In organic chemistry, this ability has been demonstrated with a high degree of predictability by controlling both thermodynamic and kinetic parameters which has led, and continues to lead, to a plethora of new molecular compounds. These parameters include the understanding of the relative stabilities and electronic structures of the reagents used, intermediates formed, and resulting products. As technology advances, new methods, such as *in situ* spectroscopy and computational characterization, have furthered this understanding, elucidating mechanisms that can be used to design syntheses and their products. Contrary to organic chemistry, solid state chemistry is generally less predictable due to the multi-dimensional bonding (i.e. 1-D, 2-D, and 3-D) that can occur in extended, crystalline structures which differs from organic molecules. While extended structures of organic molecules exist, for example with the discovery and synthesis of molecular organic frameworks (MOFs) and covalent organic frameworks (COFs), only the local environments can be predicted while the stacking of molecules and prediction of complete crystalline structures remains a challenge. In solid-state chemistry, predictability becomes even more difficult with the synthesis of novel solid-state materials that have no structural or compositional analogues which makes characterization difficult. Other synthetic parameters such as the wide range of solid state reaction temperatures (-100 to ≥ 2000 ºC), varying phase states of the reagents, intermediates, and products (e.g. solid, liquid, and gas), and stabilities of the various reagents used (i.e. elements or compounds) all play a significant role in the reaction mechanisms which makes prediction of the resulting products challenging.[1] For these reasons, the hunt for predictability of materials synthesis is an ultimate goal of solid-state chemistry that is still being pursued today.

Regardless of the aforementioned challenges, solid state chemists have already and continue to synthesize a diverse plethora of novel and complex solid-state compounds, some by serendipity, but others using fundamental chemical bonding concepts (e.g., ionic radii, electronegativity, bond valence sums, etc.) to rationalize the outcomes of reactions, bringing the solid-state chemist the closer to achieving predictability in their syntheses. To continue to build on these fundamental bonding concepts, new materials must be synthesized and characterized to gain fundamental knowledge of the structures and resulting properties of compounds. To do this, exploratory crystal growth is utilized to survey structural and compositional phase spaces to create novel compounds, the single crystal nature of which allows for relatively facile structural determination.

Exploratory Crystal Growth

Exploratory crystal growth in synthetic solid-state chemistry is a "trial and error" process that uses various crystal growth methods and experimental parameters for the synthesis of a desired product. These methods and parameters are chosen depending on the targeted composition, properties, and intended characterization of the product. Some characterization techniques, such as magnetic measurements and neutron diffraction, require bulk samples, while other characterization techniques, such as single crystal X-ray diffraction (SXRD), require single crystal products. For bulk powder measurements, traditional solid-state methods have often been employed. This synthetic technique is very sensitive as there are many parameters that can affect the resulting product, including the stoichiometry and purity of the starting reagents, the quality of the mixing (grinding) of reagents and even the state of the furnace being used as a difference in temperature gradient in one furnace versus another could cause different products to be formed.[2]

Solid State Synthesis

Solid-state synthesis is the reaction of reagents in their solid-state. In a typical solid-state reaction, powder reagents are combined using a mortar and pestle and are intimately ground. This ground mixture is then placed in a container, preferably one inert to the reagents used, and placed in a furnace set to ramp to a high temperature (typically 400-1200 °C), and is kept at these temperatures for long reaction times. The intimate mixing, high temperatures, and long reaction times are all necessary for solid state reactions to overcome the inherent diffusion limitations and to result in a phase pure product. Solid-state reactions are diffusion limited and require thermal energy to proceed at an acceptable rate. Intimate mixing of the reagents can help speed the diffusion process and also, as mentioned previously, gives the greatest chance for yielding phase pure products. Due to the nature of solid-state reactions, the products are typically polycrystalline powders. These products can be analyzed using diffraction methods, such as powder X-ray diffraction (PXRD), which can be used for phase identification and to check the crystallinity of the obtained material. The polycrystalline nature of solid-state reaction products makes structure determinations of new materials extremely challenging. While the structures of new compounds can be solved from powders by Rietveld refinement of PXRD patterns, it is limited to relatively simple cases or requires the use of a parent structure as a starting point for the refinement.[3] Therefore when targeting novel compounds, the use of traditional solid-state syntheses becomes limited. Furthermore, the high temperatures used in solid-state synthesis tend to produce the most thermodynamically stable product which leaves many lower temperature kinetic phases undiscovered. It is therefore desirable to use other synthetic methods that can operate at lower temperatures and produce single crystal products that are much more readily characterized. One method used to combat the shortcomings of traditional solid-state syntheses is the molten flux growth method.

Molten Flux Growth

The molten flux growth method is one that aims to overcome the diffusion issues of the solid-state methods by adding a “liquid” component in the form of a molten flux that allows for much faster diffusion rates. Upon heating, the molten flux dissolves the starting reagents and upon cooling creates a supersaturated solution that precipitates out the crystalline product. These molten fluxes are usually alkali or alkaline earth salts that will melt at relatively low temperatures and that can be easily removed from the reaction products by dissolution in a common solvent. When choosing a flux, the desired reaction temperature is an important determination to make. Different fluxes have varying melting points and solubilities depending on their chemical composition. Specific mixtures of fluxes, called eutectics, will have a lower melting point then the individual salts and can be used if lower temperature phases are targeted. The addition of new flux media, such as polychalcogenide fluxes, have been paramount in the discovery of new phases and surveying reactions using the same reagents but different fluxes can result in radically different products. A great advantage of the molten flux method is that the initial grinding steps necessary in traditional solid-state syntheses are no longer required. The reagents and flux are simply added to a container, again, one that is now inert to not only the reagents but also the flux, which is placed in a furnace and set to the desired heating profile. It is customary to choose a reaction temperature that is 100 ºC above the flux's melting point to ensure the full melting of the flux, which will give the greatest chance for the dissolution of the other reagents inside the flux. It is then customary to slowly cool to 100 ºC below the melting point of the flux to ensure that the flux has solidified and to give the resulting crystals the slow cooling they need to create large, well-faceted crystals. The single crystalline nature of the products resulting from a molten flux reaction allow for convenient structural characterization using SXRD which readily yields a complete structure determination. Another advantage of using the flux method is that kinetic phases that cannot be prepared at the high temperatures of solid-state reaction can now be accessed resulting in a plethora of new phases and compositions of compounds. The subjects of this dissertation will utilize both solid-state and molten flux growth methods for the exploratory crystal growth of metal chalcogenides.

Metal Chalcogenides

Metal chalcogenides are currently among the most important classes of materials based on their structural and compositional diversity, surpassed only by organic compounds and metal oxides. A chalcogenide material is one that contains a chalcogen, which are the group 16 elements, excluding oxygen. The chemistry of oxygen and the chalcogens are so different that oxygen is not included in the group of chalcogens. Therefore, the chalcogens, many times denoted by the letter Q in the literature, are sulfur, selenium, tellurium, and polonium, although polonium is radioactive and highly toxic and, therefore, not typically used in exploratory syntheses and is thus typically left out of the conversation when speaking about the chalcogens. A large difference between the chalcogens and oxygen is the ability of the chalcogens to catenate, that is to form stable Q-

Q bonds, which can result in very complex anions such as the Q_x^{2-}, where x can be up to 8. These complex anionic fragments can be incorporated into crystals and create structures not observed for oxide systems. These structures can therefore exhibit properties that also cannot be realized in oxide systems, which makes chalcogenides an attractive area of study for both synthetic and property-oriented purposes. Nonetheless, there are some similarities between oxide and chalcogenide systems especially when it comes to the combination of early transition and main group metal metals with oxygen and the chalcogens. These can create analogous molecular oxo- and chalco-anionic groups, such as the silicates and phosphates (e.g. $[SiO_4]^{4-}$, $[PO_4]^{3-}$, and $[P_2O_7]^{4-}$) that have chalcogenide analogues (i.e. $[SiS_4]^{4-}$, $[PS_4]^{3-}$, and $[P_2S_7]^{4-}$). Though, as mentioned before, the ability of the chalcogens to catenate can create chalco-anions which have no oxide analogue, such as the selenophosphate anions, $[P_2Se_6]^{4-}$, $[P_2Se_7]^{3-}$, $[P_2Se_8]^{2-}$, and even $[P_8Se_{18}]^{6-}$. The great diversity in chalcogenide structures due to their unique ability to catenate has already resulted in compounds that have shown use beyond fundamental studies.

Metal chalcogenides have become the very foundation of many important technologies, such as $CuInSe_2$ and CdTe, which are the best preforming thin-film solar voltaic materials, and the Co(Ni)/Mo/S compositions, which are paramount in the hydrodesulfurization process of crude oil all around the world.[4] Further, metal chalcogenides can be found in a variety of cutting edge research areas such as fast ion conductors[5, 6], topological insulators[7-9], radiation detectors[10-12], nonlinear[13-15], and novel magnetic materials[16-18], to name a few. The uniqueness of chalcogenide structures and the usefulness of their properties has placed a spotlight on these materials and has motivated research on existing compounds as well as encouraged the investigation of new synthetic pathways to obtain both known and novel chalcogenide materials. The latter is due to the simple fact that these chalcogenide materials are difficult to synthesize due to their tendency to react with atmospheric oxygen, which has slowed the preparation of new metal chalcogenides and thus the discovery of new materials with desired properties. It is this search for new synthetic pathways and chalcogenide materials that has been the overarching goal of my research and in this dissertation, I will present my work specifically targeting the synthesis and characterization of rare earth and actinide chalcogenides with an emphasis on exploring their optical and magnetic properties.

Rare Earth Chalcometallates

Chalcometallate compounds are those that contain the complex chalco-anions mentioned previously. These include chalco-phosphates, -silicates, -germinates, and -borates to name a few. Many chalcometallate compounds have shown interesting physical properties that have warranted their further investigation. This includes tin thiophosphate, $Sn_2P_2S_6$, which is a ferroelectric and piezoelectric material that also possesses enhanced photorefractive properties that can be exploited for use in memory devices.[19-22] The manganese analogue, $Mn_2P_2S_6$, exhibits strong non-linear optical (NLO) properties, as well as spontaneous magnetization even at temperatures as high as 40 K.[23, 24] These examples demonstrate that the exploration of different compounds that may contain the same chalcometallate building blocks could result in a range of desired properties in these materials and that the synthesis of analogous compounds is of great importance. When complexed with the rare earth elements, rare earth chalcometallates, such as those in the $LnPS_4$ family of compounds, exhibit attractive optical properties such as strong emission under UV excitation and pigment-quality properties.[25, 26] From a structural point of view, the incorporation of the lanthanides allows for the observation of the lanthanide contraction phenomenon, which can have an effect on the symmetry of the compounds. For example, the series of $Cs_2NaLn(PS_4)$ (Ln = La-Nd, Sm, and Gd-Ho) were synthesized and a change in the local coordination environment from 8 (for Ln = La-Sm) to 9 (for Ln = Gd-Ho) was observed, which resulted in structures that were almost identical but distinct from each other.[27] It is observations such as these that can help increase fundamental knowledge of the behavior of structures incorporating various size cations again with the hope of achieving some predictability in the synthesis of these compounds. As can be observed from the examples given, the thiophosphates are a rich family of compounds in both structural diversity and exhibited physical properties. The structural diversity of thiophosphates, their synthesis, characterization, and observed synthetic trends will be one subject in this dissertation.[28]

Another interesting group of chalcometallate compounds are the thioborates. Metal thioborates have been studied extensively for their great structural diversity as well as for their nonlinear optical (NLO) properties. Crystalline materials that exhibit good NLO performance are in demand applications in the fields of optical communication and laser medicine. NLO materials can generate coherent light at frequencies that commercial lasers cannot reach or at which they perform poorly, for example the infrared (IR) region.[29] This IR region is called the fingerprint region for inorganic and organic molecules and is extremely important for the sensing of dangerous materials, such as biohazards[30], pollutants[31], and chemical warfare agents.[32] While useful, the evolution of the above applications has been slowed due to the lack of available NLO materials that are efficient in the IR region, which has prompted research into their synthesis and characterization.

Many oxide NLO materials are known, including BaB_2O_4, LiB_3O_5, and KH_2PO_4, but absorption in the IR has prevented the use of these materials in the above-mentioned applications.[33] Thioborates have been considered the most promising new class of NLO materials due to attractive properties such as wide transmission range and transparency in the IR regions as well as high laser damage thresholds. For example, the barium thioborate, BaB_2S_4, exhibits a large band gap (3.55 eV), large NLO second harmonic generation (SHG) of 0.7 x the benchmark chalcogenide standard $AgGaS_2$, and a laser damage threshold 8 x $AgGaS_2$ making it a very attractive candidate for IR-NLO applications.[34]

While promising, a significant drawback of current thioborate materials are the difficulties involved with their syntheses. These include air and moisture sensitive reagents that necessitate the use of glove-boxes and inert atmospheres, and a lack of single crystalline products due to the synthetic methods used (i.e., traditional solid state and high pressure syntheses) that hinder the application of the obtained compounds. The rare earth thioborates, $LnBS_3$, for example, combine the laser active lanthanides with the $[BS_3]^{3-}$ unit, which is known to induce non-centrosymmetric structures that are a prerequisite for NLO materials. Unfortunately, only powders of these materials have been synthesized, with the exception of $PrBS_3$, for which crystals were obtained from a high pressure – high temperature reaction. The need for a more facile synthesis of these materials and, in addition, of single crystal materials, is pressing and my research into new synthetic approaches for these materials is a subject of this dissertation.[35]

Actinide Chalcogenides

Uranium and the other actinide elements are unique due to the presence of 5*f* electrons that dictate many of their physical properties. The 5*f* orbitals are intermediate between those of the lanthanide's 4*f* orbitals and the transition metal's 3*d* orbitals. The lanthanide's 4*f* orbitals do not extend far away from the nucleus, as a result of shielding by the 5*p* and 5*s* orbitals, causing the electrons within the 4f orbitals to be more localized. Comparatively, the 3*d* orbitals of the transition metals are poorly shielded by other orbitals and thus extend far out from the nucleus resulting in more delocalization of the electrons. The 5*f* orbitals of the actinides, which exhibit radial extensions between those of the 3*d* and 4*f* orbitals, still have a degree of shielding and contain electrons which are somewhat localized. Differences in the orbital extent of the ions in a compound have a profound effect on their bonding and their resulting properties, such as magnetism. Magnetism in metal complexes arises due to the spins of unpaired electrons and their interactions. The spinning charged particle creates a magnetic moment, the magnitude of which is sensitive to the orbitals that contain them. The magnetic moment produced by electrons in a 4*f* orbital is contributed to most by spin-orbit coupling, while 3*d* orbital electrons have contributions from both spin-orbit coupling and ligand field splitting. The intermediate nature of the 5*f* orbitals causes a large contribution from spin-orbit coupling and a smaller contribution from ligand field splitting.[36] In each system, the extent to which the 5*f* electrons influence the product structure and resulting magnetic properties may be different, presenting a wealth of synthetic opportunities to prepare new compounds, which may help elucidate our understanding of this phenomenon. Ultimately, our goal is to achieve the ability to tailor syntheses to create structures with desired magnetic properties.

Current research of uranium containing compounds is aimed at the creation and characterization of novel uranium (VI) compounds.[37] This focus is due to the tendency of uranium to oxidize to its +6 oxidation state in the presence of oxidizing agents, such as atmospheric oxygen. While there are examples of uranium (IV) oxides, such as the uranium (IV) phosphates, the majority of known uranium oxide phases contain uranium (VI).[3, 38, 39] Relative to uranium (VI), there has been much less research on uranium in its lower valence states as a result of the synthetic challenges associated with maintaining uranium in a reduced oxidation state. Contrary to uranium oxides, the majority of synthesized uranium chalcogenides contain uranium in its +4 oxidation state. The decreased Lewis basicity of the chalcogenides versus oxygen affords compounds with uranium in lower valence states and allows for the further exploration of these low valent uranium compositions. With uranium (VI) being diamagnetic, the ability to synthesize compositions with paramagnetic uranium (IV) will allow for the investigation of magnetic properties of uranium containing compounds.[37] Uranium chalcogenide materials began to be explored in the 1940's with a concentration on the synthesis and characterization of on binary uranium chalcogenide compounds. Higher order actinide chalcogenides were left undiscovered mostly due to a lack of viable synthetic routes and analytical technology to fully characterize obtained products.[40] Ternary and quaternary actinide chalcogenides began to be thoroughly studied in the late 1990's to 2000's especially with to the development of the flux growth method.[41, 42] Recent years have seen a large growth in complex metal chalcogenide synthesis as synthetic methodologies are developed and applications for the obtained materials are discovered. The translation of these methodologies to the actinides has been much slower mostly due to the radioactive nature of the actinides and thus the special facilities and handling that is involved with their usage. Thus, given that research into complex uranium chalcogenide chemistry relatively still in its infancy, there are many unexplored phase spaces that promise to contain interesting structures and concomitant magnetic properties.

One of the largest obstacles faced when synthesizing actinide chalcogenides is the extreme oxophylicity of the actinides which, even with careful oxygen exclusion using glove boxes, oxide free reagents, etc., will inevitably result in actinide oxide or oxychalcogenide impurities in the products. Some of these impurities, such as uranium oxysulfide, UOS, contain magnetic uranium (IV) which prevents magnetic measurements on samples contaminated with UOS. Thus, while novel uranium chalcogenides have been synthesized, the elucidation of their magnetism remains a challenge. Dealing with oxide and oxysulfide impurities in these systems thus became a major focus of my own work, as creating products without these impurities were necessary to explore the magnetism of these phases. In this dissertation, a new synthetic method which has dealt with the issue of oxygen will be presented and its use in creating chalcogenide and oxychalcogenide actinide compounds will be demonstrated. The magnetic measurements of these compounds will also be presented.[43, 44]

In summary, the goal of predictability in the synthesis of solid-state compounds remains a challenge, but fundamental research into synthetic concepts is ongoing. Metal chalcogenides are a fruitful area of study for both structural and property-oriented investigations and when new impurity free materials are created, their properties will be studied. With the completion of this dissertation, I have performed many investigations into the synthetic methods used to create rare earth and actinide chalcogenides, gaining fundamental knowledge, and then applying this knowledge to carve new paths to these chalcogenide materials. I believe that my work is a valuable contribution to the field of metal chalcogenides and has already and will continue to promote the creation of new compounds allowing for their properties to finally be investigated.

Outline

This thesis summarizes the work I have done on the synthesis and characterization of actinide and lanthanide chalcogenides. Chapter 1 will present my work on expanding the known lanthanide thiophosphate compounds while also observing synthetic trends that help increase predictability when it comes to the synthesis of certain thiophosphate structures. Chapter 2 introduces the Boron-Chalcogen Mixture (BCM) method which tackles obstacles in the synthesis of actinide chalcogenides, granting greater access to these materials and their properties. Chapter 3 shows an application of the BCM in creating new alkali platinum group metal uranium sulfides, utilizing the *in situ* polychalcogenide flux formation afforded by the BCM method, to explore their magnetic properties. Chapter 4 demonstrates the use of the BCM method as a method of carving a new low-temperature synthetic path to single crystalline lanthanide thioborates, which were previously believed to only form at high temperatures and pressures, predominately resulting in polycrystalline powder products. Chapter 5 presents the expansion of the BCM method towards the synthesis of mixed anion materials. Finally, Appendix A shows the continued use of the BCM method for the synthesis and magnetic property measurements of some Ba_3MUS_6 compounds.

CHAPTER 1

TRENDS IN RARE EARTH THIOPHOSPHATE SYNTHESES: $Rb_3Ln(PS_4)_2$ (Ln = La, Pr, Ce), $Rb_{3-x}Na_xLn(PS_4)_2$ (Ln = Pr, Ce; x = 0.50, 0.55), and $RbEuPS_4$ OBTAINED BY MOLTEN FLUX CRYSTAL GROWTH[1]

---

[1] Reproduced with permission from Breton, L. S., Smith, M. D., and zur Loye, H.-C., *CrystEngComm*, **2021**, 23, 5241-5248. © The Royal Society of Chemistry 2021

Abstract: Single crystals of new rubidium rare earth thiophosphates with the formulas $Rb_3Ln(PS_4)_2$ (Ln = La, Pr, Ce), $Rb_{3-x}Na_xLn(PS_4)_2$ (Ln = Pr, Ce; x = 0.50, 0.55), and $RbEuPS_4$ were crystallized out of a molten RbCl flux. The compounds $Rb_3Ln(PS_4)_2$ (Ln = La, Pr, Ce) and $Rb_{3-x}Na_xLn(PS_4)_2$ (Ln = Pr, Ce; x = 0.50, 0.55) both crystallize in the monoclinic crystal system adopting the space groups $P2_1$ and $P2_1/c$, respectively, while $RbEuPS_4$ crystallizes in the orthorhombic crystal system adopting the space group *Pnma*. A survey of all known rubidium rare earth thiophosphates grown using an alkali halide flux revealed trends suggesting that the $Rb_3Ln(PS_4)_2$ and $Rb_{3-x}Na_xLn(PS_4)_2$ families of compounds can be actively targeted over a wide range of temperatures by employing RbCl as at least one component of the flux. Fluorescence measurements were performed on all compounds obtained, revealing resolved f-f transitions in $Rb_3Pr(PS_4)_2$ and $Rb_{2.45(2)}Na_{0.55(2)}Pr(PS_4)_2$ and only single broad emission peaks for $Rb_3Ce(PS_4)_2$ and $Rb_{2.50(6)}Na_{0.50(6)}Ce(PS_4)_2$, behavior characteristic for cerium(III) compounds.

Introduction. Molten flux crystal growth is a popular synthetic method that has become a pillar of modern solid state chemistry due to its continued success in the production of X-ray diffraction quality single crystals of a wide variety of structural families, including metal oxides[2, 3, 45], halides[46, 47], and chalcogenides.[4, 43, 48-51] The use of alkali halide fluxes in particular has resulted in many new single crystalline compounds, while also having the added benefit of the desired crystalline products being easily removed from the product mixture using common solvents, such as water or methanol.

Molten flux synthesis has been shown to be an effective approach for the synthesis of thiophosphate compounds and, over the past decades, has resulted in the successful crystal growth of various thiophosphate compositions incorporating many elements, including transition metals[52-54], rare earth metals[55-58], and the actinides.[37, 43] The thiophosphates have garnered attention in recent years for their high ionic conductivities[59, 60] and for their non-linear optical properties.[61, 62] In addition, numerous studies have focused simply on investigating the rich structural chemistry of thiophosphates, which were found to exhibit great diversity and modularity in composition and structure due to the many thiophosphate motifs that exists and that have been incorporated into new crystal structures, such as the thiopyrophosphate building block $P(V)_2S_7^{4-}$,[63, 64] the ortho-thiophosphate building block $P(V)S_4^{3-}$,[65-71] the hexathiometadiphosphate building block $P(V)_2S_6^{4-}$,[57, 72] and the hexathiohypophosphate building block $P(IV)_2S_6^{2-}$.[57, 72-76]

Alkali halide fluxes have been demonstrated to be very effective for crystallizing new thiophosphate compounds, such as those prepared in alkali iodide melts by Klepov et al.[74], who reported on numerous rare earth containing thiophosphates, such as the two-dimensional $NaLnP_2S_6$ (Ln = La, Ce, Pr) thiohypophosphates and $CsLnP_2S_7$ (Ln = Pr, Nd, Sm, Gd, Tb, Dy, Ho, Er, Yb, Y) thiopyrophosphates[74], as well as the family of one-dimensional thiophosphates, $Cs_2NaLn(PS_4)_2$ (Ln = La-Nd, Sm, Gd-Ho).[27] Alkali bromide and chloride fluxes also function well for the synthesis of novel thiophosphates, such as the $ALnP_2S_6$ series[76] grown out of RbBr and CsBr fluxes, and $K_4Nd_2(PS_4)_2(P_2S_6)$ grown out of a KCl flux.[75] Due to the relative sparseness of rubidium containing rare earth thiophosphates, by comparison with those incorporating the other alkali metals, syntheses to create the rubidium analogues of the $Cs_2NaLn(PS_4)_2$ series created by Klepov et al. were carried out by Kutahyali Aslani et al., by employing the same reagents and ratios but replacing the cesium iodide used by Klepov et al. with rubidium bromide. The change in flux resulted, however, in a new family of thiophosphates with formulas $Rb_4Ln_2(P_2S_6)(PS_4)_2$ (Ln=La, Ce, Pr, Nd, Sm, Gd).[56]

An overarching goal of solid-state chemistry is to achieve the ability to predict structures and to ultimately engineer structures with desired properties. Given the great diversity of thiophosphate structures created in different flux environments, we decided to pursue the synthesis of new thiophosphates by exploring the role of the flux on the formation of thiophosphate products in the hope to better understand the role of the flux as well as to perhaps be able to predict product formation.[4] To probe the effects of the flux on the resulting product formed, experiments were carried out using the same reagents and molar ratios used by Kutahyali Aslani et al., however, this time employing a RbCl flux in place of the previously used RbBr. Herein we report on the synthesis, crystal structures, and select optical measurements of the new rubidium rare earth thiophosphates $Rb_3Ln(PS_4)_2$ (Ln = La, Pr, Ce), $Rb_{3-x}Na_xLn(PS_4)_2$ (Ln = Pr, Ce; x = 0.50, 0.55), and $RbEuPS_4$ obtained by employing the RbCl flux. In addition, we discuss our current thoughts concerning the role of the flux in the creation of rubidium rare earth thiophosphates.

Experimental:

Synthesis. P_2S_5 (99%, Sigma-Aldrich), Na_2S (Alfa Aesar), N,N-dimethylformamide (DMF, Sigma-Aldrich, ACS grade), methanol (MeOH, VWR, ACS grade), and La_2S_3 (STREM Chemicals inc., 99.9%) were all used as received. P_2S_5 and Na_2S were stored and handled in a nitrogen glove bag. Ce_2S_3, Pr_2S_3, and EuS were obtained according to the procedure described in the literature.[77]

The compounds $Rb_3Ln(PS_4)_2$ (Ln = La, Pr, Ce) and $Rb_{3-x}Na_xLn(PS_4)_2$ (Ln = Pr, Ce; x = 0.50, 0.55) were all obtained using the same synthetic conditions. In a nitrogen filled glove bag, powders of Ln_2S_3 (Ln = La, Ce, Pr) (0.265 mmol), Na_2S (1.063 mmol), and P_2S_5 (1.062 mmol) were loaded into a fused silica tube in a 1:4:4 molar ratio along with 1 gram of RbCl flux. The fused silica tube was flame sealed under vacuum and placed in a box furnace set to ramp up to 820 °C in 1 hour where it dwelled for 20 hours and was subsequently slow cooled to 620 °C in 30 hours. The furnace was then shut off to allow the reaction mixture to cool to room temperature. The compound $RbEuPS_4$ was synthesized using an EuS, Na_2S, P_2S_5 molar ratio of 1:2:2 which was loaded into a fused silica tube that was evacuated, flame sealed, and placed in a box furnace set to the same temperature profile detailed above. To remove the flux and to isolate the single crystals, all products were sonicated in DMF and then subsequently sonicated in MeOH. The crystalline products were filtered and dried in air. The products are moisture sensitive and were therefore stored in a desiccator. Translucent plate crystals of the $Rb_3Ln(PS_4)_2$ and $Rb_{3-x}Na_xLn(PS_4)_2$ compounds were obtained via the same product mixtures for each lanthanide sulfide reagent used. $RbEuPS_4$ was obtained as large yellow/brown plates and was a phase pure product.

Single Crystal x-ray Diffraction. X-ray intensity data from small irregular crystals were collected at 301(2) K for the compounds $Rb_3Ln(PS_4)_2$ (Ln = Pr, Ce), $Rb_{2.50(6)}Na_{0.50(6)}Ce(PS_4)_2$, and $RbEuPS_4$, at 291(2) K for $Rb_3La(PS_4)_2$, and at 100(2) K for $Rb_{2.45(2)}Na_{0.55(2)}Pr(PS_4)_2$ using a Bruker D8 QUEST diffractometer equipped with a PHOTON-II area detector and an Incoatec microfocus source (Mo Kα radiation, λ = 0.71073 Å). The raw area detector data frames were reduced and corrected for absorption effects using the SAINT+ and SADABS programs.[78, 79] Final unit cell parameters were determined by least-squares refinement of large sets of reflections taken from each data set. An initial structural model was obtained with SHELXT.[80] Subsequent difference Fourier calculations and full-matrix least-squares refinement against F^2 were performed with SHELXL-2018[81] using the Olex2 interface.[82] The crystallographic data and results of the diffraction experiments are summarized in Table 1.1

Powder X-ray Diffraction. Powder X-ray diffraction (PXRD) data for phase purity confirmation was collected using a polycrystalline sample of $RbEuPS_4$ obtained by grinding single crystals (Figure 1.1). Data was collected on a Bruker D2 PHASER diffractometer using Cu Kα radiation over a 2θ range 10–65° with a step size of 0.02°.

Energy-Dispersive Spectroscopy (EDS). EDS was performed on single crystal products using a Tescan Vega-3 SEM equipped with a Thermo EDS attachment. The SEM was operated in low-vacuum mode. Crystals were mounted on an SEM stub with carbon tape and analyzed using a 20 kV accelerating voltage and an 80 s accumulation time. SEM images of the crystals can be found in Figure 1.2. The results of EDS confirm the presence of elements found by single-crystal X-ray diffraction.

Optical Properties. Photoluminescence data were collected on HORIBA Scientific Standard Microscope Spectroscopy Systems connected with iHR320 Spectrometer and Synchrony detector operating on Labspec 6 software. Spectra were recorded from 400 to 800 nm using 375nm Laser excitation source power 0.5mW with 10xUV objective.

Table 1.1 The crystallographic information for all compounds reported herein. X-ray source (Mo Kα (0.71073 Å).

Chemical formula	$Rb_3La(PS_4)_2$	$Rb_3Pr(PS_4)_2$	$Rb_3Ce(PS_4)_2$	$Rb_{2.45(2)}Na_{0.55(2)}Pr(PS_4)_2$	$Rb_{2.50(6)}Na_{0.50(6)}Ce(PS_4)_2$	$RbEuPS_4$
Formula weight	713.74	715.74	714.95	681.32	683.76	396.64
Crystal system	Monoclinic					Orthorhombic
Space group, Z	$P2_1$	$P2_1$	$P2_1$	$P2_1/c$	$P2_1/c$	*Pnma*
a, Å	9.9053(9)	9.8265(3)	9.8512(6)	9.0570(3)	9.1218(4)	17.3308(4)
b, Å	6.7376(6)	6.7613(2)	6.7530(4)	17.3059(6)	17.4862(8)	6.6787(2)
c, Å	11.4553(10)	11.4228(4)	11.4321(7)	9.4252(3)	9.4704(4)	6.43470(10)
β, deg.	90.005(3)	90.2997(12)	90.241(2)	91.8396(13)	91.7907(17)	90
V, $Å^3$	764.50(12)	758.92(4)	760.52(8)	1476.54(8)	1509.84(11)	744.80(3)
ρ_{calcd}, g/cm^3	3.101	3.132	3.122	3.065	3.008	3.537
μ, mm^{-1}	13.545	14.040	13.800	12.644	12.317	16.132
T, K	291(2)	301(2)	301(2)	100(2)	301(2)	301(2)
Crystal dim., mm^3	0.040x0.030x0.020	0.040x0.030x0.020	0.080x0.040x0.020	0.040x0.020x0.020	0.070x0.020x0.010	0.050x0.050x0.010
2θ range, deg.	2.718-30.028	2.073-29.142	2.067-32.597	2.250-30.001	2.234-28.310	3.377- 29.992
Reflections collected	35700	27258	51419	47150	35860	12334
Data/parameters/restraints	4460/132/2	4082/134/1	5434/134/1	4311/143/0	3763/143/0	1170/43/0
R_{int}	0.0387	0.0412	0.0368	0.0462	0.0720	0.0306
Goodness of fit	1.099	1.181	1.157	1.093	1.129	1.171
$R_1(I > 2\sigma(I))$	0.0493	0.0329	0.0262	0.0297	0.0563	0.0247
wR_2 (all data)	0.0983	0.0541	0.0515	0.0503	0.1267	0.0647

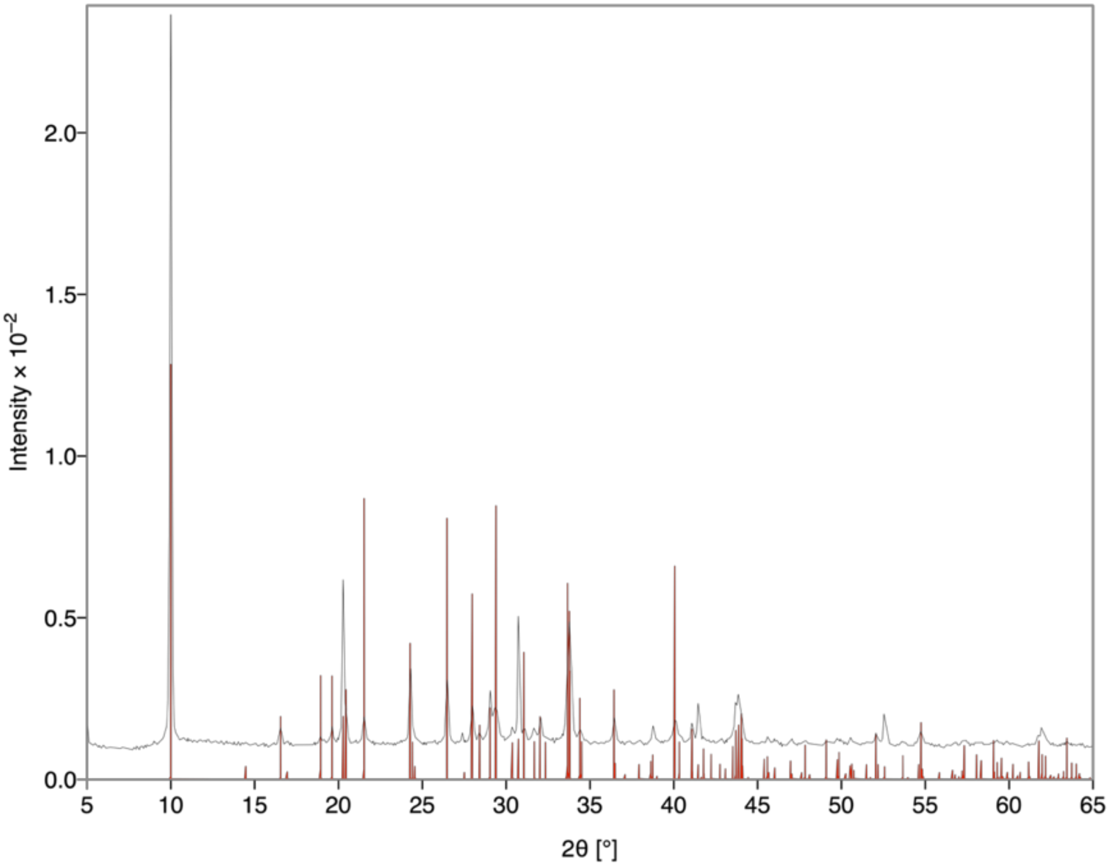

Figure 1.1 PXRD pattern (black lines) of phase pure $RbEuPS_4$ with the overlayed crystallographic information (CIF) file (red lines).

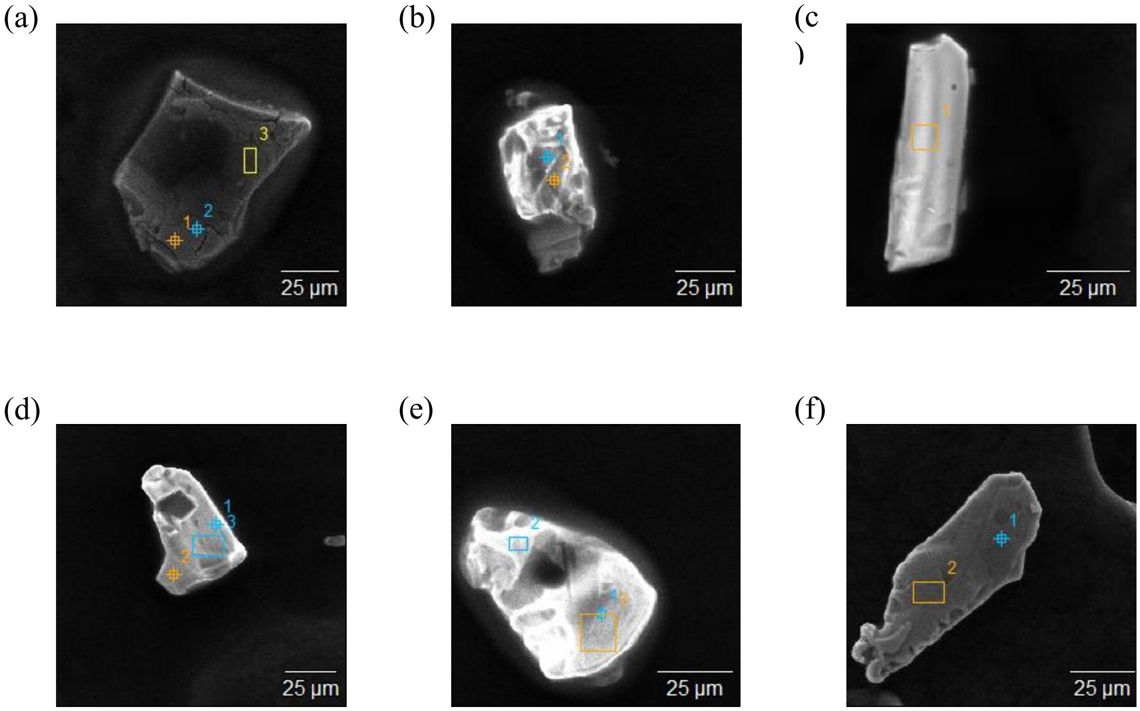

Figure 1.2 SEM images of (a) $Rb_3La(PS_4)_2$, (b) $Rb_3Ce(PS_4)_2$, (c) $Rb_3Pr(PS_4)_2$, (d) $Rb_{2.45(2)}Na_{0.55(2)}Pr(PS_4)_2$, (e) $Rb_{2.50(6)}Na_{0.50(6)}Ce(PS_4)_2$, (f) $RbEuPS_4$.

Results and Discussion:

Synthesis. To better understand the role of the flux employed in the molten flux crystal growth of rubidium rare earth thiophosphates, the same starting materials and ratios used by Kutahyali Aslani et al. to synthesize the $Rb_4Ln_2(P_2S_6)(PS_4)_2$ series[56] were employed with the only change being the use of a RbCl flux instead of the RbBr flux. This approach resulted in a new series of thiophosphates, specifically, single crystals of the rubidium rare earth thiophosphates $Rb_3Ln(PS_4)_2$ (Ln = La, Ce, Pr) and $Rb_{3-x}Na_xLn(PS_4)_2$ (Ln = Ce, Pr; x = 0.50, 0.55), which were found in the same product mixture. It is important to note that the compound $Rb_{2.61(1)}Na_{0.39(1)}La(PS_4)_2$ was also obtained in the same product mixture as $Rb_3La(PS_4)_2$, however, a similar compound has already been reported in the literature.[58]

As mentioned earlier, one goal of solid-state chemistry is to achieve predictive abilities as it pertains to the targeted synthesis of compounds with desired properties. While this goal is far from being accomplished, it is important to document observed patterns and create conversations that may help push this goal further to completion. Our group has had significant success in the growth of alkali rare earth thiophosphates using various alkali halide fluxes and, given the large number of compositions synthesized, this now allows us to look for patterns within this data. Kutahyali Aslani et al. attempted to make the rubidium analogues of the $Cs_2NaLn(PS_4)_2$ series created by Klepov et al.[27] utilizing the same starting materials and molar ratios however changing the flux from the CsI used by Klepov et al. to a RbBr flux. With just the change in flux, a new series of compounds, $Rb_4Ln_2(P_2S_6)(PS_4)_2$ (Ln = La, Ce, Pr, Nd, Sm, and Gd), was obtained. This success of crystallizing brand new rubidium rare earth thiophosphates with just a change in flux motivated the work reported herein. Using the same starting materials and reagent ratios employed by Kutahyali Aslani et al., however, changing from a RbBr to a RbCl flux, the new compounds $Rb_3Ln(PS_4)_2$ (Ln = La, Ce, Pr) and $Rb_{3-x}Na_xLn(PS_4)_2$ (Ln = Ce, Pr; $x = 0.50, 0.55$) were obtained. Table 1.2 lists the known rubidium rare earth thiophosphates grown using alkali halide fluxes.

The data in the table demonstrates that the use of different fluxes led to the crystallization of different thiophosphate compositions. To discuss the role of the flux requires, however, that we address two interconnected variables: the identity of the flux and the reaction temperature used. It is known that different products can crystallize at different temperatures depending on the kinetic and thermodynamic processes at play.[4] The change in flux from the RbBr used by Kutahyali Aslani et al. to the RbCl used herein

Table 1.2 A table listing the starting materials used, reagent ratios, flux identities, and reaction temperatures for all known rubidium rare earth thiophosphates grown using alkali halide fluxes.

Compound	Starting Material	Reagent Ratios	Flux Identity	Reaction Temperature	Reference
$Rb_{2.65}Na_{0.35}La(PS_4)_2$	Ln_2S_3:Na_2S:P_2S_5	1:2:3	RbCl-NaCl	650 for 48 hr	15
$Rb_{2.42}Na_{0.58}Nd(PS_4)_2$	Ln_2S_3:Na_2S:P_2S_5	1:2:3	RbCl-NaCl	650 for 48 hr	15
$Rb_{2.50(6)}Na_{0.50(6)}Ce(PS_4)_2$	Ln_2S_3:Na_2S:P_2S_5	1:4:4	RbCl	820 for 20 hr	This work
$Rb_{2.45(2)}Na_{0.55(2)}Pr(PS_4)_2$	Ln_2S_3:Na_2S:P_2S_5	1:4:4	RbCl	820 for 20 hr	This work
$Rb_3Gd(PS_4)_2$	Ln_2S_3:Na_2S:P_2S_5	1:2:3	RbCl-NaCl	650 for 48 hr	15
$Rb_3Ln(PS_4)_2$ Ln = La, Ce, Pr	Ln_2S_3:Na_2S:P_2S_5	1:4:4	RbCl	820 for 20 hr	This work
$Rb_2NaNd(PS_4)_2$	Ln_2S_3:Na_2S:P_2S_5	1:2:3	RbI-NaI	650 for 20 hr	15
$Rb_4Ln_2(P_2S_6)(PS_4)_2$ Ln = La, Ce, Pr, Nd, Sm, Gd	Ln_2S_3:Na_2S:P_2S_5	1:4:4	RbBr	800 for 12 hr	17
$Rb_3Pr_3(PS_4)_4$	Pr:P:S:RbBr	10:12:42:12	RbBr	950 for 14 days	16
$Rb_3Er_3(PS_4)_4$	Er:P:S:RbBr	4:4:16:3	RbBr	950 for 14 days	16
$RbLaP_2S_6$	Ln:RbBr:S:P	4:6:18:6	RbBr	800 for 24 hr	37

also necessitated a change in the reaction temperature used. It is common when using molten fluxes as crystallization media that the reaction temperature is set to 100 °C above the melting point of the flux to ensure the full liquification of the flux and maximizing the likelihood of dissolving all reagents within the flux to achieve the supersaturation necessary for crystal growth upon cooling.[1] The melting point of RbBr is ~700 °C which is the reason that Kutahyali Aslani et al. synthesized their crystals at a reaction temperature of 800 °C. The crystals reported herein, using the RbCl flux with a melting point of ~720 °C, dictated that a reaction temperature of 820 °C be used. The 20 °C difference in reaction temperature, while small, nonetheless introduces temperature as a variable. It is likely that in the case of the $Rb_3Ln(PS_4)_2$ and $Rb_{3-x}Na_xLn(PS_4)_2$ families prepared in an RbCl flux, temperature plays only a minor role in determining product formation. This is because other members of the $Rb_3Ln(PS_4)_2$ and $Rb_{3-x}Na_xLn(PS_4)_2$ families, Table 1.2, were synthesized in a RbCl-NaCl eutectic flux (melting point: 486 °C) at a reaction temperature of 600 °C.[15] The fact that $Rb_3Ln(PS_4)_2$ and $Rb_{3-x}Na_xLn(PS_4)_2$ crystallizes over a wide temperature range suggests that the identity of the flux predominantly impacts the identity of the product formed. Though the use of a RbBr flux at various temperatures resulted in different products formed, it is interesting that the use of a RbCl flux resulted in the same families of compounds. The observation suggests that these families of compounds can be readily targeted using specifically the RbCl flux as at least one component of the flux. Furthermore, it suggests that it is always worthwhile to explore different alkali halide fluxes after a new composition has been found, as the switch in fluxes may easily lead to additional series of compounds.

The single crystal growth of $RbEuPS_4$ was performed using a 1:2:2 ratio of EuS, P_2S_5, and Na_2S in order to keep the ratio of lanthanide to phosphorus pentasulfide and sodium sulfide the same as in the other syntheses reported herein. The resulting product, which utilized 1gram of RbCl flux, was phase pure yellow/brown plates of $RbEuPS_4$. It is important to note that in this structure the lanthanide, europium, is in its 2+ oxidation state where all other compounds reported herein have the lanthanides in their 3+ oxidation state. This is most likely the reason that a different compound, structure, and composition, was obtained for europium, as its ability of taking on the 2+ oxidation state is unique among the rare earths described herein.

Structure Description. $Rb_3Pr(PS_4)_2$, and $Rb_3Ce(PS_4)_2$ belong to the $Rb_3Ln(PS_4)_2$ family of thiophosphates and crystallize in a one-dimensional structure type in the monoclinic space group $P2_1$, Figure 1.3 a-e. The structures consist of two unique PS_4^{3-}

tetrahedra and one 8-coordinate LnS_8 highly distorted square antiprism. The LnS_8 polyhedra corner-share with each other creating corrugated infinite chains. Within the chains, the $P(1)S_4^{3-}$ tetrahedra share two edges with adjacent LnS_8 polyhedra and corner share with a third. The $P(2)S_4^{3-}$ thiophosphate tetrahedra then decorate the sides of the LnS_8 polyhedra via face-sharing and point into the channels between the infinite chains. These channels are populated with ordered rubidium cations which hold the infinite chains together resulting in the full structure. In these compounds the Ln—S interatomic distances range from 2.8916(19)—3.253(16) Å, the P—S interatomic distances range from 2.0004(18)—2.089(14) Å, and the Rb—S interatomic distances range from 3.290(17)—3.9974(16) Å.

$Rb_3La(PS_4)_2$ is isostructural with the other $Rb_3Ln(PS_4)_2$ compounds reported herein however exhibits rubidium/lanthanum site mixing within the structure, Figure 1.3 f. Of the 4 unique rubidium sites, the Rb1 and Rb2 sites are mixed with lanthanum with La1/Rb1 and La2/Rb2 occupancies of 0.548(4)/0.452(4) and 0.452(4)/0.548(2), respectively, while the Rb3 and Rb4 sites are fully occupied by rubidium. Due to the approximate 50/50 rubidium and lanthanum site mixing, the resulting overall chemical formula is nonetheless the same as those of $Rb_3Pr(PS_4)_2$ and $Rb_3Ce(PS_4)$. In this compound the Ln—S interatomic distances, impacted by the site mixing, range from 2.976(8)—3.384(6) Å, the P—S interatomic distances range from 1.984(12)—2.108(11) Å, and the Rb—S interatomic distances range from 3.327(8)—3.949(8) Å.

$Rb_{2.45(2)}Na_{0.55(2)}Pr(PS_4)_2$ and $Rb_{2.50(6)}Na_{0.50(6)}Ce(PS_4)_2$ belong to the $Rb_{3-x}Na_xLn(PS_4)_2$ family of thiophosphates and crystallize in the monoclinic space group $P2_1/c$,

Figure 1.4. The one-dimensional crystal structure consists of one 9-coordinate LnS_9 polyhedral unit and two unique PS_4^{3-} tetrahedra. The LnS_9 polyhedra alternate between

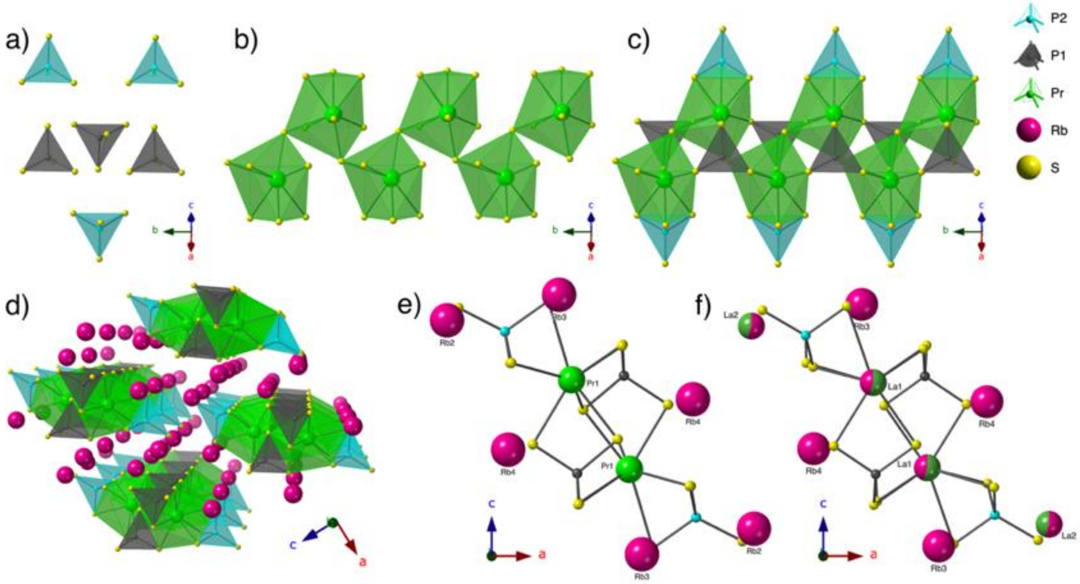

Figure 1.3 A schematic of the $Rb_3Ln(PS_4)_2$ (Ln = La, Ce, Pr) structure showing (a) the two PS_4^{3-} units, (b) the connectivity of the LnS_8 polyhedra, (c) the infinite chains of LnS_8 and PS_4^{3-} polyhedra, and (d) the full crystal structure. Figure 1e and 1f show a ball and stick representation of the infinite chains of the (e) $Rb_3Pr(PS_4)_2$ and (f) $Rb_3La(PS_4)_2$ structures to visualize where the lanthanum/rubidium site mixing (split pink/green spheres) occurs in Ln = La analogue.

edge- and face-sharing with one another creating infinite LnS_9 chains. Between two face-sharing LnS_9 polyhedra, the $P(1)S_4^{3-}$ tetrahedra face-share with one LnS_9 polyhedra and edge-share with the other. Between two edge-sharing LnS_9 polyhedra, the $P(2)S_4^{3-}$ tetrahedra share one edge with each LnS_9 polyhedra, see Figure 1.4 d. The resulting $[Ln(PS_4)_2]^{3-}$ infinite chains are held together by 3 unique disordered cationic sites. Sites Rb1 (split into Rb1a and Rb1b) and Rb3 (split into Rb3a and Rb3b) contain solely rubidium cations while site Rb2 is a disordered mixed site of both rubidium and sodium cations. In these compounds, the Ln—S interatomic distances range from 2.8731(10)—3.3038(14) Å, the P—S interatomic distances range from 1.996(4)—2.073(3) Å, and the Rb—S interatomic distances, impacted by the site mixing, range from 3.0046(16)—3.958(13) Å.

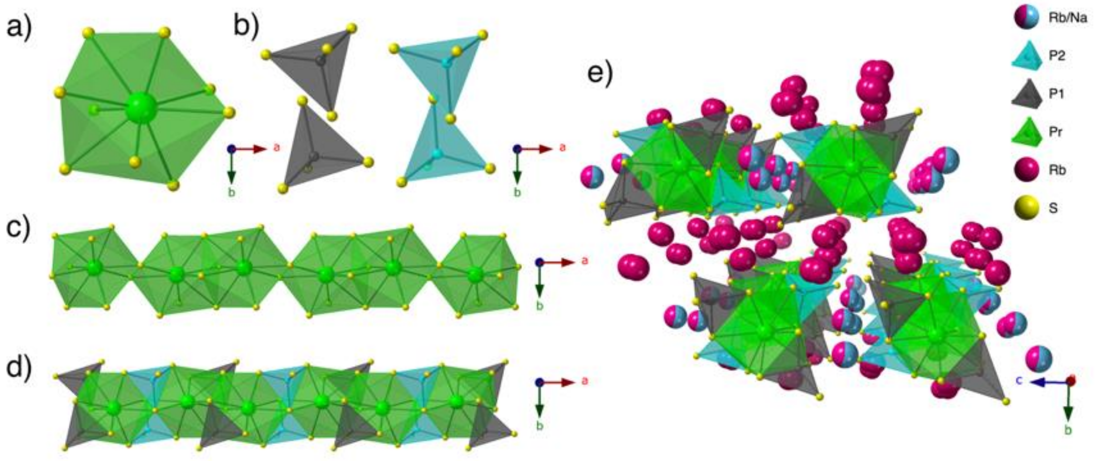

Figure 1.4 A schematic of the $Rb_{3-x}Na_xLn(PS_4)_2$ (Ln = Pr, Ce; x = 0.50, 0.55) structure showing (a) the LnS_9 polyhedral unit, (b) the two PS_4^{3-} units, (c) the connectivity of the rare earth polyhedra, (d) the $[Ln(PS_4)_2]^{3-}$ infinite chains, and (e) the full crystal structure.

$RbEuPS_4$ is the rubidium analogue of $KEuPS_4$[36] and crystallizes in the orthorhombic space group *Pnma*, Figure 1.5. The crystal structure consists of one PS_4^{3-} tetrahedral unit and one 8 coordinate EuS_8 bicapped trigonal prism. The EuS_8 polyhedra edge-share with each other creating a layer of europium polyhedra parallel to the b-c plane. The edge-sharing of the polyhedra leave trigonal prismatic holes in the layers that are filled by the thiophosphate tetrahedra. The successive layers are connected through rubidium cations which are disordered on their respective sites. In this compound the Eu—S interatomic distances range from 2.9679(16)—3.4516(4) Å, the P—S interatomic distances range from 2.021(2)—2.046(2) Å, and the Rb—S interatomic distances range from 3.327(8)—3.809(9) Å.

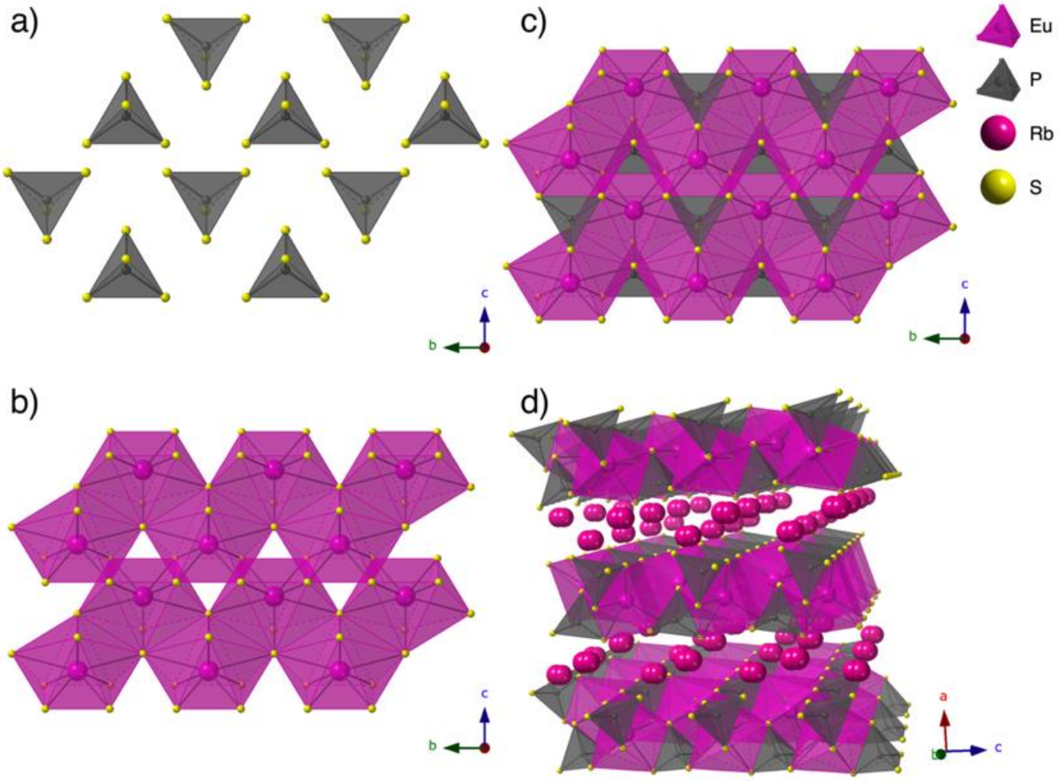

Figure 1.5 A schematic of the $RbEuPS_4$ structure showing (a) the PS_4^{3-} unit, (b) the connectivity of the EuS_8 polyhedra, (c) the layers of EuS_8 and PS_4^{3-} polyhedra, and (d) the full crystal structure.

Optical Properties. Fluorescence spectra were obtained at an excitation wavelength of 375 nm on single crystals of $Rb_3La(PS_4)_2$, $Rb_3Pr(PS_4)_2$, $Rb_3Ce(PS_4)$, $Rb_{2.45(2)}Na_{0.55(2)}Pr(PS_4)_2$, $Rb_{2.50(6)}Na_{0.50(6)}Ce(PS_4)_2$ and $RbEuPS_4$. As expected, there was no fluorescence observed for $Rb_3La(PS_4)_2$, as lanthanum compounds have a $4f^0$ electron configuration.[83] In the case of $RbEuPS_4$, where europium is $4f^7$, one might expect fluorescence; however, no fluorescence was observed from the single crystals of $RbEuPS_4$. The fluorescence spectra for $Rb_3Pr(PS_4)_2$, $Rb_{2.45(2)}Na_{0.55(2)}Pr(PS_4)_2$, $Rb_3Ce(PS_4)_2$, and $Rb_{2.50(6)}Na_{0.50(6)}Ce(PS_4)_2$ are shown in Figure 1.6. In the $Rb_3Pr(PS_4)_2$ and $Rb_{2.45(2)}Na_{0.55(2)}Pr(PS_4)_2$ spectra, the expected $^3P_0 \rightarrow {}^3H_4$, $^3P_0 \rightarrow {}^3H_5$, $^1D_2 \rightarrow {}^3H_4$, and $^3P_0 \rightarrow {}^3H_6$ f-f transitions were observed.[84] The fluorescence spectra for the $Rb_3Ce(PS_4)_2$ and

$Rb_{2.50(6)}Na_{0.50(6)}Ce(PS_4)_2$, exhibit a single broad peak covering much of the visible range measured, a phenomenon reported for other cerium compounds in the literature.[85-87]

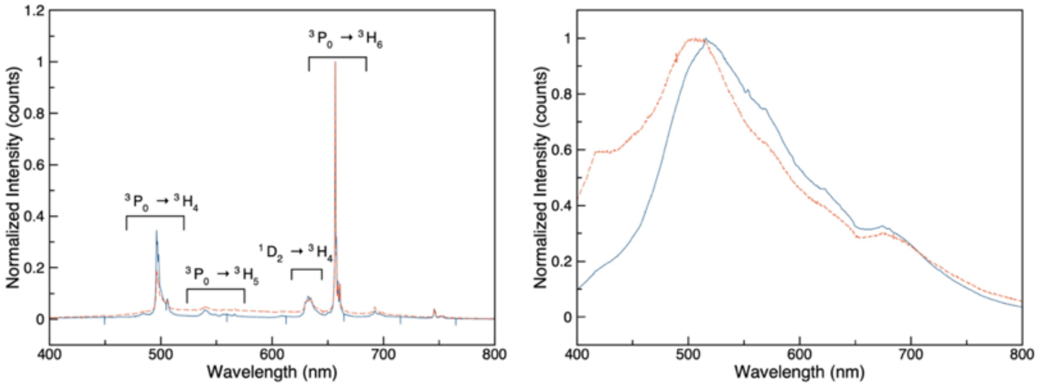

Figure 1.6 The emission spectrum of $Rb_3Pr(PS_4)_2$ (blue solid line) and $Rb_{2.45(2)}Na_{0.55(2)}Pr(PS_4)_2$ (orange dashed line) on the left, and that of $Rb_3Ce(PS_4)$ (blue solid line) and $Rb_{2.50(6)}Na_{0.50(6)}Ce(PS_4)_2$ (orange dashed line) on the right, taken at an excitation wavelength of 375 nm.

Conclusions. Single crystals of new rubidium rare earth thiophosphates with the formulas $Rb_3Ln(PS_4)_2$ (Ln = La, Pr, Ce), $Rb_{3-x}Na_xLn(PS_4)_2$ (Ln = Pr, Ce; x = 0.50, 0.55), and $RbEuPS_4$ were crystallized out of a molten RbCl flux. The role of the flux in the creation of rubidium rare earth thiophosphates was discussed and contrasted with other thiophosphate families crystallized out of similar halide fluxes. Fluorescence measurements were performed on all compounds obtained, revealing resolved f-f transitions in $Rb_3Pr(PS_4)_2$ and $Rb_{2.45(2)}Na_{0.55(2)}Pr(PS_4)_2$ and only single broad emission peaks for $Rb_3Ce(PS_4)$ and $Rb_{2.50(6)}Na_{0.50(6)}Ce(PS_4)_2$, behavior characteristic for cerium(III) compounds.

Acknowledgments. Research supported by the US Department of Energy, Office of Basic Energy Sciences, Division of Materials Sciences and Engineering under award DE-SC0018739.

CHAPTER 2

FACILE OXIDE TO CHALCOGENIDE CONVERSION FOR ACTINIDES USING THE BORON-CHALCOGEN MIXTURE METHOD[1]

---

[1] Reproduced with permission from Breton, L. S., Klepov, V. V., and zur Loye, H.-C., *J. Am. Chem. Soc.*, **2020**, 142, 14365-14373. **© 2020 American Chemical Society**

Abstract: Actinide chalcogenides are of interest for fundamental studies of the behavior of 5*f* electrons in actinides located in a soft ligand coordination environment. As actinides exhibit an extremely high affinity for oxygen, the synthesis of phase pure actinide chalcogenide materials free of oxide impurities is a great challenge and, moreover, requires the availability and use of oxygen free starting materials. Herein, we report a new method, the Boron-Chalcogen Mixture (BCM) method, for the synthesis of phase pure uranium chalcogenides based on the use of a boron/chalcogen mixture, where boron functions as an "oxygen sponge" to remove oxygen from an oxide precursor and where the elemental chalcogen effects transformation of the oxide precursor into an oxygen free chalcogenide reagent. The boron oxide can be separated from the reaction mixture that is left to react to form the desired chalcogenide product. Several syntheses are presented that demonstrate the broad functionality of the technique and thermodynamic calculations that show the underlying driving force are discussed. Specifically, three classes of chalcogenides that include both new (rare earth uranium sulfides and alkali-thorium thiophosphates) and previously reported compounds were prepared to validate the approach: binary uranium and thorium sulfides, oxide to sulfide transformation in solid state reactions, and *in situ* generation of actinide chalcogenides in flux crystal growth reactions.

Introduction. Actinide chalcogenides adopt diverse structure types with distinct chemical compositions and specific actinide oxidation states,[2, 4, 88-91] which offer unique opportunities for studying 5*f* electron properties.[36, 92-100] The synthesis of these materials can be achieved by a limited set of synthetic routes that include the traditional solid-state approach,[101-104] chemical vapor transport,[105-108] and the molten flux technique.[47, 74, 109-115] Regardless of the method chosen, there are two general actinide precursors that are consistently used – the actinide metals and binary actinide chalcogenides.[2, 116-120] One of the main obstacles faced when synthesizing the actinide chalcogenides are actinide oxide and oxychalcogenide impurities that often contaminate the resulting products and interfere with their property measurements.[121-123] Due to the high oxygen affinity of the actinides, even trace amounts of oxygen in the system will inevitably result in the formation of these impurities. Although careful oxygen exclusion from the reaction media is an intuitive and straightforward approach for avoiding oxide impurities, it is unfortunately often nearly impossible to completely eliminate oxide contamination present in the reagents themselves.[124, 125] This difficulty of needing to effectively deal with oxide or oxychalcogenide impurities in the starting materials motivated us to explore different synthetic approaches that would allow for the use of oxygen-contaminated reagents, or even oxides themselves, as the starting materials for the synthesis of oxygen free actinide chalcogenides.

In situations where oxygen cannot be avoided in the initial reagent mixture, it is reasonable to consider the use of a highly oxophilic sacrificial component that would extract oxygen and subsequently leave the reaction mixture or be dissolvable in post-reaction work-up. Aluminum powder with its high affinity for oxygen, in principle, would be a great candidate as an oxophilic component, however, its inertness, very high melting point (2072 °C) and low vapor pressure of the resulting Al_2O_3 makes its use inconvenient in typical reactions.[126] A better alternative is boron, which is almost as oxophilic as aluminum; however, it forms the much less inert B_2O_3 oxide. In fact, this approach has been successfully implemented in the sulfurization of some transition metal and rare earth oxides by incorporating a mixture of boron and sulfur into the reaction vessel.[127-132] The boron acts as an ‘oxygen sponge’ forming highly stable B_2O_3 while leaving the sulfur to replace oxygen. The success of the sulfurization is based on the differences between the formation energies of B_2O_3 ($\Delta_fG°$(vitreous-B_2O_3) = -1182.5 kJ/mol) and B_2S_3 ($\Delta_fG°$(vitreous-B_2S_3) = -247.6 kJ/mol), which strongly favors the formation of B_2O_3 thus leaving sulfur to react with the other reagents.[131] Despite the success with the rare earth and *d* elements, this approach has never been implemented for the synthesis of actinide chalcogenides. It is possible that this application was deemed unlikely to work for actinides due to their high oxophilicity and, thus, high stability of the actinide oxides. Thermodynamic calculations indicate, however, that this process should work for the actinides as well, which prompted us to investigate the effectiveness of using boron-chalcogen mixtures to achieve the formation of actinide chalcogenides when starting with actinide oxide precursors.[47]

Herein we present the first time application of the boron-chalcogen mixture (BCM) method for the synthesis of actinide chalcogenides from their respective oxide precursors (Figure 2.1). To demonstrate the efficacy of the BCM method, we present the synthesis of ThS_2 and US_2 starting from ThO_2 and U_3O_8, the solid state syntheses of UMS_3 (M = Ni and Co) perovskites starting with oxide reagents, the adaptation of the BCM method to flux crystal growth and the formation of the new family of rare earth uranium sulfides, $Ln_xU_2S_5$ (Ln = Pr, Nd, Sm, Gd-Yb) containing mixed valent U(III/IV), the crystal growth of the new complex thorium thiophosphate $Rb_{1.72}Na_{0.68}I_{0.40}[Th(PS_4)_2]$ using ThO_2 as a starting reagent, and the crystal growth of the uranium(V,VI) sulfide $Cs_6Cu_{12}U_2S_{15}$ obtained using the BCM method *in situ* generated polychalcogenide flux.[133] The single crystal structures and magnetic measurements of the new phases are presented. The new method will undoubtedly stimulate actinide chalcogenide research by bridging oxide and chalcogenide solid state chemistry and providing greatly improved access to phase pure chalcogenides and their properties.

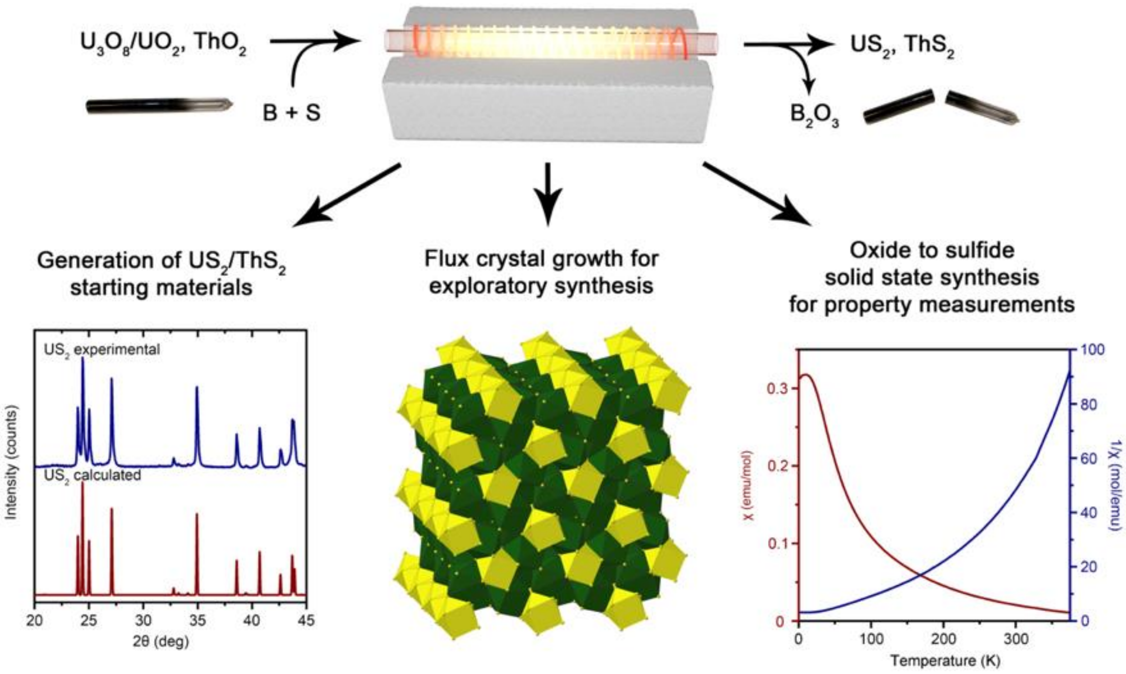

Figure 2.1 A schematic representation of the proposed method for the synthesis of actinide chalcogenides. Stable actinide oxides U_3O_8 and ThO_2 can be used as starting materials that are sulfurized to generate US_2 and ThS_2 as a final product or for *in situ* use in flux crystal growth and solid state reactions.

Results and Discussion:

Proof of Concept: Binary actinide sulfides synthesis. To probe the feasibility of oxygen replacement by sulfur in uranium oxides, we treated UO_2 and U_3O_8 with a boron-sulfur (B-S) mixture in a carbon coated evacuated silica tube at 800 °C. As boron sulfides that form during the course of the reaction are corrosive in nature and can react with silica reaction vessels, it is necessary to heavily carbon coat the inside of the silica tubes to prevent corrosion and, ultimately, tube breakage. This is readily achieved by thermally decomposing acetone inside the empty silica tube at high temperatures.[131] The carbon coating prevents the tube from corroding and minimizes the introduction of possible contaminants in the product. The treatment of UO_2 and U_3O_8 with a B-S mixture resulted in a phase pure US_2 product with no detectable oxide or oxysulfide impurities by powder X-ray diffraction (Figure 2.2). This experiment proves that despite the uranium's high affinity for oxygen, it is possible to achieve full oxygen replacement by using the BCM method, suggesting the further extension of this method to other uranium chalcogenides as well as thorium analogues. To explore this extension of the BCM method, UO_2 and ThO_2 were reacted with boron-chalcogen mixtures (S, Se, Te) under identical reaction conditions. In all cases, except for the reaction between ThO_2 and a boron-tellurium mixture, was full oxygen replacement with chalcogens achieved. Moreover, the reactions with sulfur resulted in phase pure samples of US_2 and ThS_2 (Figure 2.2 and 2.3). We also found that the addition of an excess of the boron-chalcogen mixture results in the formation of polychalcogenide actinide compounds, a known class of chalcogenide materials.[134] Notably, even if an excess of boron is present, it does not incorporate into the reaction products. For the simple binaries, the reported method can find only a limited application for the synthesis of thorium tellurides as the only stable product that forms in the reactions between thorium ThO_2 and boron-tellurium mixtures is thorium oxytelluride, ThOTe.

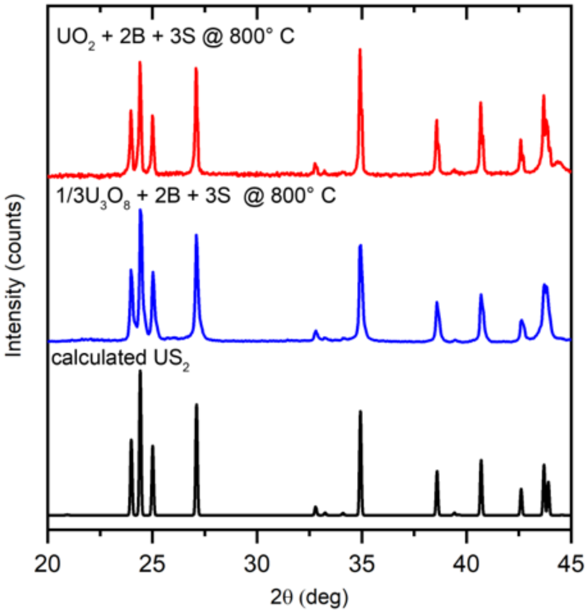

Figure 2.2 (top and middle) PXRD patterns of the products obtained from a reaction between UO_2 or U_3O_8 with B-S mixture at 800 °C and (bottom) calculated PXRD pattern of orthorhombic US_2.[135]

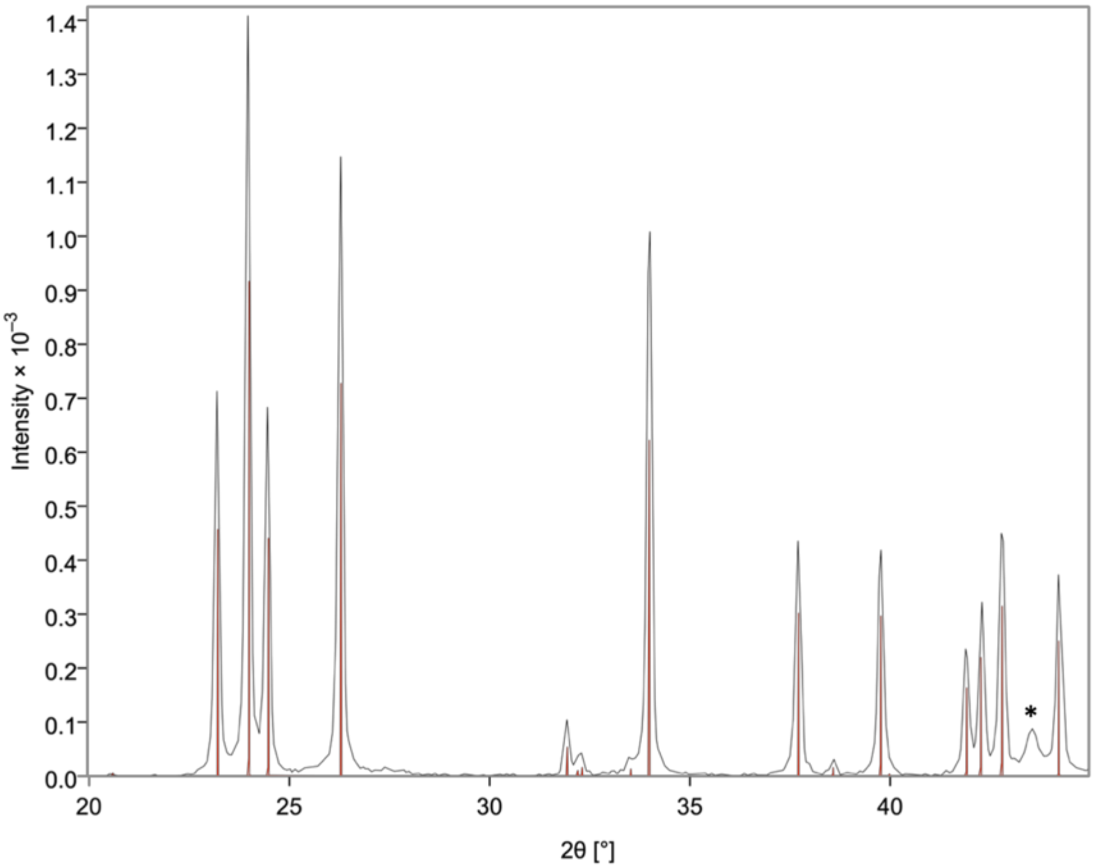

Figure 2.3 The PXRD of pure ThS_2 with the overlaid CIF from the reaction of ThO_2 with a mixture of boron and sulfur. Peak at ~43º (marked with an asterisk) corresponds to the steel slide.

To probe the temperature dependence of the oxygen replacement with sulfur in oxides, we performed several reactions between U_3O_8/ThO_2 with a boron-sulfur (B-S) mixture (Figures 2.4 and 2.5). At low temperatures (below 500 °C) the B-S mixture reduces U_3O_8 to UO_2, with no indication of sulfide phase formation. The oxygen displacement by sulfur takes place between 500 and 600 °C, and full sulfurization finishes at temperatures below 700 °C, at which point all oxygen is fully replaced by sulfur to form US_2 and U(IV)S_3. The excess sulfur in US_3 sulfide-disulfide can be separated from the product by thermal decomposition at 800 °C, resulting in a phase pure US_2 or ThS_2 product for UO_2/U_3O_8 and ThO_2 stating materials, respectively.

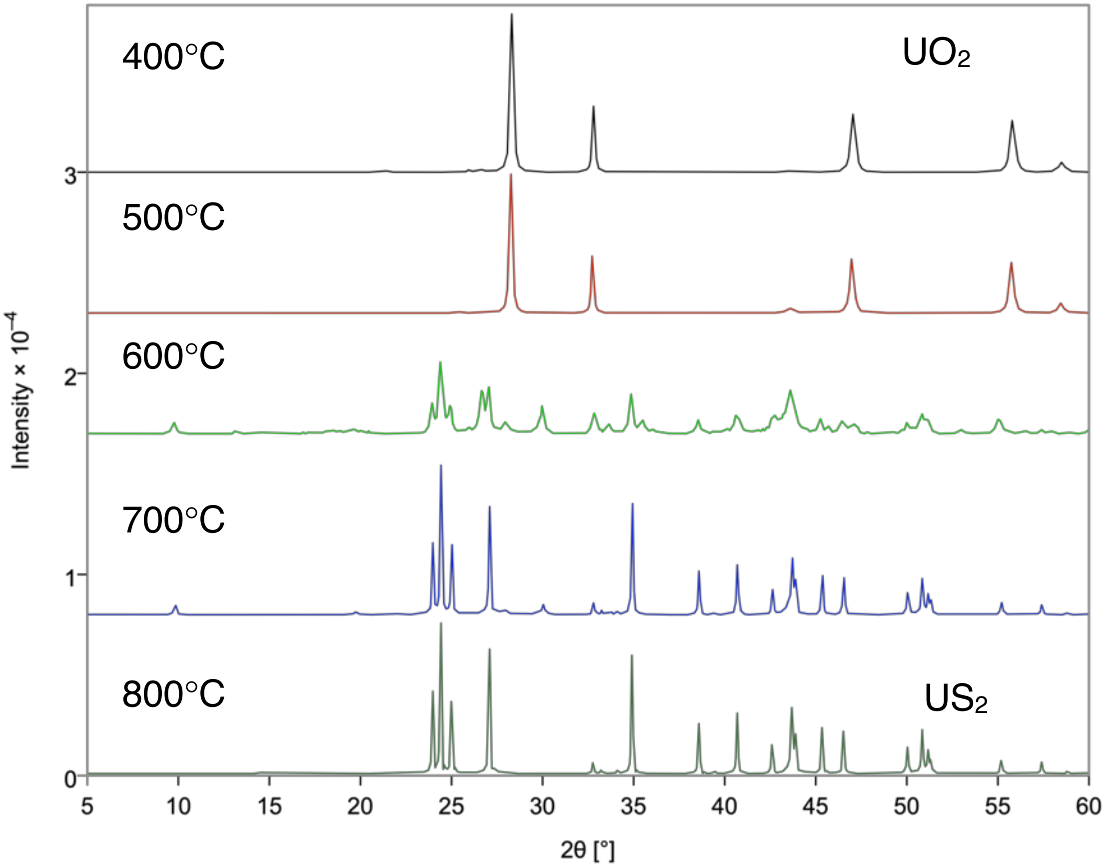

Figure 2.4 The PXRD patterns of products obtained in a reaction between U_3O_8, B, and S performed at (from top to bottom) 400, 500, 600, 700, and 800 °C. The following products were identified: UO_2 (500 °C); UOS, US_3, and US_2 (600 °C); US_3 and US_2 (700 °C); US_2 (800 °C).

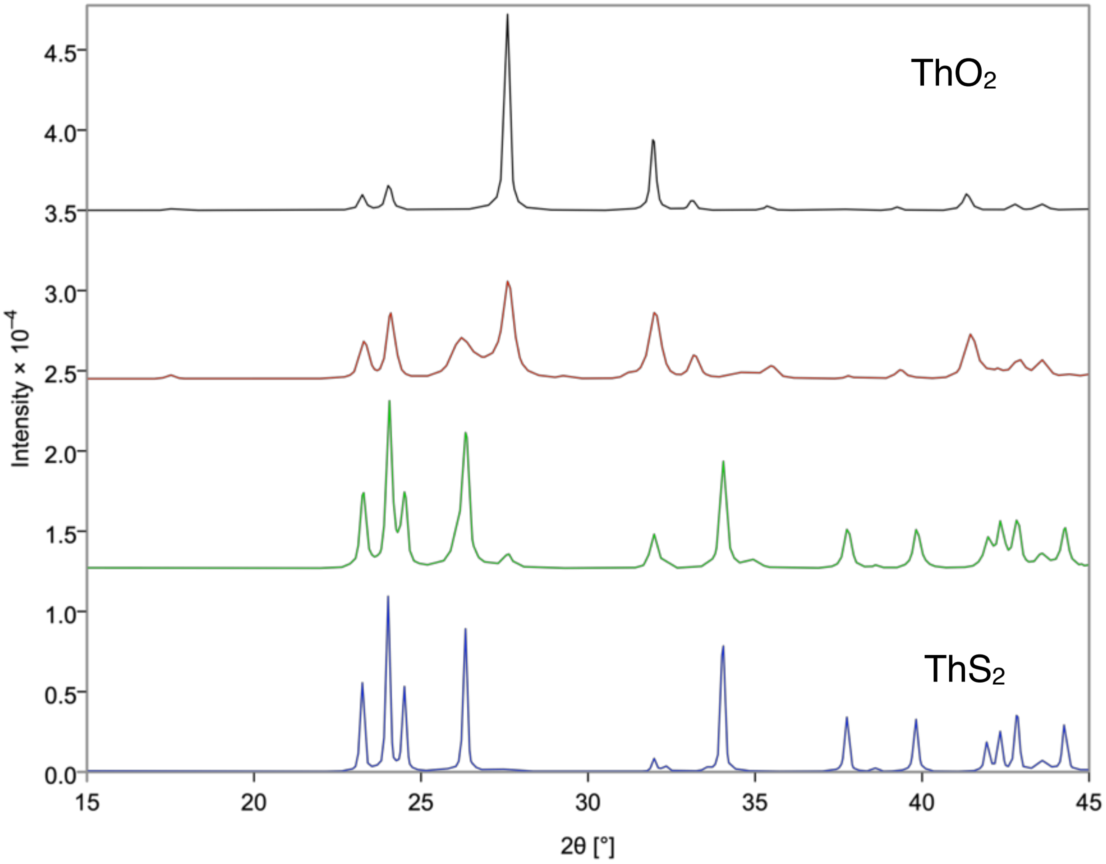

Figure 2.5 The PXRD patterns of products obtained in a reaction between ThO_2, B, and S performed at (from top to bottom) 500, 600, 700, and 800 °C. The following products were identified: ThO_2 and Th_2S_5 (500 °C); ThO_2, ThOS, and Th_2S_5 (600 °C); ThO_2 and ThS_2 (700 °C); ThS_2 (800 °C).

Thermodynamic Stability. The observation of UOS and US_2 in the reactions at intermediate temperature suggests that there exist competing forces (kinetic and or thermodynamic) at these temperatures. In order to provide a thermodynamic basis for the observed experimental data, we calculated enthalpies of the reactions that form uranium and thorium compounds according to the following equations:

$UO_2/ThO_2 + 4/3\ B + nQ \rightleftharpoons UQ_n/ThQ_n + 2/3B_2O_3$ (1);

$\Delta H_r = \Delta_f H_{0\ K}(UQ_n/ThQ_n) + 2/3\Delta_f H_{0\ K}(B_2O_3) - \Delta_f H_{0\ K}(UO_2/ThO_2)$ (2);

$UO_2/ThO_2 + 1/3B + nQ \rightleftharpoons UOQ_n/ThOQ_n + 1/3B_2O_3$ (3);

$\Delta H_r = \Delta_f H_{0\,K}(UQ_n/ThQ_n) + 1/3\Delta_f H_{0\,K}(B_2O_3) - \Delta_f H_{0\,K}(UO_2/ThO_2)$ (4).

where Q is a chalcogen. Enthalpies of formation at 0 K for all compounds were taken from the OQMD database.[136, 137] As per equations (2) and (4) the energy cost of converting an oxide to a chalcogenide has to be compensated for by the energy gained when B_2O_3 is formed, as otherwise the reaction will not be energetically favorable. To compare the stability of different products, we plotted the calculated ΔH_r values in Figure 2.6. Although the entropies were not taken into account due to the lack of reliable literature values on these materials, the obtained enthalpic values are a good guide to overall phase stability and are in reasonable agreement with our experiments. For instance, in the U-O-S system, the addition of boron (and a respective change of the energy landscape in the system)[138] can result in the formation of binary chalcogenides US_3 and US_2, and an oxysulfide UOS, which are indeed observed among the products of a reaction between UO_2 and the B-S mixture. Between the two binaries, the most enthalpically favored is US_3, which forms at lower temperatures than US_2. As the temperature is increased, US_3 decomposes to US_2 and S, which is identical to the process occurring in a reaction between metal U and S, where US_3 can be formed at temperatures below ~ 600 °C followed by subsequent decomposition to US_2 and S at higher temperatures.[139] Similar trends can be observed in the Se systems, where UQ_2 and UQ_3 are identified as the most stable compounds (Figure 2.7). The Te systems, however, are quite different from the S and Se ones in that only UOTe and ThOTe are predicted to have negative enthalpies of formation and therefore be stable. This is in good agreement with the experimental data for the Th-O-Te system, where only ThOTe was observed in the powder X-ray diffraction pattern.

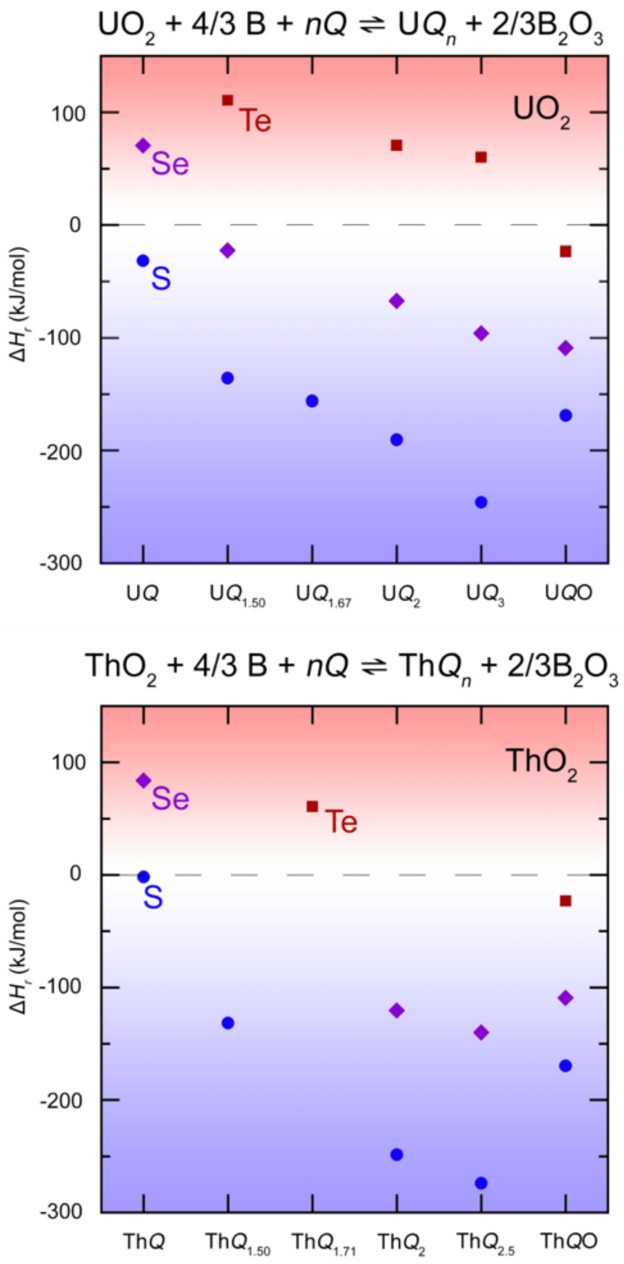

Figure 2.6 Enthalpies of formation of different uranium and thorium chalcogenide products in reaction (1) (for binary chalcogenides) and reaction (3) (for oxychalcogenides). AnOQ, AnQ_2 and AnQ_3 are among the most stable compounds in these systems. ΔH_r were estimated using calculated $\Delta_f H_{0\,K}$ values from The Open Quantum Materials Database. [136, 137]

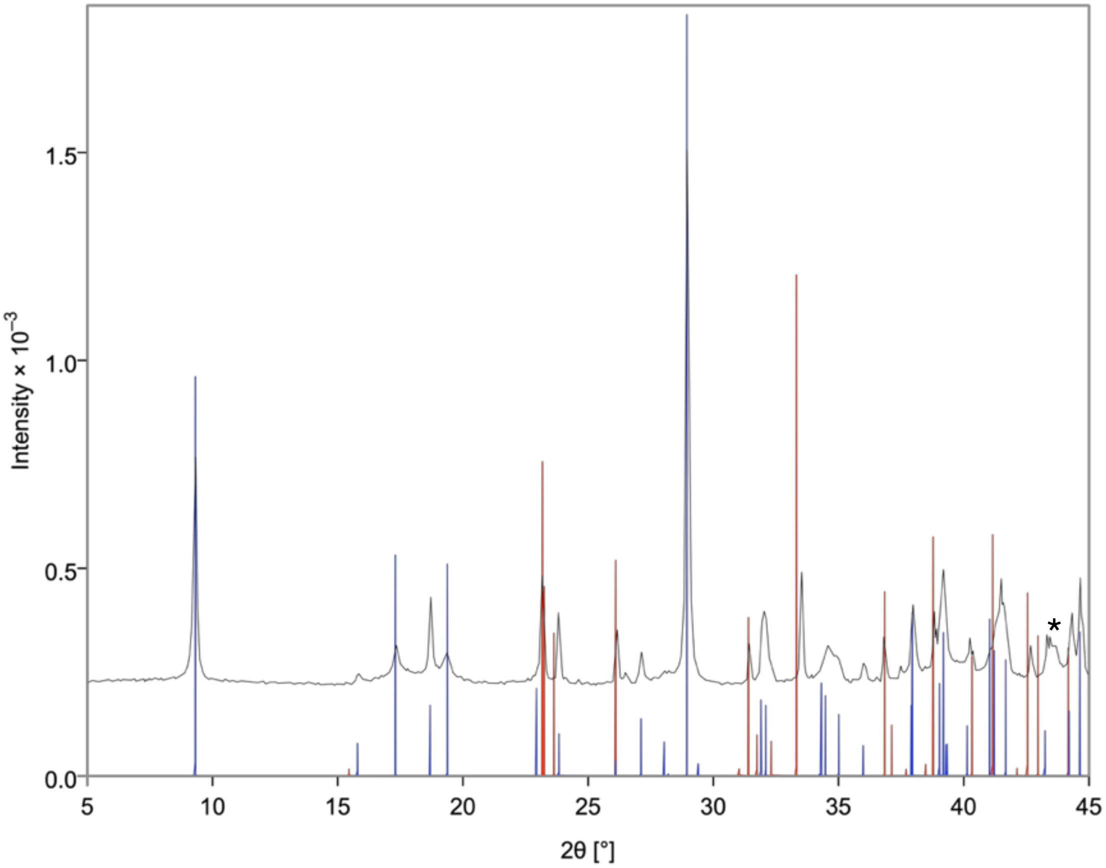

Figure 2.7 The experimental (black) PXRD pattern of the product of the reaction at 800 °C between UO_2, B, and Se in a 1:2:3 molar ratio, respectively, with the calculated PXRD patterns of the indexed phases, USe_3 (blue) and USe_2 (red). Peak at ~43° (marked with an asterisk) corresponds to the steel slide.

However, in the U-O-Te system, uranium forms a handful of telluride phases, most of which could not be identified unambiguously by PXRD but likely include polytelluride phases. Tellurium is known to have a greater ability to form polyanions compared to its sulfur and selenium congeners,[140] which could possibly give rise to additional factors not considered in the calculations and which could be the cause of the discrepancy. One can thus conclude that these predictions can be readily used when targeting specific sulfides and selenides, while targeting the telluride phases may require additional experimentation.

Overall, these experiments and thermodynamic findings provide evidence that the BCM method is an efficient and very convenient way for obtaining actinide chalcogenide and polychalcogenide precursors. Given the achieved success, it was decided to explore how generally applicable this method is and, thus, to apply this method to an *in situ* uranium chalcogenide generation in conventional solid state and flux reactions. As our interest lies in the magnetism of sulfide phases and their structural complexity, we focused mostly on the phases with magnetic ions and those that have the potential to exhibit a complex structure.

Solid state reactions using the BCM method. To date, solid state approaches for obtaining chalcogenide phases often involve the high temperature reaction of the respective elements. To probe the applicability of the BCM method for solid state reactions using oxides as starting materials, we selected $UNiS_3$ and $UCoS_3$ perovskites as target phases.[141] These compositions are of interest for a number of reasons including a +4 cation on the A site, interesting magnetic properties, and past difficulty in preparing a phase pure sample, (Figure 2.8).[142] To generate the target phases, we performed a series of two-step solid state reactions. In the first step, the precursors U_3O_8, NiO, and $CoC_2O_4 \cdot 2H_2O$ were weighed out in the proper stoichiometric quantities, pelletized, and pre-reacted at 1100 °C in air. As $NiUO_4$ forms only under high pressure,[143] we observed the formation of a mixture of NiO and U_3O_8 for the Ni-containing system, whereas the reaction with Co resulted in a pure $CoUO_4$ uranate (Figure 2.9). In the second step, the intermediate products were ground with a slight excess of the B-S mixture, pelletized, and reacted in an evacuated carbon-coated silica tube. We found that pure $UNiS_3$ forms at 850 °C, while the formation of $UCoS_3$ is not observed until a significantly higher temperature, 1100 °C, in agreement with the previous report.[141] The PXRD data confirm the formation of phase-pure, well crystalline

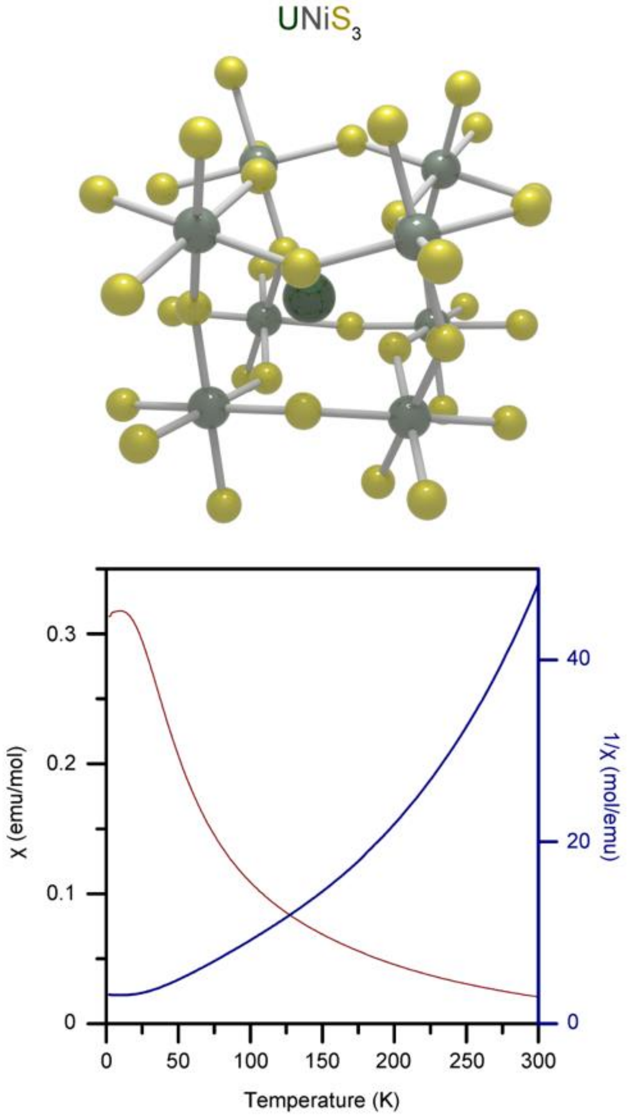

Figure 2.8 (top) Schematic of the orthorhombically distorted perovskite structure of $UNiS_3$ with U (dark-grey) and Ni (light grey) cations on the A and B sites, respectively, and (bottom) the magnetic susceptibility vs. temperature plot for $UNiS_3$.

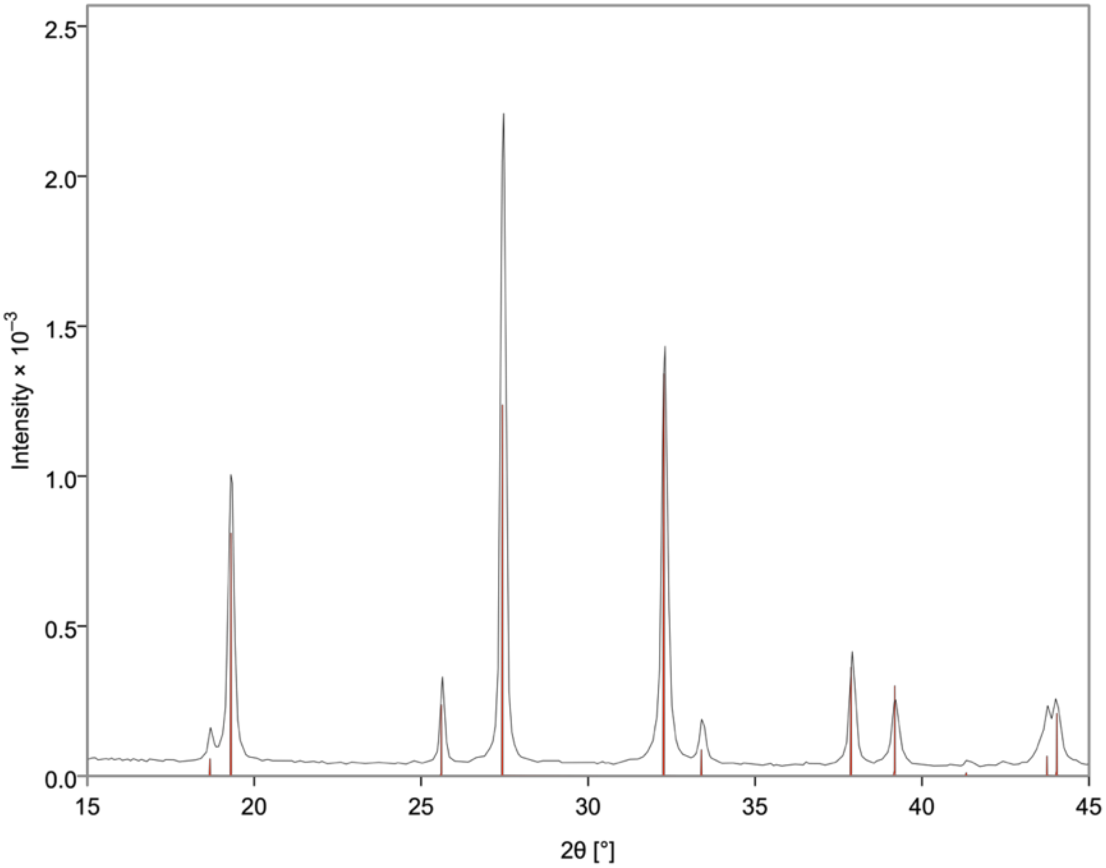

Figure 2.9 Experimental (black) and calculated (red) PXRD patterns of $CoUO_4$.

products (Figures 2.10 and 2.11). Pure $UNiS_3$ also formed in a direct reaction between NiO, U_3O_8, and the B-S mixture, circumventing the intermediate step. These experiments demonstrate the major advantage of the BCM method, namely that air stable oxides can be used as starting materials to obtain phase pure chalcogenide target phases, including those that are extremely sensitive to the presence of oxygen in the system. In fact, the B-S mixture bridges oxide and sulfide solid state chemistry as it allows for oxygen replacement in virtually any oxide material and its potential for the synthesis of sulfide phases can hardly be overestimated.

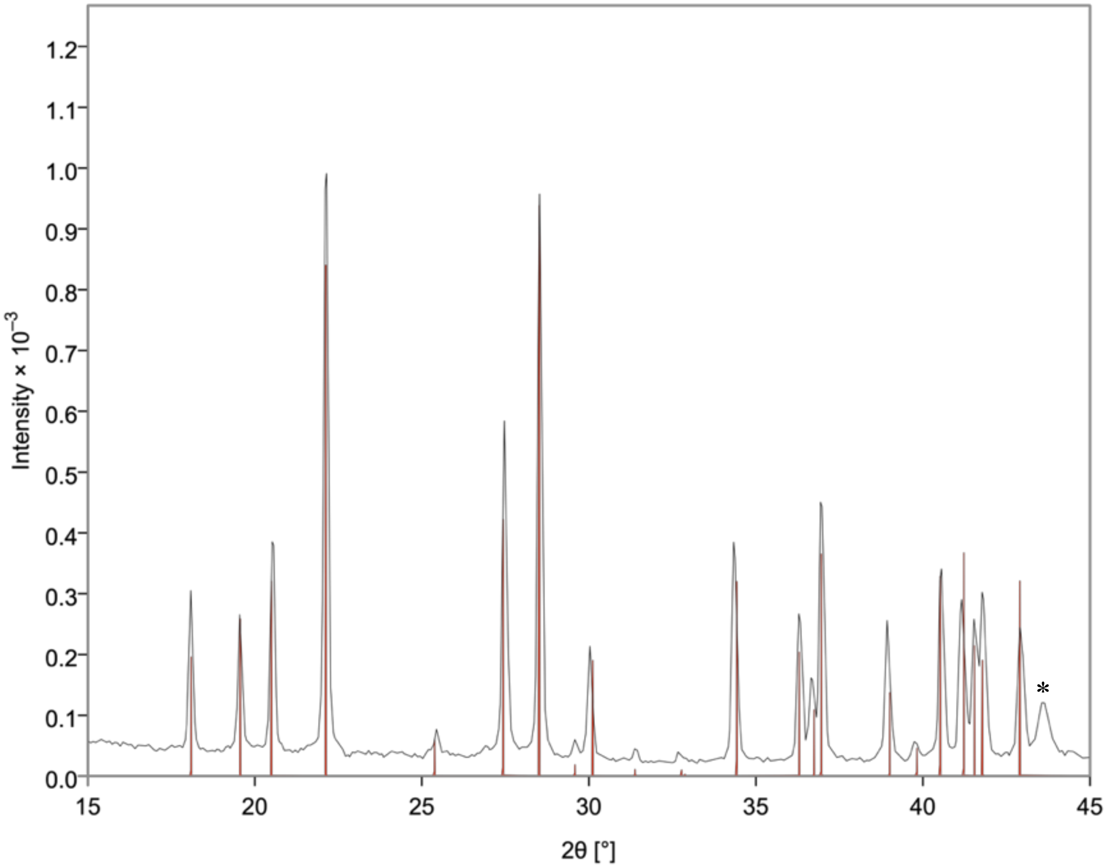

Figure 2.10 Experimental (black) and calculated (red) PXRD patterns of $UCoS_3$. Peak at ~43º (marked with an asterisk) corresponds to the steel slide.

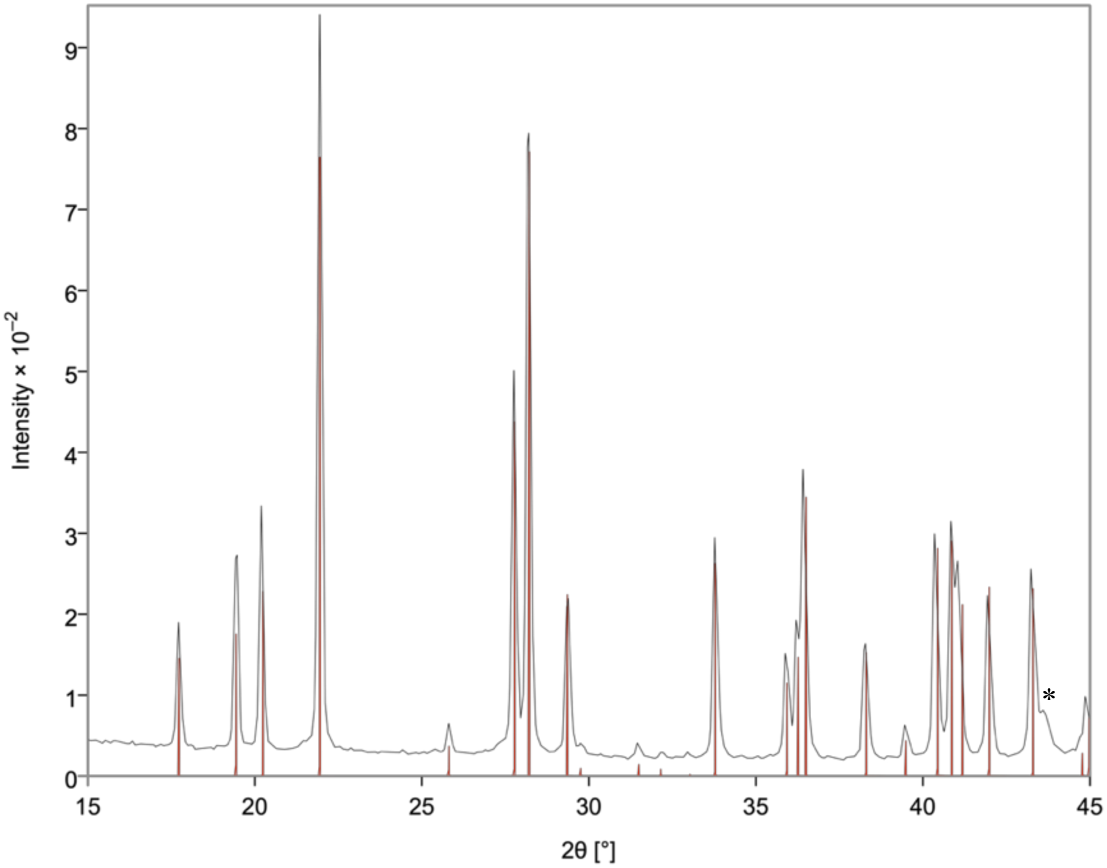

Figure 2.11 Experimental (black) and calculated (red) PXRD patterns of $UNiS_3$. Peak at ~43° (marked with an asterisk) corresponds to the steel slide.

The successful synthesis of $UCoS_3$ and $UNiS_3$ from an oxide using the BCM method allowed us to study their magnetic properties. As the magnetism of $UCoS_3$ has been reported before, we used it as a reference point, whereas the magnetic properties of $UNiS_3$ are reported here for the first time. As expected, the magnetic susceptibility of $UCoS_3$ in a range of 2 to 130 K falls in line with the previously reported data,[144] and exhibits a single magnetic transition at ~60 K, which is followed by a significant increase in the magnetic susceptibility, indicating a ferro- or ferrimagnetic transition (Figure 2.12). Unlike its Co analog, the magnetic susceptibility of $UNiS_3$ exhibits a downturn in the magnetic

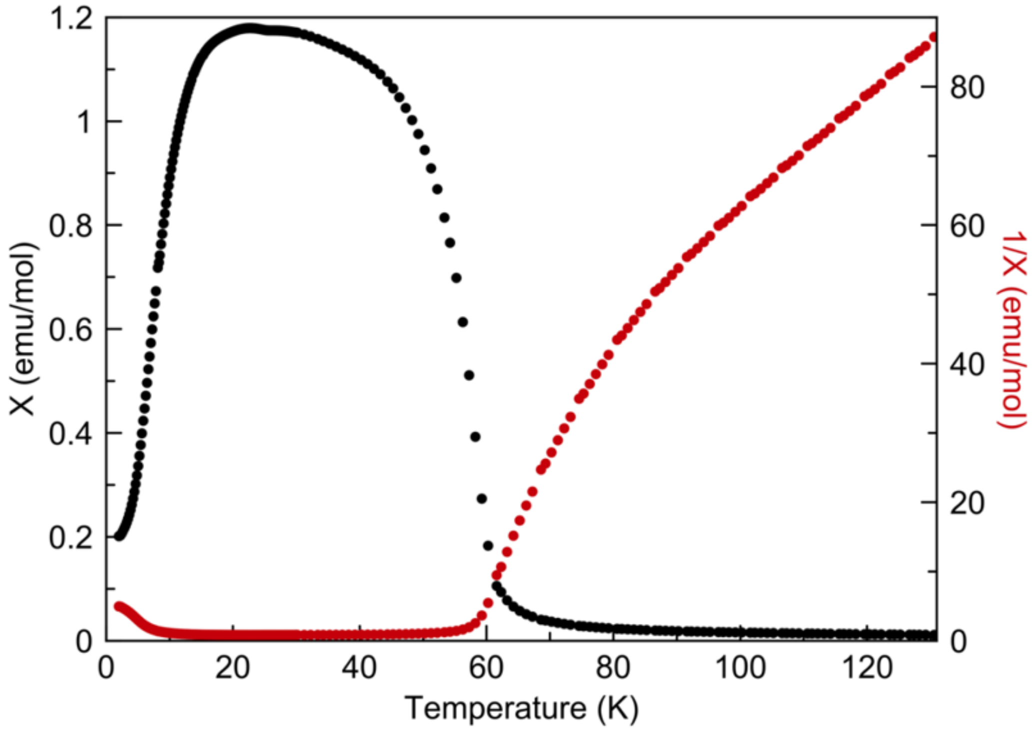

Figure 2.12 The temperature dependence of the molar susceptibility and inverse molar susceptibility for $UCoS_3$.

susceptibility at about 30 K (Figure 2.8). There is no indication of impurities in the PXRD patterns of the sample; moreover, we prepared samples that contain U and Ni in 0.98:1 and 1:0.98 molar ratios to account for possible impurities that could result from off-stoichiometry in the reagent mixture. As both samples showed the same magnetic behavior, one can surmise that this magnetic behavior is attributable to $UNiS_3$ rather than to an unidentified impurity. A magnetization vs. magnetic field plot collected from a fresh sample at room temperature showed that the sample acquires a residual magnetization when exposed to a magnetic field (Figure 2.13). This fact indicates that there is some degree of glassy behavior in $UNiS_3$ at 300 K. We collected magnetic susceptibility up to 375 K

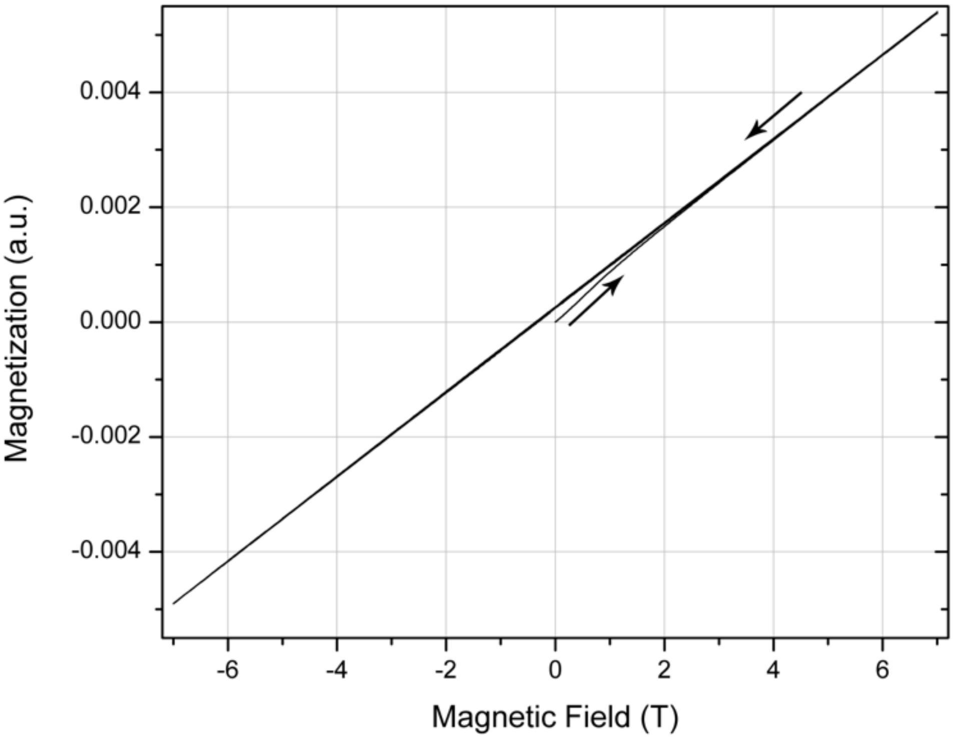

Figure 2.13 Magnetization vs. field plot for a fresh $UNiS_3$ sample at 300 K.

but no clear magnetic transition was revealed. Additional studies using neutron diffraction to learn about potential magnetic order in $UNiS_3$ are planned for the future.

Flux crystal growth using the BCM method. **Successful synthesis of the $Ln_xU_2S_5$ series.** Flux crystal growth is one of the pillars of modern solid state chemistry that has functioned very efficiently for obtaining and characterizing new phases in single crystal form.[4, 145] Due to our interest in the magnetism of uranium sulfides, we investigated the rare earth uranium sulfide system to study the magnetic behavior and identify possible magnetic interactions between 4*f* and 5*f* orbitals.[146] Prior to realizing the potential use of the BCM method, we had synthesized several compounds in the $Ln_xU_2S_5$ series (Ln = Pr, Nd, Sm, Gd, Tb, and Dy, x = 0.70–0.89) using US_2 as a starting material. Unfortunately, the majority of the reaction products were contaminated by UOS as a result of the hygroscopic nature of US_2.[126, 147] We decided to reinvestigate this system using the BCM method to study the method's effectiveness in flux crystal growth reactions.

To eliminate oxygen from the system and to obtain the target $Ln_xU_2S_5$ products, a series of reactions using UO_2 and Ln_2S_3 with the B-S mixture were performed in evacuated carbon-coated silica tubes. This resulted in the successful synthesis of the $Ln_xU_2S_5$ series without oxygen impurities. Moreover, we attempted reactions targeting the compositions that previously did not form when US_2 was used as a starting material; this led to phase pure single crystalline samples of $Ln_xU_2S_5$ with Ln = Ho, Tm, and Yb. In all cases, a white opaque layer of, presumably, B_2O_3 could be seen attached to the exposed silica at the top of each tube; the final $Ln_xU_2S_5$ products did not contain oxide impurities as determined by PXRD. Magnetic measurements were performed on phase pure samples of $Ln_xU_2S_5$ with Ln = Tb, Dy, Ho, Er, Tm, and Yb, (Figures 2.14-2.19), to show their paramagnetic behavior down to 2 K, Figures 2.20-2.25. Although the Curie-Weiss law fits allowed us to derive the magnetic moments of these compounds (Table 2.1), the exact lanthanide content varies slightly between crystals, thereby affecting the exact U(III) to U(IV) ratio, making an assignment of magnetic moments to specific species in the structures not possible. Similar issues were observed in the previously reported isotypic material $U_{1+\delta}S_2$ that also contains uranium in the +3 and +4 oxidation states, the ratio of which is a function of δ.[148]

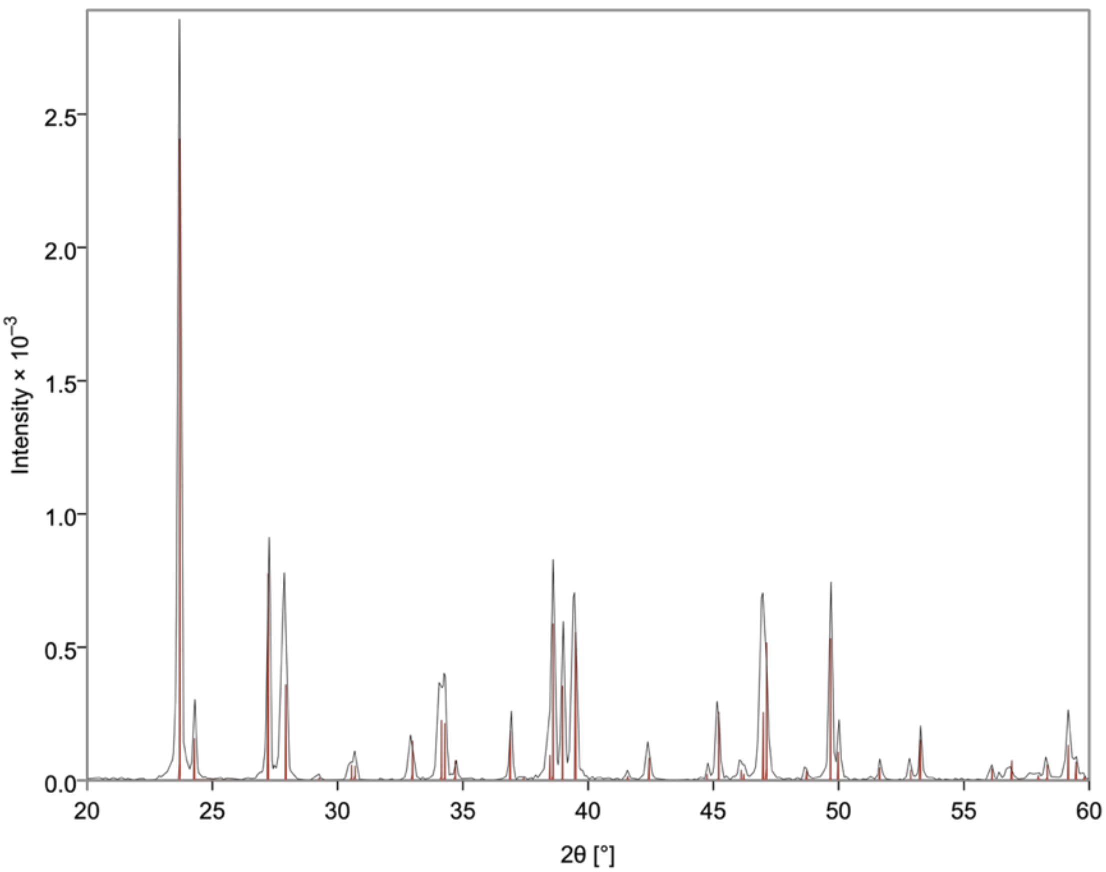

Figure 2.14 Experimental (black) and calculated (red) PXRD patterns of $Tb_{0.82(3)}U_2S_5$.

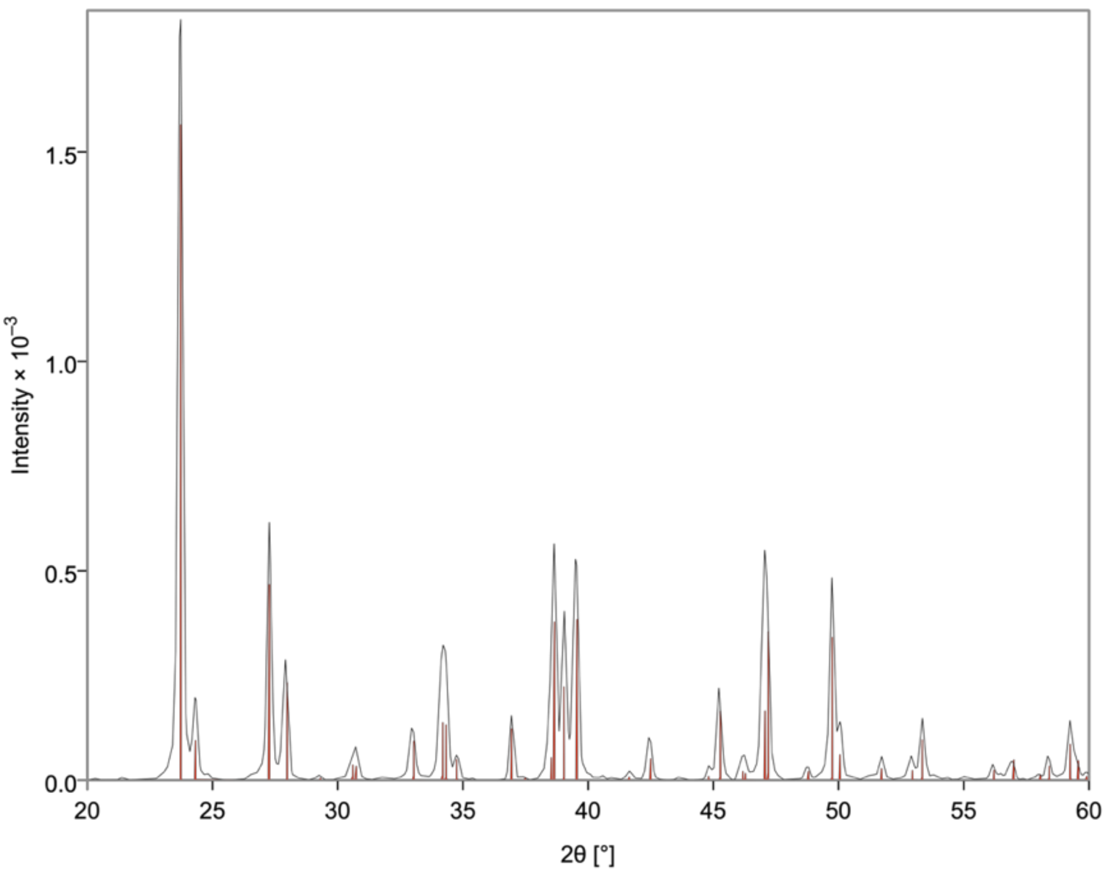

Figure 2.15 Experimental (black) and calculated (red) PXRD patterns of $Dy_{0.76(3)}U_2S_5$.

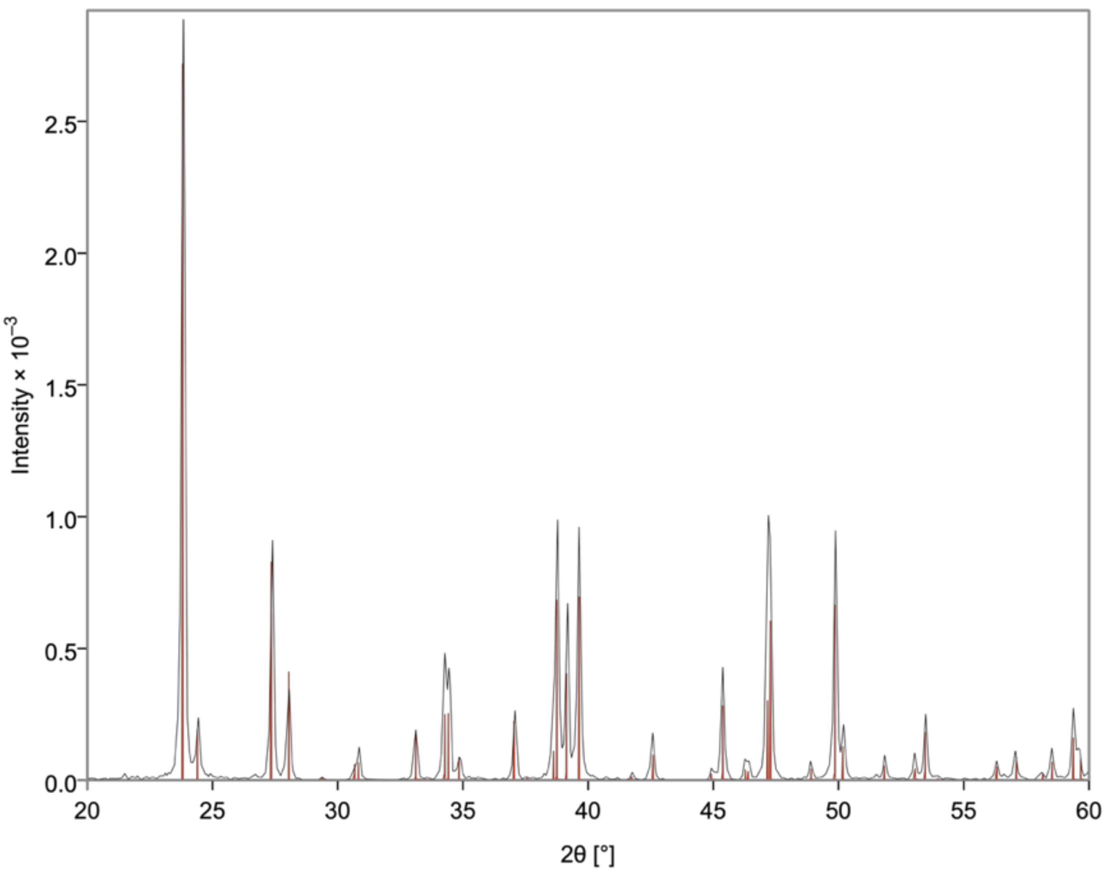

Figure 2.16 Experimental (black) and calculated (red) PXRD patterns of $Ho_{0.79(3)}U_2S_5$.

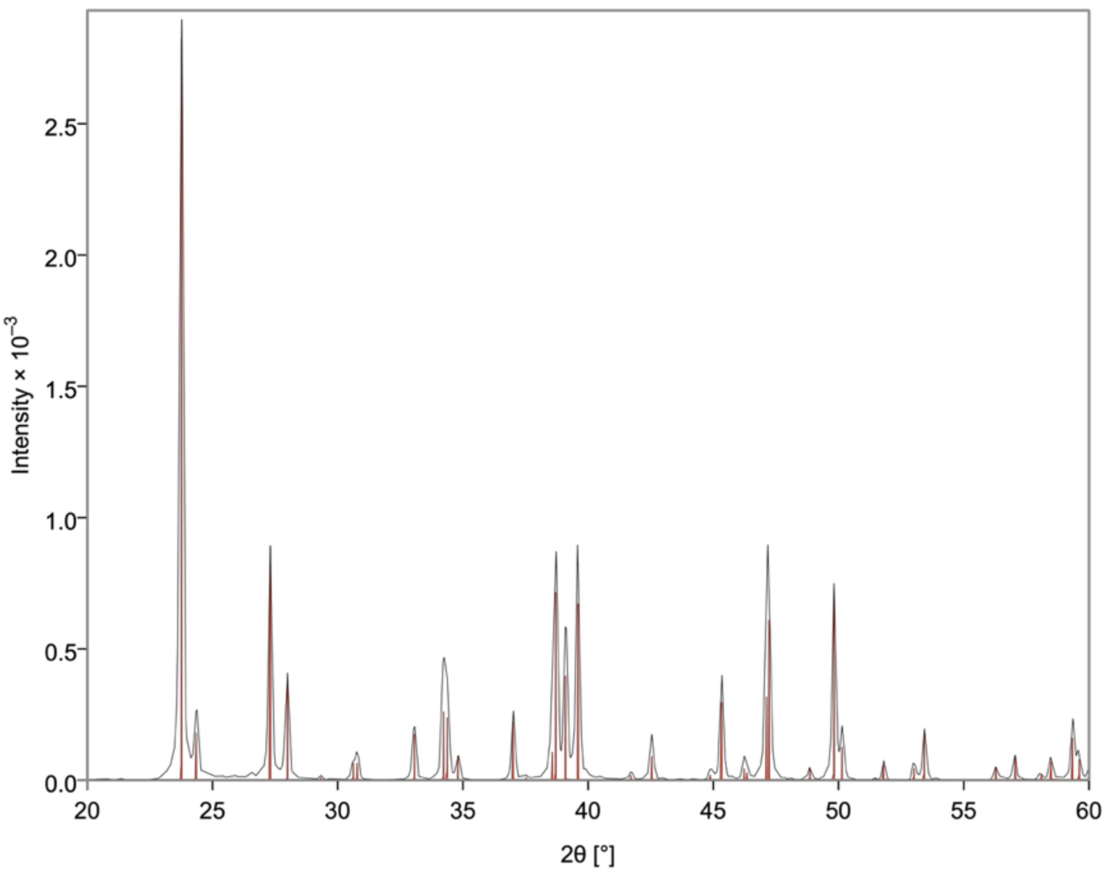

Figure 2.17 Experimental (black) and calculated (red) PXRD patterns of $Er_{0.75(1)}U_2S_5$.

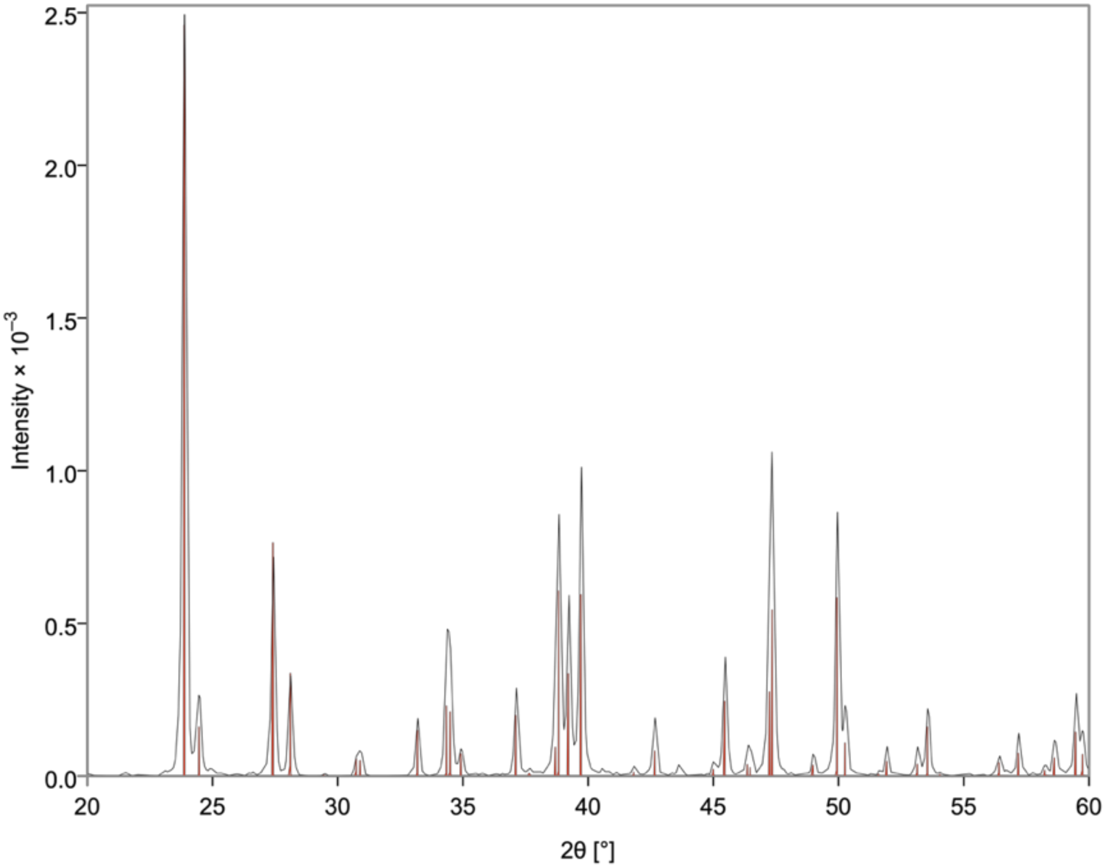

Figure 2.18 Experimental (black) and calculated (red) PXRD patterns of $Tm_{0.75(1)}U_2S_5$.

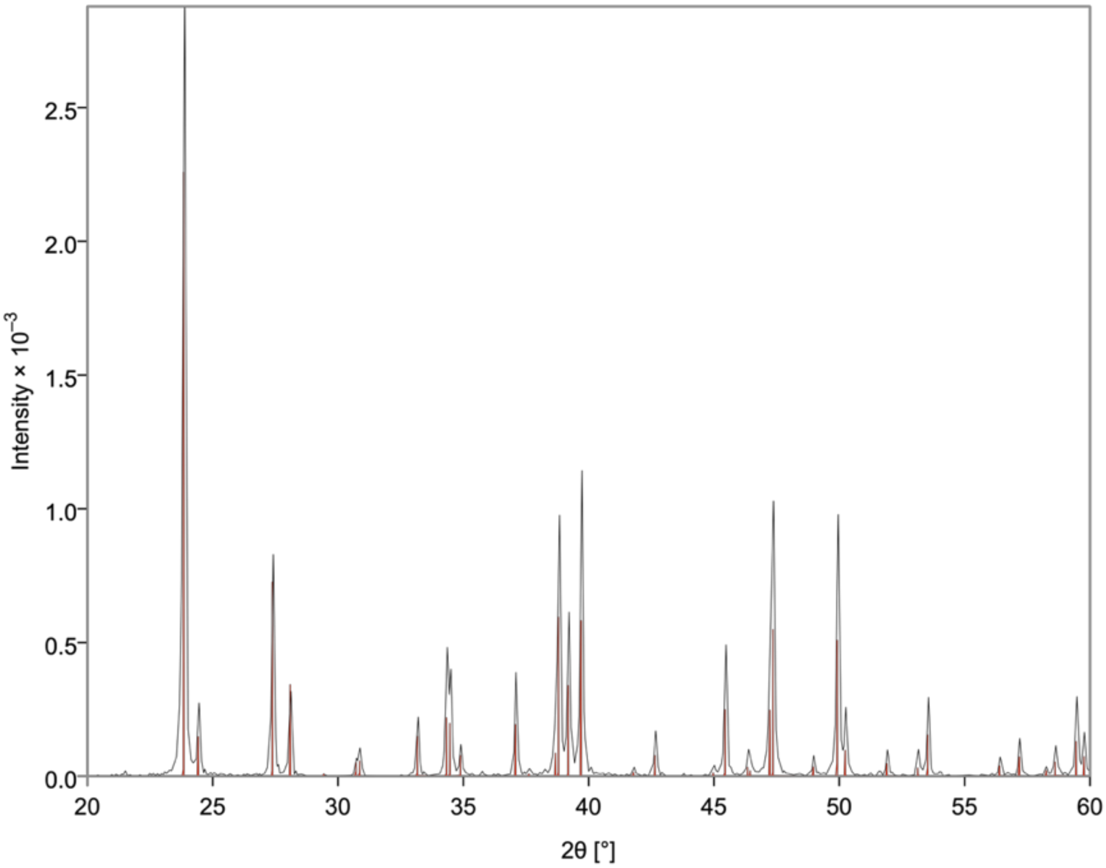

Figure 2.19 Experimental (black) and calculated (red) PXRD patterns of $Yb_{0.70(4)}U_2S_5$.

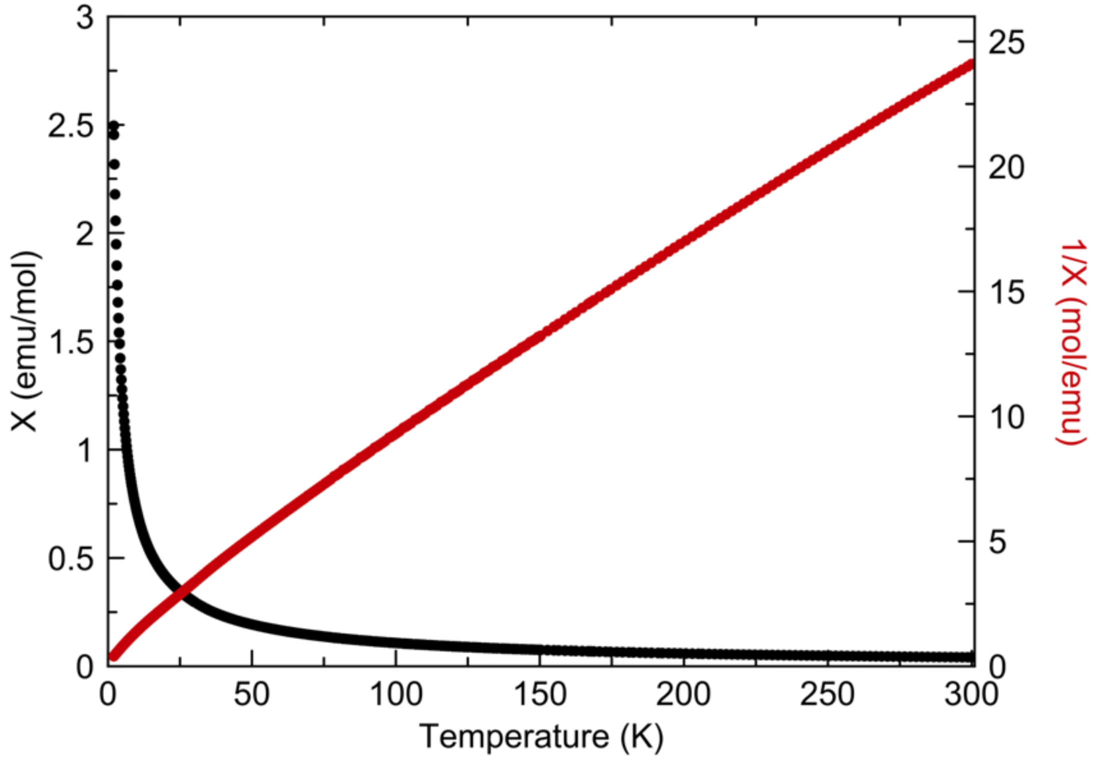

Figure 2.20 The temperature dependence of the molar susceptibility and inverse molar susceptibility for $Tb_{0.82(3)}U_2S_5$.

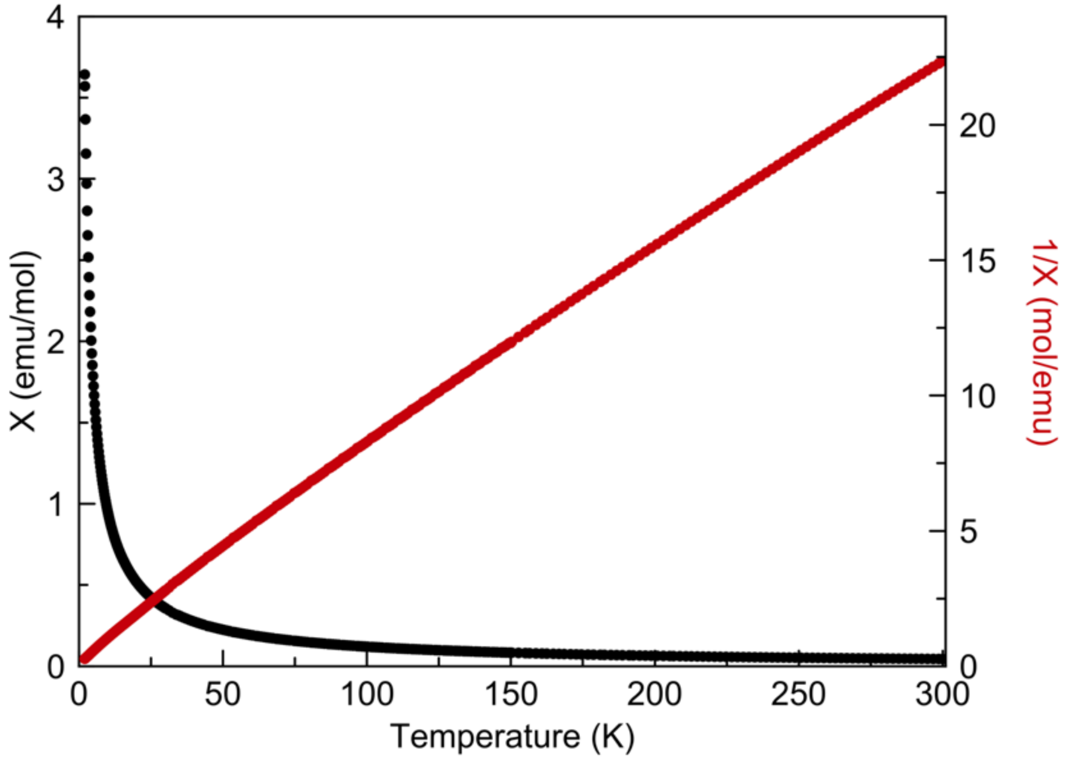

Figure 2.21 The temperature dependence of the molar susceptibility and inverse molar susceptibility for $Dy_{0.76(3)}U_2S_5$.

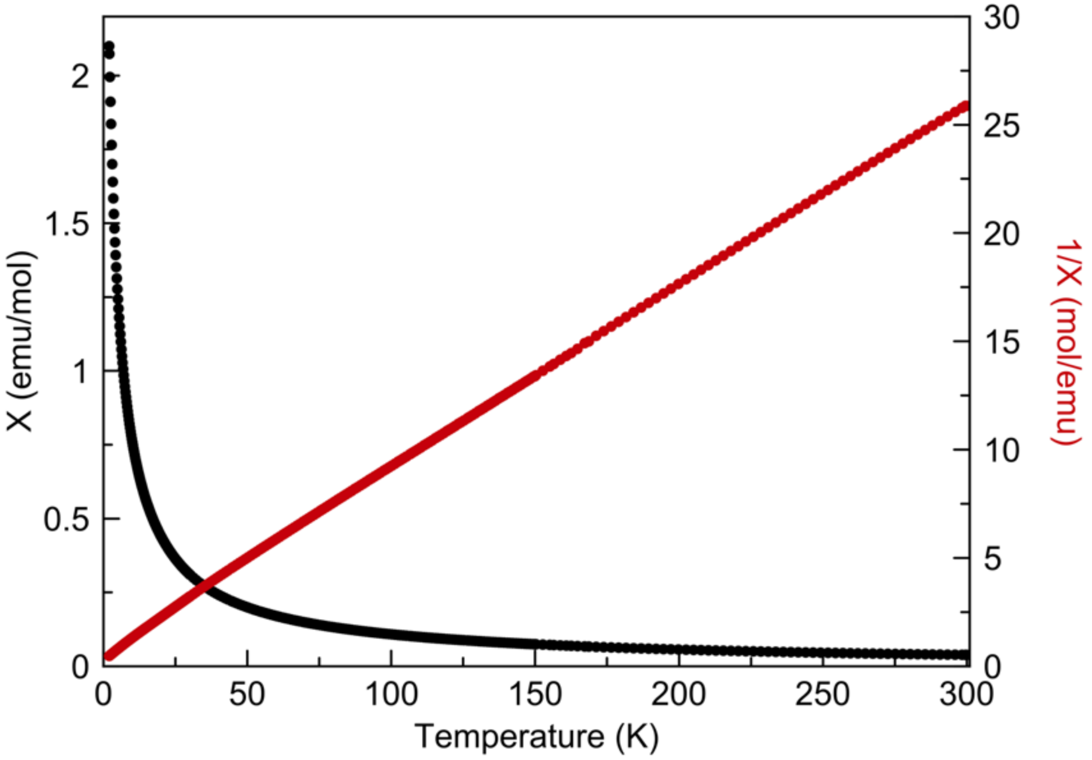

Figure 2.22 The temperature dependence of the molar susceptibility and inverse molar susceptibility for $Ho_{0.78(3)}U_2S_5$.

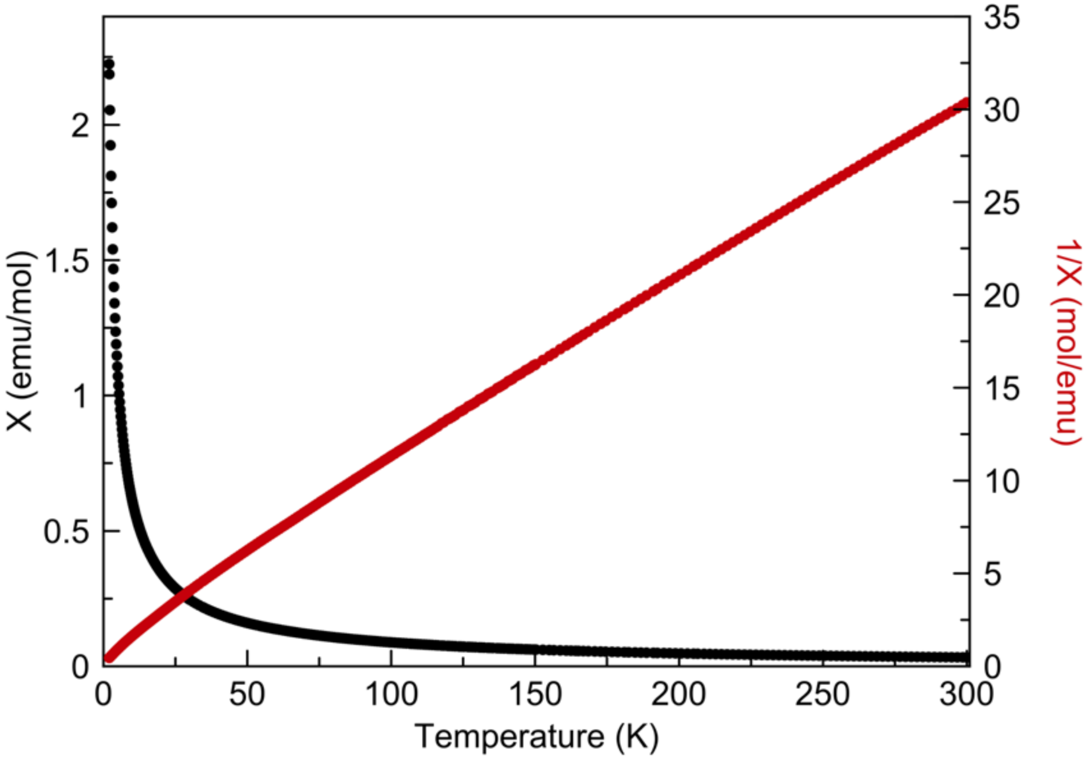

Figure 2.23 The temperature dependence of the molar susceptibility and inverse molar susceptibility for $Er_{0.75(1)}U_2S_5$.

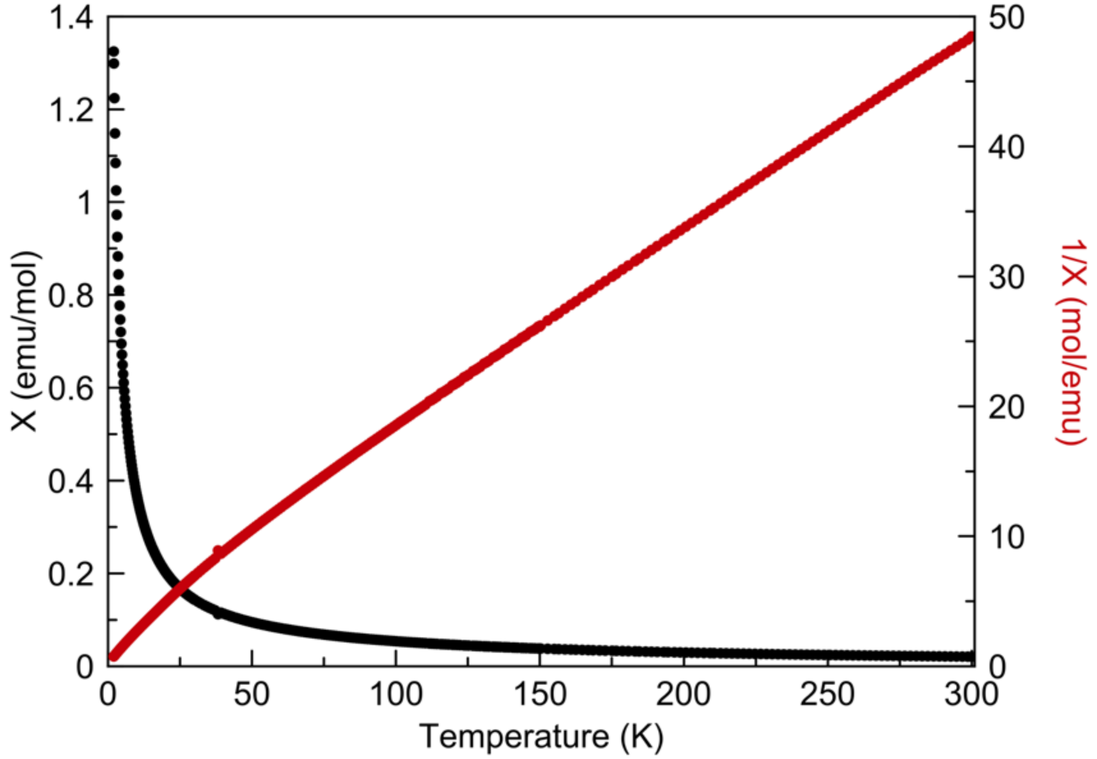

Figure 2.24 The temperature dependence of the molar susceptibility and inverse molar susceptibility for $Tm_{0.75(1)}U_2S_5$.

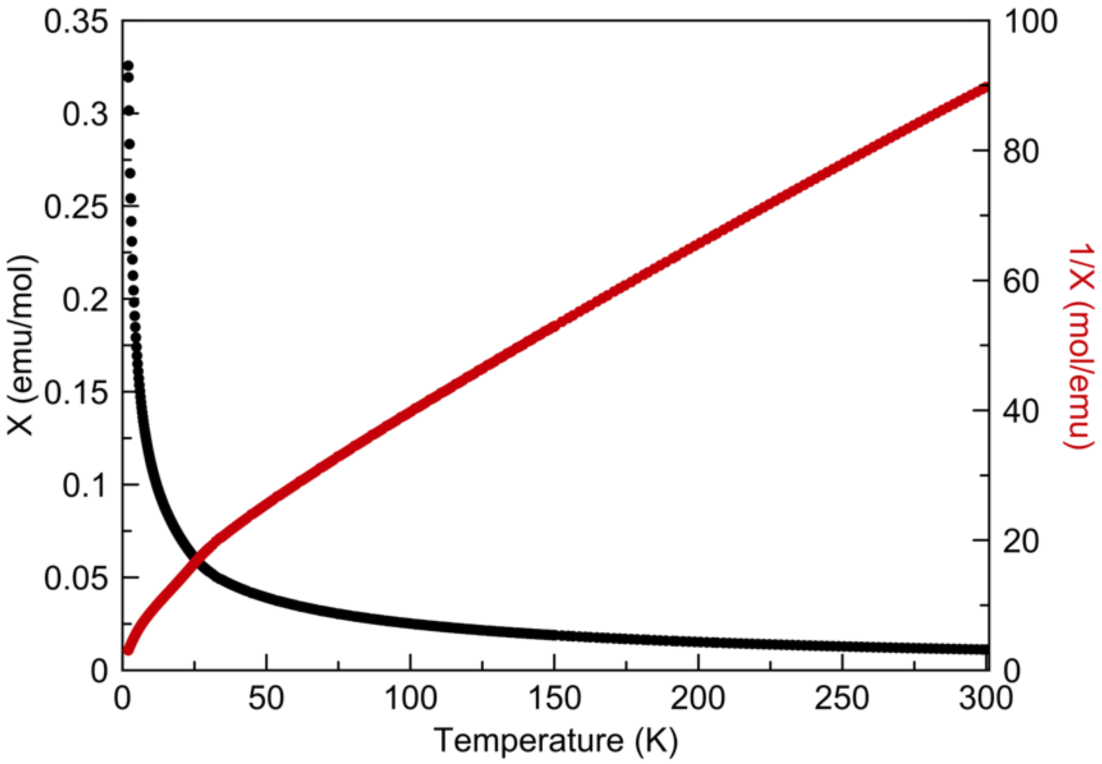

Figure 2.25 The temperature dependence of the molar susceptibility and inverse molar susceptibility for $Yb_{0.70(4)}U_2S_5$.

Table 2.1 The molar susceptibility, χ, and total effective moment, μ_{eff}, at 300 K obtained for phase pure samples of $Ln_xU_2S_5$ (Ln = Tb, Dy, Ho, Er, Tm, Yb).

$Ln_xU_2S_5$	χ(emu/mol)	μ_{eff} (μ_B)
$Tb_{0.82(3)}U_2S_5$	0.0415	9.9748
$Dy_{0.76(3)}U_2S_5$	0.0447	10.3567
$Ho_{0.78(3)}U_2S_5$	0.0387	9.6264
$Er_{0.75(1)}U_2S_5$	0.0329	8.8853
$Tm_{0.75(1)}U_2S_5$	0.0206	7.0331
$Yb_{0.70(4)}U_2S_5$	0.0111	5.1689

Thorium thiophosphates. The successful synthesis of the $Ln_xU_2S_5$ series demonstrated the use of the BCM method for the crystal growth of rare earth uranium sulfides. To see if this approach could be extended to other actinides, we utilized the BCM method for the crystal growth of thorium containing chalcogenides. We targeted a thorium analog of previously reported uranium thiophosphates with complex topology and relatively large unit cells (>7,500 Å^3).[37] The use of a RbI flux with the BCM method for *in situ* sulfurization of ThO_2 in the presence of P_2S_5 and Na_2S resulted in the formation of single crystals of $Rb_{1.72}Na_{0.68}I_{0.40}[Th(PS_4)_2]$, a close analog of previously reported $Rb_{1.35}Na_{0.93}I_{0.28}[U(PS_4)_2]$ that was obtained via a normal flux crystal growth reaction using US_2 as a starting reagent.

The new thorium compound synthesized using the BCM method is composed of $[Th(PS_4)_2]^{2-}$ slabs, identical to their $[U(PS_4)_2]^{2-}$ analogs, that are filled with severely disordered Na^+, Rb^+, and I^- ions (Figure 2.26). While uranium compounds comprise the majority of the reported actinide sulfides (253 entries in ICSD), thorium sulfides are significantly less common with only 55 entries.[149-152] The small number of reported thorium analogs can potentially be attributed to their perceived similarity to the uranium counterparts and therefore a lack of interest in their synthesis that many would consider redundant.[40] However, the synthesis of the thorium analogs of uranium compounds can be beneficial as it is sometimes difficult to determine the oxidation state of uranium based solely on crystallographic data; while uranium has a range of oxidation states from +2 to +6 in its sulfides,[153-158] thorium does not adopt an oxidation state higher than +4. Therefore, introduction of this simple and effective synthetic method for thorium sulfides can help clarify uranium oxidation states in chalcogenide systems and lead to a significant boost in the number of reported thorium sulfides in the future.

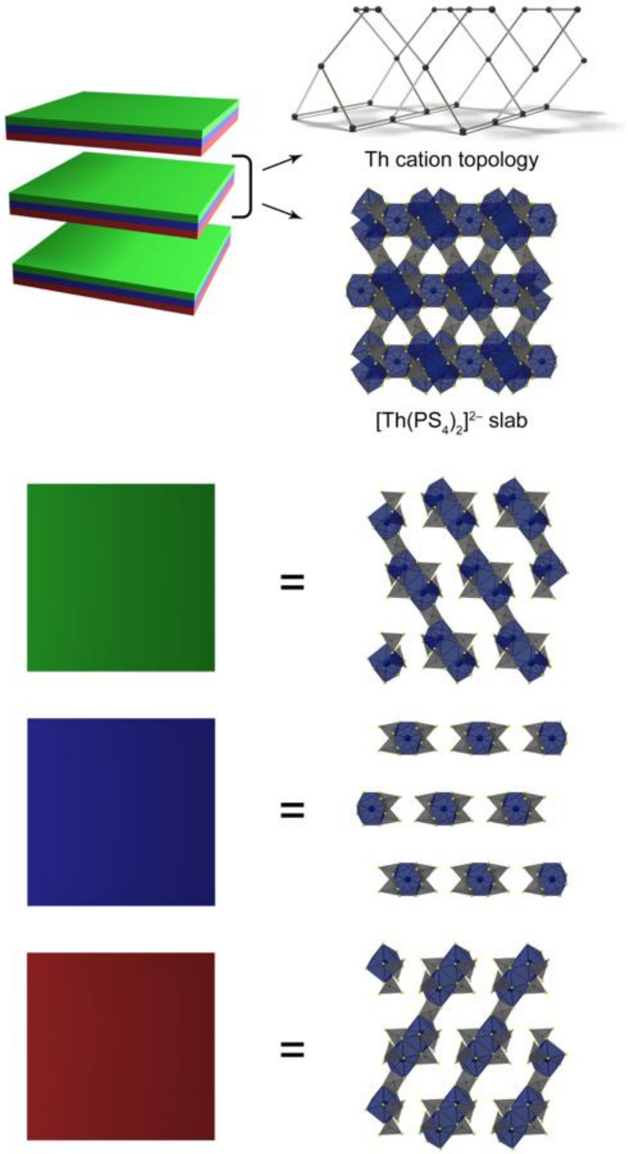

Figure 2.26 A schematic representation of the $Rb_{1.72}Na_{0.68}I_{0.40}[Th(PS_4)_2]$ structure. The main structural unit is a $[Th(PS_4)_2]^{2-}$ slab that consists of three pseudo-layers (shown as green, blue, and red plates). The slabs are filled with disordered Rb^+, Na^+, and I^- ions, maintaining its charge balance.

Application of the BCM method for the synthesis of U(V,VI) chalcogenides.

There are only few reports on uranium sulfides with uranium in oxidation states higher than +4, as the chalcogenides tend to stabilize uranium in oxidation states lower than +5. There are a few exceptions, such as the series of alkali copper uranium sulfides, $M_6Cu_{12}U_2S_{15}$ (M = K, Rb, Cs), in which uranium exhibits the formal oxidation state of +6, although there is experimental evidence of U(V) admixture in these compounds.[129] In order to probe the potential of the new BCM method for the formation of uranium sulfides in uncommon oxidation states, the synthesis of $Cs_6Cu_{12}U_2S_{15}$ was targeted by replacing U metal with U_3O_8 as a starting material. Moreover, we replaced Cs_2S (in the original synthesis) that generated a polychalcogenide flux with Cs_2CO_3 and an additional quantity of the B-S mixture to generate the flux *in situ* from a commercially available carbonate. In doing so, all air- and moisture-sensitive chalcogenide starting materials were replaced with ones that can be handled in air, i.e. U_3O_8, Cu, Cs_2CO_3, B, and S, circumventing the need of using inert atmospheres (e.g. a glovebox or a glovebag) and greatly simplifying reaction preparation. This process resulted in the successful synthesis of the target phase, as confirmed by SC XRD and powder XRD analysis. This experiment concludes a full range of actinide sulfide materials can be targeted using this new method.

Conclusions. In summary, we demonstrated the first successful application of the BCM method for a full range of actinide chalcogenide syntheses, including binary actinide chalcogenide syntheses, solid state synthesis and flux crystal growth reactions. An unprecedented one-step transformation of the stable U_3O_8 and ThO_2 actinide oxides to phase pure US_2 and ThS_2 was achieved at 800 °C. Solid state sulfurization reactions were developed to demonstrate oxygen replacement in a NiO + U_3O_8 mixture, and $CoUO_4$, to form $UNiS_3$ and $UCoS_3$ perovskites, respectively, the magnetic properties of which are reported. Further development of solid state sulfurization reactions is of paramount importance for actinide chalcogenide chemistry as it bridges oxide and chalcogenide solid state chemistry, opening a new synthetic route toward actinide chalcogenides.

To demonstrate the applicability of this method for exploratory flux crystal growth, a wide range of actinide chalcogenides with different fluxes were synthesized, particularly, a new family of mixed 4*f*/5*f* compounds $Ln_xU_2S_5$ in a CsCl flux, a thorium thiophosphate with complex topology $Rb_{1.72}Na_{0.68}I_{0.40}[Th(PS_4)_2]$ in a RbI flux, and a U(V,VI) sulfide $Cs_6Cu_{12}U_2S_{15}$ in an *in situ* generated polysulfide flux. One great advantage of this method is that it allows for actinide chalcogenide generation at relatively low temperatures, below 600 °C, allowing for the use of polychalcogenide fluxes. We believe that the combination of convenient exploratory crystal growth and an easy solid state route toward phase pure materials, which is necessity for property measurements, creates a synergy that will significantly boost research in the field of actinide chalcogenides.

Experimental:

Caution! Both thorium and uranium, although the uranium precursor used in this synthesis contains depleted uranium, require that proper procedures for handling radioactive materials are observed. All handling of radioactive materials was performed in laboratories specially designated for the study of radioactive actinide materials.

General considerations. All reagents were obtained from commercial sources and were used without further purification. All reactions with chalcogens were carried out in carbon-coated fused silica tubes (10×12mm inner and outer diameters, about 12 cm length). All reagents were handled in air, except for P_2S_5 and Na_2S, which were handled in a nitrogen filled glovebag. Phase composition of all products was determined by powder X-ray diffraction using a Bruker D2 Phaser instrument. Magnetic property measurements were performed using a Quantum Design MPMS 3 SQUID magnetometer. Single-crystal X-ray diffraction data were collected at 300(2) K on a Bruker D8 QUEST diffractometer equipped with an Incoatec IμS 3.0 microfocus radiation source (MoKα, $\lambda = 0.71073$ Å) and a PHOTON II area detector (Tables 2.2-2.4). Quantitative elemental analysis was performed on product single crystals using a Tescan Vega-3 SEM instrument equipped with a Thermo EDS attachment (SEM images seen in Figure 2.27).

Chalcogenation reactions. The reactions between actinide oxides AnO_2 (An = U and Th) and chalcogens were studied at 800 °C using 1:2:3 and 1:4:6 molar ratios of the starting materials AnO_2, B, and Q (Q = S, Se, Te); and were sulfurized at different temperatures (400, 500, 600, 700, and 800 °C) using 1:6:9 and 1:2:3 molar ratios for U_3O_8:B:S and ThO_2:B:S, respectively (see Tables 2.5 and 2.6). All reactions were placed into a programmable furnace, ramped up to the desired temperature, where it was held for 24 hours. The phase composition of the products was determined by PXRD. It is important to note that in principle boron can act as a reducing agent toward the other reagents. In practice it appears that the stability of the product phase also significantly influences the actinide oxidation state in the syntheses described.

Synthesis of Actinide Sulfides. $Ln_xU_2S_5$**.** For Ln = Pr-Dy, a 6:1 molar ratio of US_2 and Ln_2S_3 respectively was used along with 1 gram of CsCl flux. For Ln = Ho-Yb, a 1:1:6:9 molar ratio of UO_2, Ln_2S_3, B, and S, respectively, was used along with 1 gram of CsCl flux. All reactions were put in a programmable furnace and ramped up to 400 °C in 1 hour, then slowly ramped at 20 °C/hour to 750 °C where it was held for 20 hours. The furnace was then cooled to 550 °C at a rate of 8 °C/hour and subsequently shut down to cool to room temperature. The product was sonicated in water to dissolve and remove the CsCl flux from the desired product. After sonication, the water was decanted off the product, and the product was vacuum filtered, washed with water and acetone, and dried in air.

$UNiS_3$ was obtained in a solid state reaction between 0.1127 g of U_3O_8 and 0.030 g of NiO in a 1:3 molar ratio with 0.0631 g of B-S mixture (9% excess) with a 2:3 B:S molar ratio. The mixture was thoroughly ground and pelletized before reacting it at 850 °C for 12 h.

$UCoS_3$ was obtained from $CoUO_4$ that resulted from a reaction between $CoC_2O_4 \cdot 2H_2O$ and U_3O_8 in a 3:1 molar ratio at 1100 °C. After confirming phase purity by PXRD, $CoUO_4$ (0.0861 g) was ground with 0.0382 g of the B-S mixture (2% excess based on O content) and reacted at 1100 °C for 3 h. The phase purity of the obtained $UCoS_3$ was confirmed by PXRD.

$Rb_{1.72}Na_{0.68}I_{0.40}[Th(PS_4)_2]$ was obtained in a flux crystal growth reaction between ThO_2, Na_2S, P_2S_5, B, and S in a 1:4:4:4:6 ratio (based on 0.0874 g of ThO_2) with 1.0 g of a RbI flux. The reaction was ramped up to 720 °C in 1 h, dwelled for 10 h, and cooled to 500 °C at a 10 °C/h rate. The product was separated from the flux by dissolving the flux in 30 mL of DMF and filtering using vacuum filtration. While the obtained transparent crystals are somewhat moisture sensitive, they rapidly react with liquid water releasing H_2S.

$Cs_6Cu_{12}U_2S_{15}$ was obtained in a reaction between U_3O_8, Cu, Cs_2CO_3, B, and S in a 1:12:8:30 ratio. Due to hygroscopic nature of Cs_2CO_3, it was dried in an oven overnight at 260 °C. The reaction was ramped up to 600 °C at a 50 °C/h rate, dwelled for 24 h, and

Table 2.2 Crystallographic data for the $Ln_xU_2S_5$ phases with Ln = Pr, Nd, Sm, Gd, Tb, Dy. X-ray source (Mo Kα (0.71073 Å).

Chemical formula	$Pr_{0.89(4)}U_2S_5$	$Nd_{0.88(4)}U_2S_5$	$Sm_{0.87(3)}U_2S_5$	$Gd_{0.88(2)}U_2S_5$	$Tb_{0.82(3)}U_2S_5$
Formula weight	762.12	763.29	766.79	775.53	766.67
Crystal system	Tetragonal				
Space group	*P*4/*ncc*				
a, Å	10.2982(3)	10.2927(2)	10.2913(2)	10.2902(2)	10.2743(2)
b, Å	10.2982(3)	10.2927(2)	10.2913(2)	10.2902(2)	10.2743(2)
c, Å	6.3524(2)	6.3490(2)	6.34450(10)	6.35750(10)	6.3372(2)
V, Å^3	673.69(4)	672.61(3)	671.95(3)	673.18(3)	668.96(3)
ρ_{calcd}, g/cm^3	7.514	7.538	7.580	7.652	7.612
μ, mm^{-1}	55.741	56.161	56.999	58.044	58.316
T, K	302.83	303.9	302.14	302.43	303.88
Crystal dim., mm^3	0.06x0.06x0.02	0.06x0.06x0.02	0.06x0.06x0.02	0.06x0.06x0.02	0.06x0.06x0.02
2θ range, deg.	2.797—32.482	2.799—32.490	2.799—32.499	2.799—32.495	2.804—32.493
Reflections collected	11591	11311	11661	12092	11368
Data/parameters/restraints	615/26/0	612/26/0	611/26/0	614/26/0	608/26/0
R_{int}	0.0383	0.0593	0.0420	0.0406	0.0414
Goodness of fit	1.164	1.153	1.139	1.117	1.204
$R_1(I > 2\sigma(I))$	0.0162	0.0201	0.0141	0.0143	0.0186
wR_2 (all data)	0.0365	0.0402	0.0351	0.0357	0.0441

Table 2.3 Crystallographic data for the $Ln_xU_2S_5$ phases with Ln = Dy, Ho, Er, Tm, Yb. X-ray source (Mo Kα (0.71073 Å).

Chemical formula	$Dy_{0.76(3)}U_2S_5$	$Ho_{0.78(3)}U_2S_5$	$Er_{0.75(1)}U_2S_5$	$Tm_{0.75(1)}U_2S_5$	$Yb_{0.70(4)}U_2S_5$
Formula weight	760.27	765.83	762.22	762.64	757.06
Crystal system	Tetragonal				
Space group	*P*4/*ncc*				
a, Å	10.2599(2)	10.2482(5)	10.2459(2)	10.2421(2)	10.2367(2)
b, Å	10.2599(2)	10.2482(5)	10.2459(2)	10.2421(2)	10.2367(2)
c, Å	6.32830(10)	6.3239(3)	6.32500(10)	6.32210(10)	6.3145(2)
V, $Å^3$	666.15	664.17(7)	663.99(3)	663.19(3)	661.70(3)
ρ_{calcd}, g/cm^3	7.581	7.659	7.625	7.638	7.599
μ, mm^{-1}	58.419	59.363	59.541	60.091	60.071
T, K	301.92	303.21	302.56	302.82	302.32
Crystal dim., mm^3	0.06x0.06x0.02	0.06x0.06x0.02	0.06x0.06x0.02	0.06x0.06x0.02	0.06x0.06x0.02
2θ range, deg.	2.808—32.499	2.811—29.977	2.811—39.097	2.813—39.112	2.814—29.925
Reflections collected	11396	7138	60859	59232	38623
Data/parameters/restraints	606/26/0	486/26/0	970/26/0	968/26/0	485/26/0
R_{int}	0.0474	0.0505	0.0676	0.0759	0.0647
Goodness of fit	1.156	1.125	1.195	1.182	1.291
$R_1(I > 2\sigma(I))$	0.0180	0.0224	0.0152	0.0188	0.0335
wR_2 (all data)	0.0421	0.0566	0.0325	0.0460	0.0919

Table 2.4 Crystallographic data for $Rb_{1.72}Na_{0.68}I_{0.40}[Th(PS_4)_2]$ and $Cs_6Cu_{12}U_2S_{15}$. X-ray source (Mo Kα (0.71073 Å).

Chemical formula	$Rb_{1.72}Na_{0.68}I_{0.40}[Th(PS_4)_2]$	$Cs_6Cu_{12}U_2S_{15}$
Formula weight	763.86	2517.00
Crystal system	Orthorhombic	Cubic
Space group	*Ccce*	*Ia*-3*d*
a, Å	10.5566(4)	19.0822(4)
b, Å	20.6415(9)	19.0822(4)
c, Å	38.2850(15)	19.0822(4)
V, $Å^3$	8342.5(6)	6948.4(4)
ρ_{calcd}, g/cm^3	3.041	4.812
μ, mm^{-1}	15.837	23.559
T, K	301.69	301.36
Crystal dim., mm^3	0.14x0.02x0.01	0.04x0.03x0.02
2θ range, deg.	2.231—27.499	2.615—27.481
Reflections collected	227538	24038
Data/parameters/restraints	4799/220/13	676/29/0
R_{int}	0.0612	0.0405
Goodness of fit	1.174	1.170
$R_1(I > 2\sigma(I))$	0.0391	0.0245
wR_2 (all data)	0.0875	0.0485

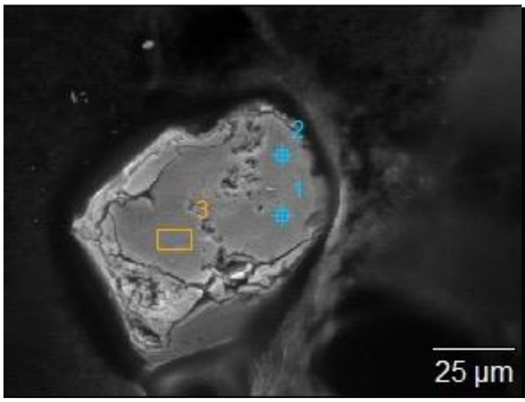

(a)

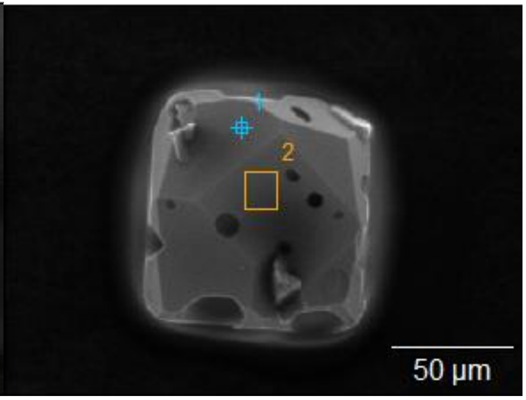

(b)

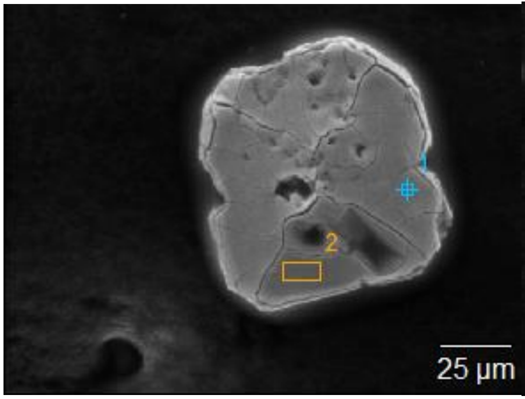

(c)

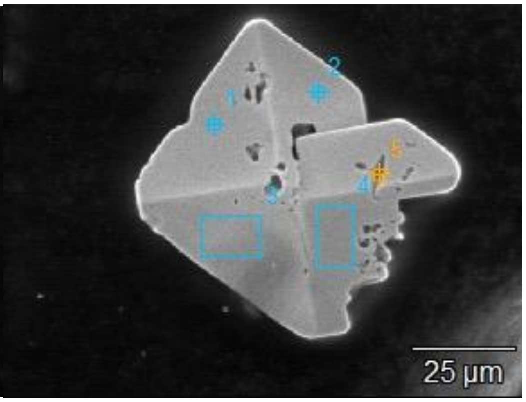

(d)

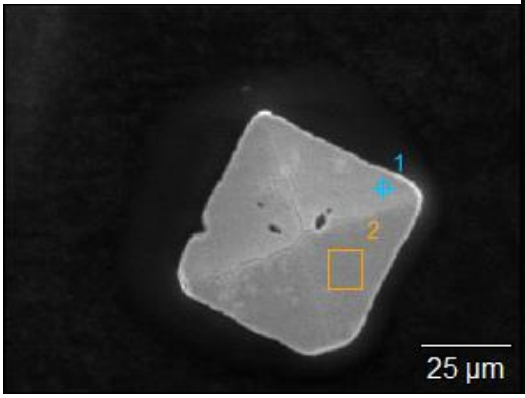

(e)

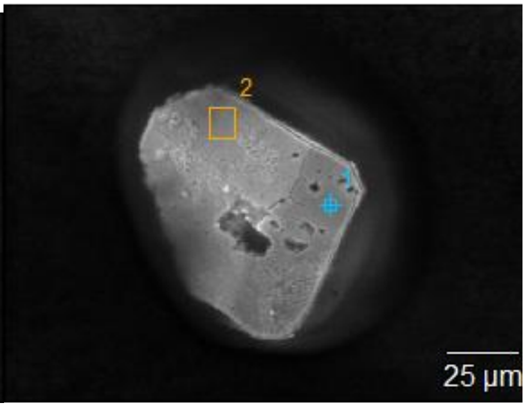

(f)

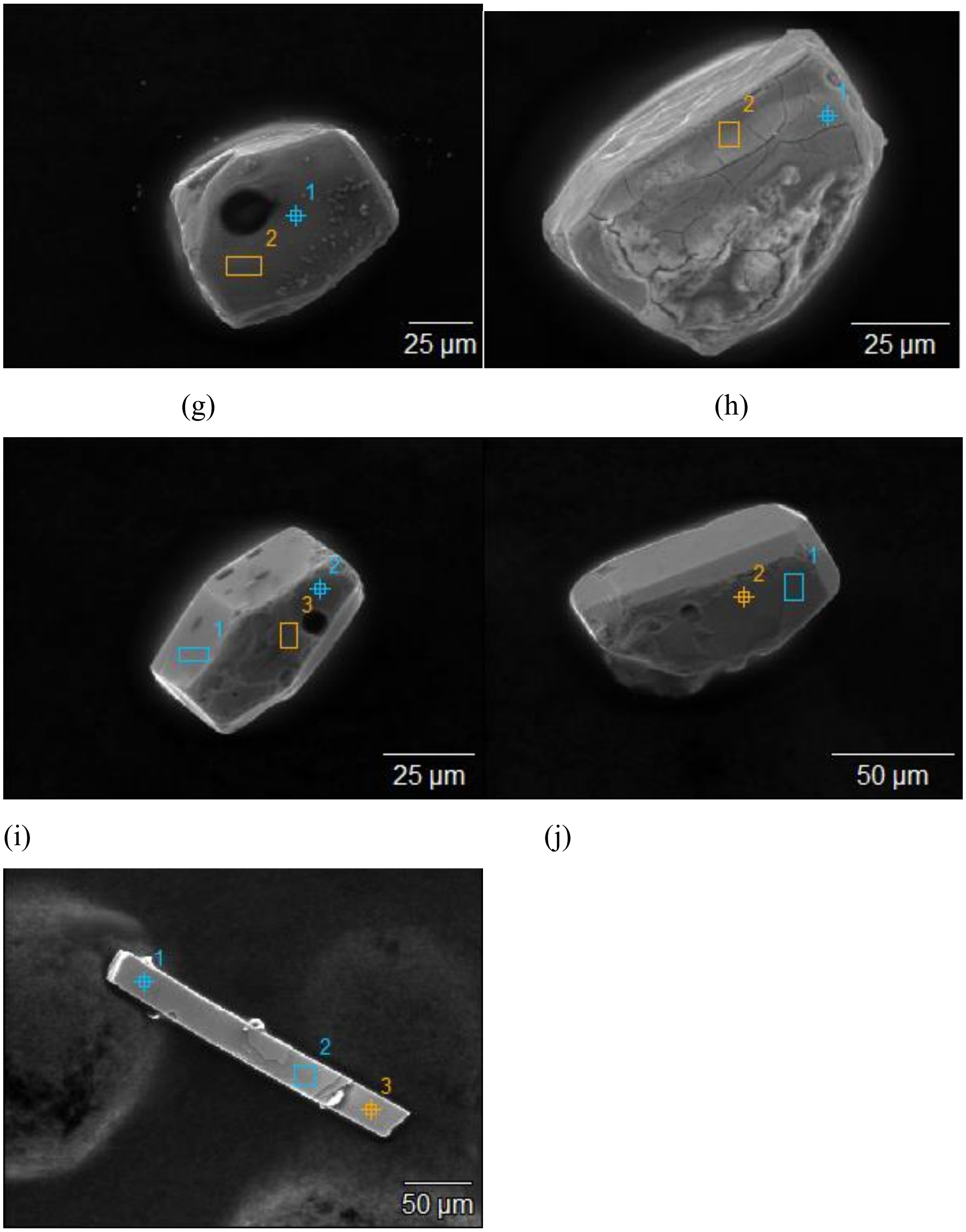

(g) (h)

(i) (j)

(k)

Figure 2.27 SEM images of single crystal of (a) $Pr_{0.89(4)}U_2S_5$, (b) $Nd_{0.88(4)}U_2S_5$, (c) $Sm_{0.87(3)}U_2S_5$, (d) $Gd_{0.89(2)}U_2S_5$, (e) $Tb_{0.82(3)}U_2S_5$, (f) $Dy_{0.76(3)}U_2S_5$, (g) $Ho_{0.79(3)}U_2S_5$, (h) $Er_{0.75(1)}U_2S_5$, (i) $Tm_{0.75(1)}U_2S_5$, (j) $Yb_{0.70(4)}U_2S_5$, and (k) $Rb_{1.72}Na_{0.68}I_{0.40}[Th(PS_4)_2]$.

Table 2.5 The molar ratios and amounts of reagents used in the chalcogenation reactions all at a reaction temperature of 800 °C.

Actinide Source	Chalcogen	Molar Ratio An:B:S	mmols Actinide Oxide	mmols Boron	mmols Sulfur
UO_2	S	1:2:3	0.741	1.48	2.224
		1:4:6	0.37	1.48	2.224
	Se	1:2:3	0.741	1.48	2.224
		1:4:6	0.741	2.96	4.444
	Te	1:2:3	0.37	0.74	1.111
		1:4:6	0.37	1.48	2.223
ThO_2	S	1:2:3	0.379	0.758	1.135
		1:4:6	0.379	1.517	2.272
	Se	1:2:3	0.757	1.517	2.272
		1:4:6	0.757	3.034	4.545
	Te	1:2:3	0.379	0.758	1.137
		1:4:6	0.379	1.517	2.275

Table 2.6 The molar ratios and amounts of reagents used in the sulfurization reactions at temperatures of 400-800 °C and 500-800 °C for reactions involving uranium and thorium, respectively.

Actinide Source	Chalcogen	Molar Ratio An:B:S	mmols Actinide Oxide	mmols Boron	mmols Sulfur
U_3O_8	S	1:6:9	0.237	1.424	2.136
ThO_2	S	1:2:3	0.189	0.378	0.567

cooled to 200 °C in 40 h. The product was separated from the formed polychalcogenide flux by dissolving the flux in several portions (about 30 mL each) of DMF. Black blocks of the target phase formed along with other unidentified phases. Structure determination from single crystal X-ray diffraction unambiguously confirmed the identity of the crystal (Table 2.4).

Crystal structure description. $Ln_xU_2S_5$ crystallizes in the *P*4/*ncc* space group and consists of edge sharing US_8 distorted bicapped trigonal prisms with channels that are filled with highly disordered face sharing LnS_8 square antiprisms (Figure 2.28).

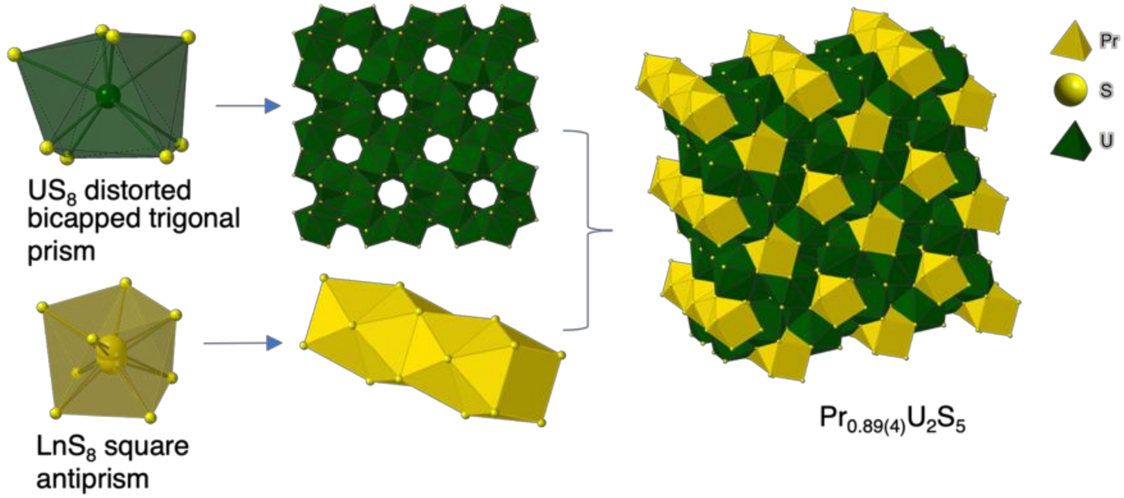

Figure 2.28 A view on the structure of $Pr_{0.89(4)}U_2S_5$ series. US_8 distorted bicapped trigonal prisms edge share to create a 3-dimensional structure with voids that run through which are filled with face sharing LnS_8 square antiprism. The lanthanides are disordered within their polyhedra.

The U–S bond lengths range from 2.7319(2) to 2.9982(9) Å and the Ln–S bond lengths range from 2.674(5) to 2.994(6) Å. The disorder of the lanthanide cations within the channels result in the nonstoichiometric formula, Ln_xUS_5. The occupancy of the lanthanide was found to be dependent on its nature, generally slightly decreasing along the lanthanide series. The obtained structures are closely reminiscent with the structure of α-"US_2" with a composition of $U_{1.1}S_2$. A comparison of the $U_{1.1}S_2$ structure with that of the $Ln_xU_2S_5$ series (Figure 2.29) suggests that the lanthanide cations replace the US_8 square antiprisms within the $U_{1.1}S_2$ parent structure. Given that uranium has a valency of +3.6 in $U_{1.1}S_2$, which implies mixed +3/+4 valency of the U cations in the structure, one can surmise that a mixed uranium valency is observed in the $Ln_xU_2S_5$ series.[148] Bond valence sums were calculated by using the U–S distances in each analogue along with R_0 and B values of 2.55

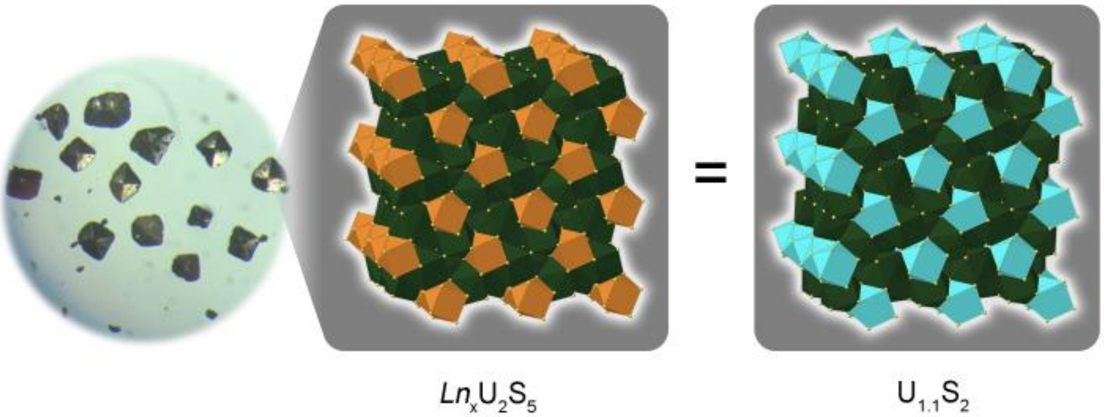

Figure 2.29 (left) An optical image of single crystals of the Nd analogue of the $Ln_xU_2S_5$ series along with a comparison of the (middle) $Ln_xU_2S_5$ structure with (right) that of the presumed parent structure, $U_{1.1}S_2$.

and 0.37, respectively,[159] and show an average uranium oxidation state of 3.76, supporting the presence of an admixture of U(III)/U(IV) on the uranium sites (Table 2.7).

$Rb_{1.72}Na_{0.68}I_{0.40}[Th(PS_4)_2]$ crystallizes in the *Ccce* space group and forms a structure that is an analogue of the previously reported $Rb_{1.35}Na_{0.93}I_{0.28}[U(PS_4)_2]$. In the structure of $Rb_{1.72}Na_{0.68}I_{0.40}[Th(PS_4)_2]$, the thorium atoms are each surrounded by 8 sulfur atoms forming trigonal dodecahedra with Th–S bond lengths of 2.813(2)–3.0392(19) Å. The phosphorus atoms form PS_4^{3-} thiophosphate tetrahedra with P–S bond lengths of 1.977(3)–2.078(3) Å (average 2.034(9) Å) and S–P–S angles ranging from 103.9(12)—113.9(17)° (average 109.5°). The complex structure of $Rb_{1.72}Na_{0.68}I_{0.40}[Th(PS_4)_2]$ is comprised of $[Th(PS_4)_2]^{2-}$ slabs held together by severely disordered Rb^+, Na^+, and I^- ions, which are located both between the slabs as well as through the pores within the slabs. Each individual slab can be dissected into three separate layers; a bottom, middle, and top layer (Figure 2.26). The bottom and top layers are both composed of parallel $[Th(PS_4)_2]^{2-}$ chains but differ in that the top layer is mirrored and rotated 60° relative to the bottom

Table 2.7 Bond Valence Sums (BVS) were performed on the $Ln_xU_2S_5$ series. The U—S distances are tabulated below along with the calculated uranium oxidation state. Each bond length describes two of the bonds in the 8-coordinate uranium polyhedra causing each to be counted twice in the BVS calculation. The calculations suggest an average uranium valency of 3.76 further supporting the assignment of mixed U^{3+}/U^{4+} in these structures.

Composition	U—S bond distances				Calculated U oxidation state
$Pr_{0.89(4)}U_2S_5$	2.83	2.80	3.00	2.75	3.70
$Nd_{0.88(4)}U_2S_5$	2.80	2.83	2.99	2.75	3.72
$Sm_{0.87(3)}U_2S_5$	2.83	2.80	2.99	2.74	3.73
$Gd_{0.89(2)}U_2S_5$	2.74	2.84	2.99	2.81	3.72
$Tb_{0.82(3)}U_2S_5$	2.74	2.80	2.99	2.83	3.78
$Dy_{0.76(3)}U_2S_5$	2.74	2.79	2.99	2.82	3.83
$Ho_{0.79(3)}U_2S_5$	2.73	2.79	2.99	2.82	3.86
$Er_{0.75(1)}U_2S_5$	2.99	2.78	2.99	2.74	3.50
$Tm_{0.75(1)}U_2S_5$	2.73	2.78	2.99	2.82	3.87
$Yb_{0.70(4)}U_2S_5$	2.99	2.78	2.81	2.74	3.89

layer. These two layers are then connected through the middle layer which is composed of $Th(PS_4)_4$ groups which connect two chains in the top layer and two chains in the bottom layer.

Acknowledgements. Research supported by the US Department of Energy, Office of Basic Energy Sciences, Division of Materials Sciences and Engineering under award DE-SC0018739.

CHAPTER 3

STRUCTURES AND MAGNETIC PROPERTIES OF $K_2Pd_4U_6S_{17}$, $K_2Pt_4U_6S_{17}$, $Rb_2Pt_4U_6S_{17}$, and $Cs_2Pt_4U_6S_{17}$ SYNTHESIZED USING THE BORON-CHALCOGEN MIXTURE METHOD[1]

---

[1] Reproduced with permission from Breton, L. S., Baumbach, R., Tisdale, H. B., and zur Loye, H.-C., *Inorg. Chem.,* **2022**, 61, 10502-10508. **© 2022 American Chemical Society**

Abstract: A series of $A_2M_4U_6S_{17}$ (A = Alkali metal, M = Pd or Pt) compounds, specifically $K_2Pd_4U_6S_{17}$, $K_2Pt_4U_6S_{17}$, $Rb_2Pt_4U_6S_{17}$, and $Cs_2Pt_4U_6S_{17}$, were synthesized using the combined Boron-Chalcogen Mixture (BCM) and molten flux crystal growth methods. The formation of the Rb- and Cs- containing analogues resulted from the *in-situ* alkali polysulfide flux formation formed from the alkali carbonates. The successful synthesis of single crystals of the title compounds allowed for their structural characterization by single crystal X-ray diffraction. The structure determination revealed disorder of the alkali cations in $Rb_2Pt_4U_6S_{17}$, and $Cs_2Pt_4U_6S_{17}$, while the potassium cations in $K_2Pd_4U_6S_{17}$ and $K_2Pt_4U_6S_{17}$ were fully ordered. Magnetic measurements were performed on samples of $K_2Pt_4U_6S_{17}$, $Rb_2Pt_4U_6S_{17}$, and $Cs_2Pt_4U_6S_{17}$ that contained small amounts of paramagnetic β-US_2 and diamagnetic PtS. Antiferromagnetic order is observed at $T_N = 9.1$ K for $K_2Pt_4U_6S_{17}$. No long-range magnetic order was observed for $Rb_2Pt_4U_6S_{17}$ and $Cs_2Pt_4U_6S_{17}$. Uranium moments of 2.5, 2.6, and 2.6 μ_B were measured for $K_2Pt_4U_6S_{17}$, $Rb_2Pt_4U_6S_{17}$, and $Cs_2Pt_4U_6S_{17}$, respectively.

Introduction. The actinide chalcogenides are of interest for their ability to stabilize uranium's paramagnetic 4+ oxidation state, which makes it possible to study the magnetic behavior of U(IV). Uranium in an oxide environment is typically found in the 6+ oxidation state, which has no unpaired f-electrons and is diamagnetic.[160] While U(IV) oxides are known, such as the uranium (IV) phosphates[39] and silicates[161], their synthesis is difficult.[3] On the other hand, the softer Lewis basicity of the chalcogens relative to oxygen results in most uranium chalcogenides stabilizing uranium's paramagnetic 4+ oxidation state.[2, 102] The ability to stabilize U(IV) in complex chalcogenides has resulted in the exploration of uranium chalcogenides to study the magnetic behavior of U(IV).[36] In addition, such uranium chalcogenides are of interest for their strongly correlated electron states and some of them exhibit unconventional superconductivity, such as UTe_2.

There are, however, synthetic challenges in the synthesis of the actinide chalcogenides that create difficulties for performing magnetic measurements. The dominant synthetic challenge is the high oxophilicity of uranium that leads to the reaction of uranium with even trace amounts of oxygen present in the reaction mixture, resulting in uranium oxide or magnetic oxychalcogenide impurities that complicate magnetic measurements.[121-123] Our recently established Boron Chalcogen Mixture (BCM) method alleviates this problem by permitting the synthesis of uranium chalcogenides from oxide reagents by adding a mixture of boron and the desired chalcogen into the reagent mixture, resulting in products devoid of uranium oxide or oxychalcogenide impurities.[43] This is effected by the much larger formation energy of boron oxide, B_2O_3 (i.e. $\Delta_f G°$(vitreous-B_2O_3) = −1182.5 kJ/mol), versus the boron chalcogenide, B_2S_3 (e.g. $\Delta_f G°$(vitreous-B_2S_3) = −247.6 kJ/mol), favoring the formation of B_2O_3 and allowing elemental boron to act as an 'oxygen sponge'.[131] The formation of B_2O_3 removes oxygen from the system and leaves the chalcogen to react with the other reagents. The BCM method has been successfully employed in the solid-state synthesis of binary actinide chalcogenides and for the molten flux crystal grow of higher order actinide chalcogenides from actinide oxide starting reagents as well as the sulfurization of ternary actinide oxides to sulfides, via solid state syntheses. The ability to use actinide oxide starting reagents to synthesize chalcogenide products greatly facilitates the ease of reaction setup allowing for greater access to actinide chalcogenide compositions and therefore access to the magnetic properties of uranium. Another great synthetic advantage of the BCM method is the *in-situ* alkali polysulfide flux formation that can be achieved by adding an alkali carbonate and an appropriate amount of boron and sulfur to the reaction mixture. The alkali polychalcogenide fluxes have been paramount in the formation of many chalcogenide phases but are highly moisture and air sensitive as well as commercially unavailable, which necessitates their synthesis "in-house" via the combination of the alkali metal and the chalcogen in liquid ammonia.[42, 115, 117, 162-164] The ability to create an alkali polysulfide flux *in-situ* thus negates the need for premade reagents and reduces the number of highly moisture and air sensitive reagents.

Herein we report the synthesis, structural characterization, and magnetic properties of several $A_2M_4U_6S_{17}$ (A = Alkali metal, M = Pd or Pt) compounds synthesized using the combined BCM and molten flux crystal growth methods. This work extends earlier reports by Oh[165, 166] concerning the synthesis of some $A_2M_4U_6Q_{17}$ (Q = chalcogen) compounds where $Rb_2Pd_4U_6S_{17}$ was reported to order antiferromagnetically at low temperature. As detailed herein, applying the BCM method coupled with molten flux crystal growth, resulted in single crystals of $K_2Pd_4U_6S_{17}$, $K_2Pt_4U_6S_{17}$, $Rb_2Pt_4U_6S_{17}$, and $Cs_2Pt_4U_6S_{17}$ whose magnetic properties were measured.

Experimental:

Synthesis. Elemental boron (Cerac, ~100 mesh, 99.5%), elemental sulfur (Fischer Chemical, sublimed), platinum metal (Engelhard corporation), palladium metal (Engelhard corporation), Cs_2CO_3 (Alfa Aesar, 99%), Rb_2CO_3 (Alfa Aesar, 99%), CsCl (VWR, ultra pure), KCl (VWR, ACS grade), and RbCl (Alfa Aesar, 99.8%) were all used as received. U_3O_8 (International Bio-Analytical Industries, Inc., 99.99%) powder was placed in a furnace set to 800 °C for 24 hours and was subsequently stored in a 260 °C oven. K_2S was prepared as stated in the literature and stored in a nitrogen filled glove bag.[167] All alkali carbonates and alkali halide fluxes were kept in a 260 °C oven before use. K_2S and the alkali halide fluxes were handled inside a nitrogen filled glove bag due to their hygroscopic nature. All grinding and mixing of reagents were performed inside the glove bag.

Warning! *Though the uranium precursor used in these syntheses contains depleted uranium, observing proper procedures for handling radioactive materials is required. All handling of radioactive materials was performed in laboratories specially designated for the study of radioactive uranium materials.*

$K_2Pd_4U_6S_{17}$ was prepared by combining 0.119 mmols U_3O_8, 0.483 mmols Pd, 2.377 mmols B, and 3.555 mmols S into an agate mortar. The agate mortar was placed into a nitrogen filled glove bag where 0.907 mmols of K_2S were weighed out and added to the reagent mixture. This mixture was intimately mixed by grinding and loaded into a carbon crucible (9.525mm OD x 6.35mm ID x 50.8 mm L). 3.353 mmols of KCl flux were loaded on top of the ground mixture inside the carbon crucible which was subsequently placed into a fused silica tube (12mm OD x 10 mm ID x 203.2 mm L) which was evacuated, and flame sealed. The silica tube was placed into a furnace set to first ramp to 400 °C in 1 hour then slowly ramp to 900 °C in 10 hours to keep the volatile sulfur from building up enough pressure to burst the tube. After dwelling for 48 hours at 900 °C, the reaction was cooled to 600 °C in 25 hours and the furnace was then shut off to allow the reaction to reach room temperature. The carbon crucible was removed from the fused silica tube and placed in a beaker of ~60 mL of water and sonicated to remove the flux. The water also dissolved and removed the B_2O_3 that formed during the reaction. Black block crystals of $K_2Pd_4U_6S_{17}$ were isolated via vacuum filtration along with β-US_2 and $U_{0.92}Pd_3S_4$.

$\mathbf{K_2Pt_4U_6S_{17}}$ was prepared using the method described above by combining 0.095 mmols U_3O_8, 0.237 mmols Pt, 2.377 mmols B, and 3.555 mmols S, 0.907 mmols of K_2S and 3.353 mmols of KCl flux. Black block crystals of $K_2Pt_4U_6S_{17}$ were isolated via vacuum filtration along with β-US_2 and PtS.

$\mathbf{Rb_2Pt_4U_6S_{17}}$ was prepared using the method described above by combining 0.095 mmols U_3O_8, 0.237 mmols Pt, 2.377 mmols B, and 3.555 mmols S, 0.346 mmols of Rb_2CO_3, and 2.067 mmols of RbCl flux. Black block crystals of $Rb_2Pt_4U_6S_{17}$ were isolated via vacuum filtration along with β-US_2 and PtS.

$\mathbf{Cs_2Pt_4U_6S_{17}}$ was prepared using the method described above by combining 0.048 mmols U_3O_8, 0.119 Pt, 1.184 mmols B, and 1.781 mmols S, 0.173 mmols of Cs_2CO_3 and 1.485 mmols of CsCl flux. Black block crystals of $Cs_2Pt_4U_6S_{17}$ were isolated via vacuum filtration along with PtS.

Warning*: Exposure of boron sulfides to air or water can result in the formation of dangerous hydrogen sulfide gas. When heating the reaction mixtures in fused silica ampules, the generation of sulfur vapor and the thermal decomposition of the alkali carbonates generating* $CO_2(g)$ *will generate an internal pressure that can cause the tube to burst violently.*

Single crystal X-ray diffraction (SXRD). X-ray intensity data from black block crystals of all title compounds were all collected at 300 K using a Bruker D8 QUEST diffractometer equipped with a PHOTON-II area detector and an Incoatec microfocus source (Mo Kα radiation, λ = 0.71073 Å). The raw area detector data frames were reduced and corrected for absorption effects using the SAINT+ and SADABS programs.[78, 79] Final unit cell parameters were determined by least-squares refinement of large sets of reflections taken from each data set. An initial structural model was obtained with SHELXT.[80] Subsequent difference Fourier calculations and full-matrix least-squares refinement against F2 were performed with SHELXL-2018 using the Olex2 interface.[81, 82] For $Rb_2Pt_4U_6S_{17}$ and $Cs_2Pt_4U_6S_{17}$ the free refinement of the alkali metal positions resulted in less than full occupancy as well as a significant q-peak close to the assigned crystallographic position. Refining the alkali metals using a split site model reduced the R-factor and flattened the residual electron density map. The crystallographic data are summarized in Table 3.1.

Powder X-ray diffraction (PXRD). PXRD data were collected on ground samples of the products obtained. Data was collected on a Bruker D2 PHASER diffractometer using Cu Kα radiation over a 2θ range 5–65° with a step size of 0.02°. A Whole Powder Pattern Fit (WPPF) was performed on the PXRD patterns obtained from the product powders of reactions targeting $K_2Pt_4U_6S_{17}$, $Rb_2Pt_4U_6S_{17}$, and $Cs_2Pt_4U_6S_{17}$ using the Rigaku SmartLab II software.[168] The WPPF analysis allowed for the determination of the relative weight percent of the target phase, β-US_2, and PtS within each product powder. The PXRD patterns and WPPF fit are shown in Figures 3.1-3.4 and 3.5-3.7, respectively.

Energy-dispersive spectroscopy (EDS). EDS was performed on single crystals of the title compounds using a Tescan Vega-3 SEM equipped with a Thermo EDS attachment. The SEM was operated in low-vacuum mode. Crystals were mounted on an SEM stub with carbon tape and analyzed using a 20 kV accelerating voltage and an 80

Table 3.1 Crystallographic data for the $A_2M_4U_6S_{17}$ (A = K, Rb, Cs; M = Pd, Pt) compounds reported herein.

Chemical formula	$K_2Pd_4U_6S_{17}$	$K_2Pt_4U_6S_{17}$	$Rb_2Pt_4U_6S_{17}$	$Cs_2Pt_4U_6S_{17}$
Formula weight	2477.00	2831.76	2924.50	3019.38
Crystal system	Tetragonal			
Space group, Z	*P*4/mnc, 2			
a, Å	10.28500(14)	10.2540(2)	10.3116(2)	10.4179(2)
c, Å	12.7001(3)	12.7359(4)	12.7543(3)	12.7935(3)
V, $Å^3$	1343.43(5)	1339.11(7)	1356.15(6)	1388.51(6)
ρ_{calcd}, g/cm^3	6.123	7.023	7.162	7.222
Radiation (λ, Å)	Mo Kα (0.71073 Å)			
μ, mm^{-1}	40.253	58.568	61.091	58.769
T, K	300(2)	300(2)	300(2)	299(2)
Crystal dim., mm^3	0.060x0.040x0.040	0.050x0.050x0.050	0.060x0.060x0.060	0.100x0.050x0.050
2θ range, deg.	2.548—36.354	2.550—30.072	2.540—30.049	2.521—30.035
Reflections collected	27721	19181	19064	19377
Data/parameters/restraints	1696/40/0	1029/40/0	1043/42/0	1067/42/0
$\Delta\rho_{max}$ (e $Å^{-3}$)	2.341	2.387	1.406	2.898
$\Delta\rho_{min}$ (e $Å^{-3}$)	-2.009	-1.477	-1.293	-3.839
R_{int}	0.0464	0.0512	0.0548	0.0710
Goodness of fit	1.295	1.433	1.420	1.301
$R_1(I > 2\sigma(I))$	0.0175	0.0217	0.0170	0.0291
wR_2 (all data)	0.0387	0.0460	0.0413	0.0717

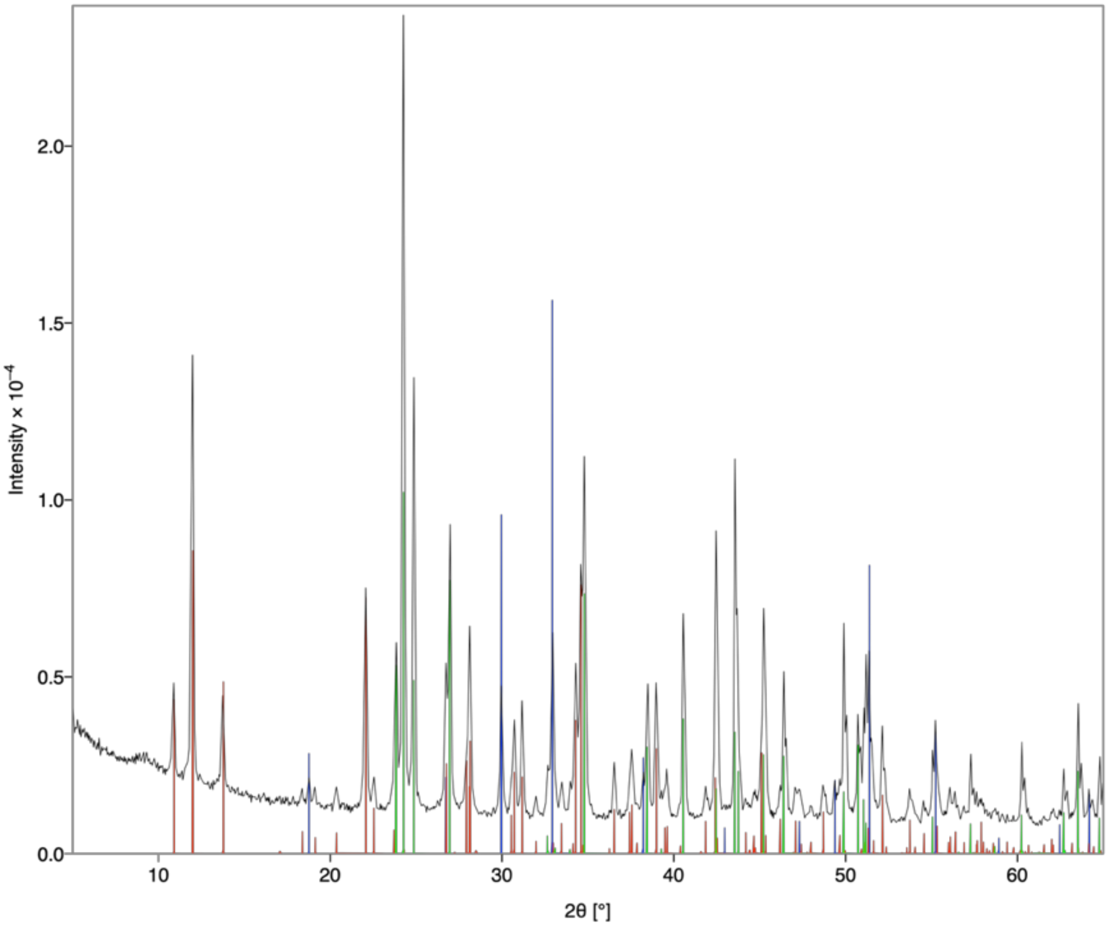

Figure 3.1 An image of the (black) experimental PXRD pattern obtained from the reaction targeting $K_2Pd_4U_6S_{17}$ with the overlayed (red) $K_2Pd_4U_6S_{17}$, (green) β-US_2, and (blue) $U_{0.92}Pd_3S_4$ crystallographic information files (CIFS).

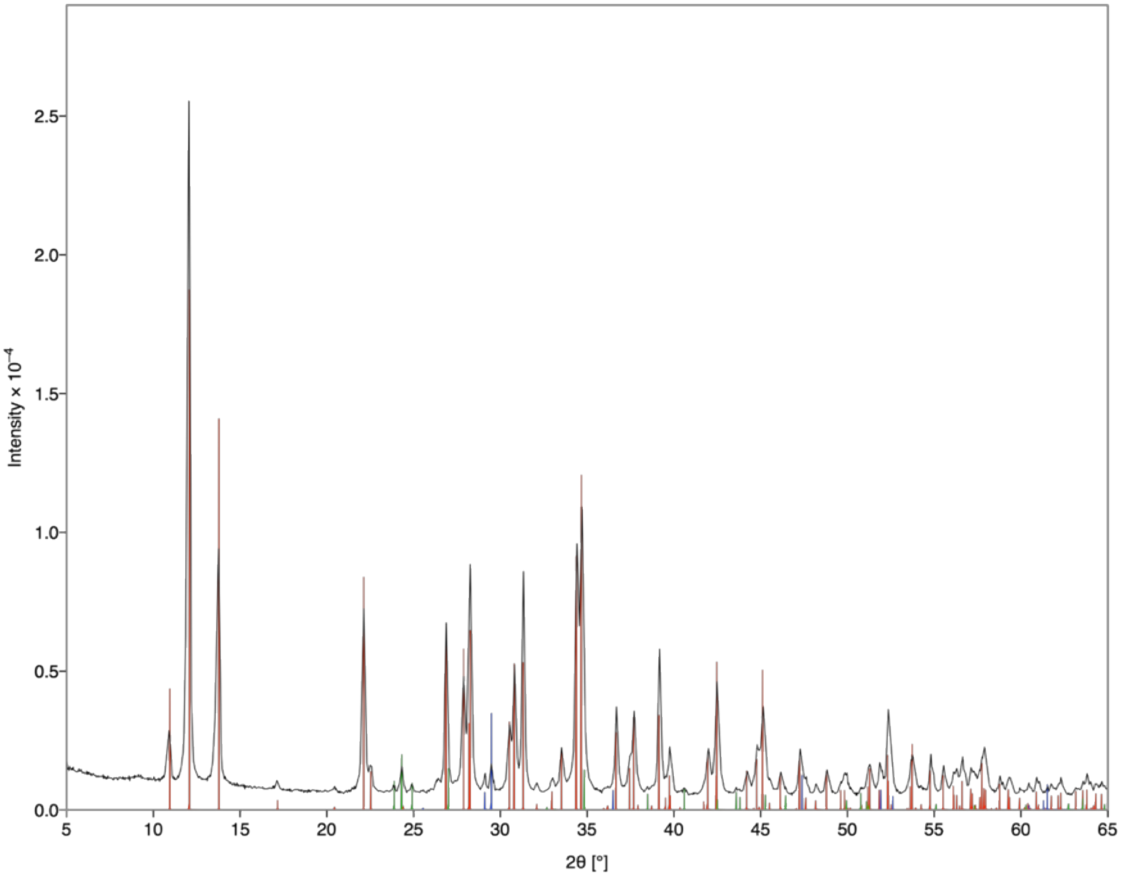

Figure 3.2 An image of the (black) experimental PXRD pattern obtained from the reaction targeting $K_2Pt_4U_6S_{17}$ with the overlayed (red) $K_2Pt_4U_6S_{17}$, (green) β-US_2, and (blue) PtS crystallographic information files (CIFS).

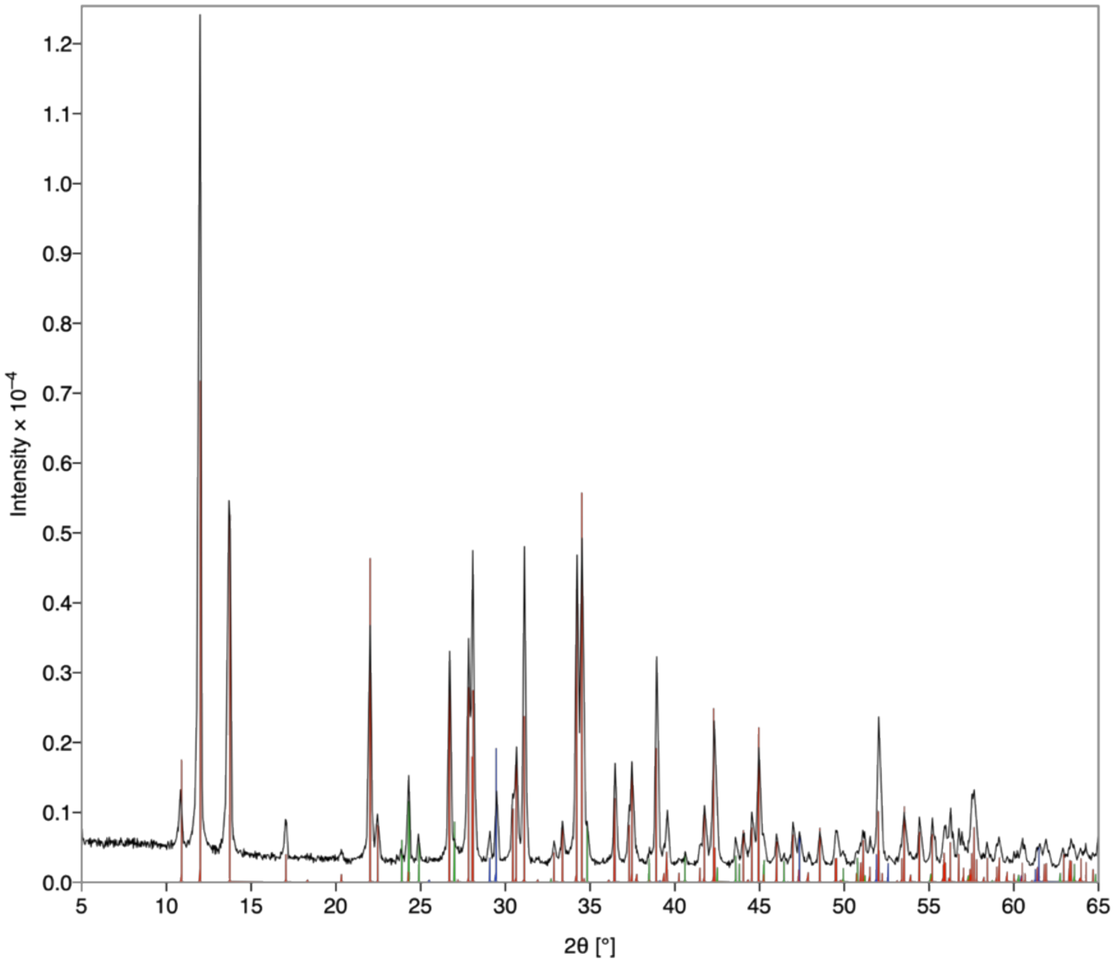

Figure 3.3 An image of the (black) experimental PXRD pattern obtained from the reaction targeting $Rb_2Pt_4U_6S_{17}$ with the overlayed (red) $Rb_2Pt_4U_6S_{17}$, (green) β-US_2, and (blue) PtS CIFS.

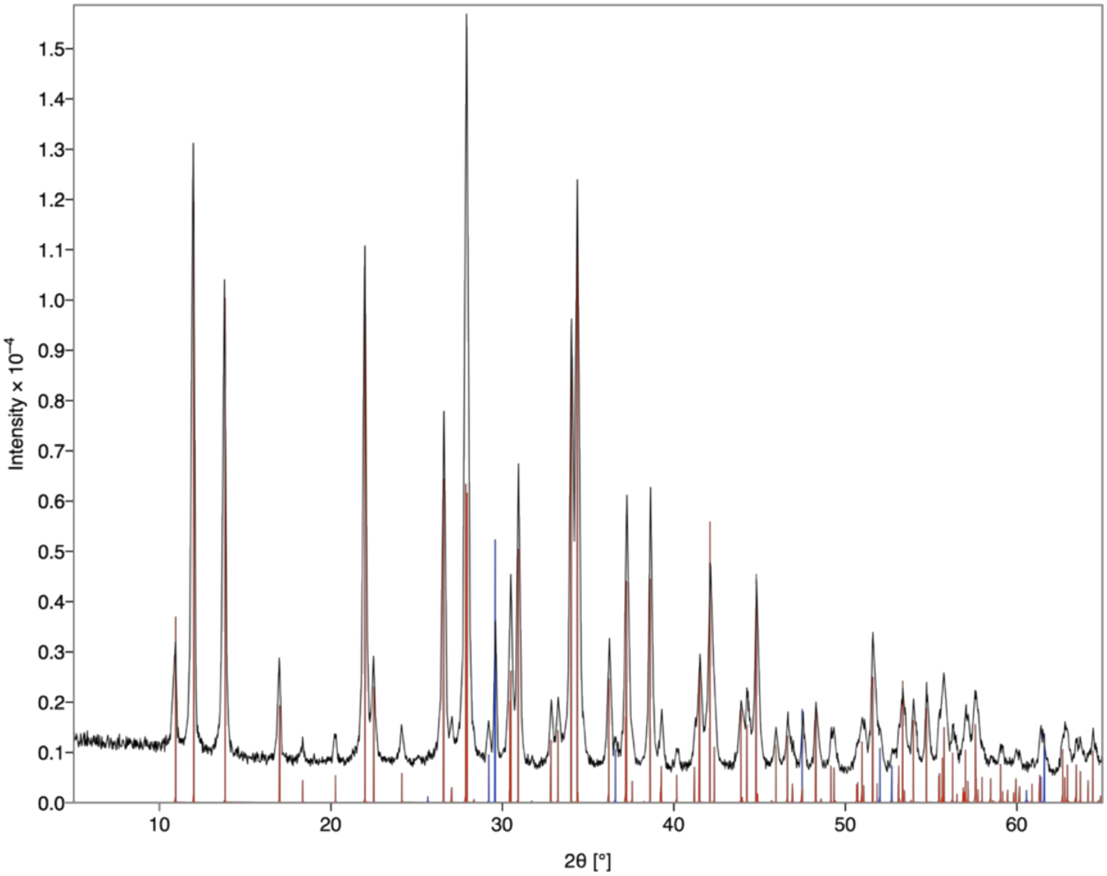

Figure 3.4 An image of the (black) experimental PXRD pattern obtained from the reaction targeting $Cs_2Pt_4U_6S_{17}$ with the overlayed (red) $Cs_2Pt_4U_6S_{17}$ and (blue) PtS CIFS.

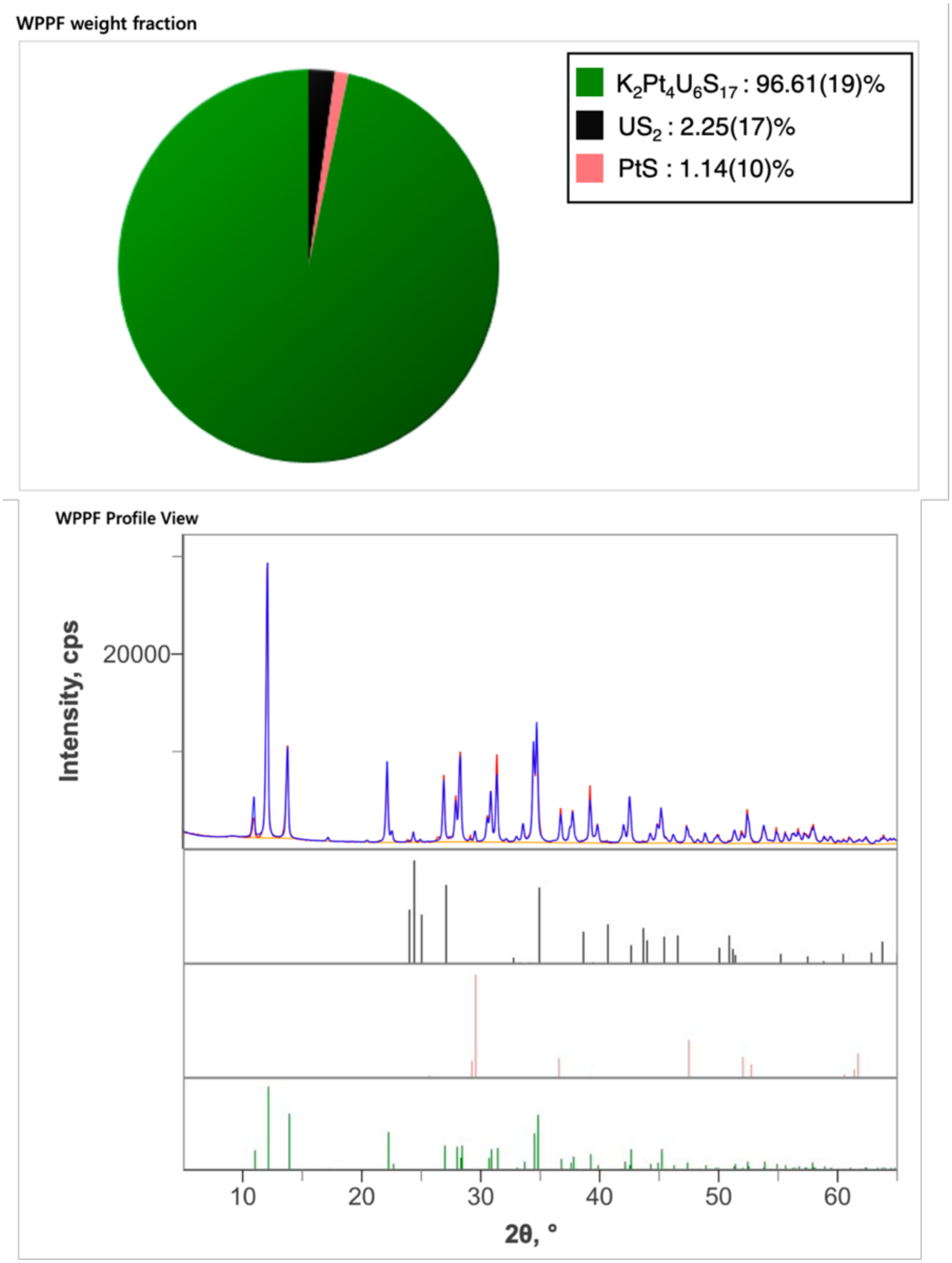

Figure 3.5 WPPF analysis of the sample of $K_2Pt_4U_6S_{17}$.

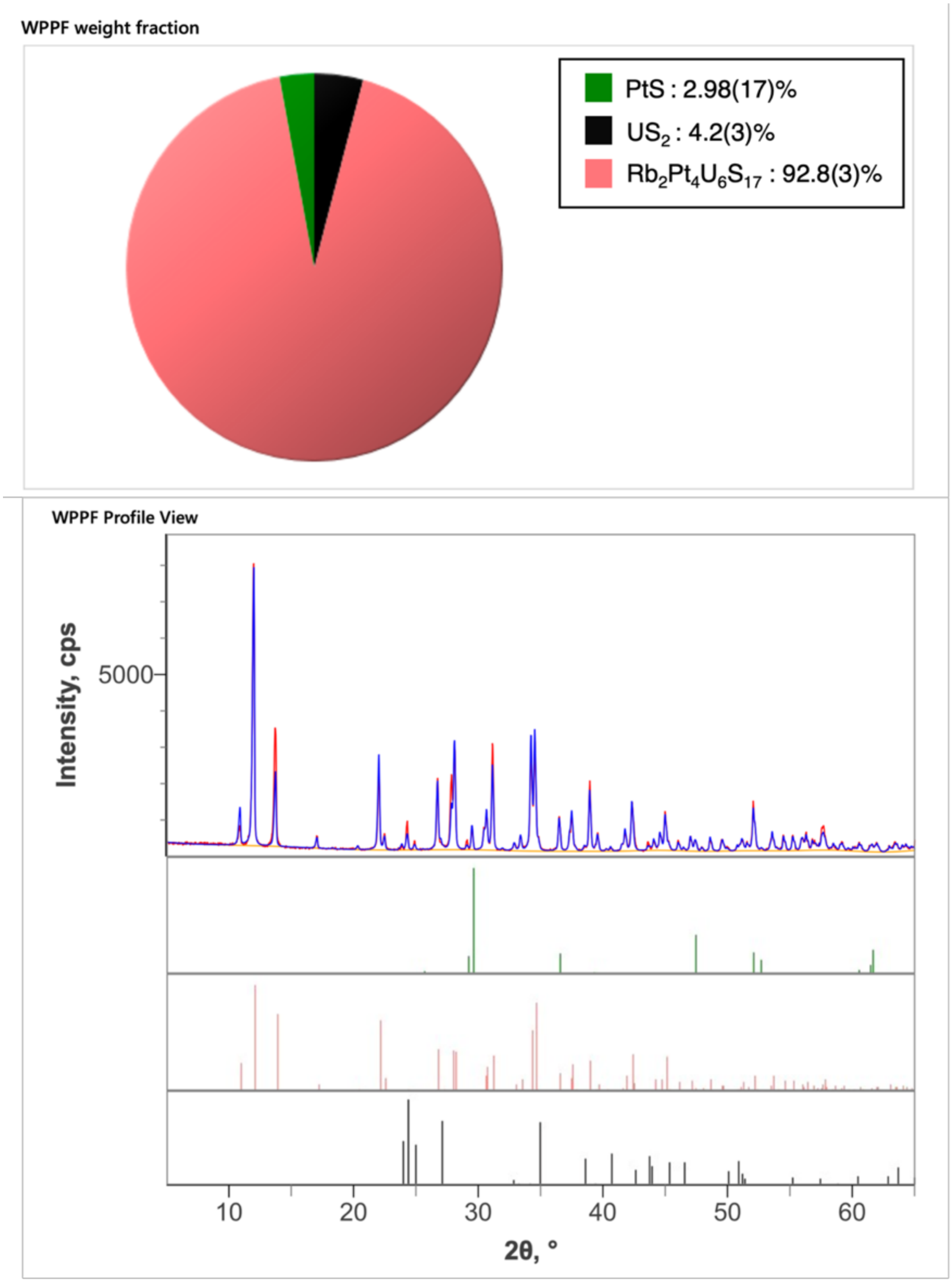

Figure 3.6 WPPF analysis of the sample of $Rb_2Pt_4U_6S_{17}$.

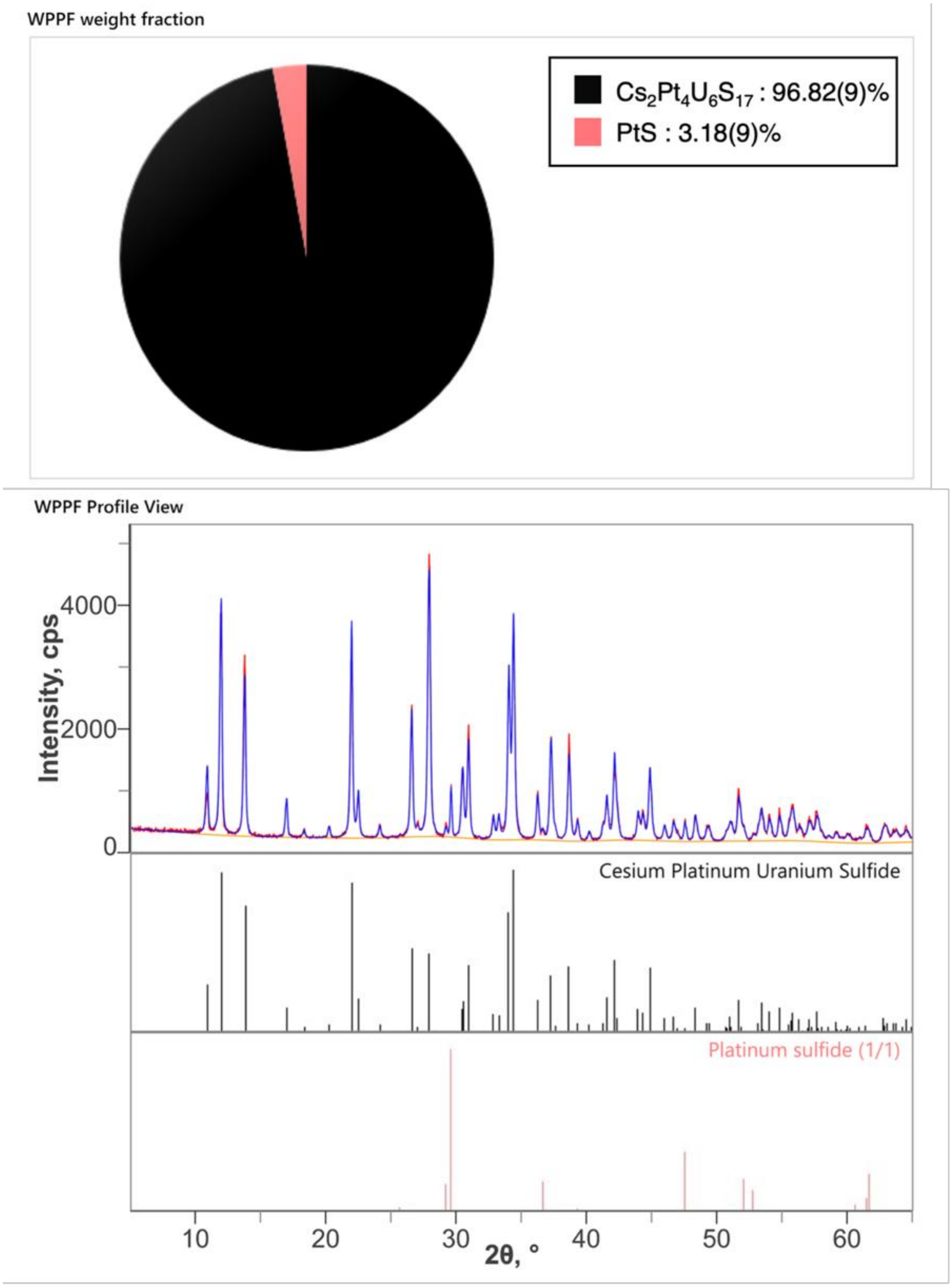

Figure 3.7 WPPF analysis for the sample of $Cs_2Pt_4U_6S_{17}$.

accumulation time. The results of EDS confirmed the presence of the elements found by single-crystal X-ray diffraction.

Magnetic Measurements. Magnetic susceptibility measurements were carried out over the temperature range of T = 1.8 – 300 K in an applied magnetic field of H = 0.5 T using a Quantum Design VSM Magnetic Property Measurement System. Measurements were performed on randomly oriented polycrystalline specimens that were loaded into VSM powder holders with a diameter of 2.60 mm. The powder holders were then suspended within straws and that were attached to the sample transport rod for measurements. The sample masses were 19.59 mg, 33.56 mg, and 16.85 mg for $K_2Pt_4U_6S_{17}$, $Rb_2Pt_4U_6S_{17}$, and $Cs_2Pt_4U_6S_{17}$, respectively.

Results and Discussion:

Synthesis. Single crystals of the compounds reported herein were synthesized using the combined BCM and molten flux growth methods. Figure 3.8. The BCM method

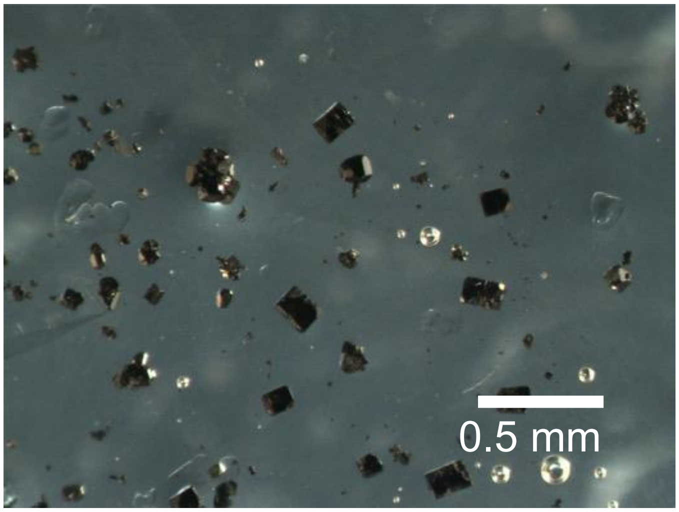

Figure 3.8 An image of the black block crystals of $K_2Pt_4U_6S_{17}$.

allowed for the use of uranium oxide, U_3O_8, as the uranium source for all reactions and the *in-situ* generation of alkali polysulfide fluxes from their respective alkali carbonates for the Cs- and Rb- containing reactions, avoiding the use of the highly air and moisture sensitive alkali polysulfide fluxes. Exploratory synthesis trials determined that the addition of both an alkali polysulfide flux and an alkali halide flux was necessary to obtain highly crystalline products of the target phases. Initial attempts at the synthesis of $K_2Pd_4U_6S_{17}$ performed without the addition of the potassium sulfide flux only resulted in products containing chunks of palladium metal, black rods of β-US_2, and black blocks of $U_{0.92}Pd_3S_4$, while reactions targeting $K_2Pt_4U_6S_{17}$ only yielded crystalline β-US_2 and PtS. No trace of the title compounds was observed among the reaction products. On the other hand, reactions forgoing the use of the alkali halide flux and only using the potassium sulfide flux resulted in products containing poorly crystalline products of $K_2Pt_4U_6S_{17}$, β-US_2, and KPt_2S_3 in reactions targeting $K_2Pt_4U_6S_{17}$, and poorly crystalline products of $K_2Pd_4U_6S_{17}$, β-US_2, and $U_{0.90}Pd_3S_4$ in reactions targeting $K_2Pd_4U_6S_{17}$. Reactions that utilized both the alkali halide flux and the potassium sulfide flux resulted in highly crystalline products of $K_2Pt_4U_6S_{17}$, β-US_2, and PtS in reactions targeting $K_2Pt_4U_6S_{17}$, and highly crystalline products of $K_2Pd_4U_6S_{17}$, β-US_2, and $U_{0.92}Pd_3S_4$ in reactions targeting $K_2Pd_4U_6S_{17}$. These observations indicate that using both the potassium sulfide flux and the alkali halide flux is the best route for the synthesis of highly crystalline products of the compounds reported herein.

After the successful synthesis of both $K_2Pd_4U_6S_{17}$ and $K_2Pt_4U_6S_{17}$, we chose to test the BCM method's ability to create *in-situ* alkali polysulfide fluxes from the alkali carbonates, thus avoiding having to prepare the alkali sulfide reagents ahead of time. In reactions targeting the $Rb_2Pt_4U_6S_{17}$ and $Cs_2Pt_4U_6S_{17}$ analogues, the synthetic procedures were kept the same as those used for $K_2Pd_4U_6S_{17}$ and $K_2Pt_4U_6S_{17}$ except for the replacement of an alkali polysulfide flux with Rb_2CO_3 or Cs_2CO_3. The resulting products obtained were highly crystalline single crystals of $Rb_2Pt_4U_6S_{17}$ and $Cs_2Pt_4U_6S_{17}$ supporting the successful *in-situ* formation of the alkali polysulfide flux by the BCM method. Attempts at creating phase pure powders for all target phases were unfortunately unsuccessful as crystalline β-US_2 and MS (M = Pt or Pd) persisted in the reaction products even after varying the relative reactant ratios and reaction temperatures. In reactions targeting the platinum containing phases, reagent ratios were extensively varied in attempts to reduce the β-US_2 and PtS impurities, and, while able to be reduced, further reduction of the uranium and platinum reagent ratios also prevented the title compounds from forming. The same attempts were carried out to obtain pure $K_2Pd_4U_6S_{17}$, however, it was not possible to avoid the formation of some $U_{0.92}Pd_3S_4$ and β-US_2 impurities.

Structure Description. The compounds reported herein join the family of $A_2M_4U_6Q_{17}$ compounds that crystallize in the tetragonal crystal system adopting the space group *P*4/mnc. The structure is comprised of two crystallographically unique uranium sites, U(1) and U(2), and one unique M (M = Pt or Pd) site. Figure 3.9 shows the local coordination environments for the metal cations in each structure. The structure consists of four unique layers, designated as A, A', B, and B', oriented in the a-b plane, as shown in Figure 3.10. Layer A is composed of $U(1)_4S_{17}$ tetramers that are connected via MS_4 (M= Pd or Pt) square planar units. The tetramers are created by four 7-coordinate $U(1)S_7$ monocapped trigonal prisms that are connected by sharing the S(3) sulfur atom occupying the capping position of the monocapped trigonal prism and S(1) sulfur atoms making up

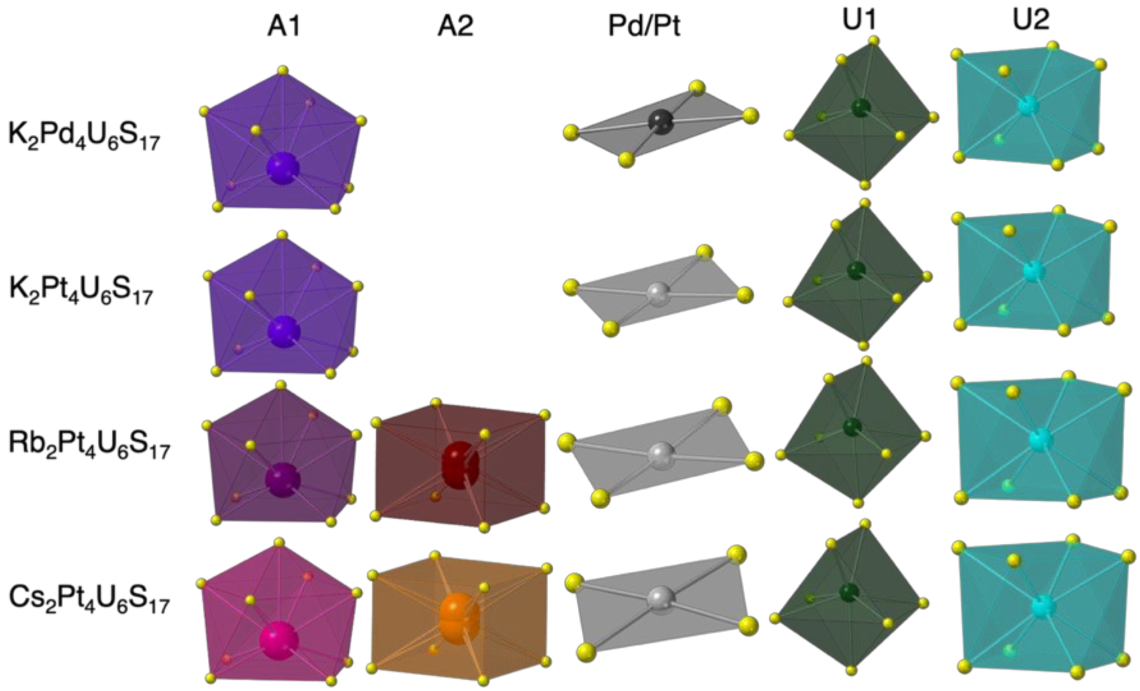

Figure 3.9 Representations of the local coordination polyhedra for the metal atoms within each $A_2M_4U_6S_{17}$ compound reported herein. $K_2Pd_4U_6S_{17}$ and $K_2Pt_4U_6S_{17}$ have only one alkali metal site, while $Rb_2Pt_4U_6S_{17}$ and $Cs_2Pt_4U_6S_{17}$ have a split site for the alkali metal and, hence, two coordination polyhedra of the alkali metals are shown for them.

two of the sides of the trigonal prism. This results in each monocapped trigonal prism sharing two triangular faces with two adjacent polyhedra. These $U(1)_4S_{17}$ tetramers connect to each other within the layer through edge-sharing MS_4 square planar units. The MS_4 units use two S(1) sulfur atoms of one tetramer and two S(2) sulfur atoms of another. Layer A' is identical to Layer A in composition but is rotated ~37 degrees and translated by ½ a and ½ b. Layer B and B' are mirror images of one another and are composed of isolated $U(2)S_8$ square antiprisms which link layers A and A' through edge sharing with two MS_4 square planar units in the layers above and two below them. Layer B and B' alternate with the A and A' layers, resulting in an overall stacking sequence of ABA'B'. To visualize the stacking of these layers, Figure 3.10 illustrates the position of each layer within the unit cell. The cesium cations fill the void spaces within $U(1)_4S_{17}$ tetramers and the $U(2)S_8$ square antiprisms within the layers of the structure.

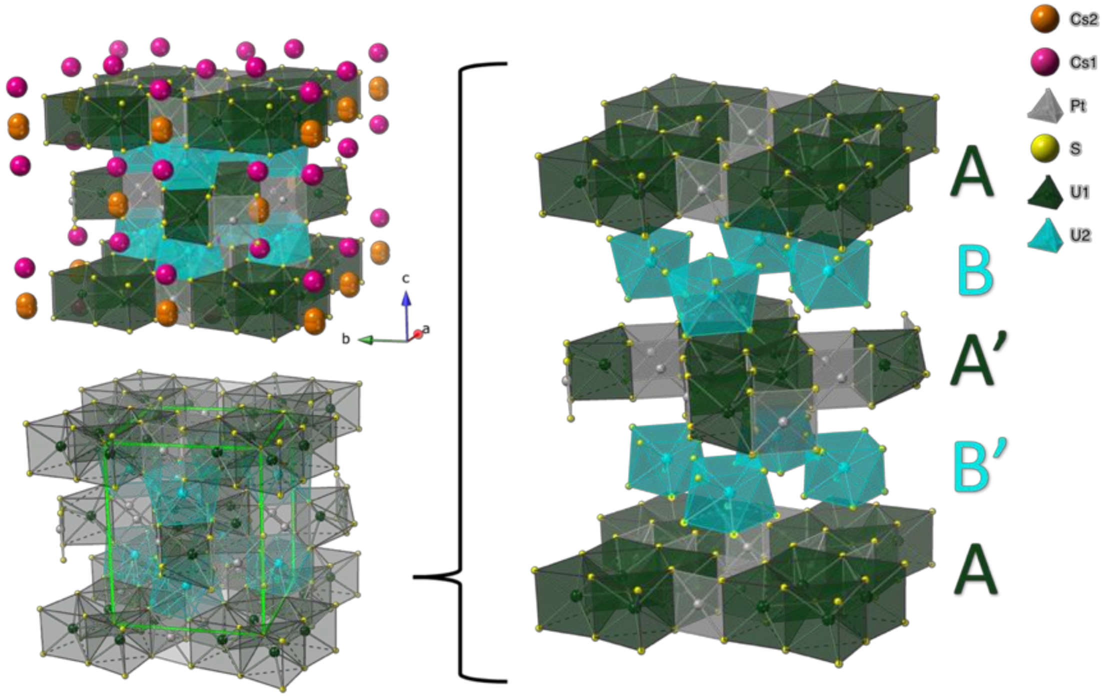

Figure 3.10 An image of (top left) the representative structure of $Cs_2Pt_4U_6S_{17}$, (bottom left) an image showing the arrangement of the atoms within the unit cell, and (right) a schematic of the separate layers within the structure and how they stack.

In $K_2Pd_4U_6S_{17}$ and $K_2Pt_4U_6S_{17}$, crystallographically ordered potassium cations fill the spaces within the B and B’ layers. Structure solutions of $Rb_2Pt_4U_6S_{17}$ and $Cs_2Pt_4U_6S_{17}$, on the other hand, refined best when modeling the A cation positions split over two sites (A1 and A2), see Figure 3.11. A similar split position for the alkali metal cations was previously reported for the structures of $Rb_2Pt_4U_6Se_{17}$ and $Cs_2Pt_4U_6Se_{17}$.[166]

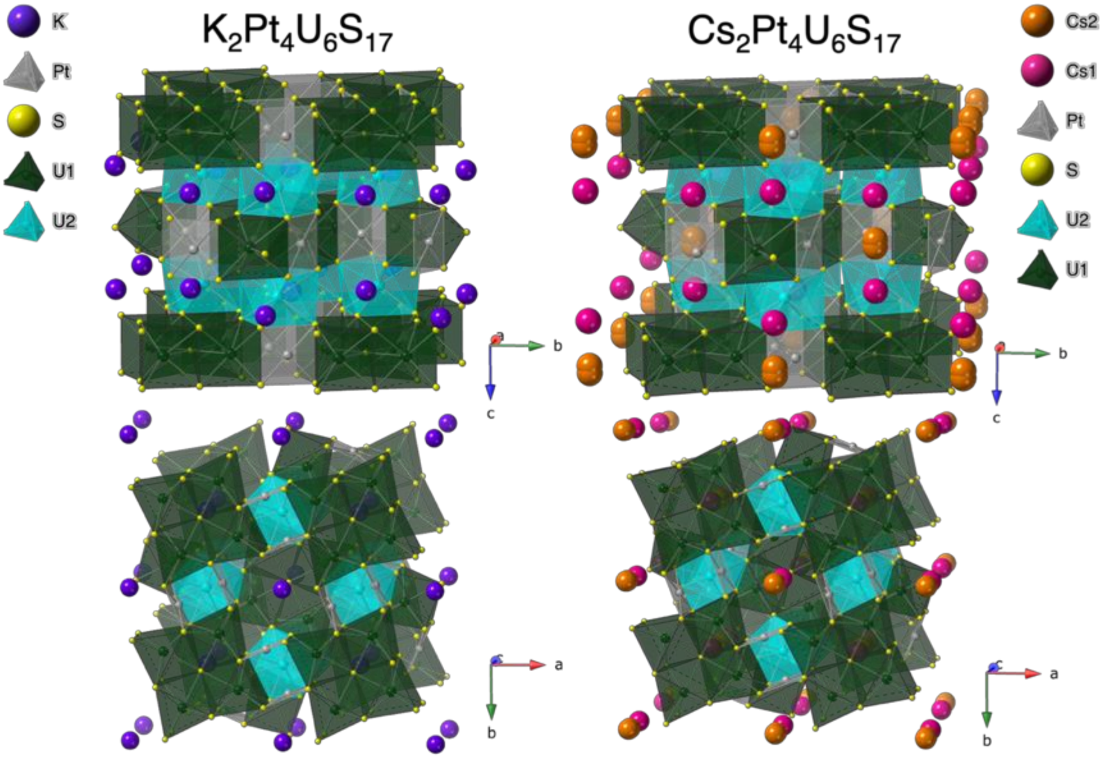

Figure 3.11 (left) An image showing an example of ordered potassium cations (purple) observed in $K_2Pt_4U_6S_{17}$ and $K_2Pd_4U_6S_{17}$ and (right) an example of alkali cations split over two positions, in this case the Cs cation is split into Cs1 (pink) and Cs2 (orange), observed in $Rb_2Pt_4U_6S_{17}$ and $Cs_2Pt_4U_6S_{17}$.

In $K_2Pd_4U_6S_{17}$ the Pd – S distances range from 2.3403(8) to 2.3662(8) and the U – S distances range from 2.6796(8) to 2.8717(8). In $K_2Pt_4U_6S_{17}$, $Rb_2Pt_4U_6S_{17}$, and $Cs_2Pt_4U_6S_{17}$ the Pt – S distances range from 2.3413(13) to 2.3711(15) and the U – S distances range from 2.6893(13) to 2.9285(18). Uranium is in its 4+ oxidation state, which is supported by charge balance, the lack of S—S bonds, and bond valence sum calculations that indicate an average uranium oxidation state of 4.04, 3.97, 3.96, and 3.90 for $K_2Pd_4U_6S_{17}$, $K_2Pt_4U_6S_{17}$, $Rb_2Pt_4U_6S_{17}$, and $Cs_2Pt_4U_6S_{17}$, respectively.

Magnetic Susceptibility Measurements. Magnetic measurements were performed on ground samples of $K_2Pt_4U_6S_{17}$, $Rb_2Pt_4U_6S_{17}$, and $Cs_2Pt_4U_6S_{17}$ containing small amounts of the β-US_2 and PtS impurities. PtS is diamagnetic and β-US_2 is paramagnetic over the 2-300 K range.[135, 169] Therefore, any observed magnetic transition would be due to $K_2Pt_4U_6S_{17}$, $Rb_2Pt_4U_6S_{17}$, or $Cs_2Pt_4U_6S_{17}$. A Whole Powder Pattern Fitting (WPPF) was performed using the Rigaku SmartLab II software to obtain the relative weight percent of the impurity phases (Table 3.2) to correct the sample mass for the impurity when calculating the molar magnetic susceptibility. No magnetic measurements were performed for $K_2Pd_4U_6S_{17}$ due to the inability to separate the black blocks of the $U_{0.92}Pd_3S_4$, which orders magnetically, from the black blocks of $K_2Pd_4U_6S_{17}$.[170]

Table 3.2 Results of the WPPF showing the relative weight percent of each phase in the product powders.

Sample	Target Product	US_2	PtS
$K_2Pt_4U_6S_{17}$	96.61(19)%	2.25(17)%	1.14(10)%
$Rb_2Pt_4U_6S_{17}$	92.8(3)%	4.2(3)%	2.98(17)%
$Cs_2Pt_4U_6S_{17}$	96.82(9)%	N/A	3.18(9)%

Figure 3.12 contains a plot of the magnetic susceptibility data for compounds $A_2Pt_4U_6S_{17}$ (A = K, Rb, Cs). Paramagnetic behavior is observed at elevated temperatures, similar to what was reported for the isostructural analogue $Rb_2Pd_4U_6S_{17}$.[166]

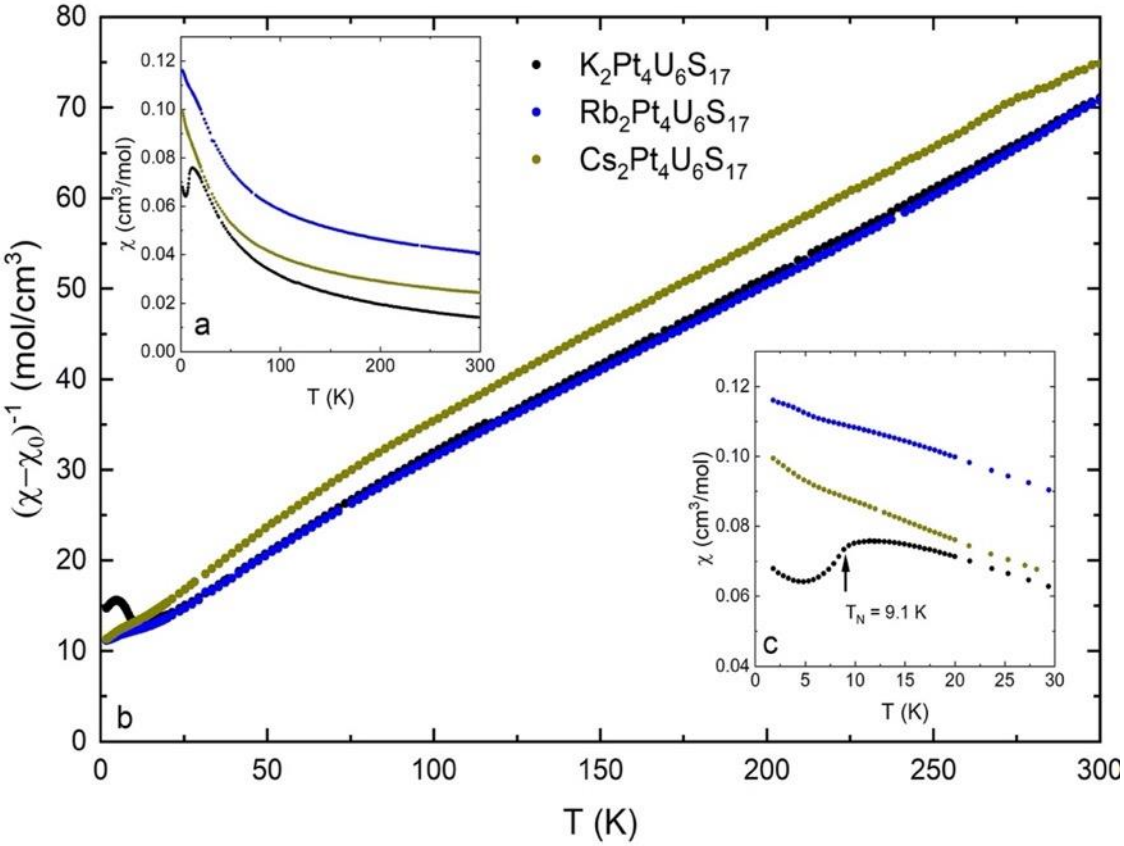

Figure 3.12 (a) Temperature dependent magnetic susceptibility $\chi(T)$ collected in an applied magnetic field H = 5000 Oe for the compounds $A_2Pt_4U_6S_{17}$ (A = K, Rb, Cs). (b) $(\chi-\chi_0)^{-1}$ vs T, where the linear behavior that is seen for T > 150 K was fitted using a modified Curie-Weiss function as described in the text. (c) Low temperature zoom of $\chi(T)$ emphasizing the antiferromagnetic ordering at T_N = 9.1 K for $K_2Pt_4U_6S_{17}$ and the absence of bulk ordering for $Rb_2Pt_4U_6S_{17}$ and $Cs_2Pt_4U_6S_{17}$. A plot showing the overlap of the zero field-cooled and field-cooled data can be seen in Figure 3.13.

The 150 K – 300 K data were fitted using a modified Curie-Weiss expression $\chi = \chi_0 + C/(T-\theta)$, where χ_0 is a temperature independent term, C is the Curie constant, and θ is the Curie-Weiss temperature. The results of the fits are listed in Table 3.3, where the negative q values indicate the presence of antiferromagnetic correlations between the uranium ions. The origin of the χ_0 term remains to be identified, but we point out that magnetic data for even single crystal specimens of $Rb_2Pd_4U_6S_{17}$ result in similar χ_0 terms whose absolute value is reduced from what is seen here.

Table 3.3 A summary of the magnetic properties of $A_2Pt_4U_6S_{17}$ (A = K, Rb, Cs).

	χ_0 (cm^3/mol)	Θ (K)	C (cm^{3}K/mol)	μ_{eff}/U	T_N (K)
$K_2Pt_4U_6S_{17}$	0	-62	5.1	2.6	9.1
$Rb_2Pt_4U_6S_{17}$	0.027	-59	5.1	2.6	---
$Cs_2Pt_4U_6S_{17}$	0.011	-71	4.7	2.5	---

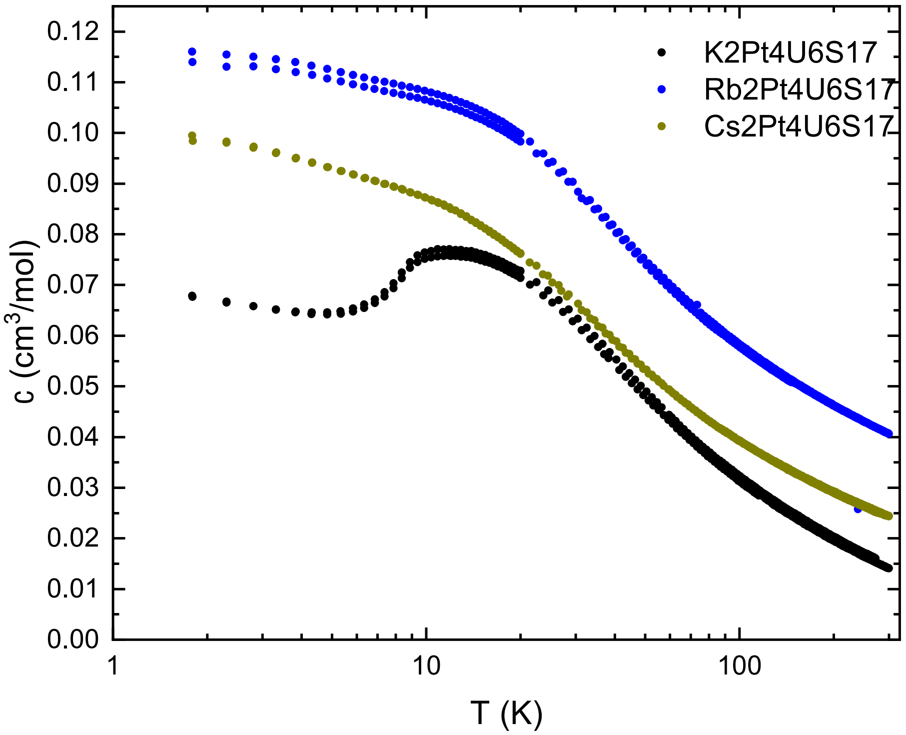

Figure 3.13 A plot of the molar susceptibility versus temperature of each compound showing the overlap between the field-cooled and zero field-cooled data.

It is reasonable to suggest that for these samples, the impurity phases may contribute to this term. The effective magnetic moment per uranium was determined and found to range from 2.5 – 2.6 μ_B for the three phases. These values are reduced from the expected moment of tetravalent uranium of 3.58 μ_B calculated using full Russell-Saunders coupling for a $^3H_4$ ground state. The published moments of U(IV) range from 1.36 to 3.79.[36]

A reduced moment was also reported for $Rb_2Pd_4U_6S_{17}$, where it was attributed to crystal electric field effects. Since uranium magnetism is known to deviate from Hund's rules expectations due to (i) strong spin orbit coupling and (ii) the tendency of the U(IV) f-electrons to take on a singlet ground state at low temperatures, moments lower than the expected, 3.58 μ_B, are common. Further work is needed to clarify this question, but broadly speaking this behavior is consistent with what is seen for many other U-based materials in which the gradual transition from a triplet to a singlet ground state for the two f-electrons impacts the measured magnetic moment.[171]

An antiferromagnetic transition is observed at $T_N = 9.1$ K for $K_2Pt_4U_6S_{17}$, similar to what is seen for $Rb_2Pd_4U_6S_{17}$. In contrast, both $Rb_2Pt_4U_6S_{17}$ and $Cs_2Pt_4U_6S_{17}$ show weak inflections in their c vs T plots over a similar temperature range. Reports in the literature indicate that the presence or absence of long-range magnetic order in U(IV) compounds in which uranium is the only magnetically active ion is a function of the U—U separation within the crystal structure, which effects the magnetic coupling ability of the uranium ions.[165, 166]

Reports in the literature indicate that the presence or absence of long-range magnetic order in U(IV) compounds in which uranium is the only magnetically active ion is a function of the U—U separation within the crystal structure, which effects the magnetic coupling ability of the uranium ions.[165, 166] In the compounds reported herein, an increase in the U—U distances occurs with an increase in the size of the alkali cation (K < Rb < Cs), as illustrated in Figure 3.14, which is expected to reduce the ability of the uranium ions to couple magnetically. It is therefore not surprising that only the potassium containing material, $K_2Pt_4U_6S_{17}$, exhibits long range magnetic order.

Figure 3.14. A plot of the (black) U(1)—U(1) and the (red) U(1)—U(2) interatomic distances. The U(2)—U(2) distances were excluded as they are too large (> 7 Å) to have magnetic coupling between them. There is an increase in the U—U distances with the increase in alkali cation incorporated into the $A_2Pt_4U_6S_{17}$ (A = K, Rb, Cs) structure.

Conclusions. A series of $A_2M_4U_6S_{17}$ (A = Alkali metal, M = Pd or Pt) compounds, specifically $K_2Pd_4U_6S_{17}$, $K_2Pt_4U_6S_{17}$, $Rb_2Pt_4U_6S_{17}$, and $Cs_2Pt_4U_6S_{17}$, were synthesized using the combined BCM and molten flux crystal growth methods with the Rb- and Cs-containing analogues taking advantage of the *in-situ* alkali polysulfide flux formation from the alkali carbonates. The successful synthesis of single crystals of the title compounds allowed for their structure determination. Magnetic measurements were performed on samples of $K_2Pt_4U_6S_{17}$, $Rb_2Pt_4U_6S_{17}$, and $Cs_2Pt_4U_6S_{17}$, and antiferromagnetic order is observed at $T_N = 9.1$ K for $K_2Pt_4U_6S_{17}$. In contrast, while both $Rb_2Pt_4U_6S_{17}$ and $Cs_2Pt_4U_6S_{17}$ show weak inflections in their χ vs T data over similar temperature ranges, they do not exhibit a magnetic transition. The absence of long-range magnetic order in the Rb- and Cs-analogues is attributed to the increased U—U interatomic distances as a function of the increased size of the alkali cations. Uranium moments of 2.5, 2.6, and 2.6 μ_B were calculated for $K_2Pt_4U_6S_{17}$, $Rb_2Pt_4U_6S_{17}$, and $Cs_2Pt_4U_6S_{17}$, respectively. The BCM method enables ease of access to actinide chalcogenide phases and its use is expected to result in further successful syntheses of actinide chalcogenide and other chalcogenide phases.

Acknowledgements. Research supported by the US Department of Energy, Office of Basic Energy Sciences, Division of Materials Sciences and Engineering under award DE-SC0018739. Synthesis and structural characterization performed at UofSC. Magnetic measurements collected at the National High Magnetic Field Laboratory, which is supported by the National Science Foundation Cooperative Agreement No. DMR-1644779 and the State of Florida.

CHAPTER 4

LANTHANIDE THIOBORATES, AN EMERGING CLASS OF NONLINEAR OPTICAL MATERIALS, EFFICIENTLY SYNTHESIZED USING THE BORON-CHALCOGEN MIXTURE METHOD[1]

---

[1] Breton, L. S., Morrison, G., Lacroix, M. R., Halasyamani, P. S., and zur Loye, H.-C., *Chem. Commun.,* **2022**, 58, 7992-7995. © The Royal Society of Chemistry 2022

Abstract: The Boron–Chalcogen Mixture method was used to obtain single crystals of the previously extremely difficult to synthesize lanthanide orthothioborates to investigate their structures and their structurally connected optical behavior, such as second harmonic generation. Using a combined halide and polychalcogenide flux, the BCM method yielded single crystals of $LnBS_3$ (Ln = La, Ce, Pr, Nd), which are iso- structural and crystallize in the non-centrosymmetric space group, $Pna2_1$. Second harmonic generation measurements confirmed the expectation that $LaBS_3$ would exhibit a strong SHG response, measured at 1.5 x KDP.

Thioborates. Thioborates are an emerging class of nonlinear optical (NLO) materials that combine the attractive NLO abilities of chalcogenides and borates, resulting in materials exhibiting a combination of highly sought-after NLO properties, specifically, the high laser damage threshold and large optical nonlinearity of borates and the wide optical and IR transmission ranges of sulfides.[29, 172, 173] The significant difficulties of their synthesis, such as difficult starting reagents and the need for high reaction temperatures and pressures, has impeded the synthesis of thioborate materials. In fact, very few have been made, despite their predicted attractive NLO behavior. Furthermore, the lack of single crystal products obtained from current thioborate synthesis reactions has made structural characterization difficult and impeded the use of this class of materials for NLO applications.

The family of lanthanide orthothioborates, $LnBS_3$ (Ln = Lanthanide), are of special interest due to the coupling of 'laser active' lanthanide ions with the orthothioborate unit, $[BS_3]^{3-}$, which is known to induce NLO behavior.[174, 175] The first syntheses of lanthanide orthothioborates by Hunger et al. utilized high temperatures (800–1050 ºC) and pressures

(3 GPa) and yielded polycrystalline powders whose structure determinations were accomplished via highly restrained Rietveld refinements.[176] The authors subsequently found that heating a pellet with nominal composition PrB_5S_9 contained in a BN crucible sealed inside a tantalum ampule under argon gas for over 30 days produced single crystals of $PrBS_3$ and they determined the first crystal structure of a lanthanide orthothioborate.[177] Unfortunately, no characterization of the physical properties of $PrBS_3$ was reported.

Synthesizing new materials that exhibit a desired property can be accomplished by numerous routes, most of them being based on existing, successful approaches. Departing from those approaches can sometimes be extremely rewarding if one can envision a different path that is more targeted or simpler. We chose to adapt the recently reported Boron–Chalcogen Mixture (BCM) method as a new low temperature reaction route that successfully leads to single crystals of lanthanide orthothioborates, allowing us to investigate their structures and their structurally connected optical behavior, specifically, second harmonic generation.

To prepare and study lanthanide orthothioborates, $LnBS_3$, we applied a combination of the BCM and molten flux growth methods to their synthesis, as these methods are easy to use, typically yield single crystals, and are fast. We recently reported the BCM method as a facile approach for the synthesis of actinide chalcogenides from their oxides by incorporating a mixture of boron and the desired chalcogen into the reagent mixture.[43] The large difference in formation energy of B_2O_3 (*i.e.* $\Delta_f G^o$ (vitreous-B_2O_3) = -1182.5 kJ mol^{-1}) over the boron chalcogenide (*e.g.* $\Delta_f G^o$ (vitreous-B_2S_3) = -247.6 kJ mol^{-1}) favors the formation of B_2O_3 allowing elemental boron to act as an 'oxygen sponge' when heated, leaving the chalcogen to react with the other reagents.[131] This method was previously successful for the synthesis of lanthanide and transition metal sulfides from their oxides and was therefore chosen as a potentially convenient path to lanthanide thioborate materials.[129, 178, 179] By utilizing the BCM method coupled with molten flux crystal growth, plentiful single crystals of lanthanide orthothioborates (Ln = La, Ce, Pr, Nd), Figure 4.1, were grown at a relatively low reaction temperature of 550 ºC, with a reaction time of under 3 days and, importantly, using the lanthanide oxides as starting reagents. The single crystalline nature of the products allowed us to determine their structures and to investigate the NLO behavior of a phase pure sample of $LaBS_3$.

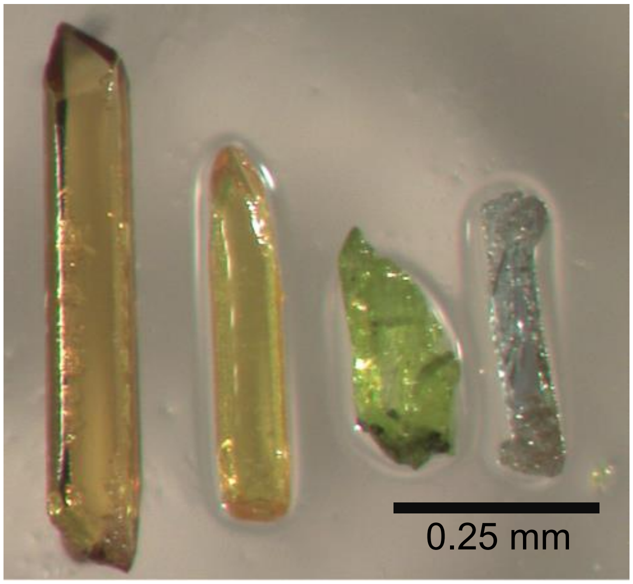

Figure 4.1: An image of single crystals of (left to right) $LaBS_3$, $CeBS_3$, $PrBS_3$, and $NdBS_3$.

To synthesize the lanthanide orthothioborates, the lanthanide oxide (Ln_2O_3 for Ln = La, Pr, Nd or CeO_2), boron, and sulfur were loaded into a carbon crucible (0.5 in OD x 0.25 in ID x 2 in L) in a 1:20:30 molar ratio. In a nitrogen filled glovebag, 0.05 grams of K_2S and then 0.25 grams of a NaI–CsI eutectic flux were layered on top of this mixture inside the carbon crucible which was subsequently placed into a carbon- coated fused silica tube. The fused silica tube was evacuated, sealed, and placed in a furnace set to step to 400 ºC and then ramp to 550 ºC in 2 hours where it dwelled for 48 hours. The furnace then slow-cooled to 350 ºC in 20 hours and was then shut off to return to room temperature. To isolate the single crystals, the flux was dissolved in methanol, aided by sonication, and the crystals isolated via vacuum filtration.

The four compositions thus obtained, $LnBS_3$ (Ln = La, Ce, Pr, Nd), all crystallize in the non-centrosymmetric space group $Pna2_1$ and are isostructural. The crystal structures, Table 4.1, are consistent with the one previously published for $PrBS_3$.[177]

Table 4.1 Crystallographic data for lanthanide orthothioborates, $LnBS_3$.

Formula	$LaBS_3$	$CeBS_3$	$PrBS_3$	$NdBS_3$
Formula weight	245.90	247.11	247.90	251.23
Space group, Z	$Pna2_1$, 4			
a, Å	7.6766(2)	7.6059(2)	7.5432(2)	7.4818(2)
b, Å	6.0445(1)	6.0181(1)	6.0072(1)	6.0037(1)
c, Å	8.9940(2)	8.9311(2)	8.8897(2)	8.8530(2)
V, Å^3	417.33(1)	408.80(1)	402.82(1)	397.66(1)
R_1 ($I > 2\sigma(I)$)	0.0076	0.0079	0.0094	0.0080
wR_2 (all data)	0.0177	0.0174	0.0204	0.0178

The flux approach used in our synthesis, which relies on alkali halide eutectics, is known to work well for the crystallization of a multitude of chalcogenide phases.[58, 139, 180-183] However, to accomplish the synthesis of lanthanide orthothioborate phases, $LnBS_3$, it was found to be essential to supplement the low temperature halide melt with a polychalcogenide flux, another low temperature melt, that is known to be stable at lower reaction temperatures. The combination of the alkali halide eutectic flux with the potassium polychalcogenide flux afforded high quality single crystals of the target compounds suitable for X-ray diffraction studies. These crystals represent the first single crystal growth of $CeBS_3$ and $NdBS_3$ that allows for the refinement of their crystal structures, and the single crystal structure of $LaBS_3$ is reported herein for the first time.

The structure of the lanthanide orthothioborates, $LnBS_3$ (Ln = lanthanide), is shown in Figure 4.2 and is comprised of two building units: 9-coordinate, LnS_9, lanthanide sulfide distorted tricapped trigonal prisms and trigonal planar, $[BS_3]^{3-}$, orthothioborate units.

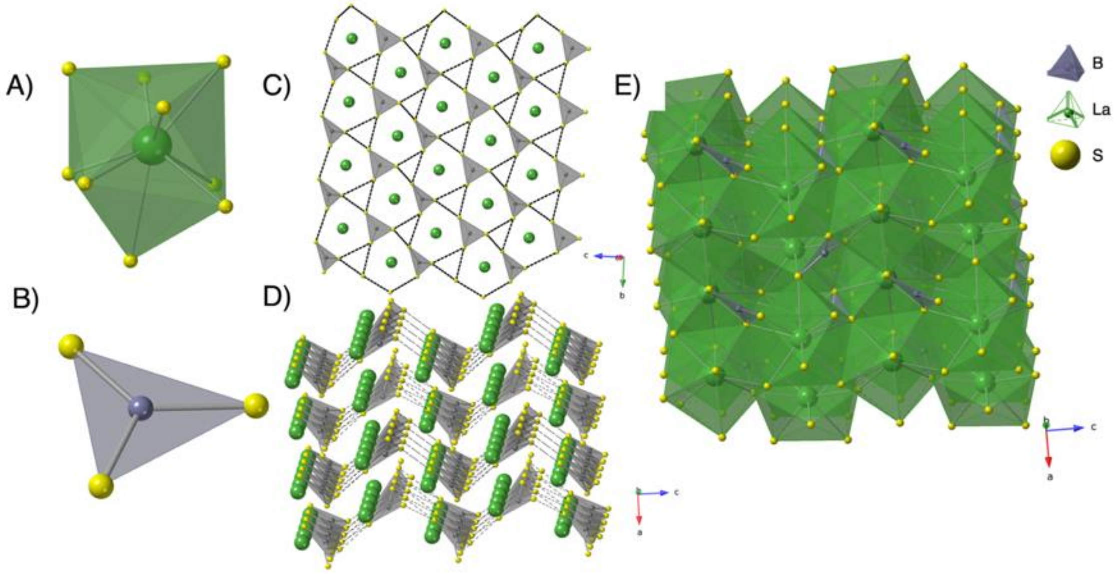

Figure 4.2: A schematic of the $LnBS_3$ structure showing the (A) LnS_9 and (B) BS_3 building blocks as well as an (C) illustration of the corrugated kagome nets, (D) how they stack within the structure, and (E) an image of the overall crystal structure.

The $LnBS_3$ 3-dimensional crystal structure is composed of corrugated sheets consisting of distorted kagome nets formed by the sulfur atoms. The sheets are stacked parallel to the b–c plane along the a-axis. In each kagome-net layer, every other sulfur triangle is occupied by a boron cation forming the BS_3 unit and the distorted hexagonal holes in the kagome lattice are filled with lanthanide cations. An alternation of the orientation of the orthothioborate unit between layers results in an ABAB stacking. Each LnS_9 polyhedron is surrounded by 6 orthothioborate units, 3 edge-sharing and 3 corner-sharing, and 12 neighboring LnS_9 polyhedra; 8 corner sharing, 2 face-sharing, and 2 edge sharing. The B—S distances range from 1.7981(26) to 1.8243(21) Å and the Ln—S distances range from 2.8579(5) to 3.3182(4) Å. The boron located in the middle of the BS_3 unit is very slightly out of the plane created by the triangle of sulfur atoms the magnitude of which slightly varies for the different lanthanide element; 0.0747, 0.0739, 0.0782, 0.0786 Å from the plane for Ln = La, Ce, Pr, and Nd, respectively.

The title compounds all crystallize in the non-centrosymmetric space group $Pna2_1$ and contain the $[BS_3]^{3-}$ unit, which literature suggests can lead to especially good SHG materials. To test for SHG, as well as test the predictions, SHG measurements were performed on ground crystals of $LaBS_3$. The lanthanum member was chosen for SHG testing as it does not exhibit any f–f transitions that cause coloration. The SHG measurements revealed that $LaBS_3$ is indeed SHG active with an SHG intensity 1.5 times that of the standard reference sample of potassium dihydrogen phosphate (KDP), Figure 4.3, though non-phase-matchable, Figure 4.4, when irradiated with 1064 nm light. It is worth mentioning, though, that a revisitation of $LaBS_3$ by Han et al. showed this compound to be type-1 phase matchable when irradiated with a 2.05 μm laser.[184] $LaBS_3$ has a calculated band gap of 2.9 eV, Figure 4.5. Fluorescence spectra were obtained at an excitation wavelength of 375 nm on single crystals of all title compounds, Figures 4.6-4.8. No fluorescence from $LaBS_3$ was observed, as expected, due to lanthanum's $4f^0$ electron configuration.

High temperature solid state chemistry generally leads to the formation of the thermodynamic phases that have high temperature stability. Hydrothermal and flux routes operate at lower temperatures and, while able to crystallize thermodynamic phases, can also lead to kinetic/metastable phases that would not survive very high temperatures, decomposing into binaries and ternaries. What is without a doubt true, however, is that

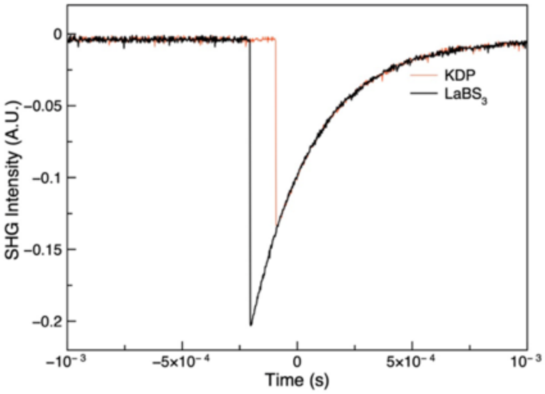

Figure 4.3: Powder SHG data of a sample of $LaBS_3$ compared to a standard sample of KDP with a particle size between 90-125 µm.

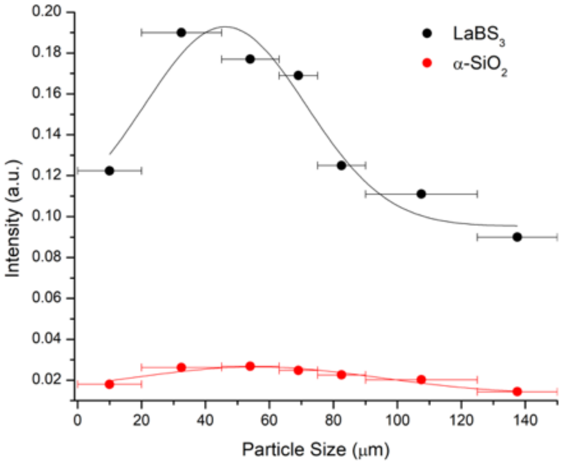

Figure 4.4: Powder SHG phase-matching experiment on $LaBS_3$ compared to a standard α-SiO_2 with particle size ranges of <20, 20-45, 45-63, 63-75, 75-90, 90-125, and 125-150 μm. The lines are not fits to data, but to guide the eye.

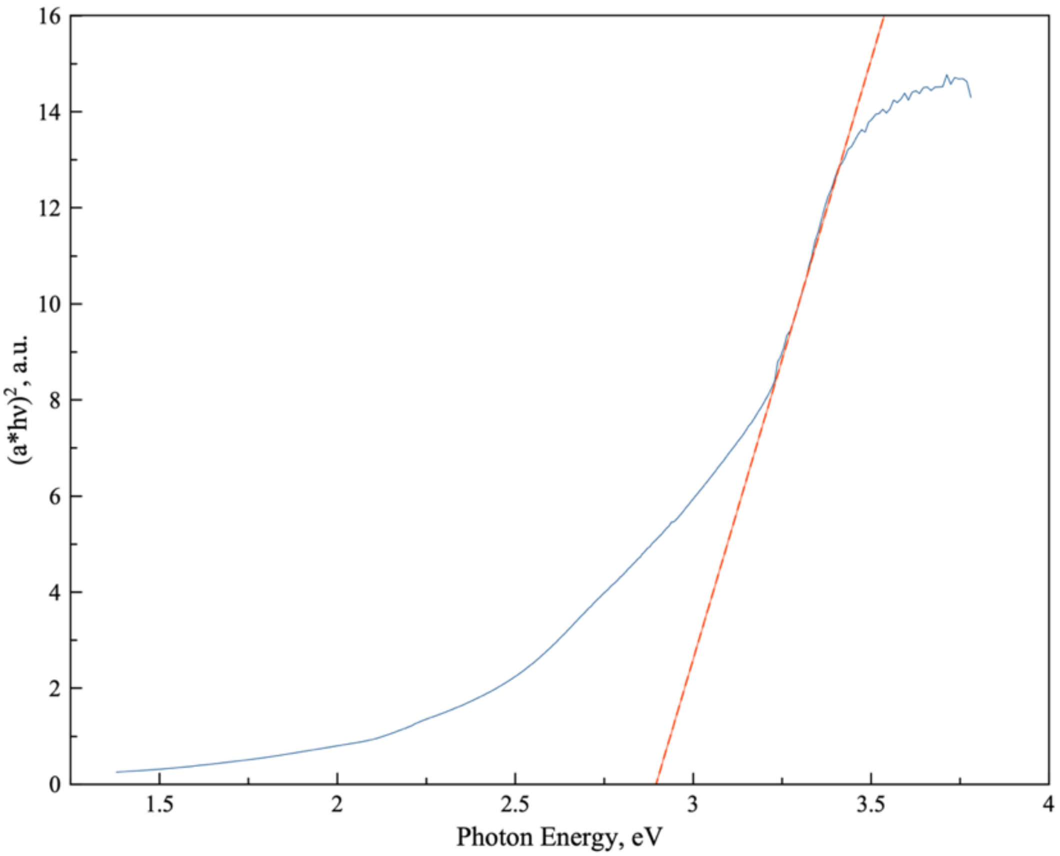

Figure 4.5 The Tauc plot created from the absorbance data for $LaBS_3$. A band gap of 2.9 eV was calculated which corresponds well to the yellow color of the $LaBS_3$ crystals.

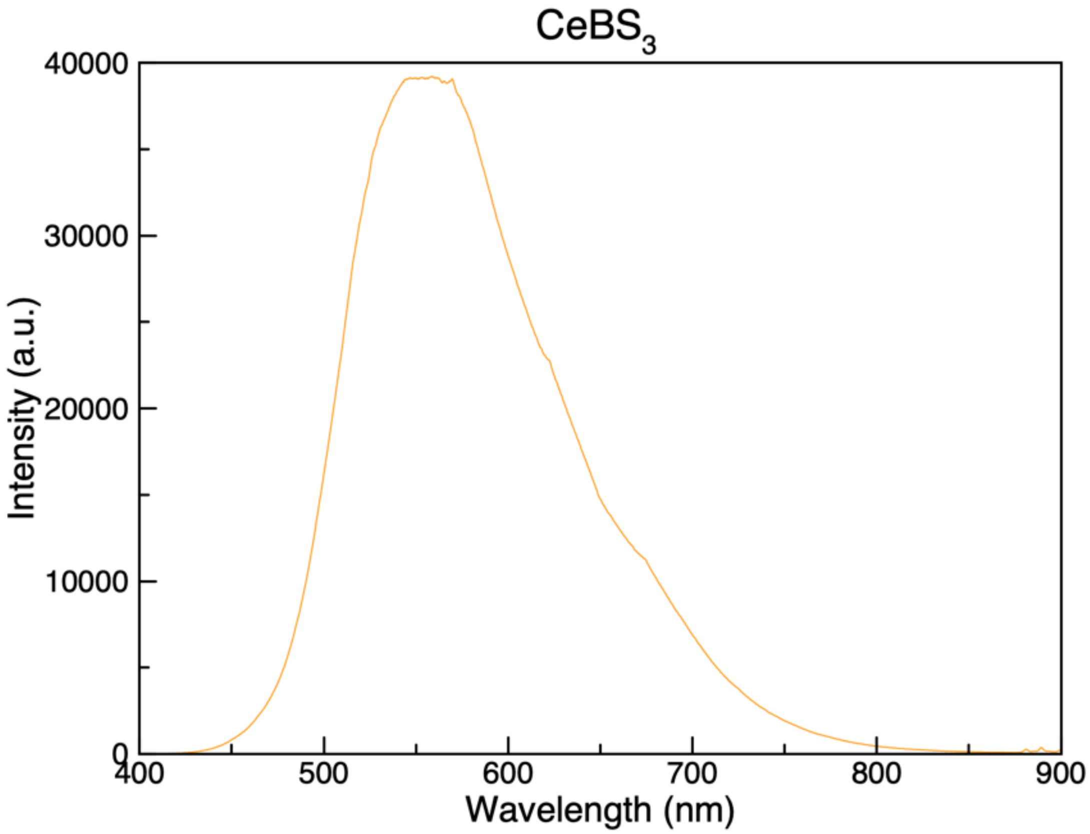

Figure 4.6 Fluorescence data obtained on a single crystal of $CeBS_3$ using an excitation wavelength of 375 nm. A single broad peak which covered much of the visible range measured was observed for $CeBS_3$, a phenomenon observed in other cerium compounds.[28, 85-87]

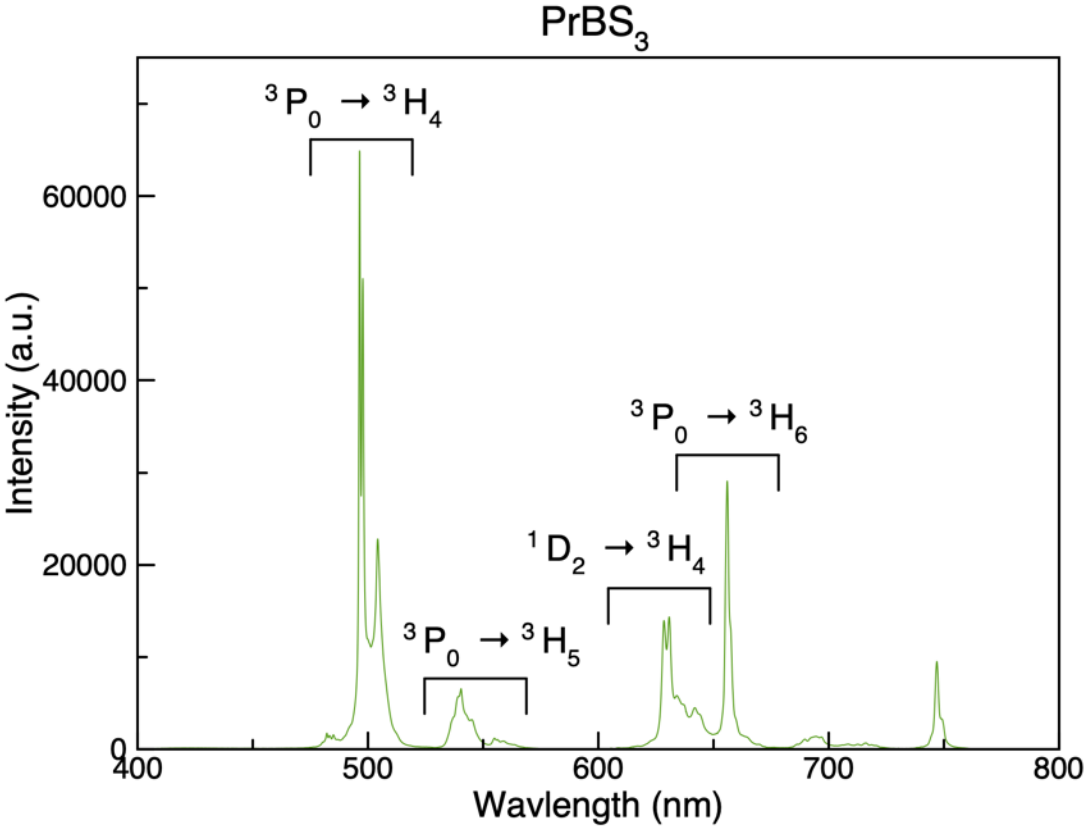

Figure 4.7 Fluorescence data obtained on a single crystal of $PrBS_3$. The expected $^3P_0$ → $^3H_4$, $^3P_0$ → $^3H_5$, $^1D_2$ → $^3H_4$, $^3P_0$ → $^3H_6$ f-f transitions were observed.[28, 84]

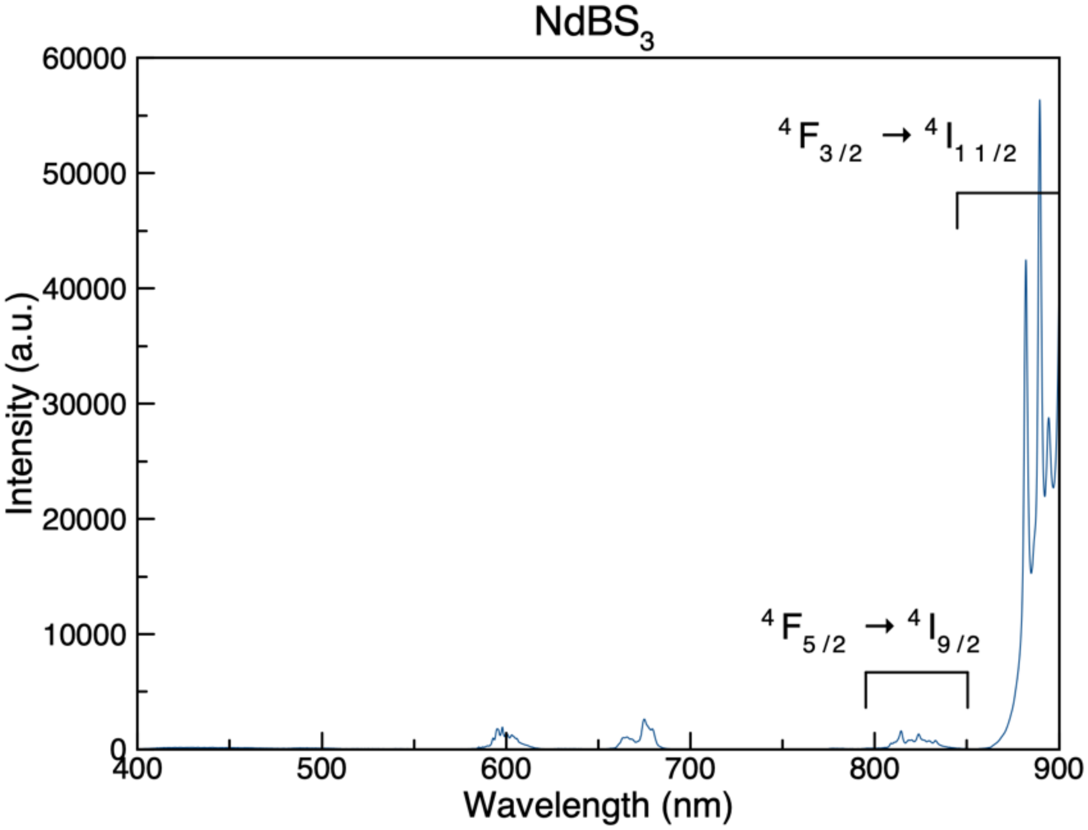

Figure 4.8 Fluorescence data obtained on a single crystal of NdBS$_3$. The characteristic $^4F_{5/2} \rightarrow {}^4I_{9/2}$ and $^4F_{3/2} \rightarrow {}^4I_{11/2}$ f-f transitions were resolved.[185]

while thermodynamic phases might be thermally more stable, they are finite in number, especially when contrasted with kinetic/metastable phases that comprise a vast frontier. While plentiful, kinetic phases are synthetically challenging to obtain, especially relative to thermodynamic phases.[4] The molten flux growth method has proven to be a successful approach for the creation of single crystals of kinetic phases, including a variety of chalcogenides.[3, 122, 145] The critical component is the low melting flux, usually an alkali halide salt, that acts as the solvent at elevated temperatures in which the reagents dissolve. The addition of the 'liquid component' aids in the diffusion of reagents, greatly reducing reaction times, and the extensive choice of alkali halide melting points offers a large range of reaction temperatures that can be utilized. For the synthesis of chalcogenides compounds in particular, low melting polychalcogenide fluxes have been employed that have been the key to the discovery and crystal growth of numerous chalcogenide phases.[2, 134, 165, 166, 186, 187] At the low temperatures afforded by polychalcogenide fluxes, the incorporation of chalcometallate molecular building blocks (i.e. $[SiS_4]^{4-}$, $[VS_4]^{3-}$, etc.) into the resulting compounds becomes increasingly possible which greatly influences their structures and resulting properties.[4]

For the growth of the lanthanide orthothioborates reported herein, a NaI–CsI eutectic flux was employed to access a reaction temperature of 550 ºC, speed up the reaction time, and to aid in single crystal growth. The addition of the K_2S polychalcogenide flux was to potentially help increase the possibility of molecular building block incorporation into the final reaction product. Finally, the BCM method was applied to these reactions allowing for the use of the lanthanide oxides as starting reagents greatly assisting in the ease of reaction setup. The combination of these three components resulted in a new unprecedented low temperature synthetic route used herein to obtain single crystals of lanthanide orthothioborates, $LnBS_3$, in only 3 days, which contain the orthothioborate, $[BS_3]^{3-}$, molecular unit that is known to induce NLO behaviors, a phenomenon validated by the strong SHG activity of $LaBS_3$. The successful low temperature approach to these compounds, which were previously thought to only form during high temperature and pressure synthetic routes, opens an entirely new energy landscape, potentially leading to the discovery of many new kinetic thioborate materials with promising optical properties. As a further demonstration to validate this low temperature approach, we used the same procedure used to prepare $LnBS_3$ to obtain single crystals of BaB_2S_4, one of the best SHG materials known to date.[34] This reaction resulted in a phase pure sample of BaB_2S_4 with crystals up to a millimeter in size; the powder X-ray diffraction pattern and crystal images can be found in Figures 4.9 and 4.10. We are in the process of extending this synthetic approach to other thioborate compositions to investigate their physical properties. This synthetic method coupled with the ease of access to chalcogenide materials afforded by the BCM method and the single crystal growth abilities of the molten flux growth technique will undoubtably boost research in the field of NLO active thioborates.

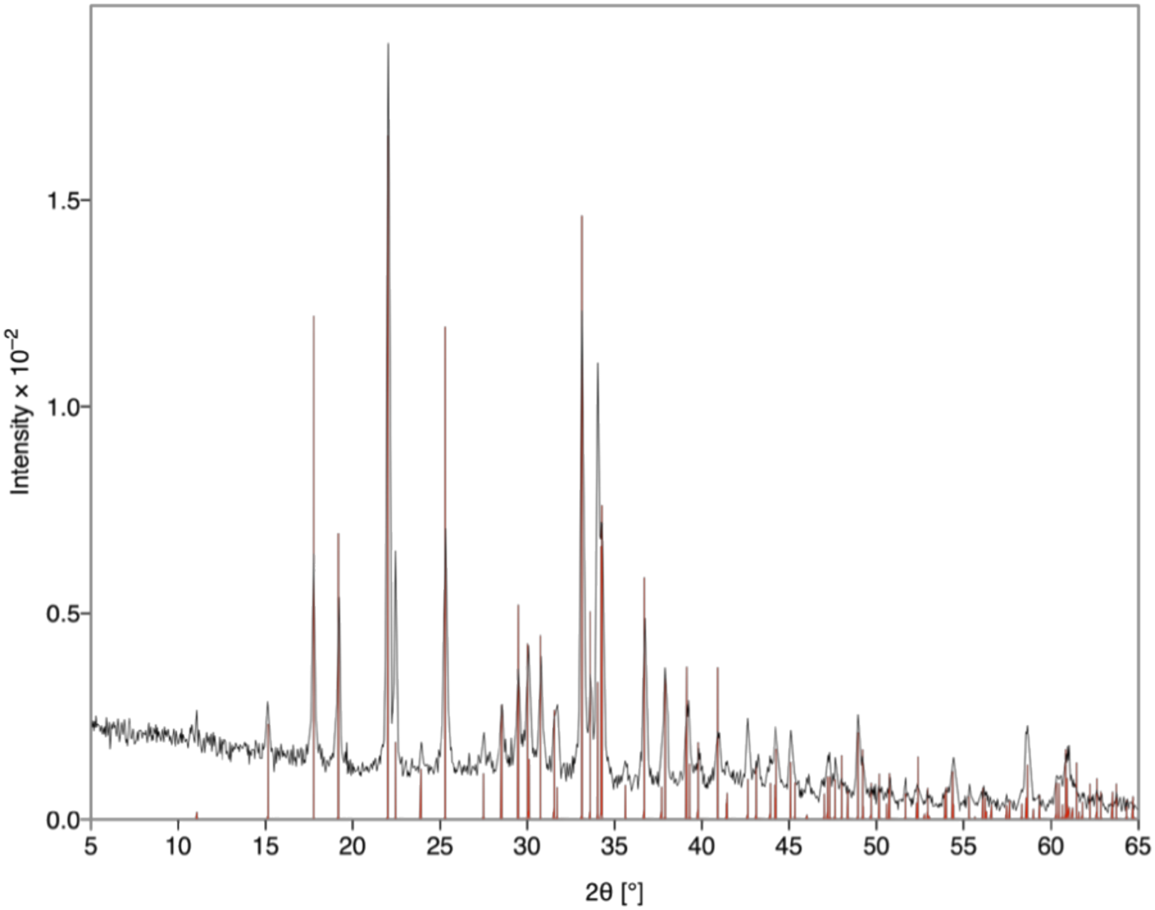

Figure 4.9 Powder X-ray Diffraction Pattern of phase pure BaB_2S_4 (black lines) and the overlayed CIF (red lines) synthesized using our low temperature route.

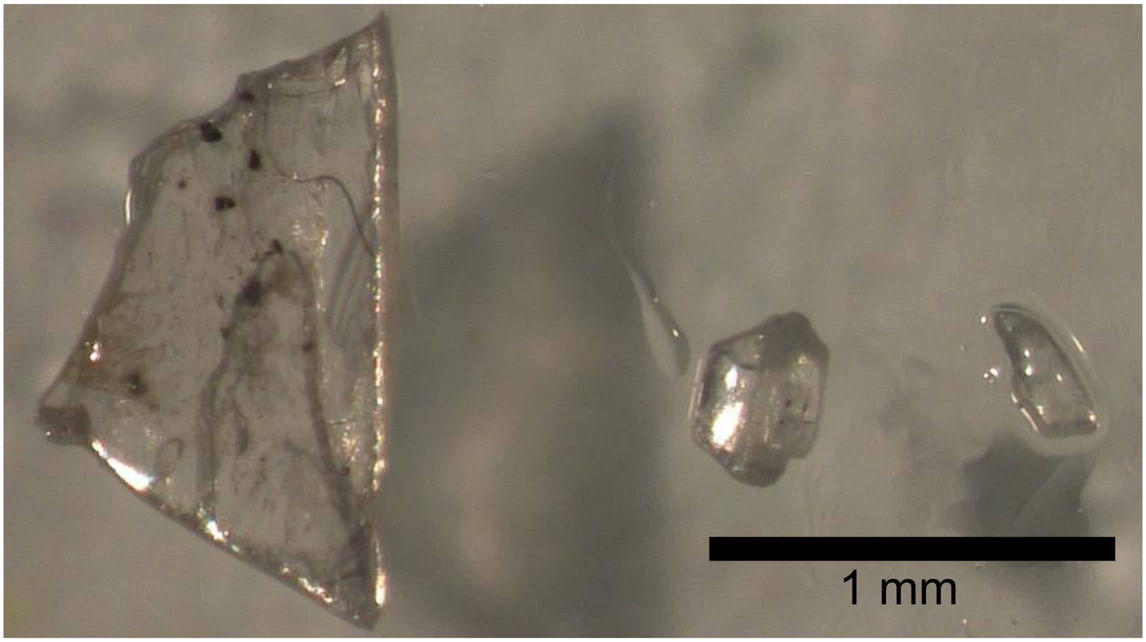

Figure 4.10 Image of the BaB_2S_4 crystals obtained using our low temperature synthetic route.

Acknowledgements: Research supported by the US Department of Energy, Office of Basic Energy Sciences, Division of Materials Sciences and Engineering under award DE-SC0018739. PSH and ML thank the Welch Foundation (Grant E-1457) and the NSF-DMR (2002319) for support. All syntheses, structural characterizations, and florescence measurements were performed at UofSC. SHG measurements performed at UH.

CHAPTER 5

SYNTHESIS OF URANIUM MIXED ANION COMPOUNDS USING THE BORON-CHALCOGEN MIXTURE METHOD: $Ba_6Co_6U_{0.91}S_{13.5}O_{0.5}$ and $Ba_{5.47}K_{0.53}Zn_6US_{13.5}O_{0.5}$.[1]

---

[1] Reproduced with permission from Breton, L. S., Smith, M. D., and zur Loye, H.-C.*, Solid State Sci.,* **2023**, 140, 107207. **© 2023 Elsevier Masson SAS.**

Abstract: Mixed anion compounds have exhibited interesting structures and properties that differ from compounds only incorporating a single anion in their composition. Unfortunately, difficulties in the synthetic methods used to obtain these materials has slowed the evolution of this field, prompting investigations into alternate synthetic pathways to these materials. Our recently establish Boron-Chalcogen Mixture (BCM) method, which was originally developed for the synthesis of pure actinide chalcogenides from oxides, has been adapted to achieve the partial oxide to sulfide conversion of Ba_2MUO_6 (M = Co, Zn) which resulted in two new uranium (IV/V) oxysulfide compounds, $Ba_6Co_6U_{0.91}S_{13.5}O_{0.5}$ and $Ba_{5.47}K_{0.53}Zn_6US_{13.5}O_{0.5}$ These compounds crystallize in the tetragonal crystal system adopting the space group $I4/mcm$. Their syntheses, crystal structures, and trends observed in the pursuit of these new mixed anion compounds are reported.

Introduction: Mixed anion compounds are usually considered to be solid state materials that contain more than one anionic species within a single structure and include oxychalcogenides[181, 188-192], oxyhalides[193-198], and oxynitrides[199-204]. The presence of multiple anionic species having differing anionic radii, polarizability, electronegativity, and charge, can lead to the formation of compounds with novel structures, crystallographic symmetries, and physical properties.[205] Some of these properties are compositionally/structurally induced in mixed anion materials, for example the removal of a center of symmetry to induce NLO or ferroelectric behavior, thus making them a new research frontier that can lead to both theoretical and technological advancements.[206-209] The majority of reported inorganic materials are metal oxides, which are traditionally synthesized via high temperature reactions in air, e.g., exposed to atmospheric oxygen.

When carrying out the synthesis of mixed-anion materials this exposure to oxygen represents a major obstacle, as the oxygen, by virtue of being present in large excess, will tend to overpower the non-oxide anions, resulting in oxides rather than mixed anion compositions. For these reasons, the targeted synthesis of mixed-anion compounds requires careful synthetic control and, usually, controlled atmospheric environments. A variety of synthetic methods have been used to obtain mixed-anion materials, such as solvothermal synthesis or high-pressure reactions, however, the infancy of this field of materials still gives promise to the development of alternate paths to new and existing mixed-anion compounds.

Recently our group developed the Boron-Chalcogen Mixture (BCM) method as a facile oxide to chalcogenide conversion route for actinides, which enables the synthesis of oxygen-free chalcogenide materials, even when starting with oxide reagents.[43] This work builds upon the method reported by Wu et al. who utilized it for the synthesis of various transition metal and rare earth chalcogenides.[129, 178, 179] The successful conversion from an oxide to a chalcogenide is driven by the greater formation energy of boron oxide, (i.e. $\Delta_f G$ (vitreous-B_2O_3) = -1182.5 Kj/mol) over the boron chalcogenides (e.g. $\Delta_f G$ (vitreous-B_2S_3) = -247.6 Kj/mol), which causes boron to act as an 'oxygen sponge', forming highly stable B_2O_3, and leaving the metal to coordinate with the added chalcogen.[131] This method has worked well for the synthesis of many actinide chalcogenides allowing for their magnetic properties, often for the first time, to be explored.[43, 44, 210] While the BCM method was originally developed for full oxide to chalcogenide conversion, the potential of this method to enable partial rather than full oxide to chalcogenide conversion, makes it of great interest as a novel synthetic route to mixed anion compounds.

The synthesis of the ternary lanthanide oxysulfides, Ln_2O_2S (Ln = La and Nd), was reported in the literature as having been accomplished by using a boron-sulfur method[129], while actinide oxysulfides have been reported synthesized (1) via solid state reactions of intimately mixed oxide and sulfide reagents, (2) via reactions using actinide oxysulfides as a reagent, and (3) by the use of H_2S and CS_2 as sulfurizing agents.[211-215] Uranium oxysulfides, such as USO, have also been identified as side products due to the presence of impure starting reagents or due to reactions with the wall of fused silica reaction vessels.[2, 216] For example, while targeting 2H-perovskite related actinide chalcogenides, Mesbah et al. isolated actinide oxysulfide side products with the formula $Ba_6M_2US_{12.5}O_{0.5}$.[122] The oxygen inclusion within these compositions arose from the etching of the fused silica tube used as the reaction vessel. In fact, all of the known compounds belonging to the $Ba_6M_2US_{12.5}O_{0.5}$ family of compounds, including M = Ti, Si/Fe, V, and Fe, were reported to be serendipitously synthesized with the oxygen content attributed to etching of the fused silica tube.[217, 218] To test the BCM method's ability to create uranium oxysulfide compounds, we chose to target similar compounds containing other first row transition metals, resulting in two new uranium (IV/V) oxysulfide compounds, namely $Ba_6Co_6U_{0.91}S_{13.5}O_{0.5}$ and $Ba_{5.47}K_{0.53}Zn_6US_{13.5}O_{0.5}$, whose synthesis and crystal structures are reported herein. Attempts at synthesizing a nickel containing uranium oxysulfide were unsuccessful and are discussed herein.

Experimental Section:

Reagents. $BaCO_3$ (Alfa Aesar, 99.95%), KI (VWR, ACS grade), NiO (Alfa Aesar, 99%), ZnO (Aldrich Chemical Company, 99.9%), CoO (BeanTown Chemicals, 99.995%), U_3O_8 (International Bio-Analytical Industries, Inc., 99.99%), elemental boron (BTC, ~100-

mesh 99.9%), and elemental sulfur (sublimed, Fischer Chemicals) were used as received. KI was stored in an oven set to 260 ºC. K_2S was synthesized as described in the literature and stored in a nitrogen glovebag.[167]

Caution! Although the uranium precursor used in these syntheses contains depleted uranium, observing proper procedures for handling radioactive materials is required. All handling of radioactive materials was performed in laboratories specially designated for the study of radioactive uranium materials.

Synthesis of Ba_2MUO_6 (M = Co, Ni, Zn) Precursors. Ba_2MUO_6 (M =Co, Ni, Zn) was prepared by adding $BaCO_3$, MO, and U_3O_8 in a 2:1:0.33 molar ratio to a pestle and mortar. Due to the hygroscopic nature of $BaCO_3$, the pestle and mortar were used in a nitrogen filled glovebag where the reaction mixture was ground for 20 minutes. The ground mixture was loaded into a 0.25-inch pellet dye and pressed into a pellet. The pellet was placed into an alumina crucible which was covered with an alumina cap and placed into a programmable furnace set to ramp to 1000 ºC in 2 hours and dwell at this temperature for 24 hours, after which the furnace was shut off and allowed to return to room temperature. The product was ground in a pestle and mortar in air for 10 minutes, pelletized, and loaded back into the same capped alumina crucible and heated a second time using the same temperature profile. The powder X-ray diffraction patterns of the obtained products are shown in Figures 5.1-5.3.

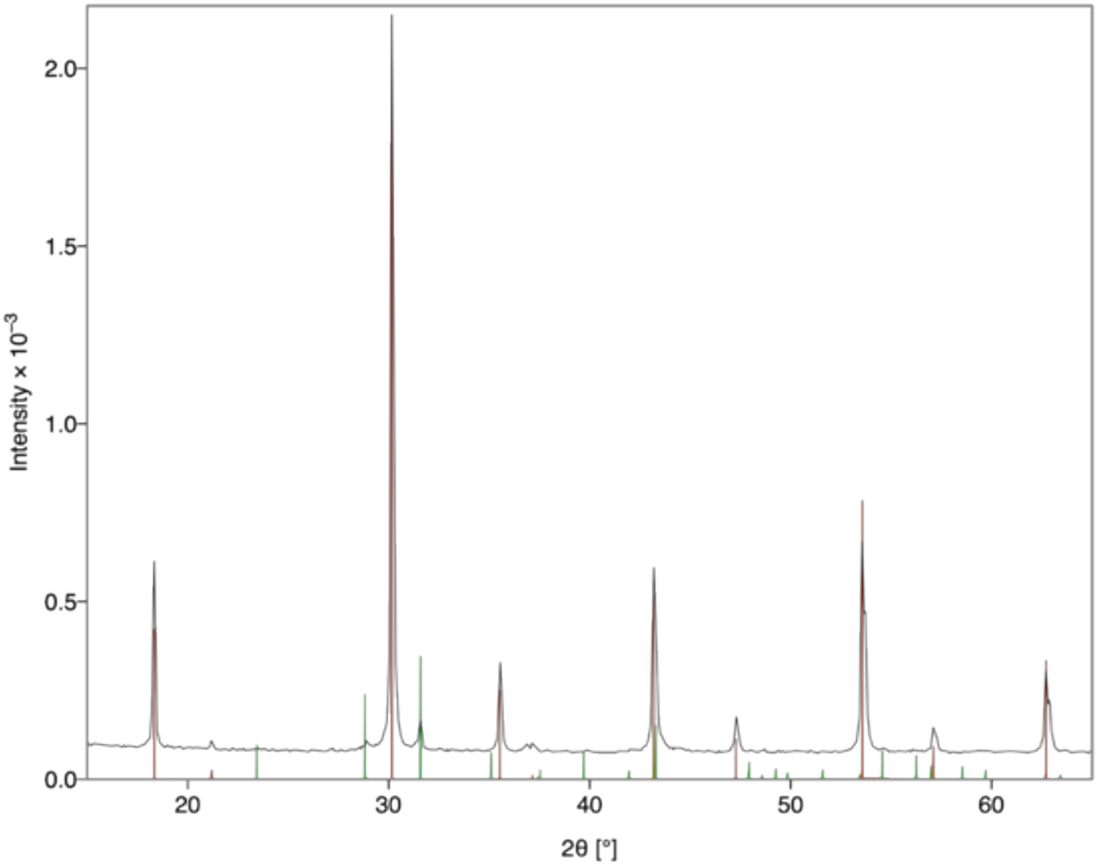

Figure 5.1 The diffraction pattern (black) of the reaction targeting Ba_2CoUO_6 with the overlayed Crystallographic Information Files (CIF) for (red) Ba_2CoUO_6, and (green) $BaCoO_2$.

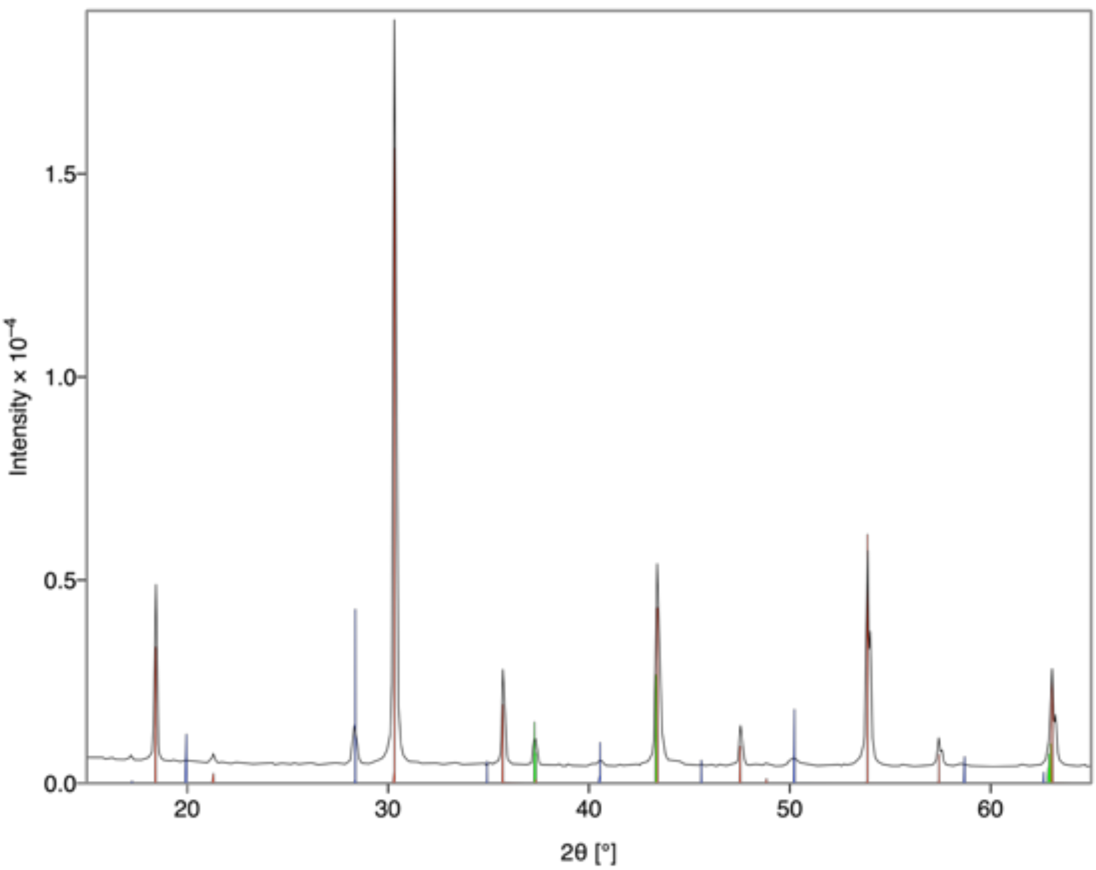

Figure 5.2 The diffraction pattern (black) of the reaction targeting Ba_2NiUO_6 with the overlayed CIFs for (red) Ba_2NiUO_6, (blue) $BaUO_3$, and (green) NiO.

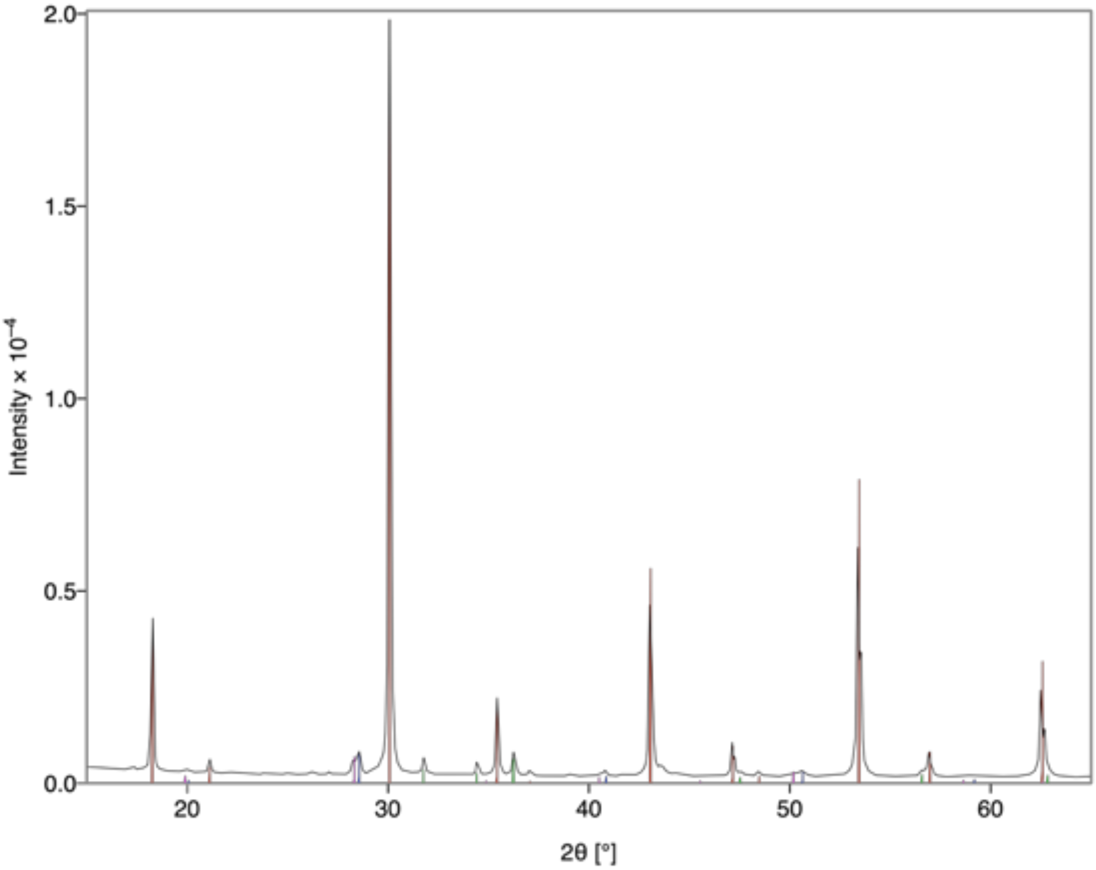

Figure 5.3 The diffraction pattern (black) of the reaction targeting Ba_2ZnUO_6 with the overlayed CIFs for (red) Ba_2ZnUO_6, (blue) $BaUO_3$, (green) ZnO, and (pink) Ba_3UO_6.

Synthesis of $Ba_6Co_6U_{0.91}S_{13.5}O_{0.5}$ and $Ba_{5.47}K_{0.53}Zn_6US_{13.5}O_{0.5}$. $Ba_6Co_6U_{0.91}S_{13.5}O_{0.5}$ and $Ba_{5.47}K_{0.53}Zn_6US_{13.5}O_{0.5}$ were synthesized by loading a carbon crucible (9.525 mm o.d. × 6.35 mm i.d. × 50.8 mm length) with sulfur, boron, Ba_2MUO_6, KI, and K_2S, in that order. Single crystals of $Ba_6Co_6U_{0.91}S_{13.5}O_{0.5}$ and $Ba_{5.47}K_{0.53}Zn_6US_{13.5}O_{0.5}$ were obtained using a Ba_2MUO_6:B:S molar ration of 1:4:6 and 1:8:12, respectively. 0.250 grams of KI and 0.030 grams of K_2S were used as the eutectic flux in all reactions. The sulfur, boron, and Ba_2MUO_6 reagents were loaded into the carbon crucible in air while the KI and K_2S were handled and added inside a nitrogen filled glovebag. The carbon crucibles were capped with a carbon cap and loaded into a fused silica tube (12 mm o.d. × 10 mm i.d. × 200 mm length) which was evacuated on a vacuum line and sealed using a methane-oxygen torch. The sealed fused silica tubes were placed into a programmable furnace set to ramp to 800 ºC in 10 hours, dwell at this temperature for 12 hours, and cool to 600 ºC in 20 hours, after which the furnace was shut off and allowed to return to room temperature. The carbon crucibles were removed from the fused silica tubes, uncapped, and placed into a beaker filled with ~60 mL of MeOH. The beaker was sonicated for about 20 minutes and then the MeOH was decanted into a separate beaker. The products inside the carbon crucible were scrapped out with a spatula into the first beaker which was refilled with another ~60 mL aliquot of MeOH. After another 20-minute sonication, the MeOH was decanted off and the product was isolated by vacuum filtration and washed with acetone.

Single Crystal X-ray Diffraction (SXRD). X-ray intensity data from black needles of the title compounds were collected at 301(2) K using a Bruker D8 QUEST diffractometer equipped with a PHOTON-II area detector and an Incoatec microfocus source (Mo Kα radiation, $\lambda = 0.71073$ Å). The raw area detector data frames were reduced and corrected for absorption effects using the SAINT+ and SADABS program.[78, 79] Final unit cell parameters were determined by least-squares refinement of large sets of reflections taken from each data set. An initial structural model was obtained with SHELXT.[80] Subsequent difference Fourier calculations and full-matrix least-squares refinement against F^2 were performed with SHELXL-2018 using ShelXle.[81, 82] The crystallographic parameters of $Ba_6Co_6U_{0.91}S_{13.5}O_{0.5}$ and $Ba_{5.47}K_{0.53}Zn_6US_{13.5}O_{0.5}$ are summarized in Table 5.1.

Table 5.1 Crystallographic data for $Ba_6Co_6U_{0.9126(28)}S_{13.5}O_{0.5}$ and $Ba_{5.470(20)}K_{0.530(20)}Zn_6US_{13.5}O_{0.5}$.

Chemical formula	$Ba_6Co_6U_{0.9126(28)}S_{13.5}O_{0.5}$	$Ba_{5.470(20)}K_{0.530(20)}Zn_6US_{13.5}O_{0.5}$
Formula weight	1835.65	1843.11
Crystal system	Tetragonal	
Space group, Z	*I*4/*mcm*, 4	
a, Å	16.4249(3)	16.5171(4)
c, Å	9.6289(3)	9.7813(3)
V, Å^3	2597.66(12)	2668.48(14)
ρ_{calcd}, g/cm^3	4.694	4.588
Radiation (λ, Å)	Mo Kα (0.71073 Å)	
μ, mm^{-1}	19.392	20.387
T, K	301(2)	301(2)
Crystal dim., mm^3	0.100x0.010x0.010	0.080x0.020x0.020
2θ range, deg.	2.480 - 31.524	2.466 - 30.520
Reflections collected	29427	24092
Data/parameters/restraints	1195/46/0	1126/48/0
$\Delta\rho_{max}$ (e Å^{-3})	1.40	0.90
$\Delta\rho_{min}$ (e Å^{-3})	-2.28	-1.24
R_{int}	0.0437	0.0500
Goodness of fit	1.177	1.208
$R_1(I > 2\sigma(I))$	0.0271	0.0262
wR_2 (all data)	0.0495	0.0411

Powder X-ray Diffraction (PXRD). PXRD data were collected on ground samples of the products. Data were collected using a Bruker D2 PHASER diffractometer using Cu Kα radiation over a 2θ range of 5−65° with a step size of 0.02°.

Energy-Dispersive Spectroscopy (EDS). EDS was performed on single crystals of $Ba_6Co_6U_{0.91}S_{13.5}O_{0.5}$ and $Ba_{5.47}K_{0.53}Zn_6US_{13.5}O_{0.5}$ using a Tescan Vega-3 scanning electron microscope equipped with a Thermo EDS attachment. Scanning electron microscopy (SEM) was operated in a low-vacuum mode. Crystals were mounted on a SEM stub with carbon tape and analyzed using a 20 kV accelerating voltage and a 120 s accumulation time. The results of EDS confirmed the presence of elements found by SXRD.

Discussion:

Synthesis. When developing the BCM method, the full oxygen to sulfur replacement of $UCoO_4$, which was synthesized by the combination of U_3O_8 and cobalt oxalate, was successfully achieved, resulting in a pure phase of the $UCoS_3$ perovskite. To target higher order oxysulfides, we therefore chose to first synthesize the quaternary barium transition metal uranium oxides, Ba_2MUO_6, and systematically add increasing amounts of boron and sulfur to promote the partial substitution of sulfur for oxygen in Ba_2MUO_6. To structurally characterize the products, we combined the BCM method with the molten flux crystal growth approach to obtain single crystals for facile structure determination.

Once the quaternary Ba_2MUO_6 (M = Co, Ni, Zn) compositions were synthesized via traditional solid-state syntheses, the obtained polycrystalline powders were used in multiple reactions with increasing amounts of boron and sulfur, but identical amounts of K_2S and KCl, which were used as a eutectic flux in these reactions. Table 5.2 summarizes the molar ratios of Ba_2MUO_6 : B : S (M = Co and Zn) used and the products obtained for each reaction. The table for the M = Ni reactions can be found in the supporting information, Table 5.3. Figures 5.4-5.16 contain the powder diffraction patterns for each reaction performed.

Table 5.2 A summary of the molar ratios used for the reactions targeting $Ba_6Co_6U_{0.91}S_{13.5}O_{0.5}$ and $Ba_{5.47}K_{0.53}Zn_6US_{13.5}O_{0.5}$. 0.030 g of K_2S and 0.250 grams of KI were used as the flux in each reaction. SiO_2 in the products was a result of glass micro fragments that were created during the opening of the fused silica tube. (Un/I = Unindexed peaks)

Sample	Ba_2CoUO_6	B	S	Products
Co-A	1	0	0	UO_2, Ba_2CoS_3, $Ba_6Co_{25}S_{27}$
Co-B	1	2	3	UO_2, Ba_2CoS_3, BaB_2O_4
Co-C	1	4	6	UO_2, Ba_2CoS_3, $Ba_6Co_6U_{0.91}S_{13.5}O_{0.5}$, SiO_2, Un/I
Co-D	1	8	12	USO, Ba_3CoUS_6, $K_{0.8}Ba_{3.2}US_6$, SiO_2 Un/I
Sample	Ba_2ZnUO_6	B	S	Products
Zn-A	1	0	0	Ba_2ZnS_3, UO_2
Zn-B	1	2	3	Ba_2ZnS_3, UO_2, ZnS, USO, BaB_2O_4
Zn-C	1	4	6	Ba_2ZnS_3, UO_2, ZnS, USO, BaB_2O_4, SiO_2, Un/I
Zn-D	1	8	12	UO_2, USO, $Ba_{5.47}K_{0.53}Zn_6US_{13.5}O_{0.5}$, BaB_2O_4, SiO_2 Un/I
Zn-E	1	12	18	USO, $BaUS_3$, $Ba_{5.47}K_{0.53}Zn_6US_{13.5}O_{0.5}$, ZnS,, Un/I, amorphous material

Table 5.3 A summary of the molar ratios used for each reaction. 0.030 g of K_2S and 0.250 grams of KI were used as the flux in each reaction. SiO_2 in the products was a result of glass micro fragments from breaking the fused silica tube container. (Un/I = Unindexed peaks)

Reaction	Ba_2NiUO_6	B	S	Products
Ni-A	1	0	0	UO_2, BaS, $Ba_6Ni_{25}S_{27}$, KI
Ni-B	1	2	3	UO_2, BaS, $Ba_6Ni_{25}S_{27}$, KI, Un/I
Ni-C	1	4	6	UO_2, BaS, $BaNiS_2$, SiO_2, BaB_2O_4, Graphite, Un/I
Ni-D	1	8	12	USO, Ba_3NiUS_6, NiS, Ni_3S_2

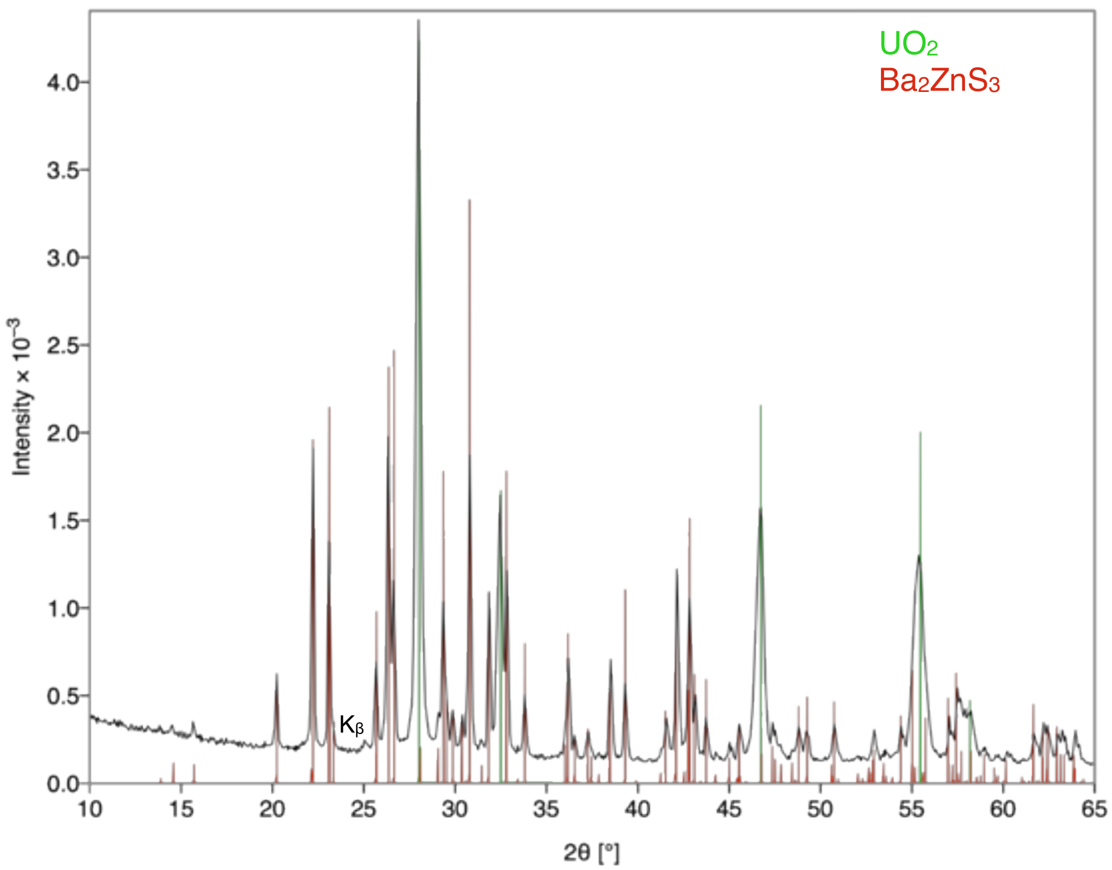

Figure 5.4 PXRD pattern of reaction Zn-A. The 100% peak for UO_2 had an indexable K_β peak which is labeled.

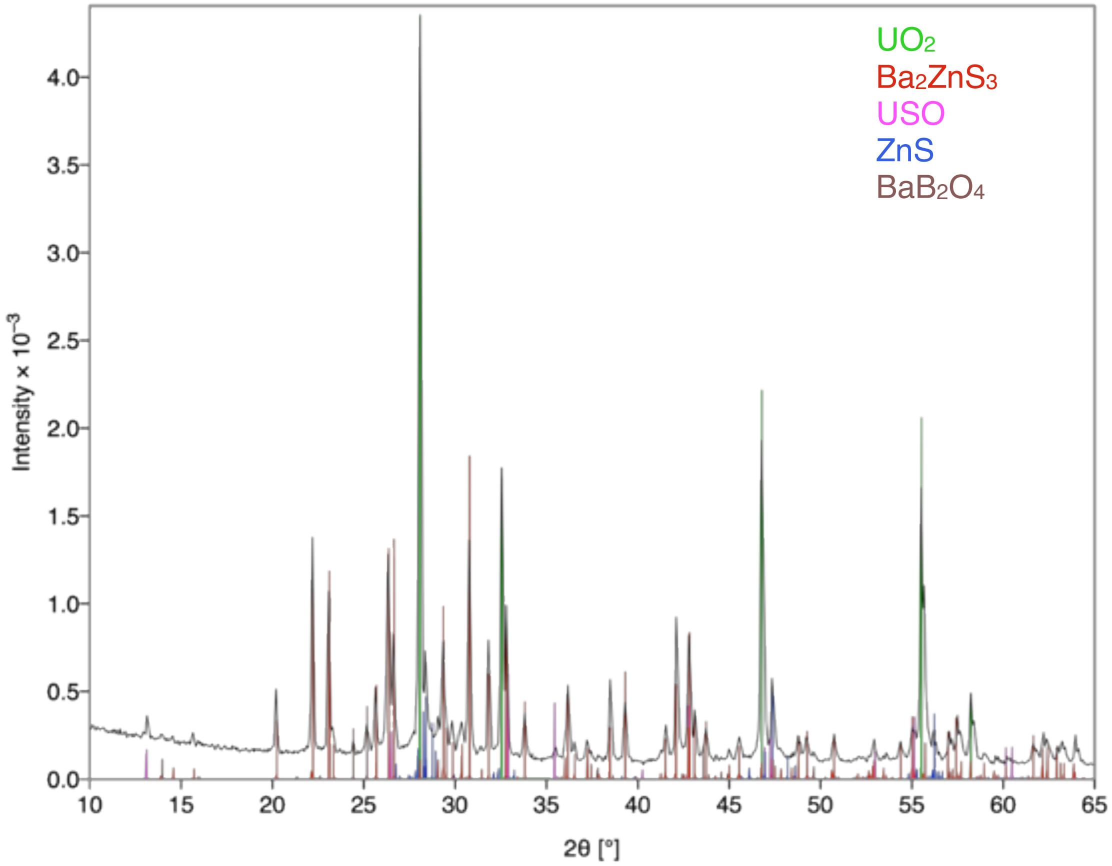

Figure 5.5 PXRD pattern of reaction Zn-B.

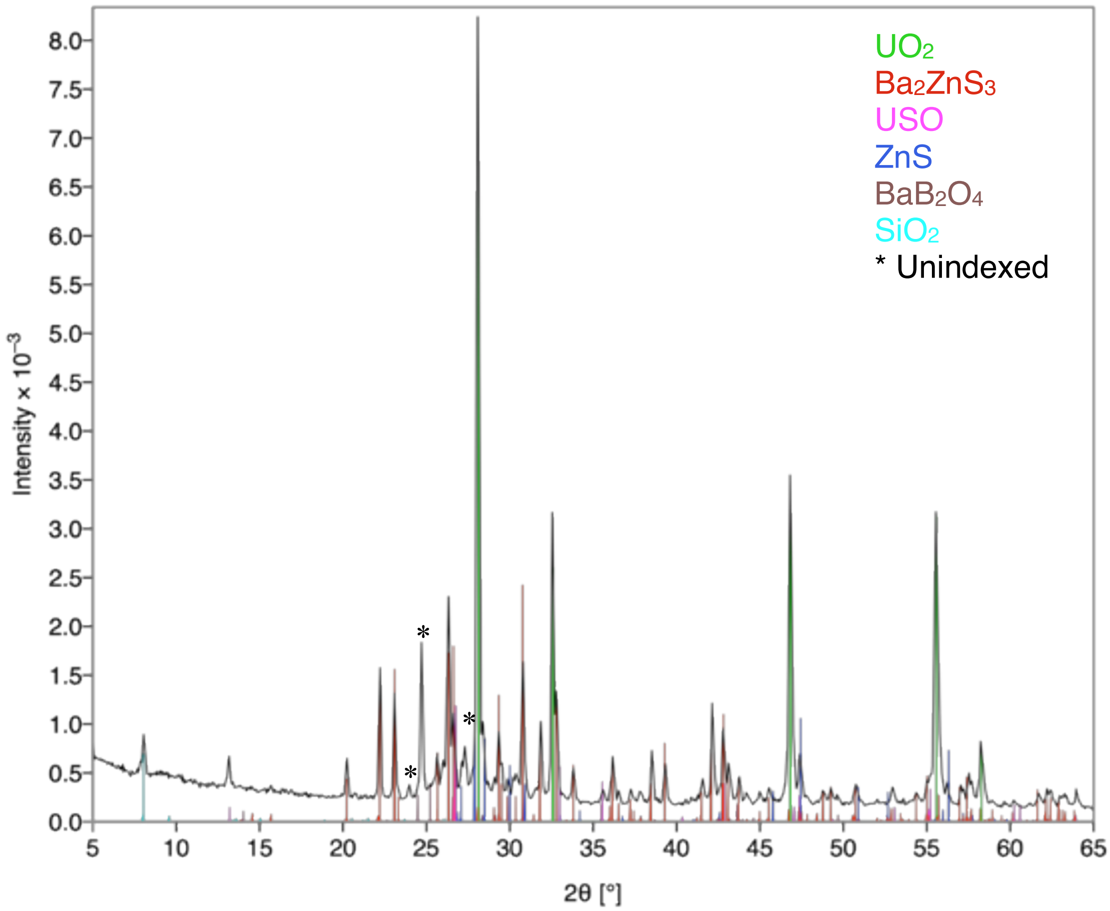

Figure 5.6 PXRD pattern of reaction Zn-C.

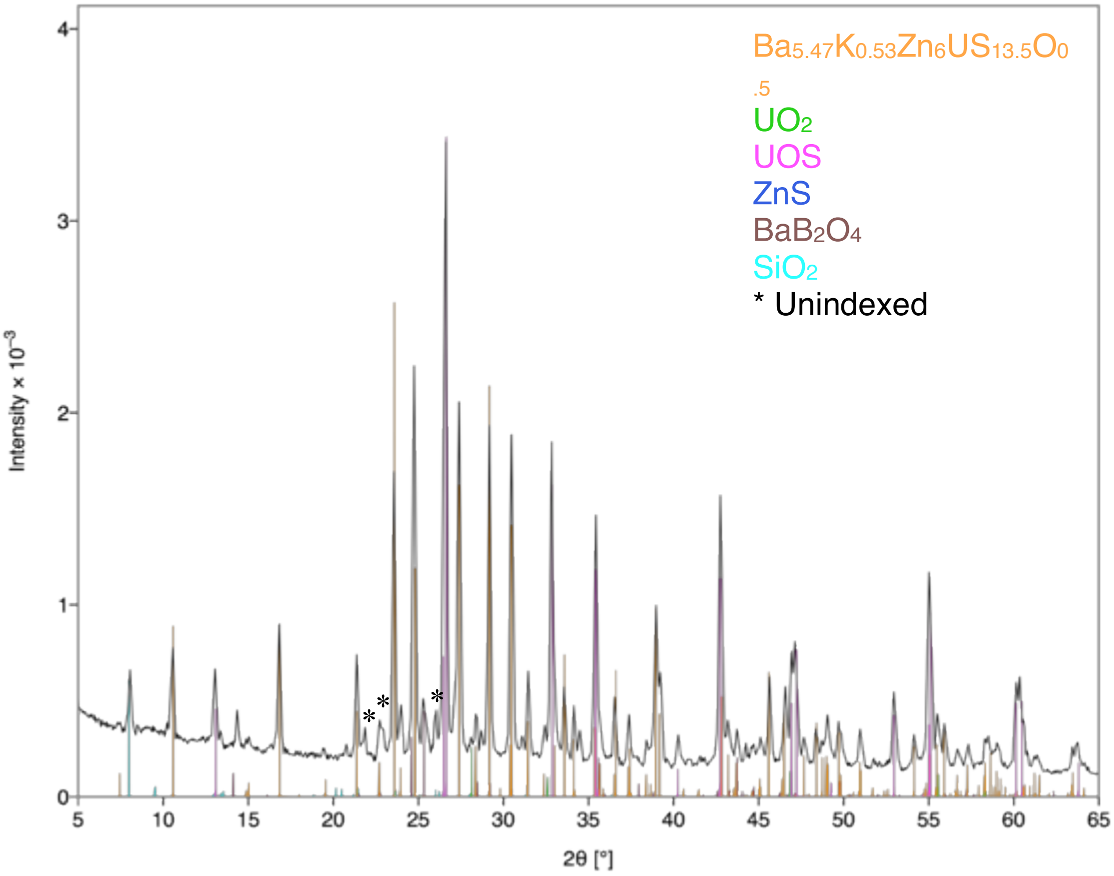

Figure 5.7 PXRD pattern of reaction Zn-D.

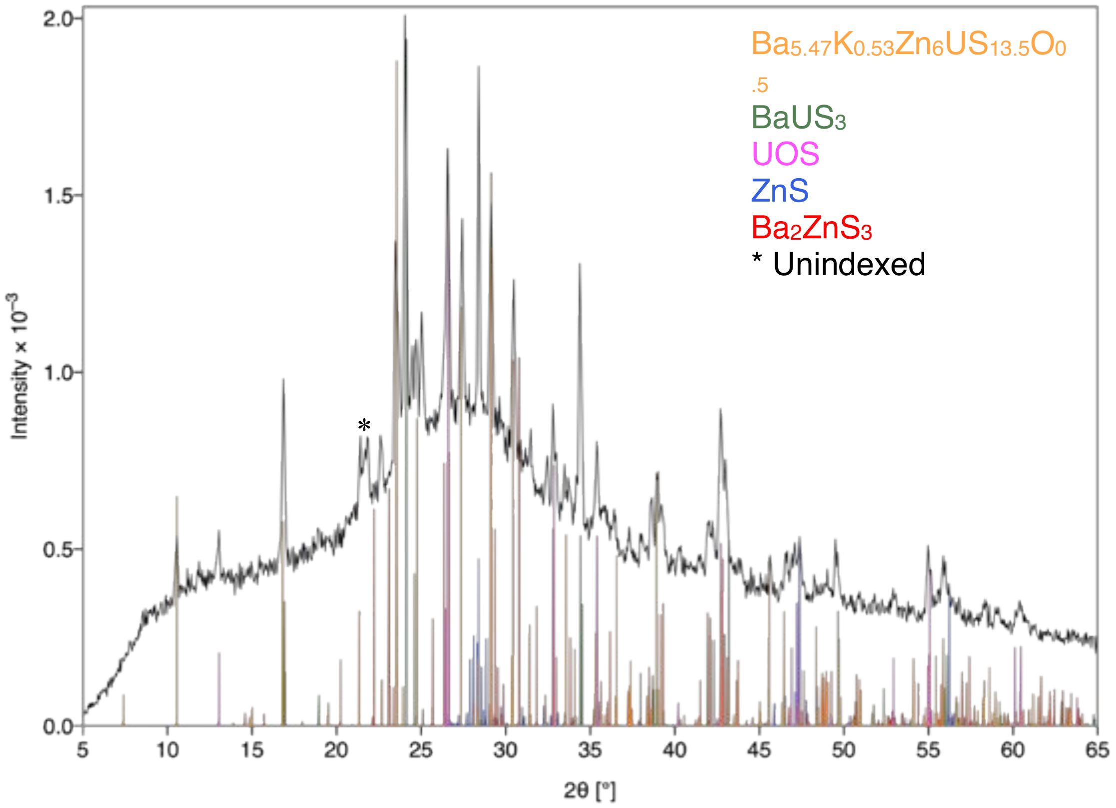

Figure 5.8 PXRD pattern of reaction Zn-E.

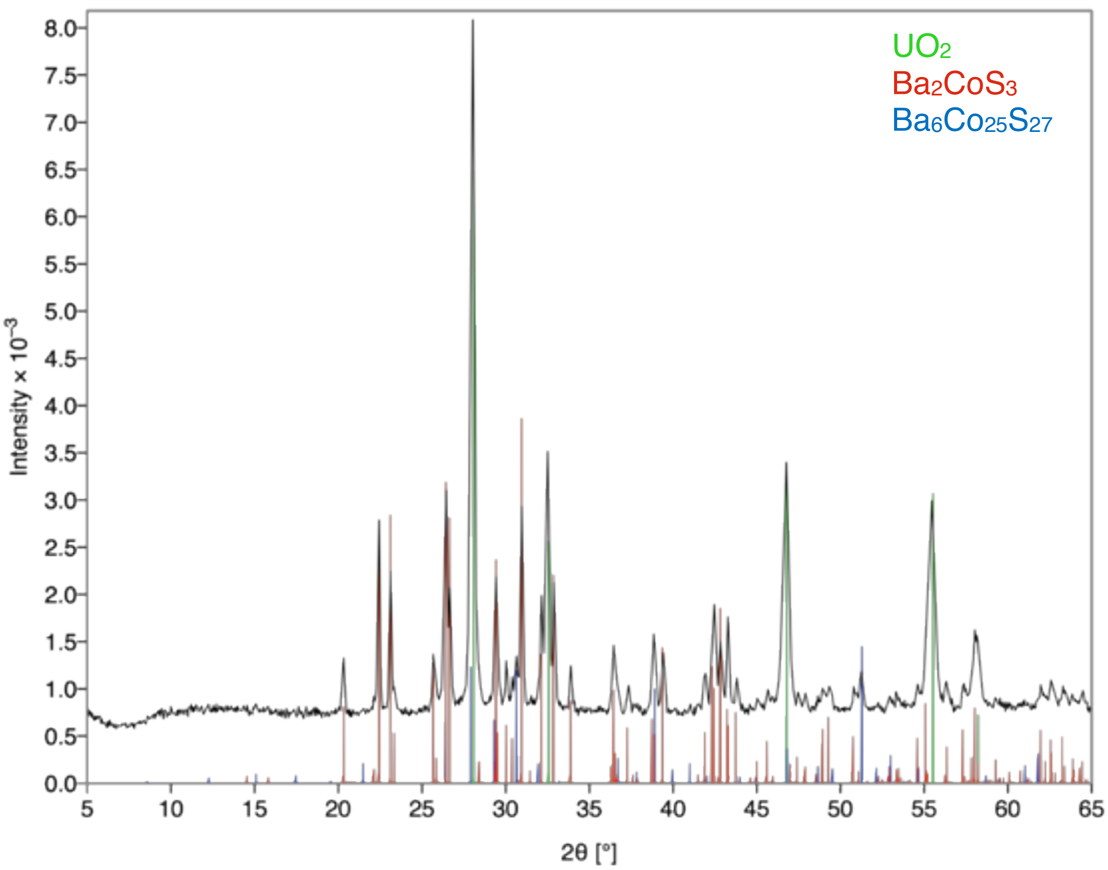

Figure 5.9 PXRD pattern of reaction Co-A.

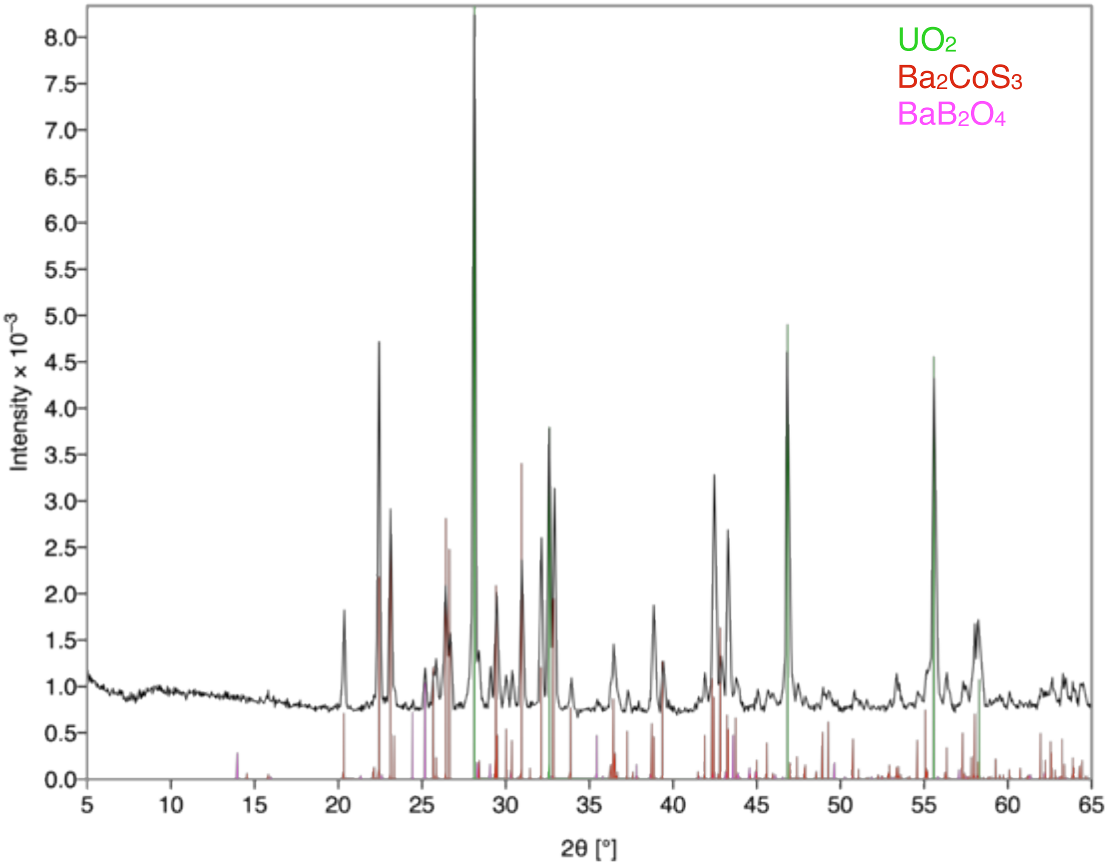

Figure 5.10 PXRD pattern of reaction Co-B.

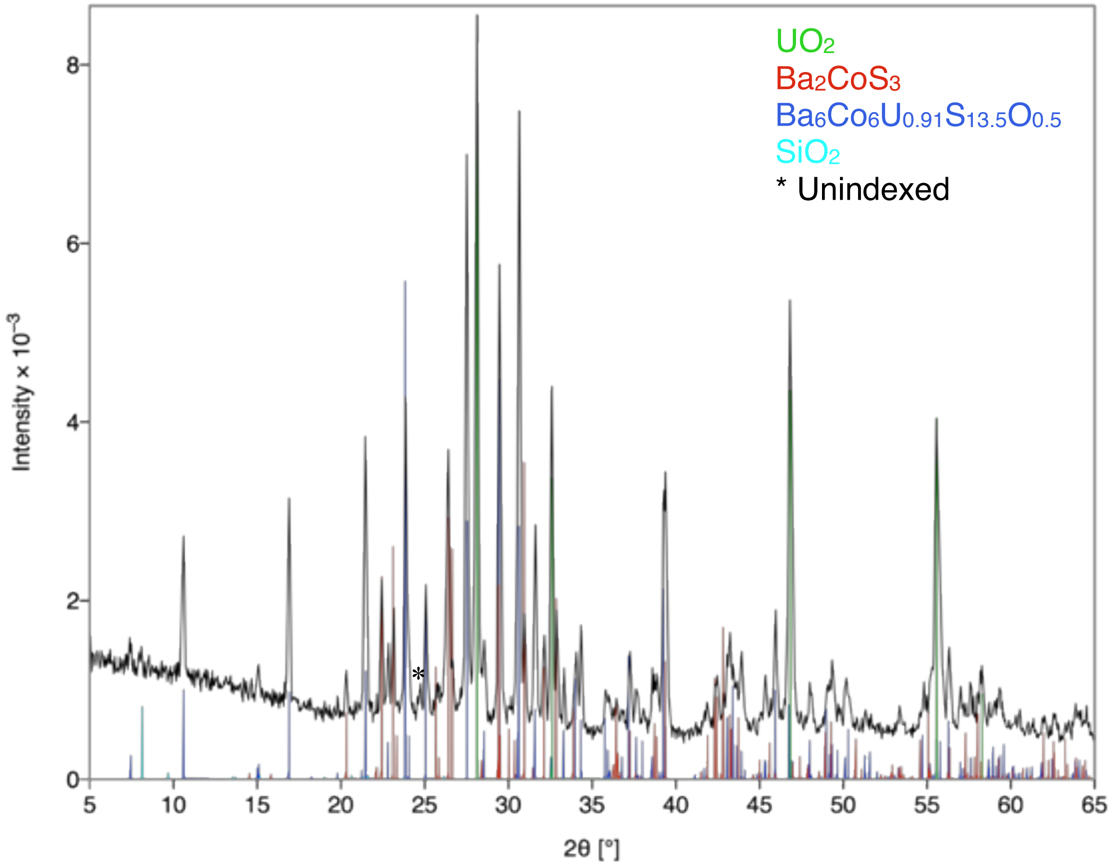

Figure 5.11 PXRD pattern of reaction Co-C.

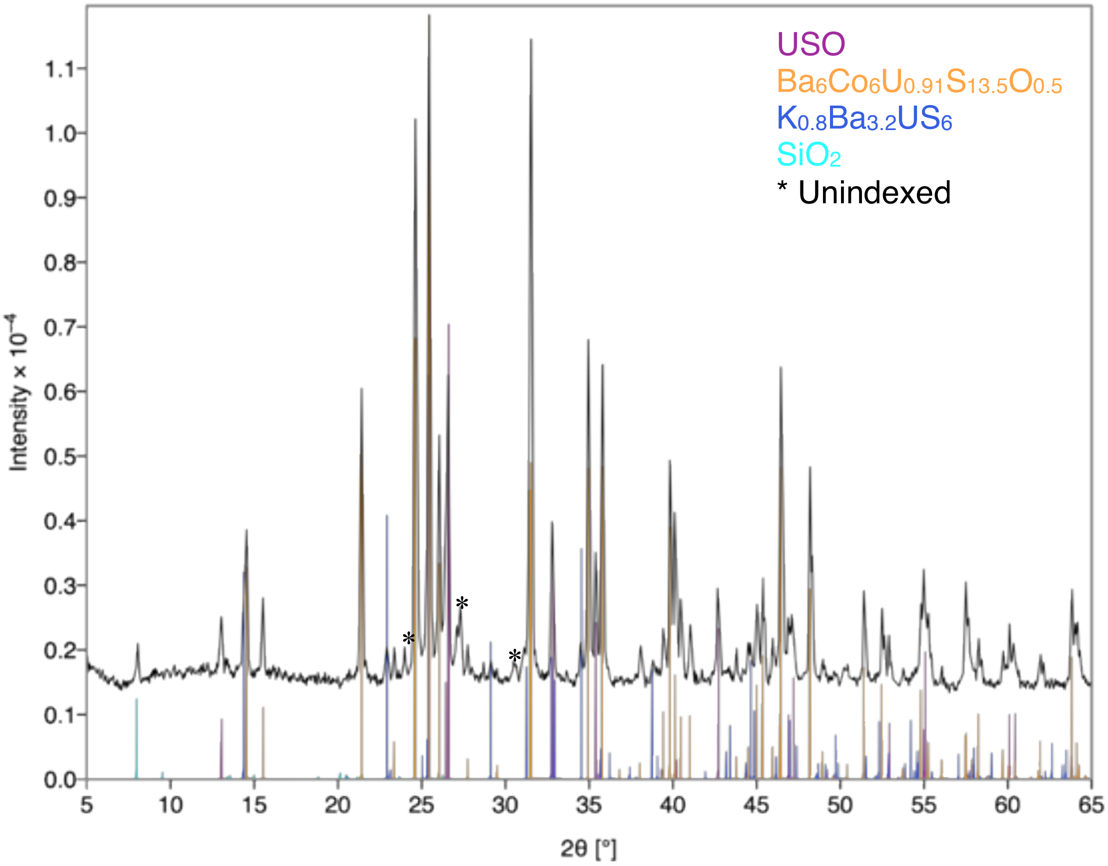

Figure 5.12 PXRD pattern of reaction Co-D.

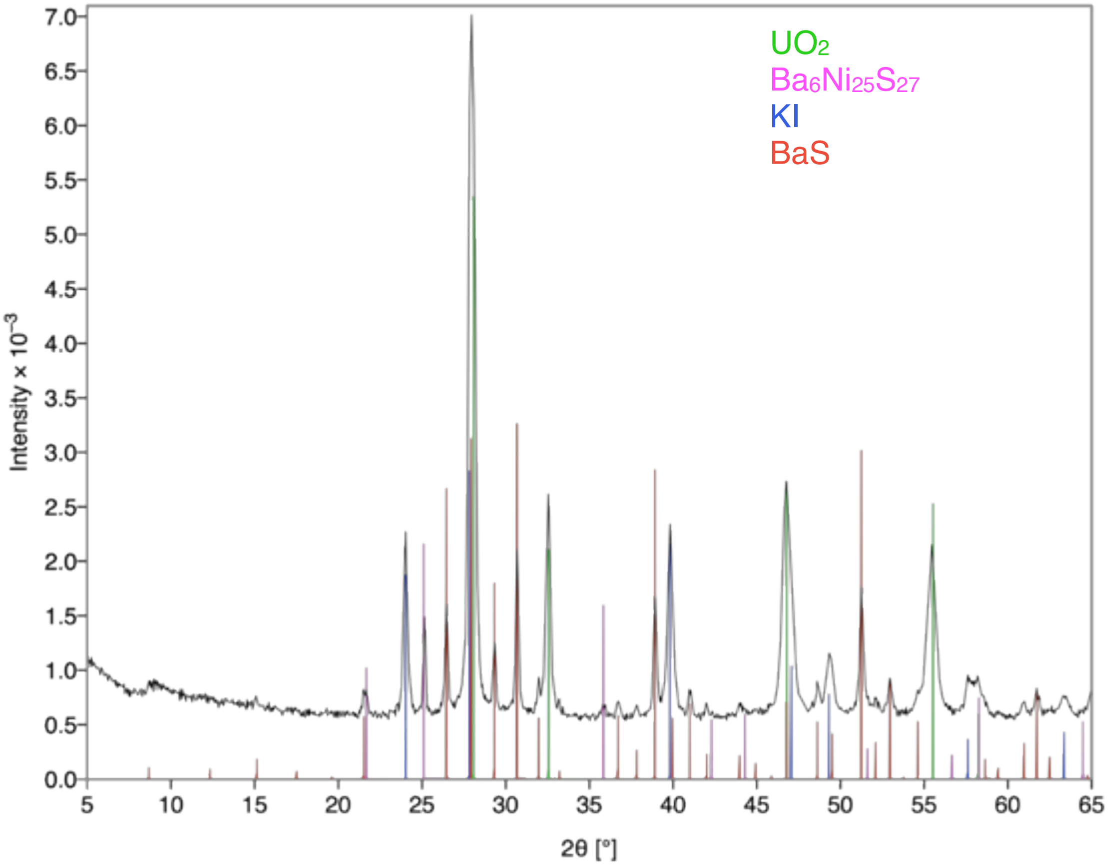

Figure 5.13 PXRD pattern of reaction Ni-A.

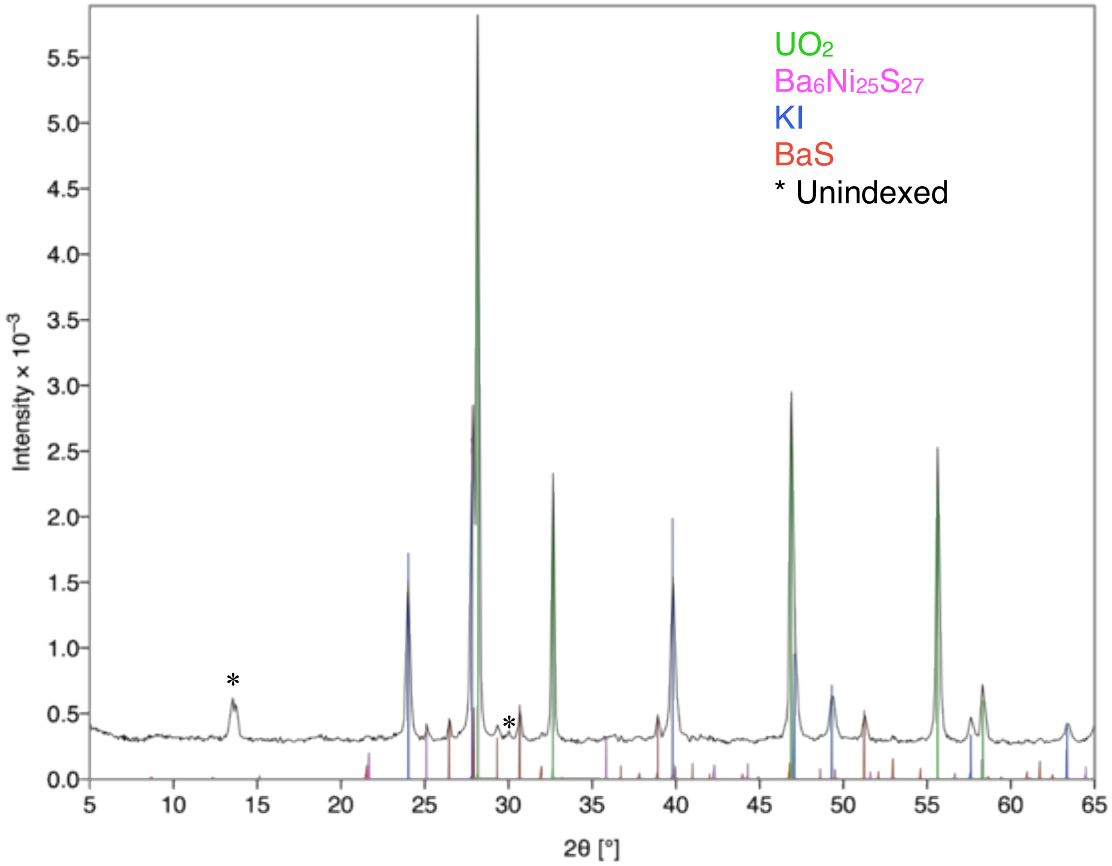

Figure 5.14 PXRD pattern of reaction Ni-B.

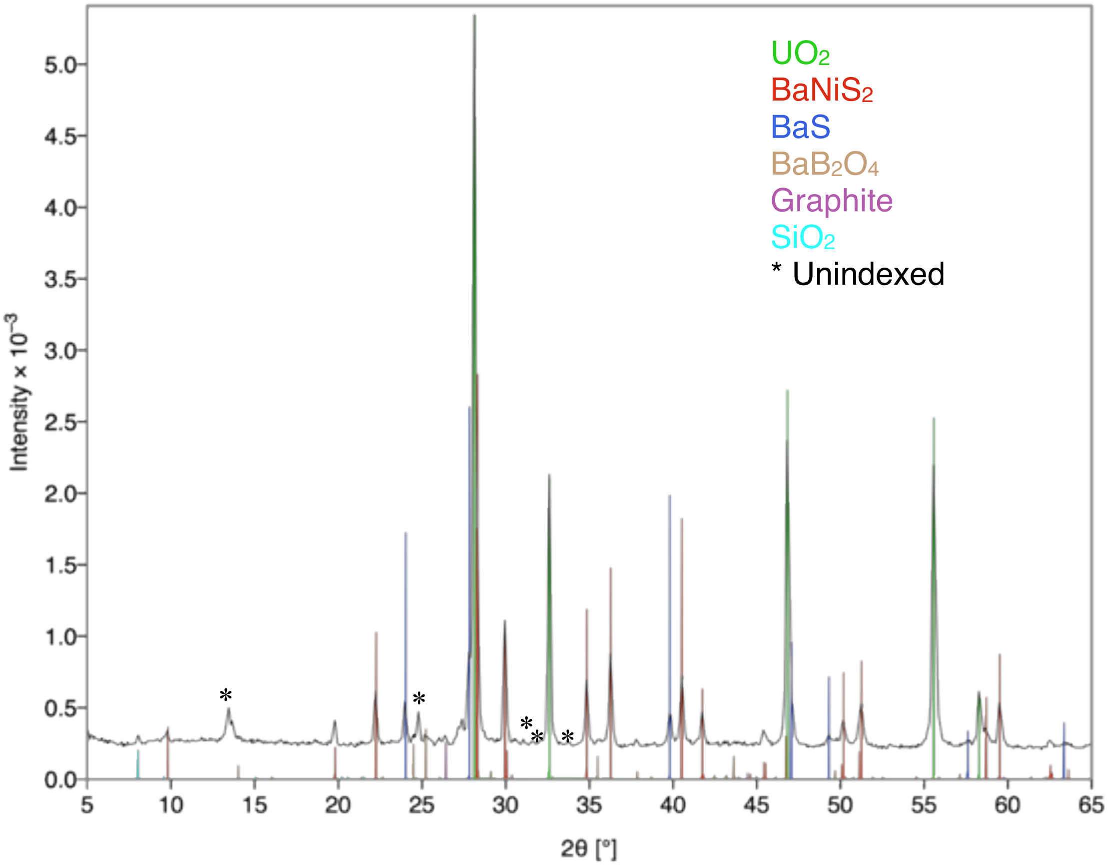

Figure 5.15 PXRD pattern of reaction Ni-C.

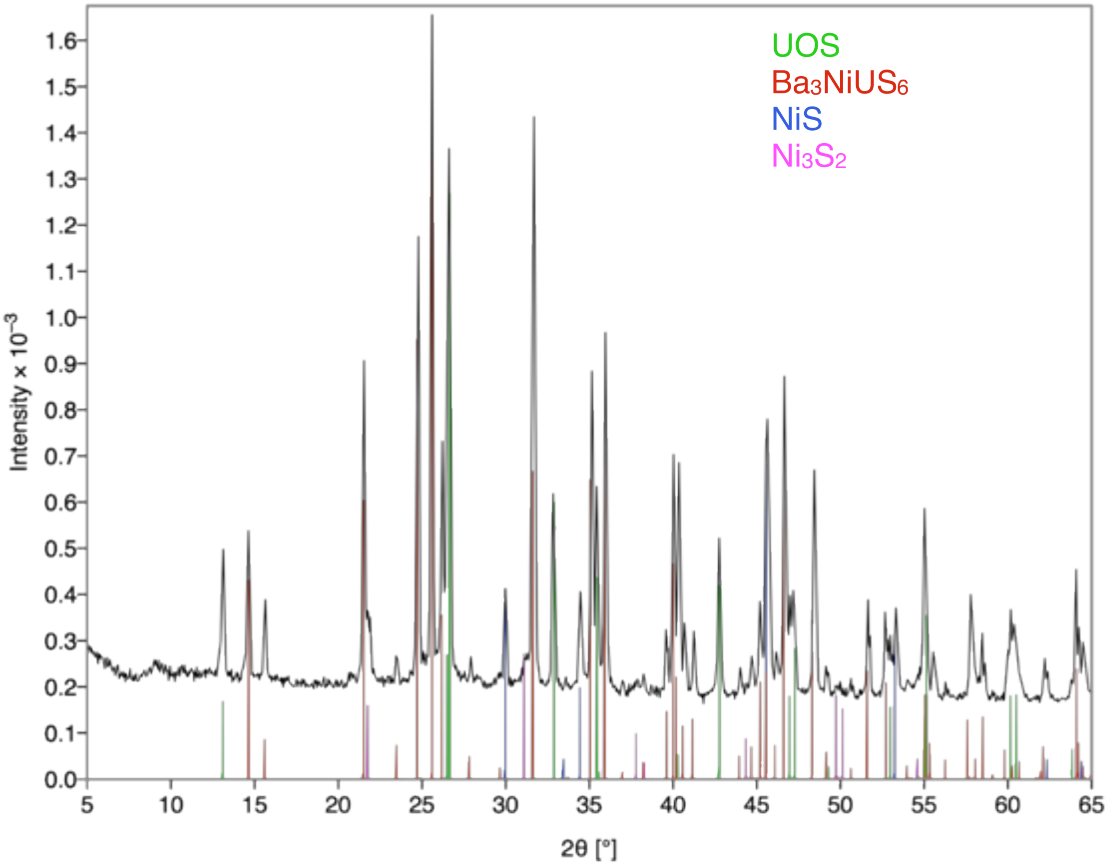

Figure 5.16 PXRD pattern of reaction Ni-D.

For reactions incorporating a 0:0 or 2:3 molar ratio of boron:sulfur, the main products were ternary barium transition metal sulfides and UO_2. For M = Zn and Co, single crystals of Ba_2MS_3 (M = Co, Zn) were formed and the presence of a minor amount of $Ba_6Co_{25}S_{27}$ could also be identified in the PXRD pattern of the cobalt reaction, Figure 5.17 a. The only ternary phase formed in the nickel containing reactions was $Ba_6Ni_{25}S_{27}$. A major difference between the structures of Ba_2MS_3 and $Ba_6M_{25}S_{27}$ are the metal polyhedra, tetrahedra and octahedra, that are present, respectively, in Ba_2MS_3 and $Ba_6M_{25}S_{27}$. Ni(II) does not commonly take on a tetrahedral geometry, which is a likely reason why the nickel analogue of Ba_2MS_3 was never formed.[219] Notably, the formation of single crystals of Ba_2CoS_3 in our reactions represents the first single crystal growth of this compound.

In the reactions targeting cobalt containing compounds, the 1:4:6 ratio of Ba_2MUO_6:B:S resulted in the formation of single crystals of $Ba_6Co_6U_{0.91}S_{13.5}O_{0.5}$ along with USO and some minor impurities, Figure 5.17 b. The use of additional boron and sulfur resulted in the full sulfur for oxygen replacement in Ba_2CoUO_6, forming a new 2H perovskite related structure, Ba_3CoUS_6, the crystal structure and properties of which will be published elsewhere, Figure 5.17 c. The zinc containing reactions required a higher ratio of boron and sulfur to form $Ba_{5.47}K_{0.53}Zn_6US_{13.5}O_{0.5}$ but did not form an analogous 2H perovskite related structure. A reaction in which the boron:sulfur ratio was increased to 12:15 resulted in the formation of USO, $BaUS_3$, ZnS, and $Ba_{5.47}K_{0.53}Zn_6US_{13.5}O_{0.5}$. The evolution of pure sulfides in this reaction product, but the lack of a 2H perovskite related structure, suggests that the analogous zinc containing 2H perovskite related structure is most likely not stable and/or is not as stable as the oxysulfide which causes $Ba_{5.47}K_{0.53}Zn_6US_{13.5}O_{0.5}$ to persist in the reaction products even with an increasing amount of sulfur and boron. Furthermore, in reactions involving nickel, no quaternary oxysulfide could be identified in any of the reaction products, but rather a new nickel 2H perovskite related structure, Ba_3NiUS_6, dominated the reaction products. Just as in the case of the ternary barium transition metal sulfides, the transition metal polyhedra in the oxysulfide compositions are tetrahedra while those in the 2H perovskite related structures are octahedra. Therefore, the formation of the oxysulfides in the M = Co and Zn reactions, and the lack thereof in the M = Ni reaction, corroborates the previous observations of the metal coordination preference of the different transition metals.

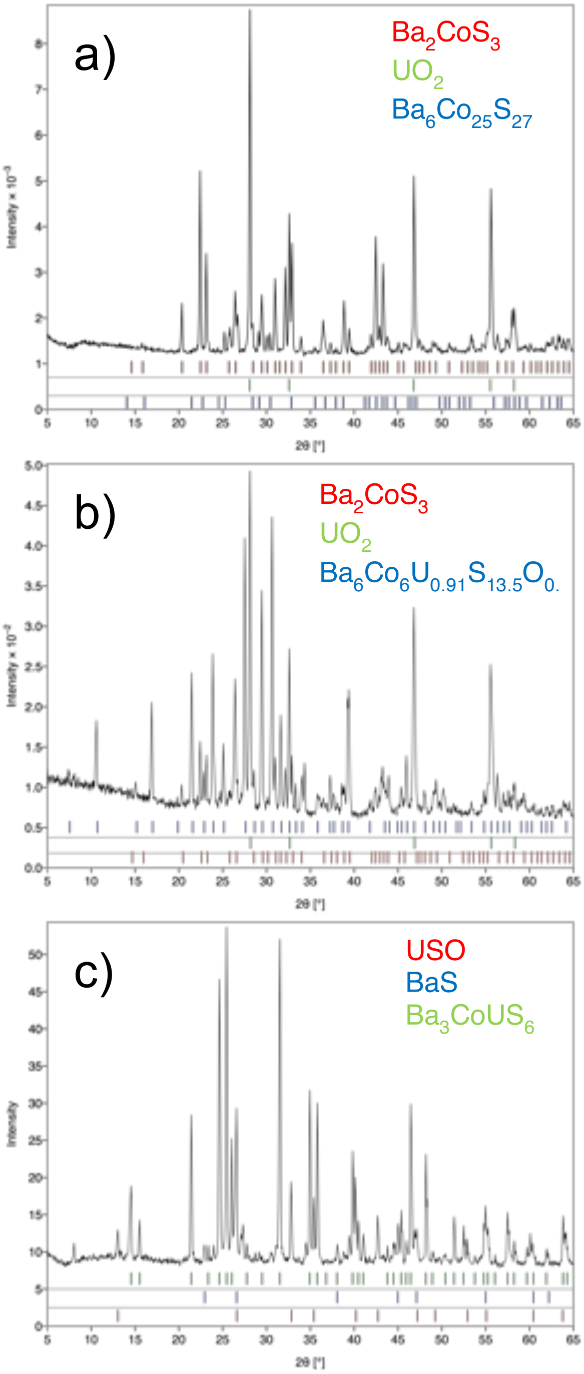

Figure 5.17 Diffraction patterns (black lines) of (a) reaction Co-A, (b) reaction Co-C, and (c) reaction Co-D, showing with the calculated patterns for the respective major products (colored lines). The PXRDs with all indexable products can be found in the supporting information. The PXRD of Reaction Co-B was identical to that of Co-A but without the inclusion of any $Ba_6Co_{25}S_{27}$ in the diffraction pattern.

Also, the formation of the $Ba_6M_{25}S_{27}$ phase is observed in only the cobalt and nickel reactions in which the metals are in an octahedral geometry. This can explain why the 2H perovskite related structures were found in the nickel and cobalt reactions but not in those involving zinc.

Reactions targeting $Ba_{5.47}K_{0.53}Zn_6US_{13.5}O_{0.5}$ without the use of K_2S, but with KCl, did not result in the oxysulfide product but rather just in USO, BaS, and ZnS. It is known that K_2S can be used as a reactive flux[220] and is most likely the reason why $Ba_{5.47}K_{0.53}Zn_6US_{13.5}O_{0.5}$, which has the split barium/potassium site in the structure, would not form without a K_2S addition. In contrast, $Ba_6Co_6U_{0.91}S_{13.5}O_{0.5}$ was originally identified in a reaction targeting the 2H perovskite related structure, a reaction that only involved CsCl as the flux, suggesting that K_2S in this reaction acted only as a component of the flux.

Crystal Structure Description. $Ba_6Co_6U_{0.91}S_{13.5}O_{0.5}$ and $Ba_{5.47}K_{0.53}Zn_6US_{13.5}O_{0.5}$ are isostructural and crystallize in the tetragonal crystal system adopting the space group *I*4/*mcm*. Their crystal structure is shown in Figure 2.

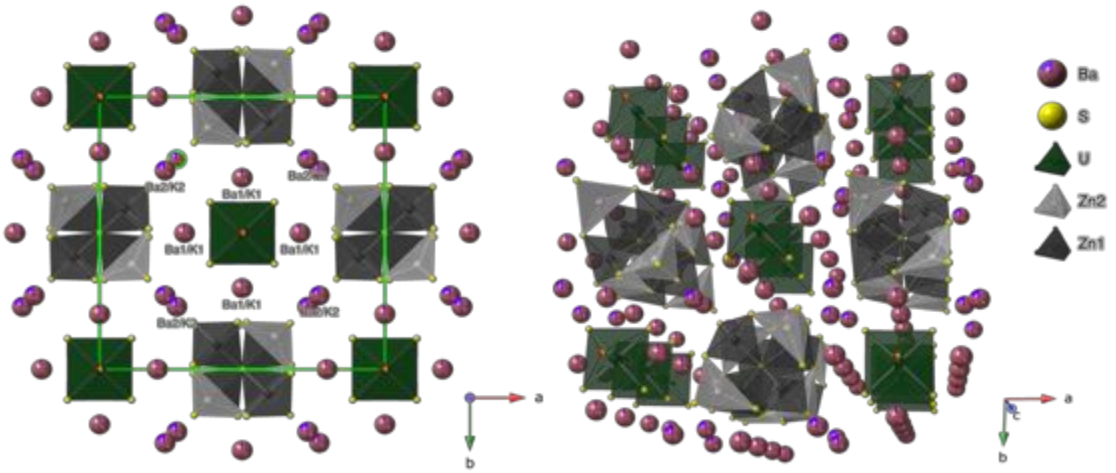

Figure 5.18 Two representations of the $Ba_{5.47}K_{0.53}Zn_6US_{13.5}O_{0.5}$ structure. Left: looking down from the top with the unit cell shown; right: tilted structure emphasizing the barium cations surrounding the infinite chains of polyhedra.

The structures of $Ba_6Co_6U_{0.91}S_{13.5}O_{0.5}$ and $Ba_{5.47}K_{0.53}Zn_6US_{13.5}O_{0.5}$ are composed of two crystallographically unique MS$_4$ tetrahedra (M = Co, Zn) and one crystallographically unique uranium US_5O octahedron, Figure 3a-c. The M(1)S$_4$ tetrahedra edge share through the S(2) atoms to create M(1)$_2$S$_6$ dimers, Figure 3d. Each dimer corner shares through two S(4) atoms with another dimer to create a M(1)$_4$S$_{10}$ tetramer. These two dimers are further connected through the M(2)S$_4$ tetrahedra that corner share with the S(3) atoms of the two dimers, Figure 3e. This combination of tetrahedra creates the main building block. The building blocks are connected above and below both through the S(2) atoms between the M(2)S$_4$ tetrahedra and M(1)$_2$S$_6$ dimers, with each building block being rotated 90 º. The building blocks are then further connected through the corner sharing of two tetramers through the S(4) atom.

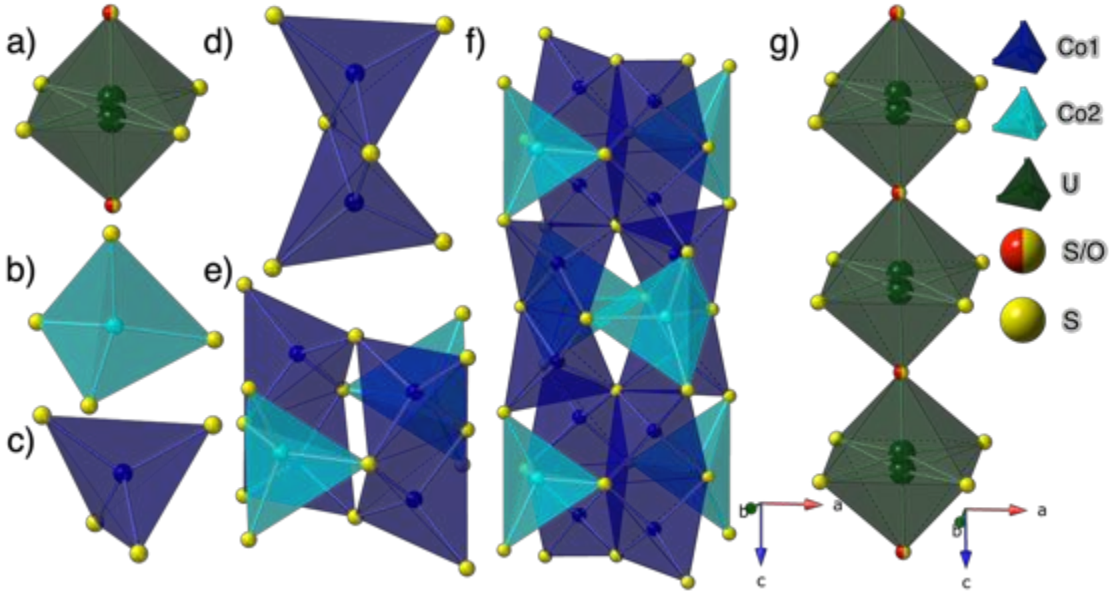

Figure 5.19 An image showing the (a) US_5O octahedron, (b) $M(2)S_4$, and (c) $M(1)S_4$ structural building blocks (M = Co, Zn), (d) the $M(1)_2S_6$ dimer, (e) the transition metal tetrahedra building block, (f) the stacking of these building blocks, and (g) the stacking of the US_5O infinite chains.

The stacking of these building blocks creates infinite columns of transition metal tetrahedra that run down the c-axis at ½ a and ½ b of the unit cell, Figure 3f. The US_5O octahedra trans corner share through the split S/O atoms, Figure 3g, forming infinite chains down the c-axis on the corners and in the center of the unit cell, Figure 2.

The uranium in the center of the octahedron is disordered across a mirror plane created by the four equatorial S(1) atoms, Figure 4. The splitting is due to the U-O bond lengths being shorter than the U-S bond lengths, which pulls the uranium closer to the oxygen and thus out of the center of the octahedron, a phenomenon previously observed in the $Ba_7M_2US_{12}O_{0.5}$ family of compounds.[217, 218] For $Ba_6Co_6U_{0.91}S_{13.5}O_{0.5}$, the split uranium position in the center of the octahedra was restrained to sum to 1, which resulted in an elongated displacement ellipsoid and a large residual electron density hole on the site.

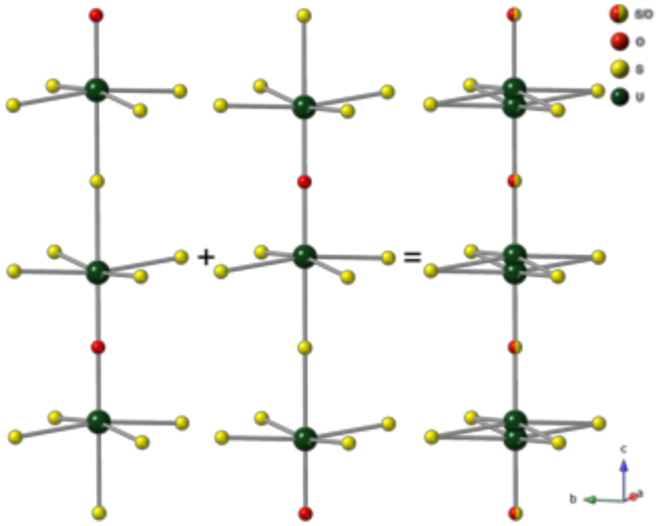

Figure 5.20 A schematic of the two possible uranium positions in the US_5O infinite chains (left and middle) and their superposition (right).

Through exhaustive refinements of the uranium site occupation factor, it was determined that a site occupation of 0.4561(1) for uranium represented the best model of this structure with the most plausible interpretation of this phenomenon being a small vacancy on the site as the other possible atomic impurities on the site (Ba, Co, K from the flux) would result in unreasonable interatomic distances to the surrounding sulfur and oxygen atoms. In $Ba_{5.47}K_{0.53}Zn_6US_{13.5}O_{0.5}$, on the other hand, the uranium site occupancies refined to 0.501(2), suggesting full occupancy of the octahedra. All transition metal sites in both compounds showed no deviation from full occupancy. The barium cations in $Ba_6Co_6U_{0.91}S_{13.5}O_{0.5}$ are ordered and exist in the spaces between the infinite chains of uranium octahedra and tetrahedra. The barium cations in $Ba_{5.47}K_{0.53}Zn_6US_{13.5}O_{0.5}$ are in the same locations as in the cobalt case, but are split Ba/K sites with occupancies of 0.961(3)/0.039(3) for Ba(1)/K(1) and 0.813(4)/0.187(4) for Ba(2)/K(2).

In $Ba_6Co_6U_{0.91}S_{13.5}O_{0.5}$, the U-S distances range from 2.6474(6) Å to 2.7002(15) Å, the U-O distance is 2.1670(6) Å, and the Co-S distances range from 2.2486(8) Å to

2.3383(16) Å. In $Ba_{5.47}K_{0.53}Zn_6US_{13.5}O_{0.5}$, the U-S distances range from 2.6519(14) Å to 2.6922(6) Å, the U-O distance is 2.1985(6) Å, and the Zn-S distances range from 2.3006(6) Å to 2.3828(15) Å. The U-S distances are typical for uranium in an octahedral, sulfide, coordination such as those in $Ba_2Cu_2US_5$ of 2.673(2) Å to 2.770(1) Å[221], $BaUS_3$ of 2.668(1) Å to 2.696(1) Å[121], and Li_2US_3 of 2.603 Å to 2.677 Å[222]. The uranium-ligand distance in the US_5O octahedra reported here are similar to those found in $Ba_7UTi_2S_{12.5}O_{0.5}$ of 2.648(1) Å to 2.667(2) Å and $Ba_7USi_{1.7}Fe_{0.3}S_{12.5}O_{0.5}$ of 2.604(1) Å to 2.690(1) Å.[218] The U-O distances present in the title compounds can be compared to those in UP_4O_{12} of 2.136 Å[223] and V_2UO_6 of 2.166 Å.[224] The Co-S bonds in the MS_4 tetrahedra are similar to those of 2.282 Å in $BaCoLa_2S_5$[225], and the Zn-S bonds are similar to those of 2.328 Å to 2.451 Å in Ba_2ZnS_3.[226] The $M(1)_2S_6$ dimers have M-M distances of 2.8620(16) Å for M = Co and 2.9537(13) Å for M = Zn. It is unlikely that bonding interactions are occurring between the metals especially due to Zn^{2+} being d^{10} in a tetrahedral environment, which lacks the available orbitals or electrons for bonding interactions. This suggests that the analogous cobalt containing dimers likely also do not have Co-Co bonding interactions.

While compositionally unique, $Ba_6Co_6U_{0.91}S_{13.5}O_{0.5}$ and $Ba_{5.47}K_{0.53}Zn_6US_{13.5}O_{0.5}$ share similar structures with the $Ba_7M_2US_{12.5}O_{0.5}$ family of compounds. Figure 5 shows a comparison of the two structures, which both contain uranium in US_5O trans corner sharing octahedra, and transition metal, MS_4, tetrahedra. The major difference between the two structures lies in the connectivity of the MS_4 tetrahedra. In the $Ba_7M_2US_{12.5}O_{0.5}$ structure, the MS_4 tetrahedra are isolated and are separated from each other by barium cations. In $Ba_6Co_6U_{0.91}S_{13.5}O_{0.5}$ and $Ba_{5.47}K_{0.53}Zn_6US_{13.5}O_{0.5}$ the similar MS_4 tetrahedra are connected through the M_4S_{10} tetramers and the barium is no longer present within the chain. The loss of the bariums and gain of the transition metal tetramers within the unit cell, leads to the difference in composition, $Ba_7M_2US_{12.5}O_{0.5}$ vs. $Ba_6Co_6U_{0.91}S_{13.5}O_{0.5}$.

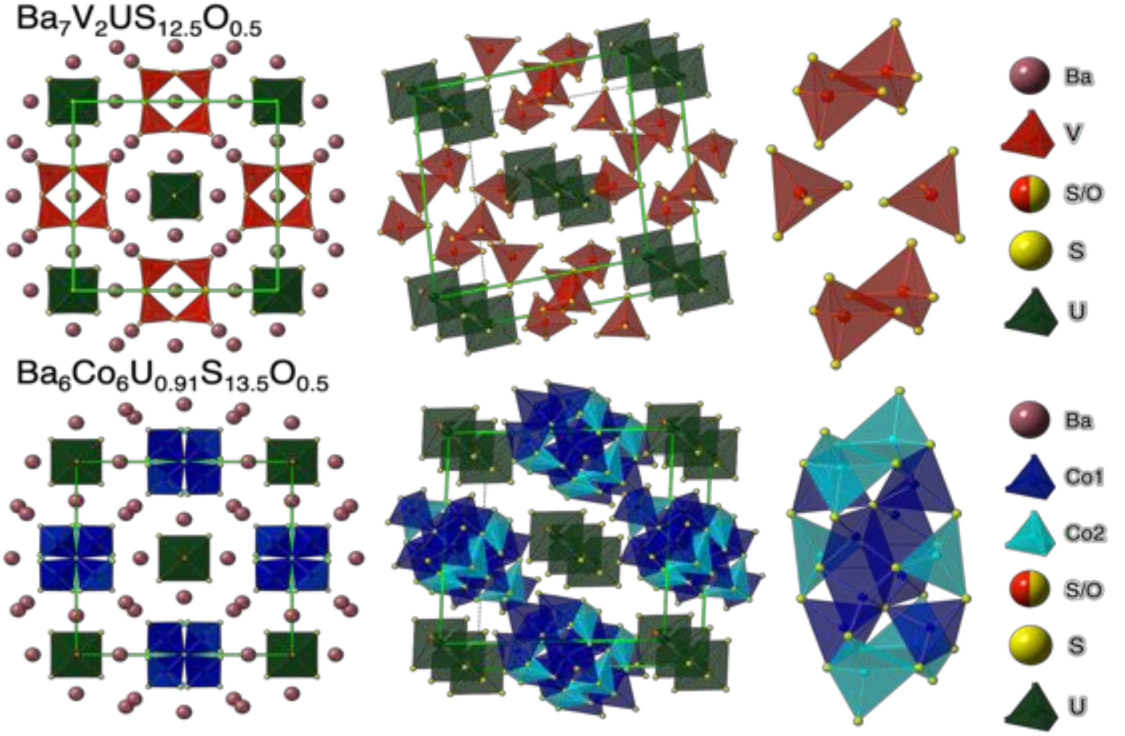

Figure 5.21 A comparison of the $Ba_7M_2US_{12.5}O_{0.5}$ structure with that of the compounds reported herein.

Oxidation States. In both oxysulfide compounds reported herein, the structures do not contain any S—S or O—O bonds. Assuming that uranium is in its +4 oxidation state, as it is found in a majority of uranium chalcogenides[2, 40], and that the transition metals are in their +2 oxidation states, the compositional formulas will not charge balance resulting in a residual negative charge. For $Ba_{5.47}K_{0.53}Zn_6US_{13.5}O_{0.5}$, an oxidation state assignment of +2/Ba, +1/K, +2/Zn, +4/U, -2/S, and -2/O leaves a -0.53 charge unaccounted for. The same situation is true for $Ba_6Co_6U_{0.91}S_{13.5}O_{0.5}$ for which an oxidation state assignment of +2/Ba, +2/Co, +4/U, -2/S, and -2/O results in -0.36 of unaccounted charge. In $Ba_{5.47}K_{0.53}Zn_6US_{13.5}O_{0.5}$, this left-over charge can only be accounted for by uranium which is the only ion in this structure with multiple accessible oxidation states, as barium and zinc only have a +2 oxidation state. In the case of $Ba_6Co_6U_{0.91}S_{13.5}O_{0.5}$ though, cobalt does have an accessible +3 oxidation state, but this oxidation state is not common in chalcogenide materials due to the softer Lewis basicity of the chalcogens which many times prefers lower oxidation states.[227-231] Furthermore, cobalt (III) is not commonly found in a tetrahedral geometry such as in barium cobalt sulfide, Ba_2CoS_3[232], as well as in cobalt oxides, such as $ZnCo_2O_4$ and Co_3O_4, which contain cobalt (II) in a tetrahedral geometry and cobalt (III) in an octahedral geometry.[233] Other compounds, such as $Ba_5Bi_2Co_2S_{10}$[234], that incorporate cobalt tetrahedra with very similar structural connectivity also assign cobalt a +2 oxidation state, giving us confidence in the assignment of cobalt (II) in $Ba_6Co_6U_{0.91}S_{13.5}O_{0.5}$.

Calculating the expected uranium oxidation states based on the chemical compositions and utilizing the above oxidation state assignment for all elements excluding uranium results in a uranium oxidation state of +4.5 for $Ba_{5.47}K_{0.53}Zn_6US_{13.5}O_{0.5}$ and +4.4 for $Ba_6Co_6U_{0.91}S_{13.5}O_{0.5}$ suggesting mixed valent uranium (IV/V). Bond valence sum calculations (BVS) were performed on the uranium octahedra for each compound, Table 5.4, which resulted in a calculated oxidation state of +4.5 for $Ba_6Co_6U_{0.91}S_{13.5}O_{0.5}$ and +4.3 $Ba_6Co_6U_{0.91}S_{13.5}O_{0.5}$ further supporting the stabilization of uranium (IV/V) in these compounds. The occurrence of mixed valent uranium (IV/V) is also observed in $Ba_7USi_{1.7}Fe_{0.3}S_{12.5}O_{0.5}$.[218]

Table 5.4 Bond Valence Sums (BVS) were performed on the title compounds. The U—S distances are tabulated below along with the calculated uranium oxidation state. The R_0 value for the U—S distances used in the calculations is 2.550 Å with a B-value of 0.37. The R_0 value for the U—O distances used in the calculations is 2.112 Å with a B-value of 0.37. The calculated uranium oxidation states suggest mixed valent U (IV/V) is present within these compounds.

Composition	U—S bond distance, Å		U—O bond distance, Å	Calculated U oxidation states
$Ba_{5.47}K_{0.53}Zn_6US_{13.50}O_{0.50}$	2.65	2.69	2.20	4.51
$Ba_6Co_6U_{0.91}S_{13.50}O_{0.50}$	2.70	2.65	2.17	4.30

Conclusions: The crystal growth of two new uranium (IV/V) compounds, $Ba_{5.47}K_{0.53}Zn_6US_{13.5}O_{0.5}$ and $Ba_6Co_6U_{0.91}S_{13.5}O_{0.5}$, demonstrates that the BCM method can indeed be used to target uranium mixed anion compounds. Furthermore, the combination of the BCM method with the molten flux crystal growth approach resulted in single crystals that enable the facile structural characterization of the products by SXRD. Trends in the metal coordination preferences and concomitant compositions and structures were observed while targeting new oxysulfide compositions. These observations can be used when targeting additional compositions or explaining the outcomes of reactions with different metal incorporations. Although only two examples of uranium oxysulfides are reported herein, it is nonetheless clear that the BCM method can readily be used for the synthesis of additional transition and actinide metal oxysulfide compounds.

Acknowledgements. Research supported by the US Department of Energy, Office of Basic Energy Sciences, Division of Materials Sciences and Engineering under award DE-SC0018739.

REFERENCES

(1) Kovnir, K., Predictive Synthesis. *Chem. Mater.,* **2021**, *33*, 4835-4841.

(2) Bugaris, D. E.; Ibers, J. A., Syntheses and characterization of some solid-state actinide (Th, U, Np) compounds. *Dalton Trans,* **2010**, *39*, 5949-5964.

(3) Juillerat, C. A.; Klepov, V. V.; Morrison, G.; Pace, K. A.; zur Loye, H.-C., Flux crystal growth: a versatile technique to reveal the crystal chemistry of complex uranium oxides. *Dalton Trans.,* **2019**, *48*, 3162-3181.

(4) Kanatzidis, M. G., Discovery-Synthesis, Design, and Prediction of Chalcogenide Phases. *Inorg. Chem.,* **2017**, *56*, 3158-3173.

(5) Kamaya, N.; Homma, K.; Yamakawa, Y.; Hirayama, M.; Kanno, R.; Yonemura, M.; Kamiyama, T.; Kato, Y.; Hama, S.; Kawamoto, K.; Mitsui, A., A lithium superionic conductor. *Nat. Mater.,* **2011**, *10*, 682-686.

(6) Kanno, R.; Murayama, M., Lithium Ionic Conductor Thio-LISICON: The Li_2S-GeS_2-P_2S_5 System. *J. Electrochem. Soc.,* **2001**, *148*, A742.

(7) Bernevig, B. A.; Hughes, T. L.; Zhang, S. C., Quantum spin Hall effect and topological phase transition in HgTe quantum wells. *Science,* **2006**, *314*, 1757-1761.

(8) Cava, R. J., Chemists join in. *Nat. Mater.,* **2013**, *12*, 379-380.

(9) Zhang, H.; Liu, C.-X.; Qi, X.-L.; Dai, X.; Fang, Z.; Zhang, S.-C., Topological insulators in Bi_2Se_3, Bi_2Te_3 and Sb_2Te_3 with a single Dirac cone on the surface. *Nat. Phys.,* **2009**, *5*, 438-442.

(10) Iwanczyk, J. S.; Nygård, E.; Meirav, O.; Arenson, J.; Barber, W. C.; Hartsough, N. E.; Malakhov, N.; Wessel, J. C., Photon Counting Energy Dispersive Detector Arrays for X-ray Imaging. *IEEE Trans. Nucl. Sci.,* **2009**, *56*, 535-542.

(11) Rogalski, A., HgCdTe infrared detector material: history, status and outlook. *Rep. Prog. Phys.,* **2005**, *68*, 2267-2336.

(12) Watanabe, S.; Ishikawa, S.-n.; Aono, H.; Takeda, S.; Odaka, H.; Kokubun, M.; Takahashi, T.; Nakazawa, K.; Tajima, H.; Onishi, M.; Kuroda, Y., High Energy Resolution Hard X-Ray and Gamma-Ray Imagers Using CdTe Diode Devices. *IEEE Trans. Nucl. Sci.,* **2009**, *56*, 777-782.

(13) Bera, T. K.; Jang, J. I.; Ketterson, J. B.; Kanatzidis, M. G., Strong second harmonic generation from the tantalum thioarsenates $A_3Ta_2AsS_{11}$ (A = K and Rb). *J. Am. Chem. Soc.,* **2009**, *131*, 75-77.

(14) Bera, T. K.; Jang, J. I.; Song, J. H.; Malliakas, C. D.; Freeman, A. J.; Ketterson, J. B.; Kanatzidis, M. G., Soluble semiconductors $AAsSe_2$ (A = Li, Na) with a direct-band-gap and strong second harmonic generation: a combined experimental and theoretical study. *J. Am. Chem. Soc.,* **2010**, *132*, 3484-3495.

(15) Lekse, J. W.; Moreau, M. A.; McNerny, K. L.; Yeon, J.; Halasyamani, P. S.; Aitken, J. A., Second-harmonic generation and crystal structure of the diamond-like semiconductors Li_2CdGeS_4 and Li_2CdSnS_4. *Inorg. Chem.,* **2009**, *48*, 7516-7518.

(16) Babo, J. M.; Choi, E. S.; Albrecht-Schmitt, T. E., Synthesis, structure, magnetism, and optical properties of $Cs_2Cu_3DyTe_4$. *Inorg. Chem.,* **2012**, *51*, 11730-11735.

(17) Caron, J. M.; Neilson, J. R.; Miller, D. C.; Llobet, A.; McQueen, T. M., Iron displacements and magnetoelastic coupling in the antiferromagnetic spin-ladder compound $BaFe_2Se_3$. *Phys. Rev. B,* **2011**, *84*, 180409(R).

(18) Luo, Q.; Nicholson, A.; Rincón, J.; Liang, S.; Riera, J.; Alvarez, G.; Wang, L.; Ku, W.; Samolyuk, G. D.; Moreo, A.; Dagotto, E., Magnetic states of the two-leg-ladder alkali metal iron selenides AFe_2Se_3. *Phys. Rev. B,* **2013**, *87*, 024404.

(19) Cho, Y. W.; Choi, S. K.; Vysochanskii, Y. M., Photovoltaic effect of $Sn_2P_2S_6$ ferroelectric crystal and ceramics. *J. Mater. Res.,* **2001**, *16*, 3317-3322.

(20) Grabar, A. A.; Kedyk, I. V.; Gurzan, M. I.; Stoika, I. M.; Molnar, A. A.; Vysochanskii, Y. M., Enhanced photorefractive properties of modified $Sn_2P_2S_6$. *Opt. Commun.,* **2001**, *188*, 187-194.

(21) Haertle, D.; Caimi, G.; Haldi, A.; Montemezzani, G.; Günter, P.; Grabar, A. A.; Stoika, I. M.; Vysochanskii, Y. M., Electro-optical properties of $Sn_2P_2S_6$. *Opt. Commun.,* **2003**, *215*, 333-343.

(22) Yum, H. N.; Salit, M.; Pati, G. S.; Tseng, S.; Hemmer, P. R.; Shahriar, M. S., Fast-light in a photorefractive crystal for gravitational wave detection. *Opt. Express,* **2008**, *16*, 20448-20456.

(23) Lacroix, P. G.; Clément, R.; Nakatani, K.; Zyss, J.; Ledoux, I., Stilbazolium-MPS$_3$ Nanocomposites with Large Second-Order Optical Nonlinearity and Permanent Magnetization. *Science,* **1994**, *263*, 658-660.

(24) Ressouche, E.; Loire, M.; Simonet, V.; Ballou, R.; Stunault, A.; Wildes, A., Magnetoelectric MnPS$_3$ as a candidate for ferrotoroidicity. *Phys. Rev. B,* **2010**, *82*,

(25) Gauthier, G.; Jobic, S.; Boucher, F.; Macaudière, P.; Huguenin, D.; Rouxel, J.; Brec, R., CePS$_4$ Electronic Structure and Optical Properties. *Chem. Mater.,* **1998**, *10*, 2341-2347.

(26) Gauthier, G.; Klur, Y.; Pourpoint, A.; Jobic, S.; Ouvrard, G.; Brec, R.; Huguenin, D.; Macaudière, P., Absence of chromatic effect: crystal relaxation around Ce^{III} in $Y_{1-x}Ce_xPS_4$ ($0 \leq x \leq 1$). *Int. J. of Inorg. Mater.,* **2000**, *2*, 717-722.

(27) Klepov, V. V.; Pace, K. A.; Breton, L. S.; Kocevski, V.; Besmann, T. M.; zur Loye, H.-C., Nearly Identical but Not Isotypic: Influence of Lanthanide Contraction on $Cs_2NaLn(PS_4)_2$ (Ln = La-Nd, Sm, and Gd-Ho). *Inorg. Chem.,* **2020**, *59*, 1905-1916.

(28) Breton, L. S.; Smith, M. D.; zur Loye, H.-C., Trends in rare earth thiophosphate syntheses: $Rb_3Ln(PS_4)_2$ (Ln = La, Ce, Pr), $Rb_{3-x}Na_xLn(PS_4)_2$ (Ln = Ce, Pr; x = 0.50, 0.55), and RbEuPS$_4$ obtained by molten flux crystal growth. *CrystEngComm,* **2021**, *23*, 5241-5248.

(29) Lian, Y. K.; Wu, L.-M.; Chen, L., Thioborates: potential nonlinear optical materials with rich structural chemistry. *Dalton Trans.,* **2017**, *46*, 4134-4147.

(30) Pestov, D.; Wang, X.; Ariunbold, G. O.; Murawski, R. K.; Sautenkov, V. A.; Dogariu, A.; Sokolov, A. V.; Scully, M. O., Single-shot detection of bacterial endospores via coherent Raman spectroscopy. *Proc. Natl. Acad. Sci. U. S. A.,* **2008**, *105*, 422-427.

(31) Pushkarsky, M.; Tsekoun, A.; Dunayevskiy, I. G.; Go, R.; Patel, C. K., Sub-parts-per-billion level detection of NO$_2$ using room-temperature quantum cascade lasers. *Proc. Natl. Acad. Sci. U. S. A.,* **2006**, *103*, 10846-10849.

(32) Pushkarsky, M. B.; Dunayevskiy, I. G.; Prasanna, M.; Tsekoun, A. G.; Go, R.; Patel, C. K., High-sensitivity detection of TNT. *Proc. Natl. Acad. Sci. U. S. A.,* **2006**, *103*, 19630-19634.

(33) Chung, I.; Kanatzidis, M. G., Metal Chalcogenides: A Rich Source of Nonlinear Optical Materials. *Chem. Mater.,* **2014**, *26*, 849-869.

(34) Li, H.; Li, G.; Wu, K.; Zhang, B.; Yang, Z.; Pan, S., BaB$_2$S$_4$: An Efficient and Air-Stable Thioborate as Infrared Nonlinear Optical Material with High Laser Damage Threshold. *Chem. Mater.,* **2018**, *30*, 7428-7432.

(35) Breton, L. S.; Morrison, G.; Lacroix, M. R.; Halasyamani, P. S.; zur Loye, H.-C., Lanthanide thioborates, an emerging class of nonlinear optical materials, efficiently synthesized using the boron-chalcogen mixture method. *Chem. Commun.,* **2022**, *58*, 7992-7995.

(36) Kindra, D. R.; Evans, W. J., Magnetic Susceptibility of Uranium Complexes. *Chem. Rev.,* **2014**, *114*, 8865-8882.

(37) Klepov, V. V.; zur Loye, H.-C., Complex Topologies from Simple Building Blocks: Uranium(IV) Thiophosphates. *Inorg. Chem.,* **2018**, *57*, 11175-11183.

(38) Bamberger, C. E.; Haire, R. G.; Begun, G. M.; Hellwege, H. E., The synthesis and characterization of crystalline phosphates of thorium, uranium and neptunium. *J. Less-Common Met.,* **1984**, *102*, 179-186.

(39) Usman, M.; Morrison, G.; Klepov, V. V.; Smith, M. D.; zur Loye, H.-C., Flux crystal growth, structure, magnetic and optical properties of a family of alkali uranium(IV) phosphates. *J. Solid State Chem.,* **2019**, *270*, 19-26.

(40) Narducci, A. A.; Ibers, J. A., Ternary and Quaternary Uranium and Thorium Chalcogenides. *Chem. Mater.,* **1998**, *10*, 2811-2823.

(41) Cody, J. A.; Mansuetto, M. F.; Pell, M. A.; Chien, S.; Ibers, J. A., New one-dimensional ternary and quaternary cesium-metal-tellurium compounds. *J. Alloys Compd.,* **1995**, *219*, 59-62.

(42) Kanatzidis, M. G.; Sutorik, A. C. The Application of Polychalcogenide Salts to the Exploratory Synthesis of Solid State Multinary Chalcogenides at Intermediate Temperatures. *Progress in Inorganic Chemistry*; John Wiley & Sons, Inc., **2007**; 151-265.

(43) Breton, L. S.; Klepov, V. V.; zur Loye, H.-C., Facile Oxide to Chalcogenide Conversion for Actinides Using the Boron-Chalcogen Mixture Method. *J. Am. Chem. Soc.,* **2020**, *142*, 14365-14373.

(44) Breton, L. S.; Baumbach, R.; Tisdale, H. B.; zur Loye, H.-C., Structures and Magnetic Properties of $K_2Pd_4U_6S_{17}$, $K_2Pt_4U_6S_{17}$, $Rb_2Pt_4U_6S_{17}$, and $Cs_2Pt_4U_6S_{17}$ Synthesized Using the Boron-Chalcogen Mixture Method. *Inorg. Chem.,* **2022**, *61*, 10502-10508.

(45) Boltersdorf, J.; King, N.; Maggard, P. A., Flux-mediated crystal growth of metal oxides: synthetic tunability of particle morphologies, sizes, and surface features for photocatalysis research. *CrystEngComm,* **2015**, *17*, 2225-2241.

(46) Habermehl, K.; Mudring, A.-V.; Meyer, G., The Last of the Five: the Elusive "Tantalum(III) Bromide", a Perovskite-Related Salt, $[Ta_6Br_{12}]Br_3[TaBr_6]_{0.86}$. *Eur. J. Inorg. Chem.,* **2010**, *26*, 4075-4078.

(47) Klepov, V. V.; Juillerat, C. A.; Pace, K. A.; Morrison, G.; zur Loye, H.-C., "Soft" Alkali Bromide and Iodide Fluxes for Crystal Growth. *Front. Chem.,* **2020**, *8*, 518.

(48) Ijjaali, I.; Mitchell, K.; Ibers, J. A., Preparation and structure of the light rare-earth copper selenides $LnCuSe_2$ (Ln=La, Ce, Pr, Nd, Sm). *J. Solid State Chem.,* **2004**, *177*, 760-764.

(49) Lissner, F.; Meyer, S. P.; Schleid, T., $CsTb_3STe_4$ und $CsTb_5S_2Te_6$: Zwei pseudo-ternäre Caesium-Terbium-Chalkogenide mit geordneten S^{2-}- und Te^{2-}-Anionen. *Z. Naturforsch. B,* **2019**, *74*, 99-107.

(50) Wang, Y.; Wu, J.; Tang, Y.; Lu, X.; Yang, C.; Qin, M.; Huang, F.; Li, X.; Zhang, X., Phase-controlled synthesis of cobalt sulfides for lithium ion batteries. *ACS Appl. Mater. Interfaces,* **2012**, *4*, 4246-4250.

(51) Yang, Y.; Ibers, J. A., Syntheses and Structures of the New Quaternary Compounds $Ba_4Nd_2Cd_3Se_{10}$ and $Ba_4Ln_2Cd_3S_{10}$ (Ln=Sm, Gd, Tb). *J. Solid State Chem.,* **2000**, *149*, 384-390.

(52) Do, J.; Lee, K.; Yun, H., Synthesis and Structures of New One-Dimensional $KTiPS_5$ and $RbTiPS_5$. *J. Solid State Chem.,* **1996**, *125*, 30-36.

(53) Dong, Y.; Kim, S.; Yun, H., A new thiophosphate, $Rb_{(0.38)}Ag_{(0.5)}Nb_2PS_{10}$. *Acta Cryst. C,* **2005**, *61*, i25-i26.

(54) Kwak, J.-E.; Yun, J.-S., Synthesis and Structure of a New Layered Thiophosphate, $K_{0.34}Cu_{0.5}Nb_2PS_{10}$. *Bull. Korean Chem. Soc.,* **2008**, *29*, 273-275.

(55) Komm, T.; Schleid, T., The first rubidium rare-earth(III) thiophosphates: $Rb_3M_3[PS_4]_4$ (M = Pr, Er). *J. Solid State Chem.,* **2005**, *178*, 454-463.

(56) Kutahyali Aslani, C.; Breton, L. S.; Klepov, V. V.; zur Loye, H.-C., A Series of Rb4*Ln*2(P2S6)(PS4)2 (Ln = La, Ce, Pr, Nd, Sm, Gd) Rare Earth Thiophosphates with Two Distinct Thiophosphate Units [PVS4]3- and [PIV2S6]4-. *Dalton Trans.,* **2021**, *50*, 1683-1689.

(57) Schoop, L. M.; Eger, R.; Nuss, J.; Pielnhofer, F.; Lotsch, B. V., The First Quinary Rare Earth Thiophosphates: $Cs_5Ln_3X_3(P_2S_6)_2(PS_4)$ (Ln= La, Ce,X= Br, Cl) and the Quasi-Quaternary $Cs_{10}Y_4Cl_{10}(P_2S_6)_3$. *Z. Anorg. Allg. Chem.,* **2017**, *643*, 1818-1823.

(58) Usman, M.; Smith, M. D.; Klepov, V.; zur Loye, H.-C., One-Dimensional Quaternary and Penternary Alkali Rare Earth Thiophosphates Obtained via Alkali Halide Flux Crystal Growth. *Cryst. Growth Des.,* **2019**, *19*, 5648-5657.

(59) Schlem, R.; Till, P.; Weiss, M.; Krauskopf, T.; Culver, S. P.; Zeier, W. G., Ionic Conductivity of the NASICON-Related Thiophosphate $Na_{1+x}Ti_{2-x}Ga_x(PS_4)_3$. *Chem. Eur. J.,* **2019**, *25*, 4143-4148.

(60) Tachez, M.; Malugani, J.-P.; Mercier, R.; Robert, G., Ionic conductivity of and phase transition in lithium thiophosphate Li_3PS_4. *Solid State Ion.,* **1984**, *14*, 181-185.

(61) Kang, L.; Zhou, M.; Yao, J.; Lin, Z.; Wu, Y.; Chen, C., Metal Thiophosphates with Good Mid-infrared Nonlinear Optical Performances: A First-Principles Prediction and Analysis. *J. Am. Chem. Soc.,* **2015**, *137*, 13049-13059.

(62) Li, Z.; Jiang, X.; Zhou, M.; Guo, Y.; Luo, X.; Wu, Y.; Lin, Z.; Yao, J., $Zn_3P_2S_8$: A Promising Infrared Nonlinear-Optical Material with Excellent Overall Properties. *Inorg. Chem.,* **2018**, *57*, 10503-10506.

(63) Goh, E.-Y.; Kim, E.-J.; Kim, S.-J., Structure Modification on Quaternary Rare Earth Thiophosphates: $NaYbP_2S_6$, $NaSmP_2S_6$, and $KSmP_2S_7$. *J. Solid State Chem.,* **2001**, *160*, 195-204.

(64) Hess, R. F.; Gordon, P. L.; Tait, C. D.; Abney, K. D.; Dorhout, P. K., Synthesis and structural characterization of the first quaternary plutonium thiophosphates: $K_3Pu(PS_4)_2$ and $APuP_2S_7$ (A = K, Rb, Cs). *J. Am. Chem. Soc.,* **2002**, *124*, 1327-1333.

(65) Klawitter, Y.; Bensch, W.; Wickleder, C., Synthesis, Crystal Structure, and Vibrational and Optical Spectroscopy of the First Quaternary Alkaline-Earth Rare Earth Thiophosphates $Ba_3Ln_2[P_4S_{16}]$ (Ln = Gd−Er). *Chem. Mater.,* **2006**, *18*, 187-197.

(66) Komm, T.; Schleid, T., $Li_9Nd_2[PS_4]_5$: A new lithium lanthanoid(III) thiophosphate(V). *J. Alloy Comp.,* **2006**, *418*, 106-110.

(67) Komm, T.; Schleid, T., Drei Alkalimetall-Erbium-Thiophosphate: Von der Schichtstruktur bei $KEr[P_2S_7]$ zur dreidimensionalen Vernetzung in $NaEr[P_2S_6]$ und $Cs_3Er_5[PS_4]_6$. *Z. Anorg. Allg. Chem.,* **2006**, *632*, 42-48.

(68) Komm, T.; Strobel, S.; Schleid, T., Two potassium gadolinium(III) ortho-thiophosphates(V): $K_3Gd_3[PS_4]_4$ and $K_9Gd[PS_4]_4$. *J. Alloy Comp.,* **2008**, *451*, 648-653.

(69) Manriquez, V.; Galdamez, A.; Guzman-Aguila, D., New quaternary alkali metal, rare earth (3+) thiophosphate, $K_2SmP_2S_7$ with both $[P_2S_6]^{4-}$ and $[PS_4]^{3-}$ anions. *Mat. Res. Bull.,* **2008**, *43*, 2469-2475.

(70) Milot, S.; Wu, Y.; Nather, C.; Bensch, W.; Klepp, K. O., Two New Quaternary Thiophosphates with Pseudo One-dimensional Structures: Syntheses and Crystal Structures of $Cs_3Sm[PS_4]_2$ and $Rb_3Sm[PS_4]_2$. *Z. Anorg. Allg. Chem.,* **2008**, *634*, 1575-1580.

(71) Muller, C.; Jorgens, S.; Mewis, A., Neue Thiophosphate: Die Verbindungen $Li_6Ln_3(PS_4)_5$ (Ln: Y, Gd, Dy, Yb, Lu) und $Ag_3Y(PS_4)_2$. *Z. Anorg. Allg. Chem.,* **2007**, *633*, 1633-1638.

(72) Kuhn, A.; Eger, R.; Nuss, J.; Lotsch, B. V., Synthesis and Structural Characterization of the Alkali Thiophosphates $Na_2P_2S_6$, $Na_4P_2S_6$, $K_4P_2S_6$, and $Rb_4P_2S_6$. *Z. Anorg. Allg. Chem.,* **2014**, *640*, 689-692.

(73) Evenson, C. R.; Dorhout, P. K., Thiophosphate phase diagrams developed in conjunction with the synthesis of the new compounds $KLaP_2S_6$, $K_2La(P_2S_6)_{1/2}(PS_4)$, $K_3La(PS_4)_2$, $K_4La_{0.67}(PS_4)_2$, $K_{9-x}La_{1+x/3}(PS_4)_4$ (x = 0.5), $K_4Eu(PS_4)_2$, and $KEuPS_4$. *Inorg. Chem.,* **2001**, *40*, 2884-2891.

(74) Klepov, V. V.; Breton, L. S.; Pace, K. A.; Kocevski, V.; Besman, T. M.; zur Loye, H.-C., Size-Driven Stability of Lanthanide Thiophosphates Grown from an Iodide Flux. *Inorg. Chem.,* **2019**, *58*, 6565-6573.

(75) Schleid, T.; Hartenbach, I.; Komm, T., $K_2NdP_2S_7$: A Mixed-Valent Neodymium(III) Thiophosphate According to $K_4Nd_2[PS_4]_2[P_2S_6]$ with Discrete $[PS_4]^{3-}$and $[S_3P\text{-}PS_3]^{4-}$Anions. *Z. Anorg. Allg. Chem.,* **2002**, *628*, 7-9.

(76) Schoop, L. M.; Eger, R.; Kremer, R. K.; Kuhn, A.; Nuss, J.; Lotsch, B. V., Structural Stability Diagram of $ALnP_2S_6$ Compounds (A = Na, K, Rb, Cs; Ln = Lanthanide). *Inorg. Chem.,* **2017**, *56*, 1121-1131.

(77) Ohta, M.; Hirai, S.; Kato, H.; Sokolov, V. V.; Bakovets, V. V., Thermal Decomposition of NH_4SCN for Preparation of Ln_2S_3 (Ln=La and Gd) by Sulfurization. *Mater. Trans.,* **2009**, *50*, 1885-1889.

(78) *APEX3 Version 2019.1-0 and SAINT+ Version 8.40A.;* Bruker Nano, Inc., **2019.**

(79) Krause, L.; Herbst-Irmer, R.; Sheldrick, G. M.; Stalke, D., SADABS-2016/2. *J. Appl. Crystallogr.,* **2015**, *48*, 3-10.

(80) Sheldrick, G. M., SHELXT - integrated space-group and crystal-structure determination. *Acta Crystallogr. A,* **2015**, *71*, 3-8.

(81) Sheldrick, G. M., A short history of SHELX. *Acta Crystallogr. A,* **2008**, *64*, 112-122.

(82) Dolomanov, O. V.; Bourhis, L. J.; Gildea, R. J.; Howard, J. A. K.; Puschmann, H., OLEX2: a complete structure solution, refinement and analysis program. *J. Appl. Crystallogr.,* **2009**, *42*, 339-341.

(83) Peijzel, P. S., A complete energy level diagram for all trivalent lanthanide ions. *J. Solid State Chem.,* **2005**, *178*, 448-453.

(84) Lin, Y.-F.; Chang, Y. H.; Chang, Y.-S.; Tsai, B.-S.; Li, Y.-C., Luminescent Properties of Trivalent Praseodymium-Doped Barium Zinc Sulfide. *J. Electrochem. Soc.,* **2006**, *153*, G543-G547.

(85) Banks, E.; Ward, R., Luminescence and Conduction in Solid Solutions of Cerium Sulfide in Strontium Sulfide. *J. Electrochem. Soc.,* **1949**, *96*, 297-303.

(86) Hazin, P. N.; Lakshminarayan, C.; Brinen, L. S.; Knee, J. L.; Bruno, J. W.; Streib, W. E.; Folting, K., Luminescence spectra and lifetimes of cerium(III) compounds as indicators of solution behavior and radiative efficiency. *Inorg. Chem.,* **1988**, *27*, 1393-1400.

(87) Klepov, V. V.; Kocevski, V.; Besmann, T. M.; zur Loye, H.-C., Dimensional reduction upon calcium incorporation in $Cs_{0.3}(Ca_{0.3}Ln_{0.7})PS_4$ and $Cs_{0.5}(Ca_{0.5}Ln_{0.5})PS_4$. *CrystEngComm,* **2021**, *23*, 831-840.

(88) Choi, K.-S.; Kanatzidis, M. G., New Uranium Chalcoantimonates, RbU_2SbS_8 and KU_2SbSe_8, with a Polar Noncentrosymmetric Structure. *Chem. Mater.,* **1999**, *11*, 2613-2618.

(89) Chondroudis, K.; Kanatzidis, M. G., Stabilization of U^{5+}in $Rb_4U_4P_4Se_{26}$. An Actinide Compound with a Mixed Selenophosphate/Polyselenide Framework and Ion-Exchange Properties. *J. Am. Chem. Soc.,* **1997**, *119*, 2574-2575.

(90) Mesbah, A.; Prakash, J.; Ibers, J. A., Overview of the crystal chemistry of the actinide chalcogenides: incorporation of the alkaline-earth elements. *Dalton Trans.,* **2016**, *45*, 16067-16080.

(91) Prakash, J.; Mesbah, A.; Beard, J. C.; Lebegue, S.; Malliakas, C. D.; Ibers, J. A., Synthesis, crystal structure, optical, and electronic study of the new ternary thorium selenide $Ba_3ThSe_3(Se_2)_2$. *J. Solid State Chem.,* **2015**, *231*, 163-168.

(92) Freeman, A. J., f-Electrons in solids: Electronic structure and properties of actinides and rare-earths. *Physica B+C,* **1980**, *102*, 3-11.

(93) Grenthe, I.; Drozdzynski, J.; Fujino, T.; Buck, E. C.; Albrecht-Schmitt, T. E.; Wolf, S. F. Uranium. *The Chemistry of the Actinide and Transactinide Elements*; Morss, L. R., Edelstein, N. M., Fuger, J.; Springer, **2008**; 412-420.

(94) Jayasinghe, A. S.; Lai, Y.; Baumbach, R.; Latturner, S. E., $U_{1.33}T_4Al_8Si_2$ (T = Ni, Co): Complex Uranium Silicides Grown from Aluminum/Gallium Flux Mixtures. *Inorg. Chem.,* **2019**, *58*, 12209-12217.

(95) Krivovichev, S. V.; P. C. Burns; I. G. Tananaev, 2006, Structural Chemistry of Inorganic Actinide Compounds: Elsevier Science, p.

(96) Li, Y.; Yang, Z.; Wang, Y.; Bai, Z.; Zheng, T.; Dai, X.; Liu, S.; Gui, D.; Liu, W.; Chen, M.; Chen, L.; Diwu, J.; Zhu, L.; Zhou, R.; Chai, Z.; Albrecht-Schmitt, T. E.; Wang, S., A mesoporous cationic thorium-organic framework that rapidly traps anionic persistent organic pollutants. *Nat. Commun.,* **2017**, *8*, 1354.

(97) Manos, E.; Kanatzidis, M. G.; Ibers, J. A. Actinide Chalcogenide Compounds. *The Chemistry of the Actinide and Transactinide Elements*; Morss, L. R., Edelstein, N. M., Fuger, J.; Springer, Dordrecht, **2010**; 4005-4077.

(98) Mar, A.; Tougait, O.; Potel, M.; Noel, H.; Lopes, E. B., Anisotropic Transport and Magnetic Properties of Ternary Uranium Antimonides U_3ScSb_5 and U_3TiSb_5. *Chem. Mater.,* **2006**, *18*, 4533-4540.

(99) Wang, S.; Alekseev, E. V.; Depmeier, W.; Albrecht-Schmitt, T. E., Recent progress in actinide borate chemistry. *ChemComm,* **2011**, *47*, 10874.

(100) Wickleder, M. S.; Fourest, B.; Dorhout, P. K. Thorium. *The Chemistry of the Actinide and Transactinide Elements*; Morss, L. R., Edelstein, N. M., Fuger, J.; Springer, **2008**; 95-97.

(101) Narducci, A. A.; Ibers, J. A., The related compounds $MThTe_3$ (M = Mn, Mg) and $ACuThSe_3$ (A = K, Cs): Syntheses and Characterization. *Inorg. Chem.,* **2000**, *39*, 688-691.

(102) Narducci, A. A.; Ibers, J. A., Ternary and Quaternary Uranium and Thorium Chalcogenides. *Chem. of Mater.,* **1998**, *10*, 2811-2823.

(103) Noel, H., Chimie Minerale — Combinaisons seleniees de l'uranium dans les systemes USe_2-MSe (M = Mg, Ti, V, Cr, Mn, Fe, Co, Ni). *C. R. Acad. Sc. Paris,* **1974**, *279*, 513-515.

(104) Yao, J.; Ibers, J. A., $Ba_4Cr_2US_9$: The First Chalcogenide Analogue of the Perovskite-related $(A_3A'BO_6)_m(A_3B_3O_9)_n$. *Z. Anorg. Allg. Chem.,* **2008**, *634*, 1645-1647.

(105) Bugaris, D. E.; Ibers, J. A., Synthesis, structures, and magnetic and optical properties of the compounds $[Hg_3Te_2][UCl_6]$ and $[Hg_4As_2][UCl_6]$. *J. Solid State Chem.,* **2008**, *181*, 3189-3193.

(106) Daoudi, A.; Lamire, M.; C., L. J.; Noel, H., New Ternary Uranium Copper Chalcogenides $Cu_2U_3S_7$ and $Cu_2U_3Se_7$: Crystal Structure and Magnetic Properties. *J. Solid State Chem.,* **1996**, *123*, 331-336.

(107) Janus, B.; Suski, W.; Blaise, A. Magnetic Properties of the Uranium Trichalcogenides. *Crystalline Electric Field Effects in f-Electron Magnetism*; Guertin, R. P., Suski, W., Zolnierek, Z.; Springer, **1982**; 539-544.

(108) Wells, D. M.; Ibers, J. A., The $[U_2I_{10}]^{2-}$ Anion: Synthesis and Structure of $[Ta_7(Se_2)_{14}][U_2I_{10}]_2$. *Z. Anorg. Allg. Chem.,* **2010**, *636*, 440-442.

(109) Choi, K.-S.; Patschke, R.; J. L. Billinge, S.; Waner, M. J.; Dantus, M.; Kanatzidis, M. G., Charge Density Wave Caused by Reducing $ThSe_3$ by One Electron. Superstructure and Short-Range Order in ATh_2Se_6 (A = K, Rb) Studied by X-ray Diffraction, Electron Diffraction, and Diffuse Scattering. *J. Am. Chem. Soc.,* **1998**, *120*, 10706-10714.

(110) Gieck, C.; Tremel, W., Interlocking Inorganic Screw Helices: Synthesis, Structure, and Magnetism of the Novel Framework Uranium Orthothiophoshates $A_{11}U_7(PS_4)_{13}$ (A = K, Rb). *Chem. - Eur. J.,* **2002**, *8*, 2980-2987.

(111) Gui, D.; Duan, W.; Shu, J.; Zhai, F.; Wang, N.; Wang, X.; Xie, J.; Li, H.; Chen, L.; Diwu, J.; Chai, Z.; Wang, S., Persistent Superprotonic Conductivity in the Order of 10−1 S·cm−1 Achieved Through Thermally Induced Structural Transformation of a Uranyl Coordination Polymer. *CCS Chemistry,* **2019**, *1*, 197-206.

(112) Jin, G. B.; Choi, E. S.; Guertin, R. P.; Brooks, J. S.; Bray, T. H.; Booth, C. H.; Albrecht-Schmitt, T. E., Syntheses, Structure, Magnetism, and Optical Properties of the Ordered Mixed-Lanthanide Sulfides γ-LnLn‘S_3 (Ln = La, Ce; Ln‘ = Er, Tm, Yb). *Chem. Mater.,* **2007**, *19*, 567-574.

(113) Neuhausen, C.; Hatscher, S. T.; Panthofer, M.; Urland, W.; Tremel, W., Comprehensive Uranium Thiophosphate Chemistry: Framework Compounds Based on Pseudotetrahedrally Coordinated Central Metal Atoms. *Z. Anorg. Allg. Chem.,* **2013**, *639*, 2836-2845.

(114) Wang, Y.; Yin, X.; Liu, W.; Xie, J.; Chen, J.; Silver, M. A.; Sheng, D.; Chen, L.; Diwu, J.; Liu, N.; Chai, Z.; Albrecht-Schmitt, T. E.; Wang, S., Emergence of Uranium as a Distinct Metal Center for Building Intrinsic X-ray Scintillators. *Angew Chem Int Ed Engl,* **2018**, *57*, 7883-7887.

(115) Yao, J.; Wells, D. M.; Chan, G. H.; Zeng, H.-Y.; Ellis, D. E.; Van Duyne, R. P.; Ibers, J. A., Syntheses, Structures, Physical Poperties, and Electronic Properties of Some AMUQ$_3$ Compounds (A = Alkali Metal, M = Cu or Ag, Q = S or Se). *Inorg. Chem.,* **2008**, *47*, 6873-6879.

(116) Bugaris, D. E.; Wells, D. M.; Yao, J.; Skanthakumar, S.; Haire, R. G.; Soderholm, L.; Ibers, J. A., Dichalcogenide Bonding in Seven Alkali-Metal Actinide Chalcogenides of the KTh$_2$Se$_6$ Structure Type. *Inorg. Chem.,* **2010**, *49*, 8381-8388.

(117) Cody, J. A.; Ibers, J. A., Uranium Tellurides: New One- and Two-Dimensional Compounds CsUTe$_6$, CsTiUTe$_5$, Cs$_8$Hf$_5$UTe$_{30.6}$, and CsCuUTe$_3$. *Inorg. Chem.,* **1995**, *34*, 3165-3172.

(118) Daoudi, A.; H., N., Synthesis, crystal structure and magnetic properties of new ternary uranium chalcogenides: RuUS$_3$ and RhUS$_3$. *Inorganica Chim. Acta,* **1987**, *140*, 93-95.

(119) Daoudi, A.; Noel, H., Synthese, structure cristalline et proprietes magnetiques du seleniure ternaire d'uranium et de palladium: PdUSe$_3$. *J. of the Less Common Met.,* **1989**, *153*, 293-298.

(120) Noel, H.; Potel, M.; Padiou, J., Structure cristalline de CrU$_8$S$_{17}$. *Acta. Crystallogr. B,* **1975**, *31*, 2634-2637.

(121) Mesbah, A.; Ibers, J. A., Syntheses and crystal structures of three barium uranium sulfides. *J. Solid State Chem.,* **2013**, *199*, 253-257.

(122) Mesbah, A.; Prakash, J.; Beard, J. C.; Pozzi, E. A.; Tarasenko, M. S.; Lebegue, S.; Malliakas, C. D.; Duyne, R. P. V.; Ibers, J. A., Positional Flexibility: Synthesis and Characterization of Six Uranium Chalcogenides Related to the 2H Hexagonal Perovskite Family. *Inorg. Chem.,* **2015**, *54*, 2851-2857.

(123) Ward, M. D.; Ibers, J. A., The Synthesis and Crystal Structure of U$_7$O$_2$Se$_{12}$. *Z. fur Anorg. Allg. Chem.,* **2014**, *640*, 1585-1588.

(124) Mesbah, A.; Prakash, J.; Beard, J. C.; Lebegue, S.; Malliakas, C. D.; Ibers, J. A., Four new actinide chalcogenides Ba$_2$Cu$_4$USe$_6$, Ba$_2$Cu$_2$ThSe$_5$, Ba$_2$Cu$_2$USe$_5$, and Sr$_2$Cu$_2$US$_5$: Crystal Structures and Physical Properties. *Inorg. Chem.,* **2015**, *54*, 9138-9145.

(125) Prakash, J.; Tarasenko, M. S.; Mesbah, A.; Lebegue, S.; Malliakas, C. D.; Ibers, J. A., Synthesis, Crystal Structure, Theoretical, and Resistivity Study of BaUSe$_3$. *Inorg. Chem.,* **2016**, *55*, 7734-7738.

(126) Ippolitova, E. A.; Dunaeva, K. M.; Mitrofanova, N. D. Investigation of the Oxidation Process of Uranium Disulfide. *Investigations in the Field of Uranium Chemistry*; Spitsyn, V. I.; U.S. Atomic Energy Commission, **1964**; 245-259.

(127) Guo, S.-P.; Guo, G.-C.; Huang, J.-S., Syntheses, structures and properties of five chiral quaternary sulfides, $Al_xLn_3(Si_yAl_{1-y})S_7$ (Ln = Y, Gd, Dy) and $In_{0.33}Sm_3SiS_7$. *Science in China Series B: Chemistry,* **2009**, *52*, 1609-1615.

(128) Guo, S.-P.; Chi, Y.; Xue, H.-G., $Sm_3S_3BO_3$: The First Sulfide Borate without S-O and B-S Bonds. *Inorg. Chem.,* **2015**, *54*, 11052-11054.

(129) Huang, Y.-Z.; Chen, L.; Wu, L.-M., Crystalline Nanowires of Ln_2O_2S, $Ln_2O_2S_2$, LnS_2 (Ln = La, Nd), and $La_2O_2S:Eu^{3+}$. Conversions via the Boron-Sulfur Method That Preserve Shape. *Cryst. Growth Des.,* **2008**, *8*, 739-743.

(130) Jeon, K.-W.; Seo, D.-K., Concomitant Thionation and Reduction of Graphene Oxide Through Solid/Gas Metathetical Sulfidation Reactions at High Temperatures. *Phosphorus, Sulfur, and Silicon and the Related Elements,* **2014**, *189*, 721-737.

(131) Wu, L.-M.; Seo, D.-K., New Solid-Gas Metathetical Synthesis of Binary Metal Polysulfides and Sulfides at Intermediate Temperatures: Utilization of Boron Sulfides. *J. Am. Chem. Soc.,* **2004**, *126*, 4676-4681.

(132) Zhang, M.-J.; Jiang, X.-M.; Zhou, L.-J.; Guo, G.-C., Two phases of Ga_2S_3: promising infrared second-order nonlinear optical materials with very high laser induced damage thresholds. *J. Mater. Chem. C,* **2013**, *1*, 4754.

(133) Malliakas, C. D.; Yao, J.; Wells, D. M.; Jin, G. B.; Skanthakumar, S.; Choi, E. S.; Soderholm, L.; Ellis, D. E.; Kanatzidis, M. G.; Ibers, J. A., Oxidation State of Uranium in $A_6Cu_{12}U_2S_{15}$ (A = K, Rb, Cs) Compounds. *Inorg. Chem.,* **2012**, *51*, 6153-6163.

(134) Sutorik, A. C.; Kanatzidis, M. G., Reactions of Lanthanides and Actinides in Molten Alkali Metal/Polychalcogenide Fluxes at Intermediate Temperatures (250-600 ºC). *Chem. Mater.,* **1997**, *9*, 387-398.

(135) Suski, W.; Gibinski, T.; Wojakowski, A.; Czopnik, A., The crystal structure and magnetic and electrical properties of β-US_2. *phys. stat. sol. (a),* **1972**, *9*, 653.

(136) Kirklin, S.; Saal, J. E.; Meredig, B.; Thompson, A.; Doak, J. W.; Aykol, M.; Ruhl, S.; Wolverton, C., The Open Quantum Materials Database (OQMD): assessing the accuracy of DFT formation energies. *npj Computational Materials,* **2015**, *1*, 15010.

(137) Saal, J. E.; Kirklin, S.; Aykol, M.; Meredig, B.; Wolverton, C., Materials Design and Discovery with High-Throughput Density Functional Theory: The Open Quantum Materials Database (OQMD). *JOM,* **2013**, *65*, 1501-1509.

(138) Jansen, M., Conceptual Inorganic Materials Discovery - A Road Map. *Advanced Materials,* **2015**, *27*, 3229-3242.

(139) Klepov, V. V.; Smith, M. D.; zur Loye, H.-C., Targeted Synthesis of Uranium(IV) Thiosilicates. *Inorg. Chem.,* **2019**, *58*, 8275-8278.

(140) Sheldrick, W. S. Polychalcogenides. *Handbook of Chalcogen Chemistry*; Devillanova, F., Du Mont, W.-W.; The Royal Society of Chemistry, **2007**; 543-557.

(141) Noel, H.; Padiou, J.; Prigent, J., Mixed Uranium and Transition Element Sulfides. *C. R. Acad. Sc. Paris,* **1971**, *272*, 206-208.

(142) Ward, M. D.; Ibers, J. A., Nickel(II) uranium(IV) trisulfide. *Acta Crystallogr. Sect. E: Struct. Rep. Online,* **2014**, *70*, i4.

(143) Murphy, G. L.; Kegler, P.; Zhang, Y.; Zhang, Z.; Alekseev, E. V.; de Jonge, M. D.; Kennedy, B. J., High-Pressure Synthesis, Structural, and Spectroscopic Studies of the Ni—U—O System. *Inorg. Chem.,* **2018**, *57*, 13847-13858.

(144) Chenevier, B.; Wolfers, P.; Bacmann, M.; Noel, H., $CoUS_3$-Proprietes et structure magnetiques. *C. R. Acad. Sc. Paris,* **1981**, *293*, 649-652.

(145) Bugaris, D. E.; zur Loye, H.-C., Materials Discovery by Flux Crystal Growth: Quaternary and Higher Order Oxides. *Angew. Chem. Int. Ed.,* **2012**, *51*, 3780-3811.

(146) Noel, H.; Prigent, J., U_3S_5: A mixed valence uranium sulfide. Magnetic susceptibility of thorium and lanthanides isomorphous derivatives. *Physica B+C,* **1980**, *102B*, 372-379.

(147) Grønvold, F.; Haraldsen, H.; Thurmann-Moe, T.; Tufte, T., Uranium chalcogenides—I structural and magnetic properties of sulphides and selenides in the range $UX_{1.5}$ to UX_3. *J. Inorg. Nucl. Chem.,* **1968**, *30*, 2117-2125.

(148) Noel, H.; Le Marouille, J. Y., Crystal structure and properties of the uranium chalcogenides α-US_2 and α-USe_2. *J. Solid State Chem.,* **1984**, *52*, 197-202.

(149) Chan, B. C.; Hess, R. F.; Feng, P. L.; Abney, K. D.; Dorhout, P. K., Synthesis and Characterization of Two Quaternary Thorium Chalcophosphates: $Cs_4Th_2P_6S_{18}$ and $Rb_7Th_2P_6Se_{21}$. *Inorg. Chem.,* **2005**, *44*, 2106-2113.

(150) Hess, R. F.; Abney, K. D.; Burris, J. L.; Hochheimer, H. D.; Dorhout, P. K., Synthesis and Characterization of Six New Quaternary Actinide Thiophosphate Compounds: $Cs_8U_5(P_3S_{10})_2(PS_4)_6$, $K_{10}Th_3(P_2S_7)_4(PS_4)_2$, and $A_5An(PS_4)_3$, (A = K, Rb, Cs; An = U, Th). *Inorg. Chem.,* **2001**, *40*, 2851-2859.

(151) Mesbah, A.; Prakash, J.; Beard, J. C; Lebegue, S.; Malliakas, C. D.; Ibers, J. A., Synthesis, Crystal Structures, Optical and Theoretical Studies of the Actinide Thiophosphates $SrU(PS_4)_2$, $BaU(PS_4)_2$, and $SrTh(PS_4)_2$. *Inorg. Chem.,* **2015**, *54*, 2970-2975.

(152) Simon, A.; Peters, K.; Peters, E.-M.; Hahn, H., Darstellung und Kristallstruktur von ZrP_2S_6 und ThP_2S_6. *Z. Anorg. Allg. Chem.,* **1982**, *491*, 295-300.

(153) Mesbah, A.; Ringe, E.; Lebegue, S.; Van Duyne, R. P.; Ibers, J. A., $Ba_2An(S_2)_2S_2$ (An = U, Th): Syntheses, Structures, Optical, and Electronic Properties. *Inorg. Chem.,* **2012**, *51*, 13390-13395.

(154) Mesbah, A.; Prakash, J.; Beard, J. C.; Malliakas, C. D.; Lebegue, S.; Ibers, J. A., Syntheses, modulated crystal structures of $Ba_{6-2x}U_{2+x}Ag_4Se_{12}$ (x = 0 and 0.5), and crystal structure and spectroscopy of $Sr_4Th_{2.78}Cu_4S_{12}$. *J. Solid State Chem.,* **2018**, *268*, 30-35.

(155) Mesbah, A.; Stojko, W.; Lebegue, S.; Malliakas, C. D.; Frazer, L.; Ibers, J. A., The U^{5+} compound $Ba_9Ag_{10}U_4S_{24}$: Synthesis, structure, and electronic properties. *J. Solid State Chem.,* **2015**, *221*, 398-404.

(156) Mesbah, A.; Prakash, J.; Lebègue, S.; Stojko, W.; Ibers, J. A., Syntheses, crystal structures, and electronic properties of $Ba_8Si_2US_{14}$ and $Ba_8SiFeUS_{14}$. *Solid State Sci.,* **2015**, *48*, 120-124.

(157) Ward, M. D.; Mesbah, A.; Minasian, S. G.; Shuh, D. K.; Tyliszczak, T.; Lee, M.; Choi, E. S.; Lebegue, S.; Ibers, J. A., Synthesis and Characterization of Eight Compounds of the MU_8Q_{17} Family: ScU_8S_{17}, CoU_8S_{17}, NiU_8S_{17}, TiU_8Se_{17}, VU_8Se_{17}, CrU_8Se_{17}, CoU_8Se_{17}, and NiU_8Se_{17}. *Inorg. Chem.,* **2014**, *53*, 6920-6927.

(158) Ward, M. D.; Lee, M.; Choi, E. S.; Ibers, J. A., Synthesis and characterization of the quaternary scandium uranium selenide $CsScUSe_3(Se_2)$. *J. Solid State Chem.,* **2015**, *226*, 307-311.

(159) Brown, I. D., Bond Valence Parameters, <https://www.iucr.org/resources/data/datasets/bond-valence-parameters>, Accessed June 10, 2020.

(160) Serezhkin, V. N. Some features of Stereochemistry of U(VI). *Structural Chemistry of Inorganic Actinide Compounds*; Krivovichev, S., Burns, P., Tananaev, I., Eds.; Elsevier, **2006**; 31-65.

(161) Morrison, G.; Ramanantoanina, H.; Urland, W.; Smith, M. D.; zur Loye, H.-C., Flux Synthesis, Structure, Properties, and Theoretical Magnetic Study of Uranium(IV)-Containing $A_2USi_6O_{15}$ (A = K, Rb) with an Intriguing Green-to-Purple, Crystal-to-Crystal Structural Transition in the K Analogue. *Inorg. Chem.,* **2015**, *54*, 5504-5511.

(162) Bugaris, D. E.; Ibers, J. A., $RbAuUSe_3$, $CsAuUSe_3$, $RbAuUTe_3$, and $CsAuUTe_3$: Syntheses and structure; magnetic properties of RbAuUSe3. *J. Solid State Chem.,* **2009**, *182*, 2587-2590.

(163) Laing, C. C.; Shen, J.; Quintero, M. A.; Weiss, B. E.; Xia, Y.; Li, Z.; He, J.; Wolverton, C.; Kanatzidis, M. G., Homologous Alkali Metal Copper Rare-Earth Chalcogenides $A_2Cu_{2n}Ln_4Q_{7+n}$ (n = 1, 2, 3). *Chem. Mater.,* **2022**, *34*, 3409-3422.

(164) Wells, D. M.; Jin, G. B.; Skanthakumar, S.; Haire, R. G.; Soderholm, L.; Ibers, J. A., Quaternary neptunium compounds: syntheses and characterization of $KCuNpS_3$, $RbCuNpS_3$, $CsCuNpS_3$, $KAgNpS_3$, and $CsAgNpS_3$. *Inorg. Chem.,* **2009**, *48*, 11513-11517.

(165) Oh, G. N.; Choi, E. S.; Ibers, J. A., Syntheses and characterization of nine quaternary uranium chalcogenides among the compounds $A_2M_3UQ_6$ (A = K, Rb, Cs; M = Pd, Pt; Q = S, Se). *Inorg. Chem.,* **2012**, *51*, 4224-4230.

(166) Oh, G. N.; Choi, E. S.; Lu, J.; Koscielski, L. A.; Ward, M. D.; Ellis, D. E.; Ibers, J. A., Syntheses and characterization of six quaternary uranium chalcogenides $A_2M_4U_6Q_{17}$ (A = Rb or Cs; M = Pd or Pt; Q = S or Se). *Inorg. Chem.,* **2012**, *51*, 8873-8881.

(167) Sutorik, A. C.; Patschke, R.; Schindler, J.; Kannewurf, C. R.; Kanatzidis, M. G., Valence fluctuations and metallic behavior in $K_6Cu_{12}U_2S_{15}$, a new quaternary sulfide with a unique three-dimensional cubic framework. *Chem. Eur. J.,* **2000**, *6*, 1601-1607.

(168) *SmartLab Studio II, ver. 4.5.286.0;* Rigaku, **2021.**

(169) Rozhdestvina, V. I.; Udovenko, A. A.; Rubanov, S. V.; Mudrovskaya, N. V., Structural investigation of cooperite (PtS) crystals. *Crystallography Reports,* **2016**, *61*, 193-202.

(170) Fujino, T.; Sato, N.; Yamada, K.; Masuda, H.; Wakeshima, M., Crystal structure and magnetic susceptibility of uranium palladium sulfide bronze, $U_xPd_3S_4$. *J. Alloys Compd.,* **1998**, *271-273*, 452-455.

(171) Yeon, J.; Smith, M. D.; Tapp, J.; Möller, A.; zur Loye, H. C., Application of a mild hydrothermal approach containing an in situ reduction step to the growth of single crystals of the quaternary U(IV)-containing fluorides Na4MU6F30 (M = Mn2+,

Co2+, Ni2+, Cu2+, and Zn2+) crystal growth, structures, and magnetic properties. *J. Am. Chem. Soc.,* **2014**, *136*, 3955-3963.

(172) Li, G.; Li, J.; Wu, K.; Yang, Z.; Pan, S., $Ba_4(BS_3S)_2S_4$: a new thioborate with unprecedented [BS_3-S] and [S_4] fundamental building blocks. *Chem. Commun.,* **2019**, *55*, 14793-14796.

(173) Zhou, J.; Chu, Y.; Li, J.; Pan, S., Ba_2BS_3Cl and $Ba_5B_2S_8Cl_2$: first alkaline-earth metal thioborate halides with [BS_3] units. *Chem. Commun.,* **2021**, *57*, 6440-6443.

(174) Kim, Y.; Martin, S. W.; Ok, K. M.; Halasyamani, P. S., Synthesis of the Thioborate Crystal $Zn_xBa_2B_2S_{5+x}$ ($x \approx 0.2$) for Second Order Nonlinear Optical Applications. *Chem. Mater.,* **2005**, *17*, 2046-2051.

(175) Kumar, R. A.; Arivanandhan, M.; Hayakawa, Y., Recent advances in rare earth-based borate single crystals: Potential materials for nonlinear optical and laser applications. *Prog. Cryst. Growth Charact. Mater.,* **2013**, *59*, 113-132.

(176) Hunger, J.; Borna, M.; Kniep, R., Synthesis and crystal structure of the isotypic rare earth thioborates Ce[BS_3], Pr[BS_3], and Nd[BS_3]. *J. Solid State Chem.,* **2010**, *183*, 702-706.

(177) Hunger, J.; Borna, M.; Kniep, R., Refinement of the crystal structure of praseodymium trithioborate, Pr[BS_3], single crystal data. *Z. Krist.-New Cryst. St.,* **2010**, *225*, 217-218.

(178) Huang, Y. Z.; Chen, L.; Wu, L.-M., Submicrosized rods, cables, and tubes of ZnE (E = S, Se, Te): exterior-interior boron-chalcogen conversions and optical properties. *Inorg. Chem.,* **2008**, *47*, 10723-10728.

(179) Ma, N.; Li, F.; Li, J. G.; Liu, X.; Zhang, D. B.; Li, Y. Y.; Chen, L.; Wu, L.-M., Mixed-Valence $CsCu_4Se_3$: Large Phonon Anharmonicity Driven by the Hierarchy of the Rigid $[(Cu^+)_4(Se^{2-})_2](Se^-)$ Double Anti-CaF_2 Layer and the Soft Cs^+ Sublattice. *J. Am. Chem. Soc.,* **2021**, *143*, 18490-18501.

(180) Carpenter, J. D.; Hwu, S. J., Synthesis and characterization of two new quaternary chalcogenides, $CaYbInQ_4$ (Q = S and Se), with an olivine-type structure. *Chem. Mater.,* **1992**, *4*, 1368-1372.

(181) Tsujimoto, Y.; Juillerat, C. A.; Zhang, W.; Fujii, K.; Yashima, M.; Halasyamani, P. S.; zur Loye, H.-C., Function of Tetrahedral ZnS_3O Building Blocks in the Formation of $SrZn_2S_2O$: A Phase Matchable Polar Oxysulfide with a Large Second Harmonic Generation Response. *Chem. Mater.,* **2018**, *30*, 6486-6493.

(182) Usman, M.; Smith, M. D.; Morrison, G.; Klepov, V. V.; Zhang, W.; Halasyamani, P. S.; zur Loye, H.-C., Molten Alkali Halide Flux Growth of an Extensive Family

of Noncentrosymmetric Rare Earth Sulfides: Structure and Magnetic and Optical (SHG) Properties. *Inorg. Chem.,* **2019**, *58*, 8541-8550.

(183) Usman, M.; Morrison, G.; zur Loye, H.-C., $La_2USe_3S_2$: A Serendipitously Grown Lanthanide/Actinide Chalcogenide from a Eutectic Halide Flux. *J. Chem. Crystallogr.,* **2019**, *49*, 169-173.

(184) Han, Y.-X.; Hu, C.-L.; Fang, Z.; Chen, Q.-Q.; Li, B.-X.; Lin, Y.; Mao, J.-G., $LaBS_3$ revisited: a promising mid-infrared nonlinear optical material. *J. of Mater. Chem. C,* **2022**, *10*, 12556-12559.

(185) Gui, Y.; Yang, Q.; Shao, Y.; Yuan, Y., Spectroscopic properties of neodymium-doped alumina (Nd 3+ :Al 2 O 3) translucent ceramics. *J. Lumin.,* **2017**, *184*, 232-234.

(186) Gray, D. L.; Backus, L. A.; von Nidda, H. A.; Skanthakumar, S.; Loidl, A.; Soderholm, L.; Ibers, J. A., A U(V) chalcogenide: synthesis, structure, and characterization of $K_2Cu_3US_5$. *Inorg. Chem.,* **2007**, *46*, 6992-6996.

(187) Zhou, J., Synthesis of heterometallic chalcogenides containing lanthanide and group 13–15 metal elements. *Coord. Chem. Rev.,* **2016**, *315*, 112-134.

(188) Clarke, S. J.; Adamson, P.; Herkelrath, S. J.; Rutt, O. J.; Parker, D. R.; Pitcher, M. J.; Smura, C. F., Structures, physical properties, and chemistry of layered oxychalcogenides and oxypnictides. *Inorg. Chem.,* **2008**, *47*, 8473-8486.

(189) Shi, Y.-F.; Wei, W.-B.; Wu, X.-T.; Lin, H.; Zhu, Q.-L., Recent progress in oxychalcogenides as IR nonlinear optical materials. *Dalton Trans.,* **2021**, *50*, 4112-4118.

(190) Tippireddy, S.; D S, P. K.; Das, S.; Mallik, R. C., Oxychalcogenides as Thermoelectric Materials: An Overview. *ACS Appl. Energy Mater.,* **2021**, *4*, 2022-2040.

(191) Ueda, K.; Hiramatsu, H.; Hirano, M.; Kamiya, T.; Hosono, H., Wide-gap layered oxychalcogenide semiconductors: Materials, electronic structures and optoelectronic properties. *Thin Solid Films,* **2006**, *496*, 8-15.

(192) Wang, F.; Yang, S.; Wu, J.; Hu, X.; Li, Y.; Li, H.; Liu, X.; Luo, J.; Zhai, T., Emerging two-dimensional bismuth oxychalcogenides for electronics and optoelectronics. *InfoMat,* **2021**, *3*, 1251-1271.

(193) Ayer, G. B.; Klepov, V. V.; Smith, M. D.; Hu, M.; Yang, Z.; Martin, C. R.; Morrison, G.; zur Loye, H.-C., $BaWO_2F_4$: a mixed anion X-ray scintillator with excellent photoluminescence quantum efficiency. *Dalton Trans.,* **2020**, *49*, 10734-10739.

(194) Cortese, A. J.; Wilkins, B.; Smith, M. D.; Morrison, G.; zur Loye, H.-C., Single crystal growth and characterization of the first reduced lanthanum molybdenum oxychloride, $La_{20}Mo_{12}O_{63}Cl_4$, with an unusual trigonal prismatic MoO_6 unit. *Solid State Sci.,* **2015**, *48*, 133-140.

(195) Latshaw, A. M.; Wilkins, B. O.; Morrison, G.; Smith, M. D.; zur Loye, H.-C., $A_5RE_4X[TO_4]_4$ crystal growth: Fluoride flux synthesis of $Na_5Ln_4F[GeO_4]_4$ (Ln=Pr, Nd), the first quaternary germanate oxyfluorides. *J. Solid State Chem.,* **2016**, *239*, 200-203.

(196) Morrison, G.; Latshaw, A. M.; Spagnuolo, N. R.; zur Loye, H.-C., Observation of Intense X-ray Scintillation in a Family of Mixed Anion Silicates, $Cs_3RESi_4O_{10}F_2$ (RE = Y, Eu-Lu), Obtained via an Enhanced Flux Crystal Growth Technique. *J. Am. Chem. Soc.,* **2017**, *139*, 14743-14748.

(197) Read, C. M.; Yeon, J.; Smith, M. D.; zur Loye, H.-C., Crystal growth, structural characterization, cation–cation interaction classification, and optical properties of uranium(vi) containing oxychlorides, $A_4U_5O_{16}Cl_2$ (A = K, Rb), $Cs_5U_7O_{22}Cl_3$, and AUO_3Cl (A = Rb, Cs). *CrystEngComm,* **2014**, *16*, 7259-7267.

(198) Yeon, J.; Felder, J. B.; Smith, M. D.; Morrison, G.; zur Loye, H.-C., Synthetic strategies for new vanadium oxyfluorides containing novel building blocks: structures of $V^{(iv)}$ and $V^{(v)}$ containing $Sr_4V_3O_5F_{13}$, $Pb_7V_4O_8F_{18}$, $Pb_2VO_2F_5$, and Pb_2VOF_6. *CrystEngComm,* **2015**, *17*, 8428-8440.

(199) Ahmed, M.; Xinxin, G., A review of metal oxynitrides for photocatalysis. *Inorg. Chem. Front.,* **2016**, *3*, 578-590.

(200) Attfield, J. P., Principles and Applications of Anion Order in Solid Oxynitrides. *Cryst. Growth Des.,* **2013**, *13*, 4623-4629.

(201) Ebbinghaus, S. G.; Abicht, H.-P.; Dronskowski, R.; Müller, T.; Reller, A.; Weidenkaff, A., Perovskite-related oxynitrides – Recent developments in synthesis, characterisation and investigations of physical properties. *Prog. Solid. State Ch.,* **2009**, *37*, 173-205.

(202) Fuertes, A., Metal oxynitrides as emerging materials with photocatalytic and electronic properties. *Mater. Horiz.,* **2015**, *2*, 453-461.

(203) Marchand, R.; Laurent, Y.; Guyader, J.; L'Haridon, P.; Verdier, P., Nitrides and oxynitrides: Preparation, crystal chemistry and properties. *J. Eur. Ceram. Soc.,* **1991**, *8*, 197-213.

(204) Yang, M.; Oró-Solé, J.; Rodgers, J. A.; Jorge, A. B.; Fuertes, A.; Attfield, J. P., Anion order in perovskite oxynitrides. *Nat. Chem.,* **2011**, *3*, 47-52.

(205) Kageyama, H.; Hayashi, K.; Maeda, K.; Attfield, J. P.; Hiroi, Z.; Rondinelli, J. M.; Poeppelmeier, K. R., Expanding frontiers in materials chemistry and physics with multiple anions. *Nat. Commun.,* **2018**, *9*, 772.

(206) Li, Y.-Y.; Wang, W.-J.; Wang, H.; Lin, H.; Wu, L.-M., Mixed-Anion Inorganic Compounds: A Favorable Candidate for Infrared Nonlinear Optical Materials. *Cryst. Growth Des.,* **2019**, *19*, 4172-4192.

(207) Pan, Y.; Guo, S.-P.; Liu, B.-W.; Xue, H.-G.; Guo, G.-C., Second-order nonlinear optical crystals with mixed anions. *Coord. Chem. Rev.,* **2018**, *374*, 464-496.

(208) Pilania, G.; Ghosh, A.; Hartman, S. T.; Mishra, R.; Stanek, C. R.; Uberuaga, B. P., Anion order in oxysulfide perovskites: origins and implications. *npj Computational Materials,* **2020**, *6*.

(209) Tripathi, T. S.; Karppinen, M., Mixed-Anion Compounds: An Unexplored Playground for ALD Fabrication. *Adv. Mater. Interfaces,* **2021**, *8*, 2100146.

(210) Berseneva, A. A.; Klepov, V. V.; Pal, K.; Seeley, K.; Koury, D.; Schaeperkoetter, J.; Wright, J. T.; Misture, S. T.; Kanatzidis, M. G.; Wolverton, C.; Gelis, A. V.; zur Loye, H.-C., Transuranium Sulfide via the Boron Chalcogen Mixture Method and Reversible Water Uptake in the $NaCuTS_3$ Family. *J. Am. Chem. Soc.,* **2022**, *144*, 13773-13786.

(211) Guittard, M.; Vovan, T.; Julien-Pouzol, M.; Jaulmes, S.; Laruelle, P.; Flahaut, J., Mise en Evidence et Etude Structurale d’une Famille de Composes en Feuillet de Formule Generale $(UO)_2RS_3$ (R = Gd a Lu et Y). *Z. Anorg. Allg. Chem.,* **1986**, *540*, 59-66.

(212) Larquet, C.; Carenco, S., Metal Oxysulfides: From Bulk Compounds to Nanomaterials. *Front. Chem.,* **2020**, *8*, 179.

(213) Marcon, J. P., Sulfures de neptunium. *C. r. hebd. seances Acad.,* **1967**, *265*, 235-237.

(214) Marcon, J. P., Oxysulfures de plutonium. *C. r. hebd. seances Acad.,* **1967**, *264*, 1475-1476.

(215) Van Tien, V.; Guittard, M.; Dugué, J.; Flahaut, J., Les combinaisons $U_2R_{2n-2}O_{2n}S_{n+1}$ formées par les lanthanides légers (R = Ce aTb) avec n = 2 et 3 et dans le cas du lanthane avec n = 2 a 6. *J. Solid State Chem.,* **1988**, *73*, 11-18.

(216) Mesbah, A.; Prakash, J.; Lebegue, S.; Stojko, W.; Ibers, J. A., Syntheses, crystal structures, and electronic properties of $Ba_8Si_2US_{14}$ and $Ba_8SiFeUS_{14}$. *Solid State Sci.,* **2015**, *48*, 120-124.

(217) Mesbah, A.; Stojko, W.; Malliakas, C. D.; Lebègue, S.; Clavier, N.; Ibers, J. A., The flexible $Ba_7UM_2S_{12.5}O_{0.5}$ (M = V, Fe) compounds: syntheses, structures and spectroscopic, resistivity, and electronic properties. *Inorg. Chem.,* **2013**, *52*, 12057-12063.

(218) Mesbah, A.; Prakash, J.; Beard, J. C.; Malliakas, C. D.; Ibers, J. A., Syntheses and crystal structures of the $Ba_7UM_2S_{12.5}O_{0.5}$ (M = Ti, Si/Fe) compounds. *Mater. Lett.,* **2019**, *252*, 293-295.

(219) Reinen, D.; Atanasov, M.; Nikolov, G.; Steffens, F., Local and cooperative Jahn-Teller distortions of nickel(2+) and copper (2+) in tetrahedral coordination. *Inorg. Chem.,* **1988**, *27*, 1678-1686.

(220) Cody, J. A.; Mansuetto, M. F.; Chien, S.; Ibers, J. A., Reactive Flux Syntheses at Low and High Temperatures. *MSF,* **1994**, *152-153*, 35-42.

(221) Zeng, H.-y.; Yao, J.; Ibers, J. A., Synthesis, structure, and magnetic properties of $Ba_2Cu_2US_5$. *J. Solid State Chem.,* **2008**, *181*, 552-555.

(222) Masuda, H.; Fujino, T.; Sato, N.; Yamada, K.; Wakeshima, M., Synthesis and crystal structure of alkali metal uranium sulfides, Li_2US_3 and Na_2US_3. *J. Alloys Compd.,* **1999**, *284*, 117-123.

(223) Linde, S. A.; Gorbunova, Y. E.; Lavrov, A. V., The crystal structure of uranium tetrametaphosphate UP_4O_{12}. *Zh. Neorg. Khim.,* **1983**, *28*, 1391-1395.

(224) Kovba, L. M., Crystal Structures of Double Uranium Compounds. *Radiokhimiya,* **1971**, *13*, 909-910.

(225) Wakeshima, M.; Hinatsu, Y.; Ishii, Y.; Shimojo, Y.; Morii, Y., Crystal structures and magnetic properties of cobalt chalcogenides BaLa2Co(S1 – xSex)5 (0.0 ≤ x ≤ 0.4). *J. Mater. Chem.,* **2002**, *12*, 631-634.

(226) Schnering, H. G.; Hoppe, R., Zur Kenntnis des Ba2ZnS3. *Zeitschrift fur anorganische und allgemeine Chemie,* **1961**, *312*, 99-109.

(227) Bronger, W.; Buttcher, P., Uber Thiomanganate und -cobaltate der schweren Alkalimetalle: $Rb_2Mn_3S_4$, $Cs_2Mn_3S_4$, $Rb_2Co_3S_4$, $Cs_2Co_3S_4$. *Z. Anorg. Allg. Chem.,* **1972**, *390*, 1-12.

(228) Bronger, W.; Bomba, C., Ternäre cobaltchalkogenide A_2CoX_2 MIT A = Na, K, Rb, Cs und X = S, Se. Synthese, struktur und magnetismus. *J. less-common met.,* **1990**, *158*, 169-176.

(229) Chan, G. H.; Sherry, L. J.; Van Duyne, R. P.; Ibers, J. A., Syntheses, Crystal Structures, and Optical and Magnetic Properties of Some $CsLnCoQ_3$ Compounds (Ln = Tm and Yb, Q = S; Ln = Ho and Yb, Q = Se). *Z. Anorg. Allg. Chem.,* **2007**, *633*, 1343-1348.

(230) Oledzka, M.; Lee, J.-G.; Ramanujachary, K. V.; Greenblatt, M., Synthesis and Characterization of Quaternary Sulfides with $ThCr_2Si_2$-Type Structure: $KCo_{2-x}Cu_xS_2$($0.5 \leq x \leq 1.5$) and $ACoCuS_2$ (A= K, Rb, Cs). *J. Solid State Chem.,* **1996**, *127*, 151-160.

(231) Wakeshima, M.; Hinatsu, Y., Crystal Structures and Magnetic Properties of New Quaternary Sulfides $BaLn_2MS_5$ (Ln=La, Ce, Pr, Nd; M=Co, Zn) and $BaNd_2MnS_5$. *J. Solid State Chem.,* **2001**, *159*, 163-169.

(232) Harrison, M. R.; Maignan, A.; Hardy, V.; Lebedev, O. I.; Young, N. A.; Francesconi, M. G., Structure and Electronic Properties of the Quasi-One-Dimensional $Ba_2Co_{1-x}Zn_xS_3$ Series. *Inorg. Chem.,* **2017**, *56*, 213-223.

(233) Cossee, P., Structure and magnetic properties of Co_3O_4 and $ZnCo_2O_4$. *Recl. Trav. Chim. Pays-Bas,* **2010**, *75*, 1089-1096.

(234) Bu, K.; Zhang, X.; Huang, J.; Luo, M.; Zheng, C.; Wang, R.; Wang, D.; He, J.; Zhao, W.; Che, X.; Huang, F., Crystal structure design and multiband physical properties of quaternary sulfide $Ba_5Bi_2Co_2S_{10}$ for optoelectronic conversion. *Chem. Commun. (Camb),* **2019**, *55*, 4809-4812.

(235) Bozovic, I.; Logvenov, G.; Belca, I.; Narimbetov, B.; Sveklo, I., Epitaxial strain and superconductivity in $La_{2-x}Sr_xCuO_4$ thin films. *Phys. Rev. Lett.,* **2002**, *89*, 107001.

(236) Sato, H.; Naito, M., Increase in the superconducting transition temperature by anisotropic strain effect in (001) $La_{1.85}Sr_{0.15}CuO_4$ thin films on $LaSrAlO_4$ substrates. *Physica C: Superconductivity,* **1997**, *274*, 221-226.

(237) Ishigaki, T.; Yamauchi, S.; Mizusaki, J.; Fueki, K.; Tamura, H., Tracer diffusion coefficient of oxide ions in $LaCoO_3$ single crystal. *J. Solid State Chem.,* **1984**, *54*, 100-107.

(238) Takahashi, T.; Iwahara, H., Ionic conduction in perovskite-type oxide solid solution and its application to the solid electrolyte fuel cell. *Energy Conversion,* **1971**, *11*, 105-111.

(239) Cao, Y.; Zhu, Z.; Li, X.; Xi, J.; Singh, D. J.; Xi, L.; Yang, J.; Zhang, W., Unraveling the relationships between chemical bonding and thermoelectric properties: n-type ABO_3 perovskites. *Journal of Materials Chemistry A,* **2022**, *10*, 11039-11045.

(240) Woo, S.; Lee, S. A.; Mun, H.; Choi, Y. G.; Zhung, C. J.; Shin, S.; Lacotte, M.; David, A.; Prellier, W.; Park, T.; Kang, W. N.; Lee, J. S.; Kim, S. W.; Choi, W. S., Enhanced magnetic and thermoelectric properties in epitaxial polycrystalline $SrRuO_3$ thin films. *Nanoscale,* **2018**, *10*, 4377-4384.

(241) Hwang, H. Y.; Cheong, S. W.; Radaelli, P. G.; Marezio, M.; Batlogg, B., Lattice effects on the magnetoresistance in doped $LaMnO_3$. *Phys. Rev. Lett.,* **1995**, *75*, 914-917.

(242) Ju, H. L.; Kwon, C.; Li, Q.; Greene, R. L.; Venkatesan, T., Giant magnetoresistance in $La_{1-x}Sr_xMnO_z$ films near room temperature. *Appl. Phys. Lett.,* **1994**, *65*, 2108-2110.

(243) zur Loye, H.-C.; Zhao, Q.; Bugaris, D. E.; Chance, W. M., 2H-perovskite related oxides: Synthesis, structures, and predictions. *CrystEngComm,* **2012**, *14*, 23-39.

(244) Randall Jnr, J. J.; Katz, L., The crystal structure of Sr4PtO6 and two related compounds. *Acta Crystallographica,* **1959**, *12*, 519-521.

(245) Cussen, E. J.; Vente, J. F.; Battle, P. D., Neutron Diffraction Study of $Ba_6Mn_4MO_{15}$ (M = Cu, Zn): Long-Range Magnetic Order in Pseudo-1D Materials. *J. Am. Chem. Soc.,* **1999**, *121*, 3958-3967.

(246) Davis, M. J.; Smith, M. D.; zur Loye, H.-C., Crystal growth, structural characterization and magnetic properties of Ca_3CuRhO_6, $Ca_3Co_{1.34}Rh_{0.66}O_6$ and Ca_3FeRhO_6. *J. Solid State Chem.,* **2003**, *173*, 122-129.

(247) Sun, J.; Li, G.; Li, Z.; You, L.; Lin, J., Crystal growth and structure determination of oxygen-deficient $Sr_6Co_5O_{15}$. *Inorg. Chem.,* **2006**, *45*, 8394-8402.

(248) James, M.; Attfield, J. P., A new nickel(III) oxide family: MSr_3NiO_6 (M = Sc, In, Tm, Yb and Lu). *Chemistry - A European Journal,* **1996**, *2*, 737-741.

(249) Layland, R. C.; Kirkland, S. L.; zur Loye, H.-C., Synthesis, Characterization, and Magnetic Properties of New Rh(III) Compounds with the K_4CdCl_6Structure-Type: Sr_3MRhO_6 (M=Sm, Eu, Tb, Dy, Ho, Er, and Yb). *J. Solid State Chem.,* **1998**, *139*, 79-84.

(250) Smith, M. D.; zur Loye, H.-C., Sr_3MCrO_6 (M = Sc, In, Lu, Yb, Tm, Er, Ho, Y): The First Chromium-Containing $A_3A'BO_6$ Oxides. *Chem. Mater.,* **2000**, *12*, 2404-2410.

(251) Battle, P. D.; Burley, J. C.; Cussen, E. J.; Darriet, J.; Weill, F., Incommensurate phases in the Ba-Mn-Pd-O system. *J. Mater. Chem.,* **1999**, *9*, 479-483.

(252) Kageyama, H.; Yoshimura, K.; Kosuge, K., Synthesis and Magnetic Properties of New Series of One-Dimensional Oxides $Ca_3Co_{1+x}B_{1-x}O_6$ (B=Ir, Ru). *J. Solid State Chem.,* **1998**, *140*, 14-19.

(253) Nguyen, T. N.; zur Loye, H.-C., A Family of One-Dimensional Oxides: Sr_3MlrO_6 (M = Ni, Cu, Zn): Structure and Magnetic Properties. *J. Solid State Chem.,* **1995**, *117*, 300-308.

(254) Mesbah, A.; Malliakas, C. D.; Lebègue, S.; Sarjeant, A. A.; Stojko, W.; Koscielski, L. A.; Ibers, J. A., Syntheses, structures, and electronic properties of Ba_3FeUS_6 and Ba_3AgUS_6. *Inorg. Chem.,* **2014**, *53*, 2899-2903.

(255) Breton, L. S.; Smith, M. D.; zur Loye, H.-C., Synthesis of uranium mixed anion compounds synthesized using the Boron-Chalcogen Mixture method: $Ba_6Co_6U_{0.91}S_{13.5}O_{0.5}$ and $Ba_{5.47}K_{0.53}Zn_6US_{13.5}O_{0.5}$. *Solid State Sciences,* **2023**, *140*, 107207.

(256) Morrison, G.; zur Loye, H.-C., Simple correction for the sample shape and radial offset effects on SQUID magnetometers: Magnetic measurements on Ln_2O_3 (Ln=Gd, Dy, Er) standards. *J. Solid State Chem.,* **2015**, *221*, 334-337.

(257) Noel, H.; Troc, R., Magnetic properties of mixed uranium and 3d element chalcogenides of the MU_8X_{17} type. *J. Solid State Chem.,* **1979**, *27*, 123-135.

(258) Wang, X. X.; Li, J. J.; Shi, Y. G.; Tsujimoto, Y.; Guo, Y. F.; Zhang, S. B.; Matsushita, Y.; Tanaka, M.; Katsuya, Y.; Kobayashi, K.; Yamaura, K.; Takayama-Muromachi, E., Structure and magnetism of the postlayered perovskite $Sr_3Co_2O_6$: A possible frustrated spin-chain material. *Physical Review B,* **2011**, *83*, 100410(R).

APPENDIX A

SYNTHESIS, CHARACTERIZATION, AND MAGNETIC PROPERTIES OF SOME 2H-PEROVSKITE RELATED URANIUM SULFIDES: Ba_3MUS_6 (M = Mn, Fe, Co, Ni) and $Ba_3Co_{0.858(5)}Mg_{0.142(5)}US_6$

Abstract: The 2H-perovskite related uranium chalcogenide family of compounds was revisited using the recently developed Boron-Chalcogen Mixture (BCM) method for actinides to aid in their syntheses and obtain first time magnetic measurements. Two known 2H-perovskite related structures, Ba_3MnUS_6 and Ba_3FeUS_6 were resynthesized using the BCM method and exhibited antiferromagnetic transitions at $T_N = \sim 7.65$ K and 10.85 K, respectively. Combining the BCM method with the molten flux crystal growth technique resulted in single crystals of three new compositions, Ba_3NiUS_6, Ba_3CoUS_6, and $Ba_3Co_{0.858(5)}Mg_{0.142(5)}S_6$, the synthesis and characterization of which is reported herein. Magnetic measurements on Ba_3NiUS_6 shows a complex susceptibility plot with a weak, glassy, antiferromagnetic transition at about 65 K followed by an antiferromagnetic transition at $T_N = \sim 18.45$ K.

Introduction. The ABO_3 perovskites are an extensively studied group of materials due to their interesting physical properties, including superconductivity,[235, 236] ionic conductivity,[237, 238] thermoelectricity,[239, 240] and complex magnetic phenomena.[241, 242] The ABO_3 perovskite structure, where A and B are differently sized cations, is composed of a cubic arrangement of corner-sharing BO_6 octahedra with the A cation located in the middle of the cube coordinated by 12 oxygen atoms. Changing the size of the A or B cations will induce a change in the symmetry of the overall perovskite structure, resulting in many polymorphs of the ABO_3 structure. For example, beginning with the ideal cubic $SrTiO_3$ perovskite, the replacement of strontium with a smaller cation, such as calcium, will cause tilting of the BO_6 octahedra resulting in orthorhombic $CaTiO_3$. Substituting a larger cation for strontium, such as barium, will cause the BO_6 octahedra to switch from corner-sharing to face-sharing resulting in infinite chains of face sharing BO_6 octahedra with barium cations located between the chains. This modification crystallizes in the hexagonal crystal system and results in a class of compounds called the 2H-perovskites.[243] Randall and Kratz discovered a variant of the 2H-perovskite structure when they synthesized Sr_4PtO_6, which included trigonal prismatic coordination environments in the infinite chains, resulting in a new class, the so called 2H-perovskite related oxides.[244] These 2H-perovskite related compounds showed great flexibility to accommodate a diverse group of elements within the structure including transition metals,[245-247] rare earths,[248-250] platinum group metals,[251-253] and actinides.[104, 122, 254]

As we are interested in the magnetic behavior of uranium's 5*f* electrons, we chose to explore the magnetic properties of uranium containing 2H-perovskite related compounds. Due to the propensity of uranium to take on its diamagnetic 6+ oxidation state in oxide environments, we chose to target 2H-perovskite related uranium sulfides, as the lower Lewis basicity of sulfur (as compared to oxygen) stabilizes the uranium 4+ oxidation state in a majority of uranium sulfide materials.[37] Mesbah et al. has discovered many 2H-perovskite related uranium sulfides and selenides and reported on their synthesis and characterization. The magnetic behavior of the reported compounds, however, could not be determined due to side products and UOQ (Q = S, Se) impurities that could not be separated from the reaction products, which complicates magnetic measurements.[122, 254] Our group recently developed the Boron Chalcogen Mixture (BCM) method for actinides,[43] and has used this method to obtain a multitude of actinide containing chalcogenides.[43, 44, 210, 255] The success of this method prompted us to expand this method towards the system of 2H-perovskite related uranium sulfides to resynthesize some known compounds, to explore their magnetic behaviors, as well as to synthesize new compositions to add to the limited number of existing compounds. Herein we report on the synthesis and magnetic behavior of two known 2H-perovskite related uranium chalcogenides with the formula Ba_3MUS_6 (M = Mn, Fe), as well as the synthesis and characterization of three new additions to the family, Ba_3NiUS_6, Ba_3CoUS_6, and $Ba_3Co_{0.858(5)}Mg_{0.142(5)}US_6$, along with the magnetic behavior of Ba_3NiUS_6.

Single Crystal X-ray Diffraction (SXRD). X-ray intensity data from black block crystals of $Ba_3Co_{0.858(5)}Mg_{0.142(5)}US_6$, Ba_3CoUS_6, and Ba_3NiUS_6 were collected at 298(2) K, using a Bruker D8 QUEST diffractometer equipped with a PHOTON-II area detector and an Incoatec microfocus source (Mo Kα radiation, λ = 0.71073 Å). The raw area detector data frames were reduced and corrected for absorption effects using the SAINT+ and SADABS programs.[78, 79] Final unit cell parameters were determined by least-squares refinement of large sets of reflections taken from each data set. An initial structural model was obtained with SHELXT.[80] Subsequent difference Fourier calculations and full-matrix least-squares refinement against F^2 were performed with SHELXL-2018 using ShelXle.[81, 82] The crystallographic parameters of $Ba_3Co_{0.858(5)}Mg_{0.142(5)}US_6$, Ba_3CoUS_6, and Ba_3NiUS_6 are summarized in Table A.1.

Powder X-ray Diffraction (PXRD). PXRD data were collected on ground samples of the products. Data were collected using a Bruker D2 PHASER diffractometer using Cu Kα radiation over a 2θ range of 5−65° with a step size of 0.02°. Weight fractions for each phase in the product powders were calculated using a Whole Powder Pattern Fit (WPPF) preformed using the Rigaku SmartLab II software.[168] The PXRD patterns for the products obtained in reactions targeting Ba_3MnUS_6, Ba_3FeUS_6, and Ba_3NiUS_6 used for magnetic measurements can be seen in Figures A.1-A.3. Results of the WPPF can be found in Figures A.4-A.6.

Energy-Dispersive Spectroscopy (EDS). EDS was performed on single crystals of Ba_3MUS_6 (*M* = Co, Co/Mg, Ni) using a Tescan Vega-3 scanning electron microscope equipped with a Thermo EDS attachment. Scanning electron microscopy (SEM) was operated in a low-vacuum mode. Crystals were mounted on a SEM stub with carbon tape and analyzed using a 20 kV accelerating voltage and a 120 s accumulation time. The EDS spectra for the crystals are shown in Figures A.7−A.9.

Table A.1 Crystallographic parameters for $Ba_3Co_{0.858(5)}Mg_{0.142(5)}US_6$, Ba_3CoUS_6, and Ba_3NiUS_6.

Chemical formula	$Ba_3Co_{0.858(5)}Mg_{0.142(5)}US_6$	Ba_3CoUS_6	Ba_3NiUS_6
Formula weight	896.44	901.34	901.11
Crystal system	Trigonal		
Space group, Z	*R*-3c, 6		
a, Å	12.0407(1)	12.0415(2)	12.0002(3)
c, Å	13.4895(3)	13.4266(3)	13.4221(3)
α, β, γ deg.	90, 90, 120	90, 90, 120	90, 90, 120
V, $Å^3$	1693.67(7)	1686.00(7)	1673.89(9)
ρ_{calcd}, g/cm^3	5.273	5.326	5.364
Radiation (λ, Å)	Mo Kα (0.71073 Å)		
μ, mm^{-1}	26.891	27.207	27.605
T, K	298	297	300
Crystal dim., mm^3	0.03—0.03—0.03	0.02—0.02—0.01	0.05—0.04—0.03
2θ range, deg.	3.384—36.352	3.384—36.343	3.395—36.344
Reflections collected	22369	61530	53411
Data/parameters/restraints	920/21/0	916/20/0	904/20/0
R_{int}	0.0415	0.0389	0.0323
Goodness of fit	1.164	1.216	1.233
$R_1(I > 2\sigma(I))$	0.0087	0.0114	0.0108
wR_2 (all data)	0.0194	0.0308	0.0256

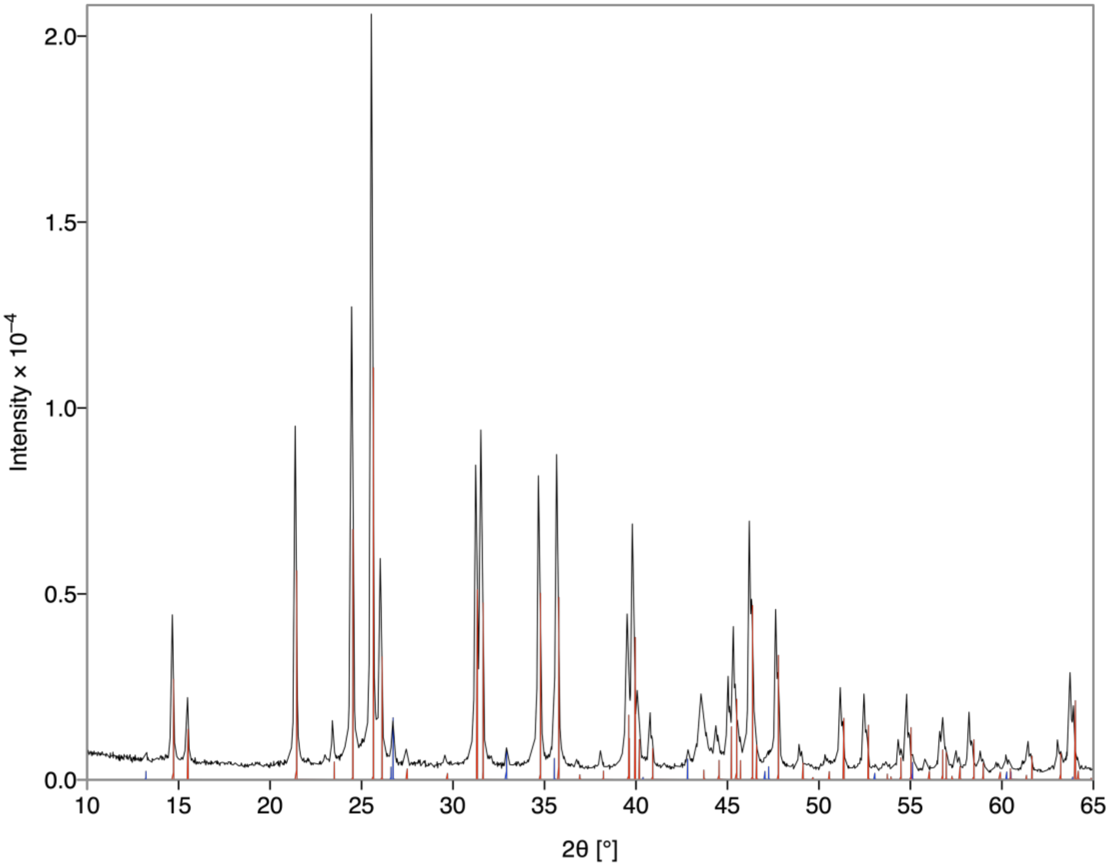

Figure A.1 The PXRD pattern of the powder product in the reaction targeting Ba_3MnUS_6 with the overlayed CIFs of Ba_3MnUS_6 (red lines) and UOS (blue lines).

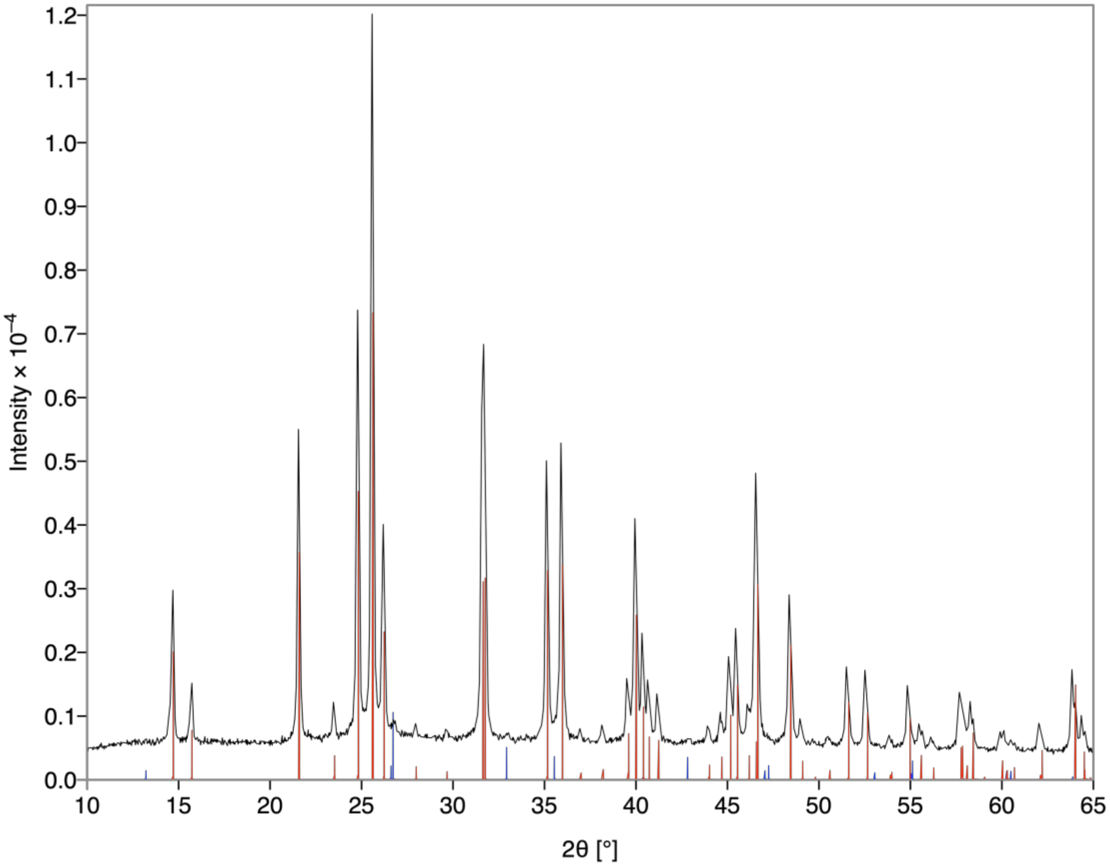

Figure A.2 The PXRD pattern of the powder product in the reaction targeting Ba_3FeUS_6 with the overlayed CIFs of Ba_3FeUS_6 (red lines) and UOS (blue lines).

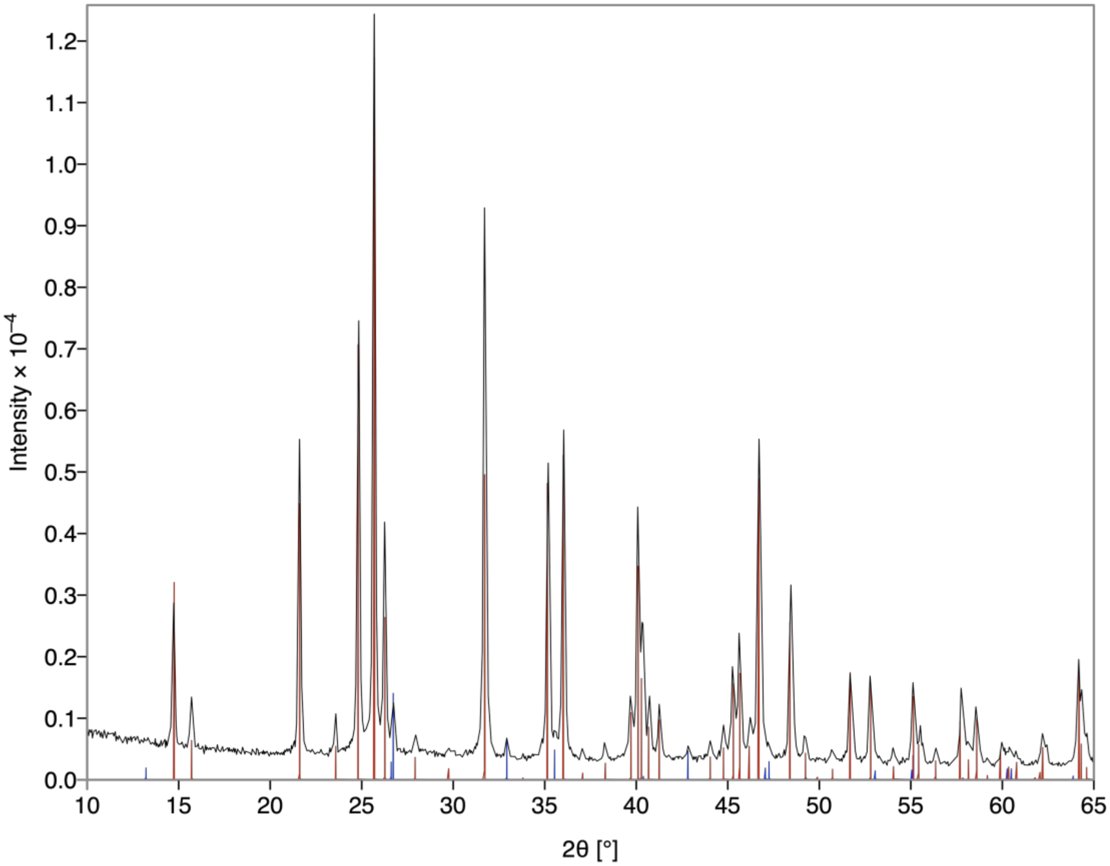

Figure A.3 The PXRD pattern of the powder product in the reaction targeting Ba_3NiUS_6 with the overlayed CIFs of Ba_3NiUS_6 (red lines) and UOS (blue lines).

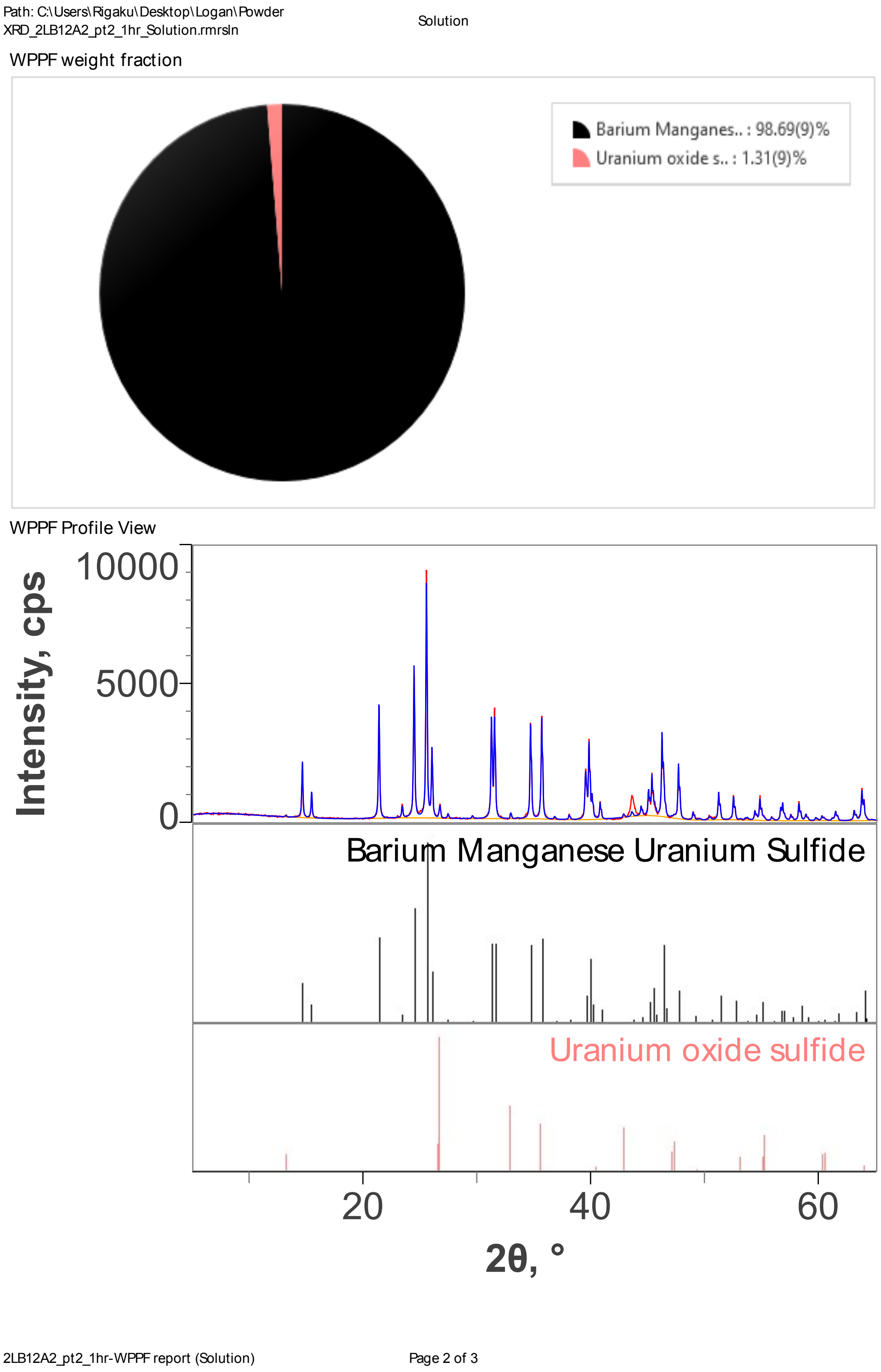

Path: C:\Users\Rigaku\Desktop\Logan\Powder XRD_2LB12A2_pt2_1hr_Solution.rmrsln

Solution

WPPF weight fraction

Barium Manganes.. : 98.69(9)%

Uranium oxide s.. : 1.31(9)%

WPPF Profile View

2LB12A2_pt2_1hr-WPPF report (Solution)

Page 2 of 3

Figure A.4 Results of the WPPF on the product powder of the reaction targeting Ba_3MnUS_6.

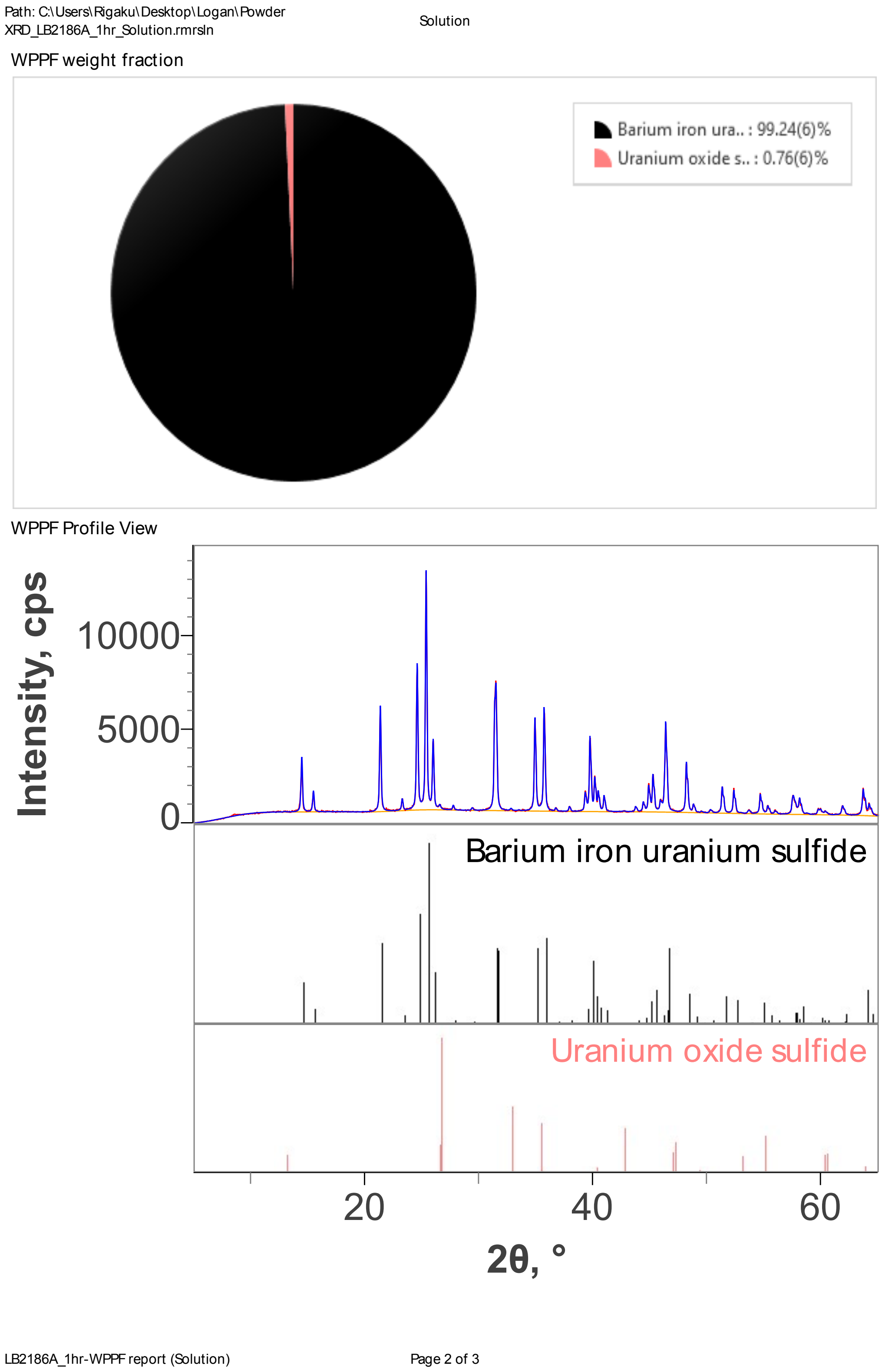

Path: C:\Users\Rigaku\Desktop\Logan\Powder XRD_LB2186A_1hr_Solution.rmrsln

Solution

WPPF weight fraction

WPPF Profile View

LB2186A_1hr-WPPF report (Solution)

Page 2 of 3

Figure A.5 Results of the WPPF on the product powder of the reaction targeting Ba_3FeUS_6.

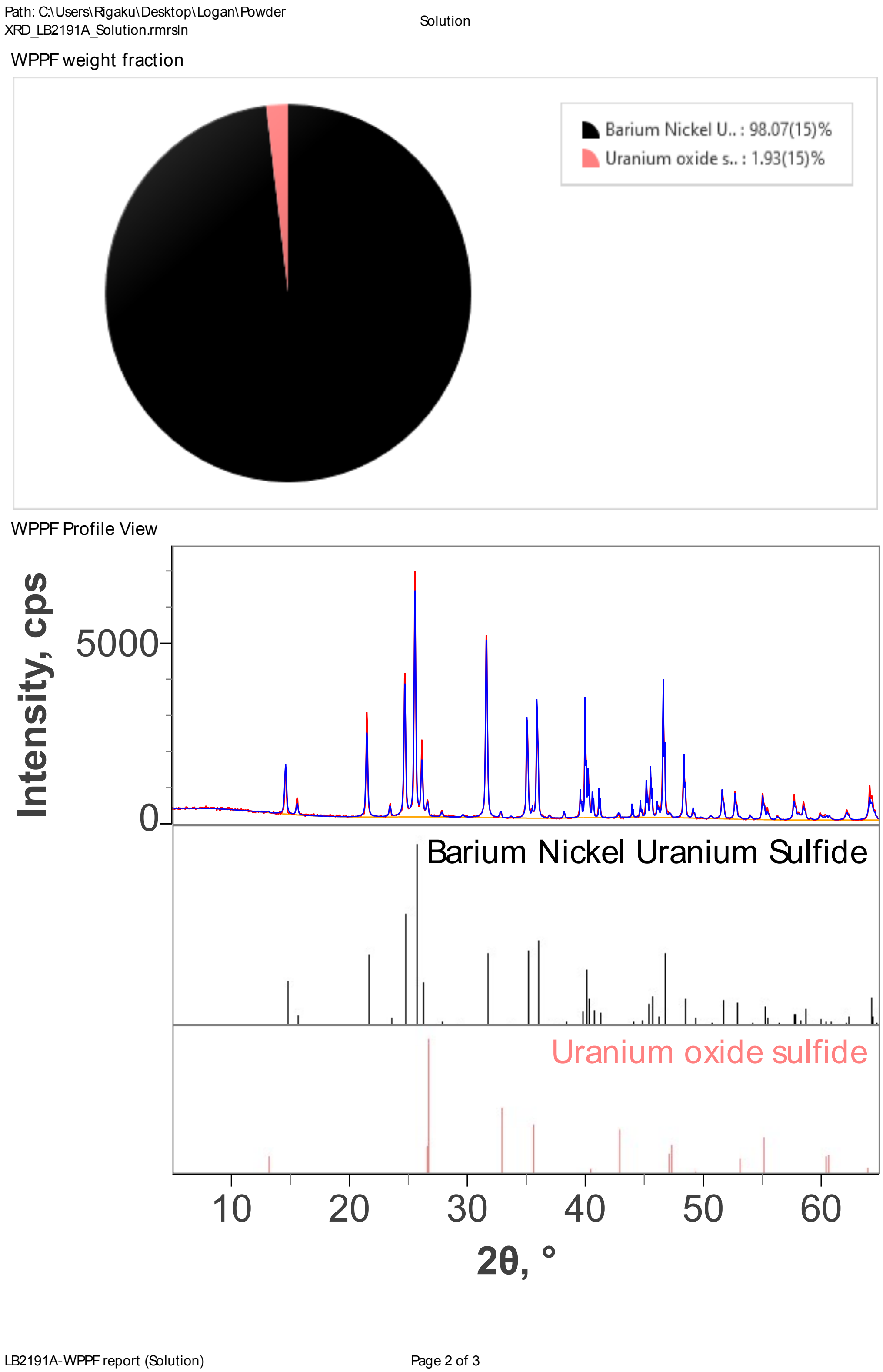

Path: C:\Users\Rigaku\Desktop\Logan\Powder XRD_LB2191A_Solution.rmrsln

Solution

WPPF weight fraction

🟥 Barium Nickel U.. : 98.07(15)%

🟥 Uranium oxide s.. : 1.93(15)%

WPPF Profile View

LB2191A-WPPF report (Solution)

Page 2 of 3

Figure A.6 Results of the WPPF on the product powder of the reaction targeting Ba_3NiUS_6.

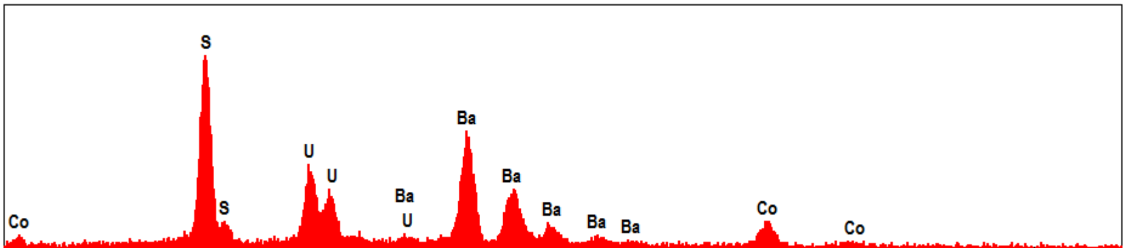

Figure A.7 EDS spectrum of Ba_3CoUS_6.

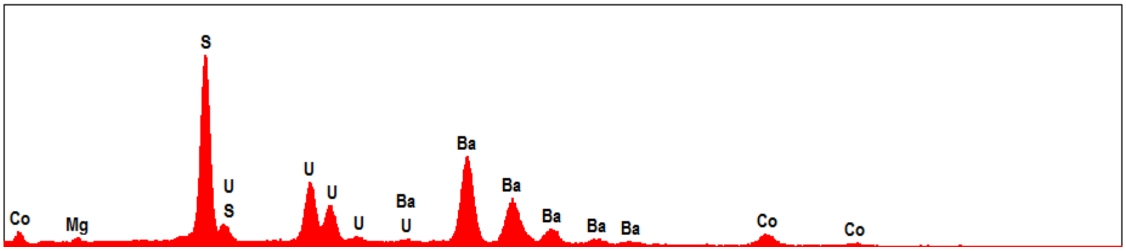

Figure A.8 EDS spectrum of $Ba_3Co_{0.858(5)}Mg_{0.142(5)}US_6$.

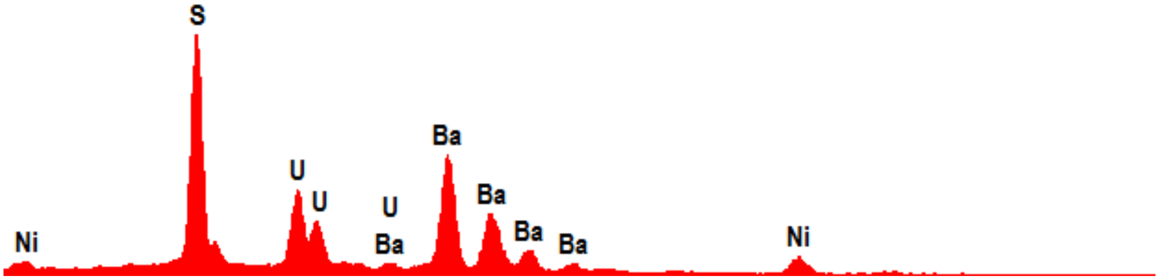

Figure A.9 EDS spectrum of Ba_3NiUS_6.

Magnetic Susceptibility Measurements. Magnetic property measurements for Ba_3MUS_6 (M = Mn, Fe, Ni) were performed using a Quantum Design magnetic property measurement system (QD MPMS 3 SQUID Magnetometer). The magnetic susceptibility was measured under zero-field-cooled (zfc) and field-cooled (fc) conditions from 2 to 300 K in an applied magnetic field of 0.1 T. Magnetization as a function of applied field was measured from −5 to 5 T at 2 K. Data were corrected for the sample shape and radial offset effects as described previously.[256]

Synthesis. U_3O_8 (International Bio-Analytical Industries, Inc., 99.99%), elemental boron (BTC, ~100-mesh, 99.9%), elemental sulfur (sublimed, Fischer Chemicals), BaS (Alfa Aesar, 99.7%), MnS (alfa Aesar, 99.9%), Fe powder (Alfa Aesar, spherical, 1-3 micron, 98%+), Cobalt (II) oxalate dihydrate (BTC), $BaCO_3$ (Alfa Aesar, 99.95%), CoO (BeanTown Chemicals, 99.995%) and CsCl (VWR, ultra pure) were used as received. CsCl was stored in an oven set to 260 ºC. K_2S was synthesized as described in the literature and stored in a nitrogen glovebag.[167]

Ba_3MnUS_6. Ba_3MnUS_6 was synthesized by combining BaS, MnS, and US_2 in a 3:0.9:1 molar ratio into a mortar and pestle inside a nitrogen filled glove bag. The mixture was ground for 20 minutes, pressed into a pellet, and then loaded into a carbon-coated fused silica tube (12 mm o.d. x 10 mm i.d. x 200 mm length) which was evacuated and sealed using a methane-oxygen torch. The sealed fused silica tube was placed in a furnace set to step to 950 ºC and dwell at this temperature for 48 hrs. The furnace was then shut off and allowed to return to room temperature. The resulting product powder was approximately 98.69(9)% Ba_3MnUS_6 and 1.31(9)% UOS by weight.

Ba_3FeUS_6. Ba_3FeUS_6 was synthesized by first creating the starting $UFeS_3$ reagent using the BCM method. U_3O_8, Fe metal, B, and S were loaded into a mortar and pestle in a 1:3.2:8:12 molar ratio, respectively. The mixture was ground for 20 minutes and subsequently placed inside a carbon crucible (9.53 mm o.d. x 6.35 mm i.d. x 50.80 mm length) which was loaded into a fused silica tube. The fused silica tube was evacuated and sealed using a methane-oxygen torch and placed into a furnace set to step to 700 ºC where it dwelled for 24 hours. The furnace was then shut down and allowed to return to room temperature. The product was pure $UFeS_3$ as determined by PXRD. The $UFeS_3$ was then added to a mortar and pestle along with BaS in a $UFeS_3$:BaS molar ratio of 1:3, respectively, in a nitrogen filled glovebag. This mixture was ground for 10 minutes, pelletized, and placed into a carbon-coated fused silica tube. The fused silica tube was evacuated and sealed and placed into a programmable furnace set to step to 900 ºC and dwell at this temperature for 12 hours. The furnace was subsequently turned off and allowed to return to room temperature. The resulting product powder was approximately 99.24(6)% Ba_3FeUS_6 and 0.76(6)% UOS by weight.

Ba_3NiUS_6. Ba_3NiUS_6 was synthesized by first creating the starting $UNiS_3$ reagent as described in the literature.[43] $UNiS_3$ and BaS were then loaded into a mortar and pestle in a 1:3 molar ratio, respectively, which was ground for 20 minutes in a nitrogen filled glove bag. The ground mixture was then pressed into a pellet and loaded into a carbon-coated fused silica tube which was then evacuated and sealed using a methane-oxygen torch. This sealed tube was placed into a furnace set to step to 900 ºC where it dwelled for 12 hours. The furnace was then shut down and allowed to return to room temperature. The resulting product powder was approximately 98.07(15)% Ba_3NiUS_6 and 1.93(15)% UOS by weight.

To grow single crystals, the same reagents and ratios (1 $UNiS_3$: 3 BaS) were used along with the addition of 0.50 g of CsCl as a flux. All reagents were loaded into a carbon crucible which was placed in a carbon-coated fused silica tube. The fused silica tube was evacuated and sealed and placed into a furnace set to step to 900 ºC, dwell for 48 hours, and then slow cool to 550 ºC in 30 hours. After, the furnace was shut off and allowed to return to room temperature. The carbon coated tube was then removed from the fused silica tube and placed into a beaker of ~ 60 mL of methanol and sonicated for about 20 minutes.

The products were then scraped out of the carbon crucible into the beaker using a spatula. The methanol was decanted off and ~ 60 mL of fresh methanol was added. After another 20-minute sonication the methanol was decanted off and the products were vacuum filtered and washed with acetone. The resulting products were black block crystals of Ba_3NiUS_6, clear crystals of $Ba_2B_5O_9Cl$, and polycrystalline UOS.

Ba_3CoUS_6. Ba_3CoUS_6 crystals were created by loading sulfur, boron, Ba_2CoUO_6, KI and K_2S, in that order, into a carbon crucible. A 12:8:1 molar ratio of S:B:Ba_2CoUO_6 was used as well as 0.030 g of K_2S and 0.250 g of KI. The sulfur, boron, and Ba_2CoUO_6 reagents were loaded into the carbon crucible in air while the KI and K_2S were handled inside a nitrogen filled glovebag. The carbon crucible was then capped with a carbon cap and placed inside a fused silica tube which was evacuated and sealed. The sealed fused silica tube was then placed into a programmable furnace set to ramp to 800 ºC in 10 hours, dwell at this temperature for 12 hours, then cool to 600 ºC in 20 hours. The furnace was then shut down and allowed to return to room temperature. The products were isolated using the same procedure used for Ba_3NiUS_6. The indexable products in the PXRD pattern were Ba_3CoUS_6, UOS, $K_{0.8}Ba_{3.2}US_6$, and SiO_2 (from the breaking of the fused silica tube).

$Ba_3Co_{0.858(5)}Mg_{0.142(5)}US_6$. $Ba_3Co_{0.858(5)}Mg_{0.142(5)}US_6$ was synthesized by accident due to the use of boron powder with a large impurity of magnesium. First $UCoS_3$ was synthesized by combining U_3O_8, CoC_2O_4 x H_2O, B (BTC, ~ 325 mesh, 99%), and sulfur in a 1:3:45.5:73.5 molar ratio respectively. This mixture was intimately ground and pelletized and placed into a carbon-coated fused silica tube. The fused silica was heated in a programmable furnace to 1100 ºC in 10 hours, where it dwelled for 3 hours, and the furnace was subsequently turned off and allowed to return to room temperature. The products of this reaction were $UCoS_3$, CoU_8S_{17}, and MgS. The product powder was then loaded into a carbon crucible along with 3 molar equivalents of BaS and 0.34 grams of CsCl. The carbon crucible was loaded into a fused silica tube which was evacuated and sealed and placed into a programmable furnace set to ramp to 900 ºC in 5 hours, dwell at this temperature for 20 hours, then cool to 550 ºC in 20 hours. The furnace was subsequently turned off and allowed to return to room temperature. The products were isolated using the same procedure as described for Ba_3NiUS_6, and the resulting products were $Ba_3Co_{0.858(5)}Mg_{0.142(5)}US_6$, USO, CoS, Co_3S_4, and $BaCoS_2$.

Crystal Structure Description. Ba_3CoUS_6, $Ba_3Co_{0.858(5)}Mg_{0.142(5)}US_6$, and Ba_3NiUS_6 join the $A_{3n+3m}A'_nB_{3m+n}Q_{9m+6n}$ (m = 0, n =1) family of 2H-perovskite related structures. All three compounds are isostructural crystallizing in the trigonal crystal system and adopting the space group *R*-3*m*. The structure is composed of uranium, US_6, trigonal prisms and metal, MS_6 (M = Co, Co/Mg, Ni/U), octahedra that face-share to each other, thus forming infinite chains down the c-axis; these chains are separated from each other by chains of barium cations. See Figure A.10 for the representative structure of Ba_3CoUS_6. In Ba_3CoUS_6, the Co—S distance is 2.5478(5) Å and the U—S distances are 2.7052(5) Å to 2.7053(5) Å. The structure of $Ba_3Co_{0.858(5)}Mg_{0.142(5)}US_6$ is very similar to that of Ba_3CoUS_6, although during the structure refinement it was found that, when freely refined, the cobalt site preferred to be underoccupied while the Ba and U sites preferred full occupation. A mix site of Co and Mg was modeled after Mg was discovered in the EDS spectrum. Modeling a Co/Mg mixed site resulted in a combined occupancy of 1, when freely refining, with a site mixing of 85.8(5)% Co / 14.2(5)% Mg. The U—S distances in $Ba_3Co_{0.858(5)}Mg_{0.142(5)}US_6$ are 2.7154(3) Å to 2.7155(3) Å and the Co/Mg—S distances are

2.5881(3) Å to 2.5582(3) Å. The structure of Ba_3NiUS_6 is very similar to that of its cobalt analogues, however, there exists uranium-nickel anti-site mixing of 94.5(1)% U/ 5.5(1)% Ni on the trigonal prismatic site and 5.5(1)% U/ 94.5(1)% Ni on the octahedral site. In this structure the U/Ni—S distances in the trigonal prisms are 2.7085(5) Å to 2.7086(5) Å and the U/Ni—S distances in the octahedra are 2.5260 (5) Å to 2.5261(5) Å.

Synthesis. The synthesis of each member of the $Ba_3\mathit{M}US_6$ family of compounds reported herein required individual careful consideration of the synthetic parameters used. The first analogue targeted was Ba_3MnUS_6 whose crystal structure was known and had been synthesized by the combination of the elements with the observed products being Ba_3MnUS_6 and UOS.[122] We first attempted a one pot reaction using the BCM method combining UO_2, BaS, MnS, B, and S in a 1:3:1:6:9 ratio, respectively. This mixture was intimately ground, pelletized, and then sealed in an evacuated carbon-coated fused silica tube and reacted at 900 ºC for 72 hours. The resulting products were Ba_2SiS_4 and MnU_8S_{17}. The barium thiosilicate is a very stable product and most likely results from a reaction between the silica ampule and the boron sulfides created during the reaction, which are known to be corrosive to the glass.[131] Once the barium was pulled out of the reaction by the formation of the thiosilicate phase, the emergence of MnU_8S_{17} is unsurprising as the $\mathit{M}U_8S_{17}$ phases are very stable and form at the same temperature used.[257] Due to this result, we

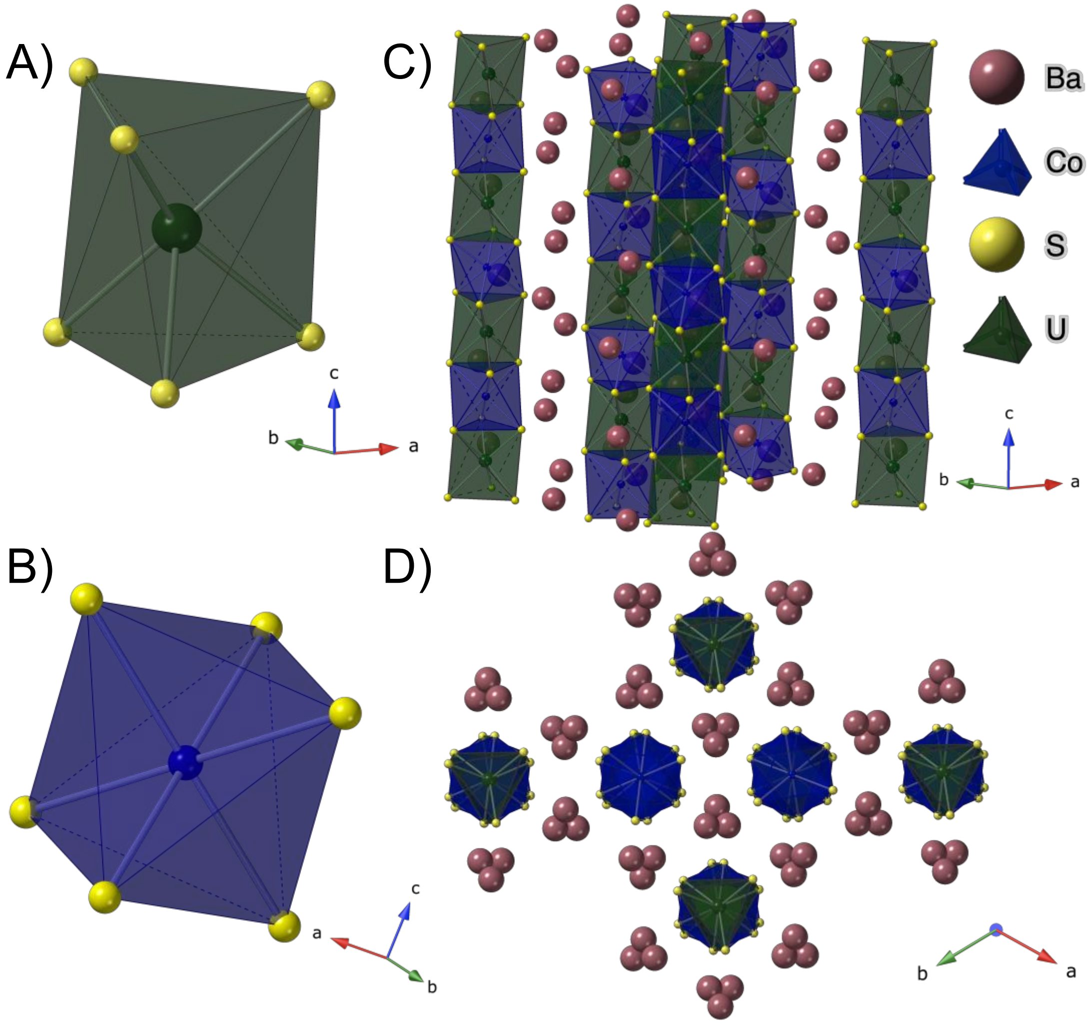

Figure A.10 A representative image showing the (A) US_6 trigonal prism, (B) MS_6 octahedra, (C), the infinite chains of face sharing trigonal prisms and octahedra with chains of barium atoms separating the uranium metal chains, and (D) a better view of the barium atom positions looking down the c-axis.

chose to utilize the BCM method to obtain pure US_2 as a starting reagent and combined this with BaS and MnS in a BaS:US_2:MnS molar ratio of 3:1:1. Using this approach resulted in a sample of Ba_3MnUS_6 with a very minor UOS impurity.

When trying to target other analogues using this same approach, we quickly realized that the commercial reagents we were purchasing were not always what was advertised. For example, a commercially obtained sample of CoS was analyzed using powder X-ray diffraction to reveal the actual composition as Co_8S_9. The same was true with nickel and iron sulfides, which were either non-stoichiometric or were a mixture of multiple polymorphs. The reactions targeting the $Ba_3\mathit{M}US_6$ family of compounds are very sensitive to the stoichiometry of the reagents and non-stoichiometric commercial reagents were causing side products to form, hindering progress on these materials. We therefore chose to use a different route to these materials that would not require commercial transition metal sulfides to be used. This route involved the use of the BCM method to create uranium transition metal sulfide perovskites, $U\mathit{M}S_3$ (M = Fe, Co, Ni), using elemental or transition metal oxide reagents, which were more reliable. Once obtained, the $U\mathit{M}S_3$ products were combined with a stoichiometric amount of BaS to synthesize $Ba_3\mathit{M}US_6$. This method worked well to synthesize the known Ba_3FeUS_6, as well as new compositions, Ba_3CoUS_6, $Ba_3Co_{0.858(5)}Mg_{0.142(5)}US_6$, and Ba_3NiUS_6. To obtain single crystals for structure determinations, the molten flux growth technique was employed and a CsCl flux was added to the reaction between $U\mathit{M}S_3$ and BaS resulting in single crystals of $Ba_3\mathit{M}US_6$ (M = Co/Mg, Ni) that were used for single crystal X-ray diffraction measurements. The reactions targeting single crystals of Ba_3CoUS_6 using this route resulted in polycrystalline samples of Ba_3CoUS_6 irrespective of changes in the synthetic parameters. By first creating Ba_2CoUO_6 and adding boron and sulfur with a different flux, a KCl/K_2S eutectic, single crystal X-ray diffraction quality crystals of Ba_3CoUS_6 were obtained.

As mentioned previously, the crystals of $Ba_3Co_{0.858(5)}Mg_{0.142(5)}US_6$ were grown by accident due to a large magnesium impurity present in the boron used to create the $UCoS_3$

perovskite in pursuit of Ba_3CoUS_6. The initial attempts at creating $UCoS_3$, as done previously, resulted in mixed $UCoS_3$, CoU_8S_{17}, and MgS. We had decided to simply use $UCoS_3$ in a reaction to obtain single crystals of Ba_3CoUS_6, but discovered the incorporation of Mg using the combination of EDS and SXRD.

Magnetic Properties. Magnetic measurements were performed on ground samples of Ba_3MUS_6 (M = Mn, Fe, Ni) which all contained small amounts of a UOS impurity. The molar susceptibility versus temperature plots can be seen in Figure A.11. UOS has an antiferromagnetic transition at T_N = 55 K which was not observed in any of the susceptibility plots due to the small quantity present. Ba_3MnUS_6 and Ba_3FeUS_6 exhibited antiferromagnetic transitions at T_N = 7.65 K and 10.85 K with measured room temperature (300 K) susceptibilities of 7.33 μ_B and 5.43 μ_B, respectively. Ba_3NiUS_6 exhibited a more complicated magnetic susceptibility with a weak antiferromagnetic inflection near 65 K followed by an increase in the susceptibility. There is a second antiferromagnetic transition at T_N = 18.45 K. The magnetic susceptibility of Ba_3NiUS_6 is similar to that of exhibited by $Sr_3Co_2UO_6$ which also shows two transitions, a weak glassy antiferromagnetic interaction and a more pronounced antiferromagnetic transition at lower temperature.[258] $SrCo_2UO_6$ was deemed a frustrated spin-chain material which suggests that Ba_3NiUS_6 could be affected by the spin-chain magnetic effects as well. To probe the magnetic behavior of these compounds further, neutron measurements are planned for the future. Calculating the moments of the magnetic ions present in these compounds is difficult to determine due to the range of observed magnetic values for both the transition metals and the uranium present within the chains. For this reason, the room temperature magnetic susceptibilities and Weiss constants calculated using the Curie-Weiss law are reported in Table A.2.

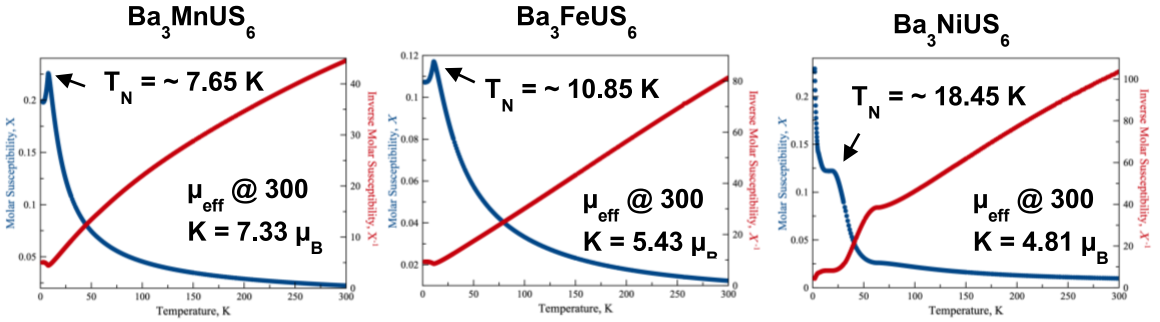

Figure A.11 Molar susceptibility (blue) and inverse molar susceptibility (red) versus temperature plots for Ba_3MUS_6 (M = Mn, Fe, Ni).

Table A.1 Magnetic susceptibilities of each measured compound at room temperature and their calculated Weiss constants.

Compound	Ba_3MnUS_6	Ba_3FeUS_6	Ba_3NiUS_6
μ_{eff} @ 300 K, μ_B	8.73	5.60	5.35
Weiss constant- Θ, ºC	-128.92	-20.58	-82.46

Conclusion. To elucidate the magnetic behavior of 2H-perovskite related actinide chalcogenides, the recently reported BCM method was employed to synthesize samples used for magnetic measurements. Two previously reported 2H-perovskite related actinide chalcogenides, Ba_3MnUS_6 and Ba_3FeUS_6, were successfully synthesized utilizing the BCM method and magnetic measurements revealed the presence of antiferromagnetic transitions at 7.65 K and 10.85K, respectively. In addition, three new additions to the Ba_3MUS_6 family of compounds were synthesized and characterized, namely Ba_3CoUS_6, $Ba_3Co_{0.858(5)}Mg_{0.142(5)}US_6$, and Ba_3NiUS_6, with Ba_3NiUS_6 showing very interesting magnetic phenomena including a weak magnetic transition at about 65.24 K and another antiferromagnetic transition at 18.45 K. Neutron diffraction measurements are planned to further probe the magnetic behavior of these 2H-perovskite systems and to determine the magnetic structure of these compounds.

APPENDIX B

PERMISSIONS TO REPRODUCE PUBLISHED MATERIALS

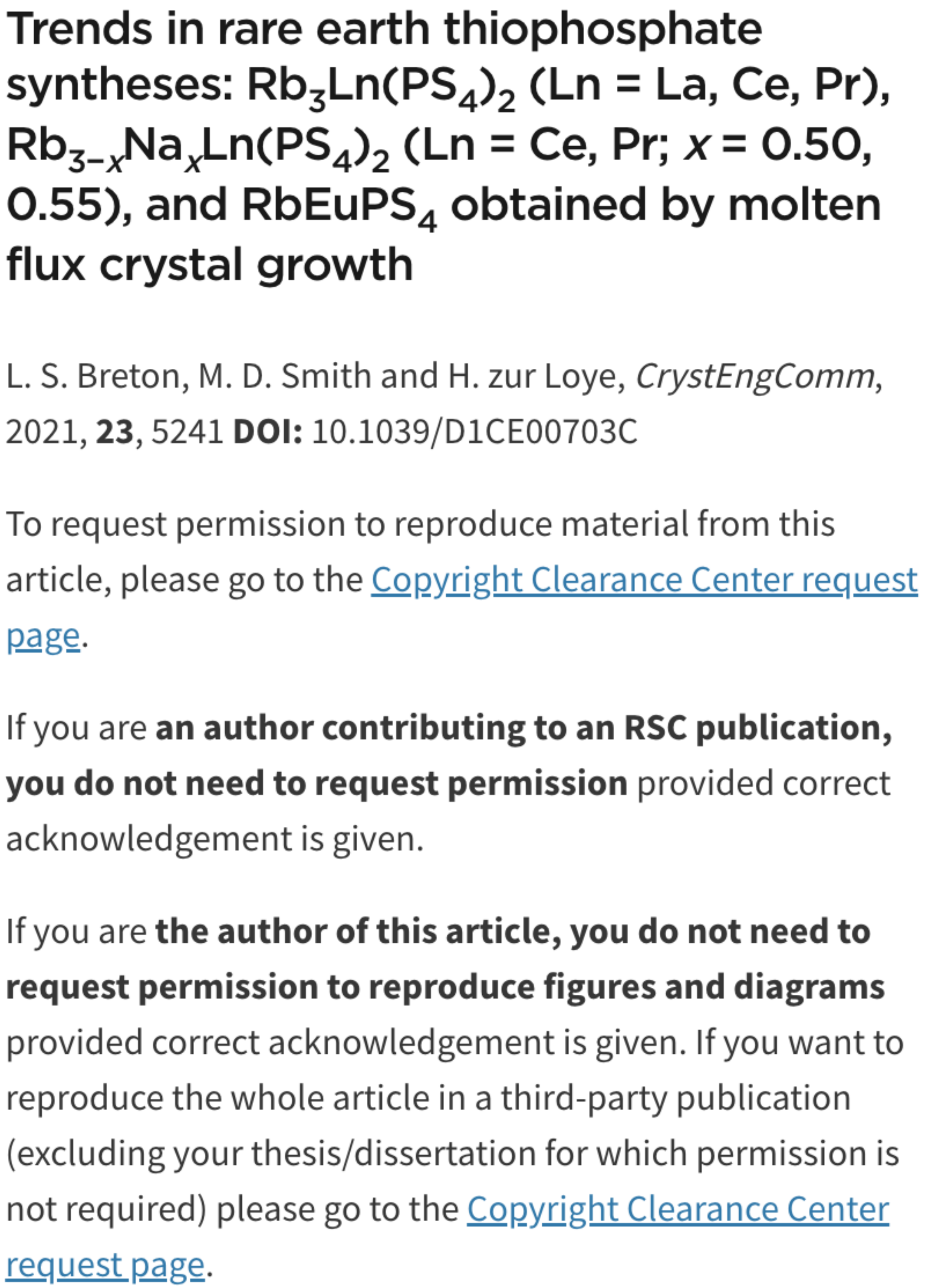

Trends in rare earth thiophosphate syntheses: $Rb_3Ln(PS_4)_2$ (Ln = La, Ce, Pr), $Rb_{3-x}Na_xLn(PS_4)_2$ (Ln = Ce, Pr; $x = 0.50, 0.55$), and $RbEuPS_4$ obtained by molten flux crystal growth

L. S. Breton, M. D. Smith and H. zur Loye, *CrystEngComm*, 2021, **23**, 5241 **DOI:** 10.1039/D1CE00703C

To request permission to reproduce material from this article, please go to the Copyright Clearance Center request page.

If you are **an author contributing to an RSC publication, you do not need to request permission** provided correct acknowledgement is given.

If you are **the author of this article, you do not need to request permission to reproduce figures and diagrams** provided correct acknowledgement is given. If you want to reproduce the whole article in a third-party publication (excluding your thesis/dissertation for which permission is not required) please go to the Copyright Clearance Center request page.

Chapter 2

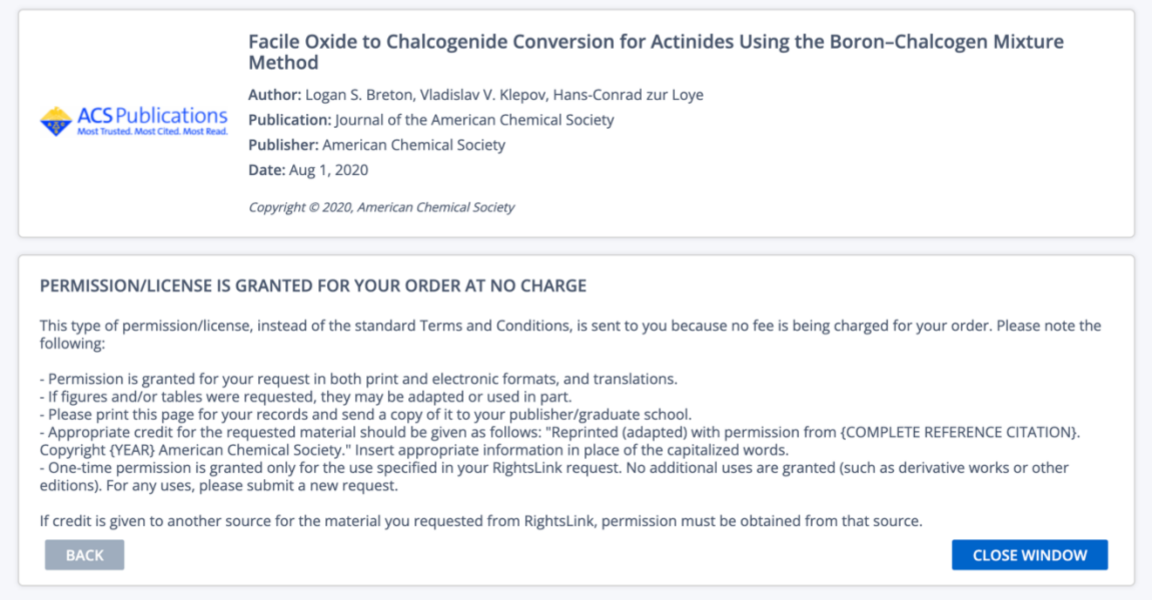

Facile Oxide to Chalcogenide Conversion for Actinides Using the Boron–Chalcogen Mixture Method

Author: Logan S. Breton, Vladislav V. Klepov, Hans-Conrad zur Loye
Publication: Journal of the American Chemical Society
Publisher: American Chemical Society
Date: Aug 1, 2020

Copyright © 2020, American Chemical Society

PERMISSION/LICENSE IS GRANTED FOR YOUR ORDER AT NO CHARGE

This type of permission/license, instead of the standard Terms and Conditions, is sent to you because no fee is being charged for your order. Please note the following:

- Permission is granted for your request in both print and electronic formats, and translations.
- If figures and/or tables were requested, they may be adapted or used in part.
- Please print this page for your records and send a copy of it to your publisher/graduate school.
- Appropriate credit for the requested material should be given as follows: "Reprinted (adapted) with permission from {COMPLETE REFERENCE CITATION}. Copyright {YEAR} American Chemical Society." Insert appropriate information in place of the capitalized words.
- One-time permission is granted only for the use specified in your RightsLink request. No additional uses are granted (such as derivative works or other editions). For any uses, please submit a new request.

If credit is given to another source for the material you requested from RightsLink, permission must be obtained from that source.

Chapter 3

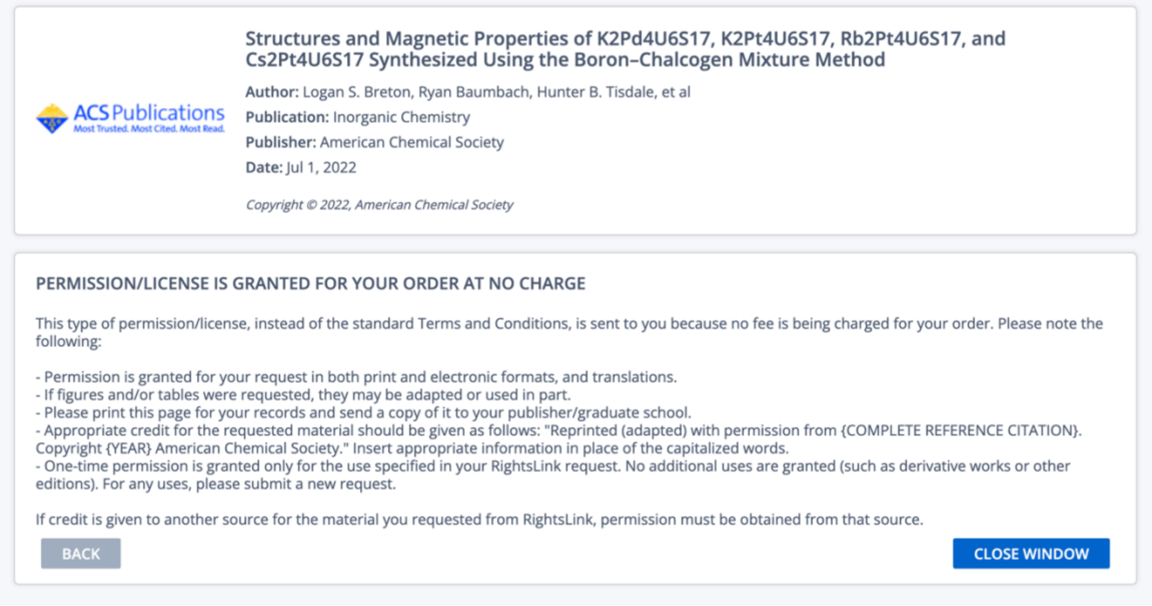

Structures and Magnetic Properties of K2Pd4U6S17, K2Pt4U6S17, Rb2Pt4U6S17, and Cs2Pt4U6S17 Synthesized Using the Boron–Chalcogen Mixture Method

Author: Logan S. Breton, Ryan Baumbach, Hunter B. Tisdale, et al
Publication: Inorganic Chemistry
Publisher: American Chemical Society
Date: Jul 1, 2022

Copyright © 2022, American Chemical Society

PERMISSION/LICENSE IS GRANTED FOR YOUR ORDER AT NO CHARGE

This type of permission/license, instead of the standard Terms and Conditions, is sent to you because no fee is being charged for your order. Please note the following:

- Permission is granted for your request in both print and electronic formats, and translations.
- If figures and/or tables were requested, they may be adapted or used in part.
- Please print this page for your records and send a copy of it to your publisher/graduate school.
- Appropriate credit for the requested material should be given as follows: "Reprinted (adapted) with permission from {COMPLETE REFERENCE CITATION}. Copyright {YEAR} American Chemical Society." Insert appropriate information in place of the capitalized words.
- One-time permission is granted only for the use specified in your RightsLink request. No additional uses are granted (such as derivative works or other editions). For any uses, please submit a new request.

If credit is given to another source for the material you requested from RightsLink, permission must be obtained from that source.

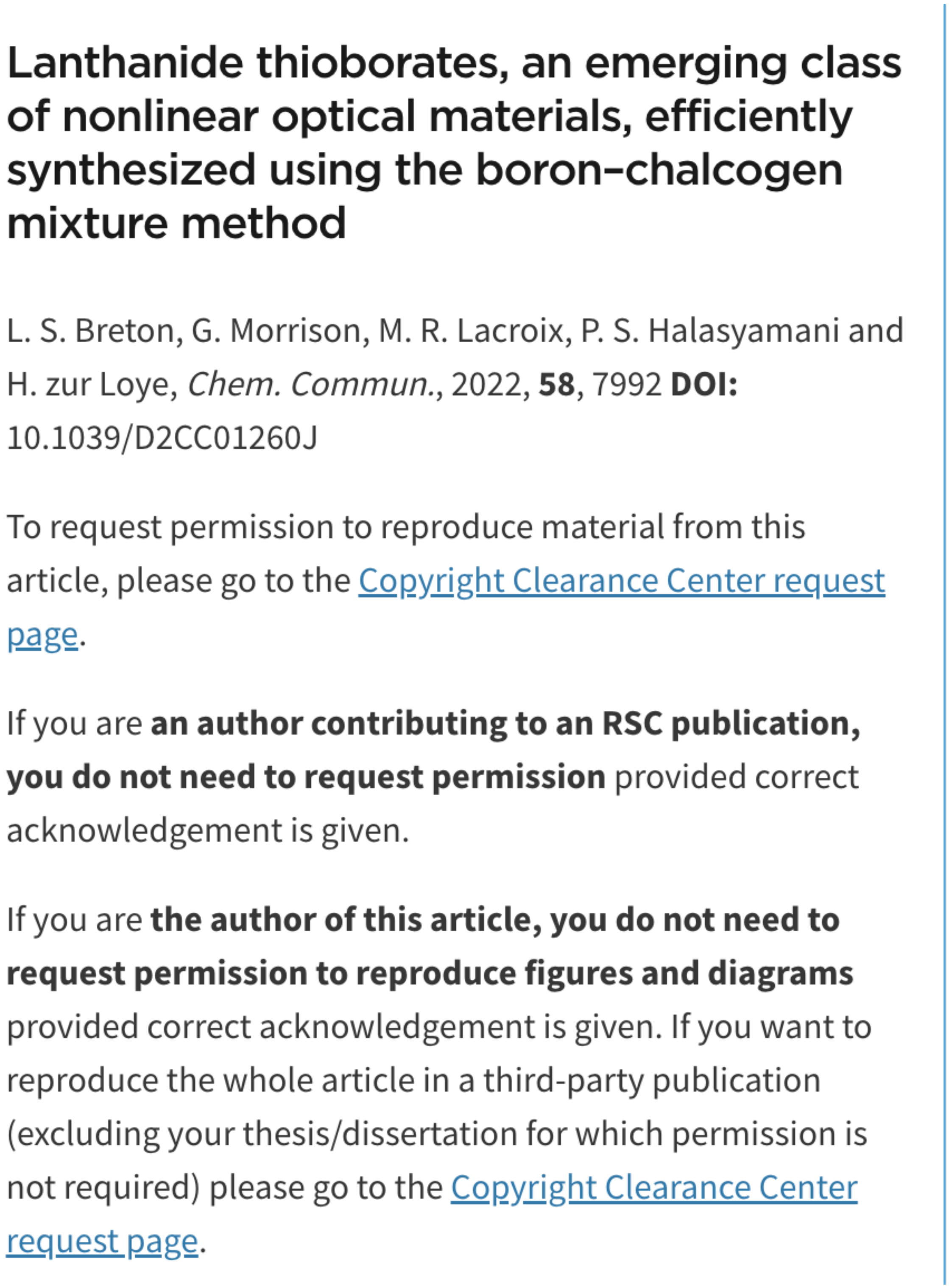

Lanthanide thioborates, an emerging class of nonlinear optical materials, efficiently synthesized using the boron–chalcogen mixture method

L. S. Breton, G. Morrison, M. R. Lacroix, P. S. Halasyamani and H. zur Loye, *Chem. Commun.*, 2022, **58**, 7992 **DOI:** 10.1039/D2CC01260J

To request permission to reproduce material from this article, please go to the Copyright Clearance Center request page.

If you are **an author contributing to an RSC publication, you do not need to request permission** provided correct acknowledgement is given.

If you are **the author of this article, you do not need to request permission to reproduce figures and diagrams** provided correct acknowledgement is given. If you want to reproduce the whole article in a third-party publication (excluding your thesis/dissertation for which permission is not required) please go to the Copyright Clearance Center request page.

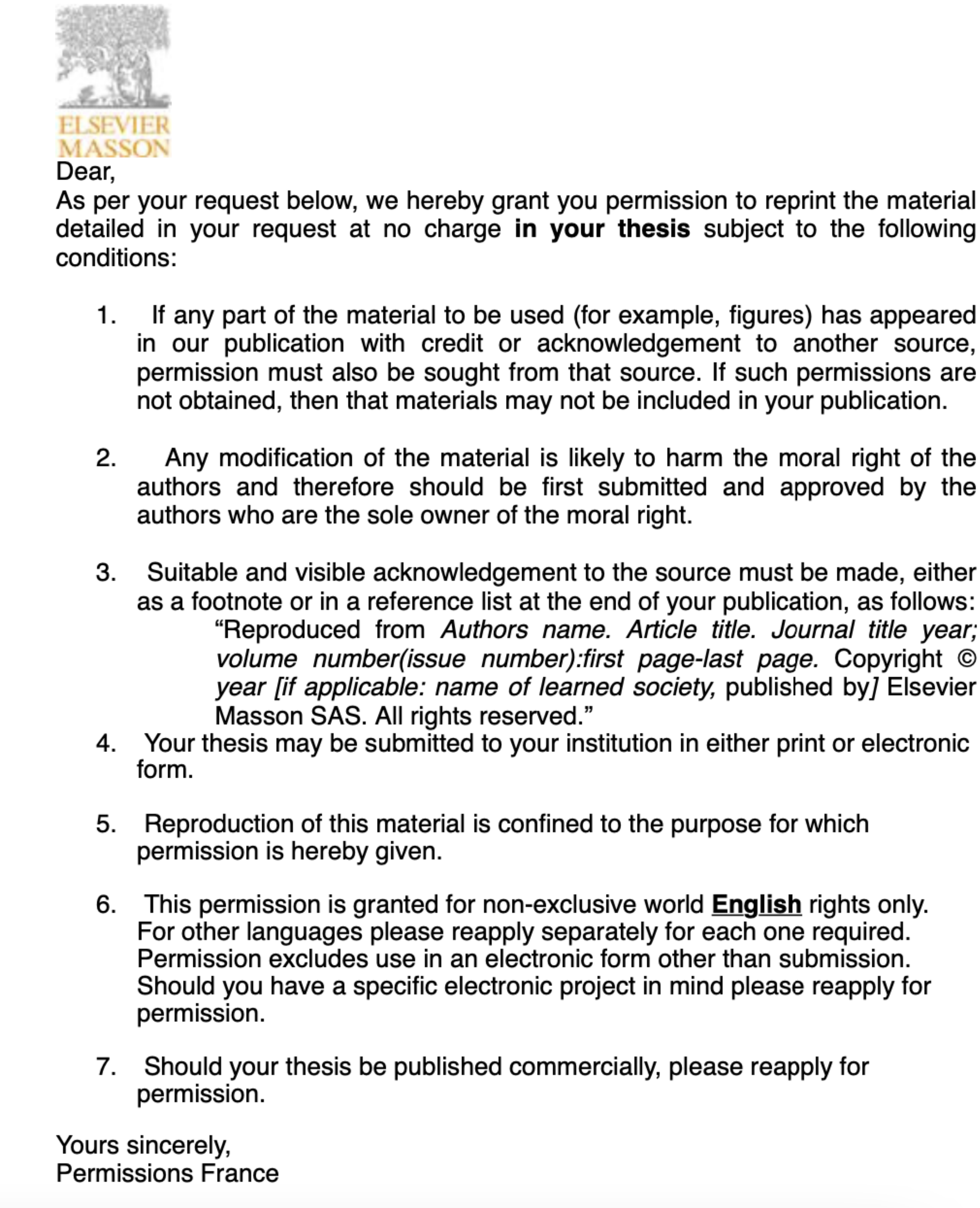

ELSEVIER
MASSON

Dear,

As per your request below, we hereby grant you permission to reprint the material detailed in your request at no charge **in your thesis** subject to the following conditions:

1. If any part of the material to be used (for example, figures) has appeared in our publication with credit or acknowledgement to another source, permission must also be sought from that source. If such permissions are not obtained, then that materials may not be included in your publication.

2. Any modification of the material is likely to harm the moral right of the authors and therefore should be first submitted and approved by the authors who are the sole owner of the moral right.

3. Suitable and visible acknowledgement to the source must be made, either as a footnote or in a reference list at the end of your publication, as follows:
   "Reproduced from *Authors name. Article title. Journal title year; volume number(issue number):first page-last page.* Copyright © *year [if applicable: name of learned society,* published by*]* Elsevier Masson SAS. All rights reserved."
4. Your thesis may be submitted to your institution in either print or electronic form.

5. Reproduction of this material is confined to the purpose for which permission is hereby given.

6. This permission is granted for non-exclusive world **English** rights only. For other languages please reapply separately for each one required. Permission excludes use in an electronic form other than submission. Should you have a specific electronic project in mind please reapply for permission.

7. Should your thesis be published commercially, please reapply for permission.

Yours sincerely,
Permissions France